Radiative Capture of Polarized Protons by Deuterium in the Energy Range E_p(lab)=80-0 keV

by

Gregory Joseph Schmid

Department of Physics
Duke University

Date: June 9, 1995

Approved:

Henry R. Weller, Supervisor

Calvin R. Howell

D. Randolph Tilley

Mark W. Ferguson

Kenneth P. Lynch

An abstract of a dissertation submitted in partial fulfillment of the requirements for the degree of Doctor of Philosophy in the Department of Physics in the Graduate School of Duke University

1995

Abstract

(Physics-Nuclear)

Radiative Capture of Polarized Protons by Deuterium in the Energy Range E_p(lab)=80-0 keV

by

Gregory Joseph Schmid

Department of Physics
Duke University

Date: June 9, 1995

Approved:

Henry R. Weller, Supervisor

An abstract of a dissertation submitted in partial fulfillment of the requirements for the degree of Doctor of Philosophy in the Department of Physics in the Graduate School of Duke University

1995

Abstract:

Radiative Capture of Polarized Protons by Deuterium

in the Energy Range E_p(lab)=80-0 keV

The D($\vec{p}$,γ)^{3}He reaction has been studied in the energy range E_p(lab)=80-0 keV (E_{cm}=53.3-0 keV). The quantities measured were the cross-section, $\sigma(\theta,E)$, the astrophysical S-factor, $S(\theta,E)$, the vector analyzing power, $A_y(\theta,E)$, and the γ-ray polarization $P_\gamma(\theta)$. The primary goal of the present work has been to extract, with better accuracy than the existing results, the D(p,γ)^{3}He electric dipole (E1) and magnetic dipole (M1) cross-section and S-factor components over the energy region E_p(lab)=80-0 keV. The novel contributions of the current work include the following: the use of polarized beams for the purpose of measuring $A_y(\theta)$ (sensitive to E1/M1 mixing); and the use of a high purity germanium (HPGe) γ-ray detector. The high intrinsic resolution of the HPGe detector (4.2 keV at E_γ = 5.5 MeV) has allowed us to directly observe the energy dependence of the D(p,γ)^{3}He reaction in our spectra. By measuring angular distributions with this detector, we have thus been able to obtain the $\sigma(\theta)$, $S(\theta)$, and $A_y(\theta)$ observables as a function of E_p(lab).

The primary result of the current experiment is that the total D(p,γ)^{3}He S-factor is significantly lower than previously measured throughout the energy region studied. In particular, we obtain an S(0) value of 0.136 ± 0.013 eV b (including systematic error) as compared with the previous result of 0.25 ± 0.04 eV b. This result should have bearing on astrophysical calculations dealing with protostellar evolution. We have also compared all of our acquired data with the results of modern D(p,γ)^{3}He three-body calculations. The agreement with the $A_y(\theta)$ data is good, while the cross-section and S-factor data fall 20-30% below the predicted values.

Acknowledgments

This project would not have been possible without the help and understanding of many people. First of all I would like to thank my thesis advisor Henry Weller for all of his advice and guidance over the past five years. I have greatly appreciated the opportunity to participate in his research effort here at TUNL. Furthermore, I would like to thank all the other members of the TUNL Radiative Capture group, both present and past, for their help. To Mark Balbes, Laird Kramer and Zandy Williams: thank you for helping me get started at TUNL...your patience and understanding was appreciated. To Bob Chasteler, Jerry Feldman, and Chip Laymon (the "post-docs"): thank you for sharing your wealth of knowledge with me. I owe special thanks to Chip Laymon for devoting a non-negligible fraction of his time to helping me with my data analysis. In particular, his help with the deconvolution analysis, and with EGS4, was of great help. I also owe special thanks to Bob Chasteler for his experimental abilities which were of great help in the early phases of this experiment. To Mark Godwin: thanks for your collaboration and friendship over the past six years. To Ken O'Hara, Kunal Pujara, and Bryan Rice: Thanks for your help, and good luck in the future. To Dick Prior, Evans Hayward, Don Lehman, Tony Fonseca, and Ron Tilley : thanks for taking an interest in my work, and thanks for taking the time to discuss physics with me. I have learned a lot from all of you.

I would also like to thank Russell Roberson and Ed Bilpuch (the director, and former director, of TUNL) for having me as a student here. In addition, I would like to give my most heartfelt thanks to all of the support staff at TUNL. To Paul Carter, John Dunham, Sidney Edwards, Bob Hogan (and the whole instrument shop), Pat Mulkey, Richard O'Quinn and Chris Westerfeldt: I have greatly appreciated your high quality

work. I would also like to acknowledge the help and support of the TUNL secretaries who have been here during my tenure: Patti Atkinson, Mari Cheeves, Jessica Farnham, Pat Gibson, Karen Mitchell, Bobbie Collins-Perry, and Mary-Robyn Tutor. Finally, I would like to thank my fellow graduate student classmates here at Duke for all their help and support over the years. The best of luck to all of you! Special thanks goes to Corinne Wallis for all of her friendship, support, and chocolate-chip cookies. I have greatly appreciated her support while writing this thesis. Thanks Cori!

I would like to dedicate this thesis to my parents, Greg (Sr.) and Joyce Schmid. Their support and encouragment has always been greatly appreciated.

Table of Contents

Abstract i
Acknowledgments ii
Table of Contents iv
Figures vii
Tables ix
Chapter 1: Introduction 1
1.1 Three-Body Nuclear Physics 1
1.1.1 Nucleon-Nucleon Potential Models 2
1.1.2 The Coulomb Interaction in the Three-Body System 4
1.1.3 Meson Exchange Currents 5
1.2 Nuclear Astrophysics 7
1.2.1 The source of Stellar Energy 7
1.2.2 The Astrophysical S-factor 9
1.2.3 The Proton-Proton Chain 11
1.2.4 Protostellar Evolution 13
1.3 Previous $D(p,\gamma)^3He$ Experiment 14
1.4 Goals of the Current $D(\vec{p},\gamma)^3He$ Experiment 16
1.5 Overview of Current Experimental Program 17
Chapter 2: Experimental Techniques and Data Acquisition 19
2.1 Polarized Proton Beams 20
2.1.1 Atomic Beam Polarized Ion Source 21
2.1.2 Proton Beam Polarimeter 24
2.2 Experimental Set-up for $D(\vec{p},\gamma)^3He$ 27
2.2.1 D_2O Ice Target 28
2.2.2 Beam Current Integration 30
2.2.3 The High Purity Germanium Detector 33
2.3 Electronics 34
2.4 Computer Interface 39
Chapter 3: Data Analysis 41
3.1 Raw Energy Spectra 42
3.2 Observables Measured 46

3.2.1 Differential Cross Section and S-factor... 47
3.2.2 Vector Analyzing Power..... 60
3.2.3 Gamma-ray Polarization..... 62
3.3 Analysis Using Thick Target Yields..... 62
3.4 The Binning Analysis..... 63
3.5 The Deconvolution Analysis..... 67
3.5.1 Parameterized $D(\vec{p},\gamma)^3He$ Yield Function..... 68
3.5.2 HPGe Response Function..... 69
3.5.3 Convolution Fit to Data..... 76
Chapter 4: Gamma-ray Polarization..... 79
4.1 Definition of $P_\gamma(\theta)$..... 79
4.2 Previous Measurements of $P_\gamma(\theta)$..... 82
4.3 TME Expansion for $P_\gamma(\theta)$..... 84
4.4 Compton Polarimeter..... 86
4.5 Polarization Sensitivity..... 90
4.5.1 Procedure for Obtaining Polarized γ-rays..... 91
4.5.2 Measuring the Polarization Sensitivity..... 94
4.5.3 Extrapolating S to E_γ=5.5 MeV..... 99
4.6 Acquiring $P_\gamma(\theta)$ data for $D(p,\gamma)^3He$..... 100
4.6.1 Introduction to the Data Acquisition Process..... 101
4.6.2 Experimental Details..... 102
Chapter 5: Experimental Results..... 108
5.1 The Legendre Polynomial Expansions..... 108
5.1.1 Definitions..... 108
5.1.2 The Q_k Coefficients..... 110
5.1.3 Extracting the Legendre Coefficients..... 112
5.2 Transition Matrix Element Expansions..... 114
5.2.1 Introduction..... 114
5.2.2 Transition Matrix Elements for $D(\vec{p},\gamma)^3He$..... 116
5.2.3 Constraining the Fit. 117
5.2.4 Performing the TME fit..... 119
5.3 Thick Target Yield Results..... 122
5.4 Results from the Binning Analysis..... 130

5.5 Deconvolution Results 144
5.6 Summary of Current Experimental Results 150
5.7 Comparison to Previous Experimental Results 151
Chapter 6: Theory 158
6.1 The Direct Capture Model 160
6.1.1 Introduction 160
6.1.2 The Continuum Wavefunction 162
6.1.3 The Bound State Wavefunction 165
6.1.4 The Electromagnetic Operator 166
6.1.5 Calculating the Observables 168
6.1.6 Direct Capture Results 169
6.1.7 Discussion 176
6.1.8 Previous Direct Capture Work 178
6.2 Three-Body Calculations 180
6.2.1 Faddeev Calculation 180
6.2.2 Variational Calculation 188
6.3 Theoretical Conclusions 198
Chapter 7: Conclusions 200
7.1 Summary and Discussion of Results 200
7.2 Astrophysical Implications 206
7.3 Final Comments 207
Appendix A: Computer Code for Kinematic Response Function 208
Appendix B: Deconvolution Computer Code 222
References 237
Biography 242

Figures

Figure 1.1: The $D(p,\gamma)^3He$ data of Griffiths et al..... 15
Figure 2.1: Coordinate system for proton polarization..... 20
Figure 2.2: The Zeeman and hyperfine structure of hydrogen..... 22
Figure 2.3: The electronics for the proton polarimeter..... 26
Figure 2.4: The experimental set-up for the $D(\vec{p},\gamma)^3He$ experiment..... 29
Figure 2.5: The target chamber set-up for the $D(\vec{p},\gamma)^3He$ experiment..... 31
Figure 2.6: Diagram of the electronics set-up for the $D(\vec{p},\gamma)^3He$ experiment..... 35
Figure 3.1: Typical $D(\vec{p},\gamma)^3He$ spectrum acquired with HPGe detector..... 43
Figure 3.2: Typical NaI(Tl) spectrum from one of the four shield segments..... 46
Figure 3.3: The stopping cross section data for protons on D_2O ice..... 49
Figure 3.4: The efficiency times solid angle curve for the HPGe detector..... 52
Figure 3.5: The geometry of the Cu disk target..... 58
Figure 3.6: The $D(\vec{p},\gamma)^3He$ count rate vs. time..... 59
Figure 3.7: The $D(\vec{p},\gamma)^3He$ full energy peak showing the 7 binned regions..... 64
Figure 3.8: The intrinsic HPGe response function at 5.5 MeV..... 73
Figure 3.9: The result of the EGS4 simulation (HPGe kinematic response)..... 75
Figure 3.10: The total HPGe response function..... 76
Figure 3.11: $D(\vec{p},\gamma)^3He$ spectra of Fig.3.1 shown along with convolution fit.... 77
Figure 4.1: The $D(p,\gamma)^3He$ reaction plane shown with polarization directions.... 80
Figure 4.2: The HPGe and NaI(Tl) annular shield..... 88
Figure 4.3: The nuclear level scheme for the $^{12}C(p,p'\gamma)^{12}C$ reaction..... 92
Figure 4.4: Angular distribution of γ-rays from $^{28}Si(p,p'\gamma)^{28}Si$..... 96
Figure 4.5: Angular distribution of γ-rays from $^{12}C(p,p'\gamma)^{12}C$..... 99
Figure 4.6: Data for the polarization sensitivity, S..... 101
Figure 4.7: Figure of Merit plotted vs. θ_c..... 104
Figure 4.8: Figure of Merit plotted vs. E_{recoil}..... 105
Figure 4.9: Summed energy spectrum for HPGe+NaI(Tl) set-up..... 106
Figure 4.10: Coincidence energy spectra for NaI(Tl) segment..... 107
Figure 5.1: Angular momentum coupling diagram for $D(\vec{p},\gamma)^3He$..... 117
Figure 5.2: Thick target yield data for $D(\vec{p},\gamma)^3He$ shown with Legendre fit..... 124
Figure 5.3: Thick target yield data for $D(\vec{p},\gamma)^3He$ shown with TME fit..... 126

Figure 5.4: $D(p,\gamma)^3He$ and $p(d,\gamma)^3He$ data plotted for E_{cm}=16.6-26.7 keV..... 128
Figure 5.5: Thick target yield data for $D(\vec{p},\gamma)^3He$ shown with two TME fits..... 129
Figure 5.6: The binned $D(\vec{p},\gamma)^3He$ data at $\overline{E}_p$=75 keV..... 133
Figure 5.7: The binned $D(\vec{p},\gamma)^3He$ data at $\overline{E}_p$=65 keV..... 134
Figure 5.8: The binned $D(\vec{p},\gamma)^3He$ data at $\overline{E}_p$=55 keV..... 135
Figure 5.9: The binned $D(\vec{p},\gamma)^3He$ data at $\overline{E}_p$=45 keV..... 136
Figure 5.10: The binned $D(\vec{p},\gamma)^3He$ data at $\overline{E}_p$(lab)= 35 keV..... 137
Figure 5.11: The binned $D(\vec{p},\gamma)^3He$ data at $\overline{E}_p$=25 keV..... 138
Figure 5.12: The binned $D(\vec{p},\gamma)^3He$ data at $\overline{E}_p$=15 keV..... 139
Figure 5.13: Legendre coefficients from the binned $D(\vec{p},\gamma)^3He$ data..... 140
Figure 5.14: The $D(p,\gamma)^3He$ M1 fraction of the total cross section vs. energy.... 143
Figure 5.15: The $D(p,\gamma)^3He$ E1 and M1 cross sections plotted vs. energy..... 143
Figure 5.16: The deconvolution results for $D(\vec{p},\gamma)^3He$ at E=0..... 146
Figure 5.17: The $D(p,\gamma)^3He$ S-factor results vs.energy..... 149
Figure 5.18: $A_y(90^\circ)$ plotted vs. E_p(lab)..... 150
Figure 5.19: Current $D(p,\gamma)^3He$ S-factor results along with previous results..... 152
Figure 5.20: Extracted $D(p,\gamma)^3He$ E1 and M1 S-factors..... 154
Figure 6.1: The radial wavefunction for ^3He used in DC calculation..... 167
Figure 6.2: DC results for E1 $D(p,\gamma)^3He$ cross section..... 172
Figure 6.3: DC results for total $D(p,\gamma)^3He$ cross section.. 174
Figure 6.4: DC results for $D(p,\gamma)^3He$ $\sigma(\theta)$ at E_p(lab)=75 keV..... 175
Figure 6.5: DC results for $D(\vec{p},\gamma)^3He$ $A_y(\theta)$ at E_p(lab)=25 keV..... 175
Figure 6.6: The dominant MEC diagrams..... 181
Figure 6.7: Faddeev result for $D(p,\gamma)^3He$ M1 S(0)..... 187
Figure 6.8: Variational result for total $D(p,\gamma)^3He$ S-factor..... 195
Figure 6.9: Variational result for $D(\vec{p},\gamma)^3He$ $A_y(\theta)$ at E_p(lab)=25 keV..... 197
Figure 6.10: Variational result for $D(p,\gamma)^3He$ E1 S-factor..... 197
Figure 7.1: $D(p,\gamma)^3He$ E1 and M1 S-factor results..... 202
Figure 7.2: Current $D(p,\gamma)^3He$ S-factor data shown with previous results..... 203
Figure 7.3: Variational calculation and current results for $D(p,\gamma)^3He$ S-factor.... 205

Tables

Table 3.1: Parameter values for $\varepsilon d\Omega$ curve..... 53
Table 3.2: Component systematic errors leading to 9% total systematic error..... 56
Table 3.3: The deterium areal density for each energy bin in binning analysis.... 67
Table 5.1: The four dominant transition matrix elements in $D(\vec{p},\gamma)^3He$..... 119
Table 5.2: The acquired $D(\vec{p},\gamma)^3He$ thick target yield data..... 123
Table 5.3: The Legendre coefficients extracted from the thick target data..... 123
Table 5.4: Parameters extracted from the TME fit to the thick target data..... 125
Table 5.5: $\sigma(\theta,E)$ data obtained from the binning analysis..... 131
Table 5.6: $A_y(\theta,E)$ data obtained from the binning analysis..... 131
Table 5.7: The Legendre coefficients extracted from the binned data..... 132
Table 5.8: The total cross section extracted from each energy bin..... 141
Table 5.9: Parameters extracted from the TME fits to each energy bin..... 142
Table 5.10: The $D(p,\gamma)^3He$ E1 and M1 cross section components (TME fits)..... 142
Table 5.11: $S_0(\theta)$ and $S_1(\theta)$ parameters extracted from deconvolution..... 144
Table 5.12: $A_y(\theta)$ at E=0 from the deconvolution analysis..... 145
Table 5.13: Legendre coefficients extracted from the E=0 data..... 145
Table 5.14: Parameters extracted from the TME fit to the E=0 data..... 146
Table 5.15: The $D(p,\gamma)^3He$ E1 and M1 S(0) values from the E=0 TME fit..... 147
Table 6.1: Optical model parameters for the DC calculation..... 165
Table 6.2: Results of the DC calculation for $D(\vec{p},\gamma)^3He$..... 171

Chapter 1

Introduction

This thesis presents an experimental study of the $D(\vec{p},\gamma)^3He$ radiative capture reaction in the energy regime E_p(lab)=80-0 keV (E_{cm}=53.3-0 keV). The motivation to study the $D(\vec{p},\gamma)^3He$ reaction in the E_p(lab)<80 keV energy region is twofold: first of all, to provide a stringent testing ground for theoretical three-body calculations which have been (and are still being) performed in this very low energy regime; and secondly, to obtain an accurate value for the low energy $D(p,\gamma)^3He$ astrophysical S-factor which astrophysicists need in order to understand stellar processes. In the discussion below, the relationship between the $D(\vec{p},\gamma)^3He$ reaction and current theoretical work in the fields of three-body physics and astrophysics will be explored in detail. This will be followed by an overview of the previous low energy $D(p,\gamma)^3He$ work, and an outline of the goals for the current study. A brief presentation of the present experimental program will conclude this chapter.

1.1 Three-Body Nuclear Physics

It is well known that the Schrödinger equation can be solved exactly for the one and two-body nuclear systems, both in the bound and scattering states (see Chapter 6). The natural question to ask, then, is how far into the n-body nuclear system can we can push this "exact" treatment before we have to resort to effective models and macroscopic

treatments? The starting point for this quest is clearly the three-body nuclear system. However, despite a lot of recent progress in this field [Fri92,Pic92], the goal of a complete and precise theoretical description of the three-body nuclear system has not yet been realized.

This section will discuss several aspects of three-body nuclear physics which are of current theoretical interest: the validity of two-body nucleon-nucleon (NN) potential models in the three-body system; the description of the Coulomb effect (non-trivial for the three body system); and the description of meson exchange current effects. A good understanding of all these issues is necessary in order to properly describe the $D(\vec{p},\gamma)^3He$ reaction.

1.1.1 Nucleon-Nucleon Potential Models

Based on experimental observations of the two-nucleon system, one can derive the following form for the NN nuclear potential, V(r) [Kra88]:

$$V(r) = V_c(r) + V_S(r)(\vec{S}_1 \cdot \vec{S}_2) + V_T S_{12} + V_{SO}(\vec{L} \cdot \vec{S}) \qquad (1.1)$$

where $V_C(r)$ is the central potential, $V_S(r)$ is the spin dependent potential, $V_T(r)$ is the tensor potential, S_{12} is the non-central tensor operator, V_{SO} is the spin-orbit potential, $\vec{L}$ is the orbital angular momentum operator, and $\vec{S}$ is the spin operator. By parameterizing this potential, and then fixing the free parameters so as to match the NN elastic scattering data (over all energies), a very good picture of the nuclear two-body system can be formed.

The big question is this: will these two-body NN potentials, also known as "realistic" potentials (because they are fit to the two-body data) work well in the three-body system? In other words, can we solve the three-body Schrödinger equation using these potentials and get results that agree with experiment? Although techniques for solving the n-body Schrödinger equation in both the continuum and bound states have existed since the early 1960's (see Chapter 6), it is only recently that numerical computing power has advanced to the stage where accurate calculations are possible. Unfortunately, modern three-body calculations with realistic two-body NN potential models have encountered some problems. Perhaps the most serious problem is that the binding energies of the three-body bound systems (^{3}H and ^{3}He) cannot be accurately reproduced; they are under-predicted by ~10% [Pic92].

In order to solve this problem of binding energies, theorists have experimented with the concept of a nuclear three-body force (TBF) [Coo79,Coe83]. An often quoted classical example of a TBF that is of the earth-moon-satellite system. One would initially think that the total force on an orbiting satellite would be given by the vector sum of the earth-satellite and moon-satellite forces. However, the moon warps the shape of the earth (specifically with regards to the oceans), and thus the earth-satellite force is changed from what it would be if the moon were not present. Thus, in order to describe this system properly, a TBF must be included. It is clear that the TBF in this classical example arises as a consequence of the internal structure, and "deformability", of the earth. In nuclear physics, the nucleons under consideration (protons and neutrons) also have internal structure and "deformability" in the form of Δ-isobars [Fri92], and thus the concept of a nuclear TBF seems feasible. Using two pion exchange, theorists have developed models of a nuclear TBF which, when added to the well established two-body NN potential models, can almost exactly reproduce the experimental three body binding energies

[Sch95]. If this model of the three-body bound system is valid, one would expect that the ^{3}He wavefunctions derived from such potentials should be valid in calculations of the D($\vec{p}$,γ)^{3}He process (since D($\vec{p}$,γ)^{3}He represents a transition from a three-body scattering state to a three-body bound state). This is an issue that we would hope to explore in the current experiment.

In addition to the three-body bound system, one also seeks to describe the three-body scattering system. This is often done through elastic scattering experiments. While theoretical treatments have had a good deal of success in describing unpolarized observables [Kie94], there are some indications of possible problems describing the polarized observables. For example, nucleon-deuteron elastic-scattering experiments have shown that the analyzing powers are not adequately predicted with modern NN potential models [Tor91]. The validity of NN potential models in the scattering system can also be tested by means of the D($\vec{p}$,γ)^{3}He reaction. The same wavefunctions which are valid in the elastic-scattering process should also be valid for the continuum wavefunctions in the radiative capture process. Of course, in the radiative capture process, we are essentially testing the continuum and bound states simultaneously, and thus the information which we can glean about one state individually will be limited.

1.1.2 The Coulomb Interaction in the Three-body System

Until 1991, an exact treatment of the Coulomb interaction for the three-body system had never been performed. The difficulty in handling the Coulomb interaction, in p-d scattering, arises from the long-range polarization effect, whereby the charge of the incident proton polarizes the deuteron and thus induces an electric dipole moment. Also associated with the long range nature of the Coulomb interaction is the problem that when

the potential is expanded into partial waves, it is very slowly convergent. This makes calculations very susceptible to series-truncation errors (see Chapter 6). The first exact three-body treatment of the Coulomb interaction was done at zero energy by Friar et al. [Fri91] in 1991. This work has now been extended to finite energies by Schiavilla et al. [Sch95]. By comparing these calculations to the currently acquired $D(\vec{p},\gamma)^3He$ data, we can hope to get an idea of just how accurately this "three-body" Coulomb interaction has been taken into account.

1.1.3 Meson Exchange Currents

All realistic NN potential models use meson exchange currents (MEC's) to transmit the nuclear force between nucleons. Radiative capture reactions, which go by the electromagnetic operator, can be sensitive to these currents. As we will now discuss, the $D(\vec{p},\gamma)^3He$ reaction at low energies constitutes an especially sensitive testing ground for a theoretical description of MEC's.

Although electric dipole (E1) transitions can be described without explicit reference to MEC effects, magnetic dipole (M1) transitions cannot, and thus it is typically in M1 transitions that we look for signatures of MEC's. As discussed by Friar [Fri90], it was the discrepancy between theory and experiment in the M1 driven $^1H(n,\gamma)^2H$ reaction (at thermal energies) that first motivated a strong theoretical examination of the role of MEC's in nuclei [Bet50]. However, the MEC's are only expected to play a small role in the n-p capture cross section (~10%). A much more sensitive testing ground for MEC's is found in the $D(n,\gamma)^3H$ and $D(p,\gamma)^3He$ reactions at low (thermal) energies. This has to do with the form of the M1 operator in the impulse approximation (IA). In this form, the M1 operator is calculated using only the magnetic moments and orbital motions of the

nucleons (i.e. the effects of MEC's are not included). Since the dominant symmetric S-states of ^{3}He and ^{3}H are eigenfunctions of the IA M1 operator (see Chapter 6), this usually dominant part of the M1 strength is greatly quenched in D(p,γ)^{3}He and D(n,γ)^{3}H (once orthogonality of initial and final wavefunctions is enforced). Because of this, the typically small MEC part of the operator is greatly enhanced in importance.

Most three-body studies of MEC's in the past have focused on the thermal energy region (E~0). This is because M1 transitions are typically most important in this region, and hence MEC effects should be most noticeable. Because of its large thermal cross section, σ_T=.508 mb [Jur82], and because it goes largely by M1 radiation, the D(n,γ)^{3}H reaction has been the most thoroughly studied three-body reaction with regard to MEC effects. For example, a three-body calculation by Torre [Tor83] showed that the predicted cross section was increased by a factor of 2.6 by the explicit inclusion of MEC's. A more recent calculation of D(n,γ)^{3}H by Friar [Fri90] has indicated a somewhat smaller effect, with the MEC's increasing the cross section by a factor of approximately 1.6. The D(p,γ)^{3}He reaction has been much less studied for two reasons: (1) the thermal cross section is expected to be many orders of magnitude lower, and thus harder to study experimentally; and (2), a theoretical treatment of the Coulomb interaction must be included because of the two protons which are now present. Of course, these two factors are related: it is the Coulomb repulsion of the two protons which lowers the cross section of D(p,γ)^{3}He with respect to D(n,γ)^{3}H. In any event, one would expect that a successful description of MEC effects in D(n,γ)^{3}H should lead to a good description of MEC effects in D(p,γ)^{3}He. This is something that can be checked in the current D($\vec{p}$,γ)^{3}He experiment. The opportunity to learn more about MEC effects could perhaps be considered the primary theoretical motivation for the current study.

1.2 Nuclear Astrophysics

The $D(p,\gamma)^3He$ reaction at low energies plays a central role in such astrophysical processes as the stellar proton-proton chain and protostellar evolution. At somewhat higher energies it is also important in Big-Bang nucleosynthesis, but that is beyond the scope of the current discussion. In what follows, the relationship of the $D(p,\gamma)^3He$ reaction to the stellar proton-proton chain and to protostellar evolution will be explored. The core of much of this discussion can be found in a book by Claus Rolfs [Rol88]. This book offers a very complete discussion of astronomy and astrophysics from both a quantitative and qualitative point of view, and is highly recommended to the interested reader.

1.2.1 The Source of Stellar Energy

The determination of the power source of our sun has an interesting history. It was long ago realized that gravitational energy could not possibly be the source of the sun's large energy output [Rol88]. One possible argument for this conclusion is derived from the virial theorem, which states that the total thermal energy (i.e. kinetic energy) of the sun is equal to 1/2 the total gravitational potential energy. By taking the total possible energy output of the sun to be 1/2 the total gravitational potential energy, and taking into account the observed luminosity of the sun, a maximum solar lifetime of $\sim 10^7$ years is estimated. However, it is known from geological dating methods that the earth (and hence the sun) must be at least $\sim 10^9$ years old [Rol88]. Hence there is simply not enough gravitational energy in the sun to account for the observed lifetime.

Although it had been speculated in the early 1920's that nuclear processes (specifically, hydrogen-hydrogen fusion) could be responsible for the energy output of the sun, a serious problem was encountered. From a classical point of view, hydrogen-hydrogen fusion can only occur when the relative kinetic energy of the colliding protons exceeds the 550 keV Coulomb barrier, and this happens at a temperature of 6 billion Kelvin. The mean core temperature of the sun, however, was known from calculations utilizing the equation of state to be only about 15 million Kelvin. It is thus clear that *nuclear fusion in the sun is classically impossible.* However, in 1928, George Gamow [Gam28] showed, using quantum mechanics, that there is a finite probability of tunneling through the Coulomb barrier. This probability, P, can be derived by solving the Schrödinger equation for the Coulomb potential. At low energies, the relative s-wave tunneling probability takes the form [Bet37,Rol88]:

$$P \propto \exp(-2\pi\eta), \tag{1.2}$$

where η is the Sommerfeld parameter, defined as

$$\eta = \frac{Z_1 Z_2 e^2}{\hbar v}, \tag{1.3}$$

where Z_1 and Z_2 are the atomic numbers of the interacting nuclei, e is the electron charge, and v is the relative velocity. For future use, we note that the Sommerfeld parameter can also be written in terms of the center of mass energy, E_{cm}, as follows [Rol88]:

$$\eta = \frac{1}{2\pi}(31.29) Z_1 Z_2 \left(\frac{\mu}{E_{cm}} \right)^{1/2}, \tag{1.4}$$

where μ is the reduced mass in amu, and E_{cm} is in keV.

This tunneling phenomenon, although small, proved to provide an adequate p-p fusion rate so as to account for the energy production of the sun [Rol88]. It is thus concluded that *nuclear fusion in the sun is a quantum mechanical phenomenon.* As it turns out, the $D(p,\gamma)^3He$ reaction also plays a central role in stellar energy production, and this will be discussed in sub-section 1.2.3. However, as will be shown in sub-section 1.2.4, it is in the realm of proto-stellar evolution that the current $D(\vec{p},\gamma)^3He$ experiment can be expected to have the greatest impact.

1.2.2 The Astrophysical S-factor

In order to understand the details of stellar nucleosynthesis, astrophysicists need to know as much as possible about the nuclear reaction rates at the sun's core. Although the mean temperature of the sun (15 million Kelvin) would indicate a nuclear burning energy of E_{cm}~1 keV (because the Maxwell-Boltzmann distribution, representing the distribution of velocities in the stellar "gas", peaks at E_{cm}=kT), the actual effective burning energy is somewhat higher. This is because the nuclear reaction rates depend upon the product of a velocity distribution function (decreasing for E_{cm}>kT) and a reaction cross section function (increasing for E_{cm}>kT), and this causes the reaction rates to peak at an energy E_{cm}>kT. This peak in the nuclear reaction rates is referred to as the Gamow peak [Rol88], and for hydrogen-hydrogen (or hydrogen-deuterium) fusion in the sun, this peak occurs at E_{cm}~6 keV. Therefore, it is clear that if we wish to perform a direct laboratory study of the nuclear reactions which take place in the sun's core, we will need to use a center-of-mass beam energy of E_{cm}~6 keV. It should also be noted that in

the case of protostellar evolution, where temperatures are on the order of 1 million Kelvin, the Gamow peak occurs at the much lower energy of E_{cm}~1 keV.

From an experimentalist's point of view, a direct measurement of charged particle nuclear reactions at these low "stellar" energies can be very difficult, if not impossible, due to the Coulomb repulsion between the two particles. For example, based on the results of the current experiment (presented in Chapter 5), the total cross section for $D(p,\gamma)^3He$ at E_{cm}=1 keV is about 1 femto-barn (i.e. 10^{-15} b). Under the laboratory conditions of the current experimental set-up (outlined in Chapter 3), this translates into approximately one detected γ-ray every few hundred years! Clearly, a direct laboratory measurement at this energy is not possible. Fortunately, at slightly higher energies, the cross-section is much more amenable to laboratory experiments. For example, at E_{cm}=10 keV, the total $D(p,\gamma)^3He$ cross section (according to the current results) is about 6 nb. Under the same experimental conditions, this translates into a few detected γ-rays every hour. With this in mind, the technique that is typically employed to study reactions at stellar energies is to do the measurements at somewhat higher energies, and then extrapolate the results down to the desired energy.

One way to do this extrapolation utilizes the concept of the Astrophysical S-factor, $S(E_{cm})$ (also referred to as just "the S-factor"). The cross section can be defined in terms of the S-factor as shown below [Rol88]:

$$\sigma(E_{cm}) = \frac{S(E_{cm})e^{-2\pi\eta}}{E_{cm}}, \qquad (1.5)$$

with η as defined in Equation 1.4.

As discussed in [Rol88], the form of Equation 1.5 is defined so as to explicitly take into account explicitly the known energy dependencies of the cross section. The

exponential factor in Equation 1.5 is simply the low energy Coulomb tunneling probability (for s-waves) as defined in Equation 1.2. The $1/E_{cm}$ factor in Equation 1.5 is the energy dependence resulting from the "geometrical area" consideration of classical physics, except that in the transition to the quantum regime, we replace $\sigma=\pi(r_1+r_2)^2$ with $\sigma=\pi\lambda\!\!\!^{-2}$, where $\lambda\!\!\!^{-}$ is the reduced de Broglie wavelength. Since $E_{cm} \propto 1/\lambda\!\!\!^{-2}$, we get the $1/E_{cm}$ energy dependence in the cross section. With these energy dependent forms explicitly taken into account in Equation 1.5, the $S(E_{cm})$ term can then be interpreted as containing "all the strictly nuclear effects" [Rol88] (at least for relative s-wave reactions). It should be pointed out that the basic form of Equation 1.5 is essentially that which results from a direct capture model calculation at very low energies [Gri63].

The great advantage of the $S(E_{cm})$ function is that, in the absence of resonance structure, it is empirically found that $S(E_{cm})$ often varies linearly with energy [Rol88]. Thus, for example, if one desires to know the cross section of a reaction at zero energy, one can do the following: measure the cross section over a range of higher energies; calculate an S(E) value for each cross section point using Equation 1.5; fit these S(E) values to a simple (perhaps linear) function; and then extrapolate the function to zero energy. This is, in fact, what has been done in the current experiment in order to extract a cross section at thermal energies (E~0) for $D(p,\gamma)^3He$.

1.2.3 The Proton-Proton Chain

In medium mass stars, like our sun, the primary energy production mechanism is a sequence of nuclear reactions known as the proton-proton chain [Rol88]. The net result of this process is that four protons are effectively converted into a ^4He nucleus with the corresponding release of 26.73 MeV of energy. The first step in the proton-proton chain

is the $p+p \rightarrow D + e^{+}+\nu$ reaction, which goes by the weak force operator. The deuterium produced in this reaction then can participate in a second reaction, $D(p,\gamma)^{3}He$, which goes by the electromagnetic operator. Although the $D(p,\gamma)^{3}He$ reaction is prominently located as the second step on the proton-proton chain, its effect on the solar energy production is essentially nil. This is because its reaction rate is severely bottlenecked (by about 18 orders of magnitude) due to the fact that it follows a weak interaction in the sequence of events.

In recent years, there has been a renewed emphasis on understanding the proton-proton chain due to an astrophysical anomaly known as the "solar neutrino problem" [Rol88]. In theory, a good understanding of the solar core can be obtained by an experimental measurement of the solar neutrinos emanating from the sun. These neutrinos come not only from the first step in the proton-proton chain, as shown above, but also on subsequent steps, such as the $^{7}Be(p,\gamma)^{8}B$ reaction (where $^{8}B \rightarrow {}^{8}Be+e^{-}+\nu$). As it turns out, experimental neutrino detectors register only about half of the neutrinos predicted by the standard solar model. This is the "solar neutrino problem". It has been suggested that better experimental knowledge of the nuclear reactions in the proton-proton chain (specifically, the $^{7}Be(p,\gamma)^{8}B$ reaction) could perhaps solve this problem [Wel95]. The important point to make, in the context of the current discussion, is that the $D(p,\gamma)^{3}He$ reaction, despite it prominent position in the proton-proton chain, should not affect solar neutrino production. This is because of the bottlenecking effect mentioned earlier.

1.2.4 Protostellar Evolution

The $D(p,\gamma)^3He$ reaction is known to play a much more significant role in the process of protostellar evolution towards the main sequence (the Hayashi track [Hay62]). In protostellar evolution, a cloud of interstellar gas collapses on itself, and begins to heat up. Once the temperature reaches about 1 million Kelvin (a Gamow peak of E_{cm}~1 keV), the $D(p,\gamma)^3He$ reaction "ignites". The deuterium that is burned in this case is primordial deuterium (i.e. deuterium produced in the Big-Bang) which happens to be present in the protostellar gas. Since the $D(p,\gamma)^3He$ reaction is the first nuclear reaction to turn on, its burning can have a very significant effect on the protostellar evolution process. This has been recently discussed by Stahler [Sta88], who shows that deuterium burning via the $D(p,\gamma)^3He$ reaction has the effect of a "thermostat" in low mass protostars, whereby the temperature of the protostellar core is maintained at ~10^6 K. As a result of this thermostat effect, the mass-radius relation of the core is tightly constrained. This constraint has a noticeable affect on calculations [Sta88] relating to the "stellar birthline". The stellar birthline is a locus of points on an H-R diagram (a diagram which plots luminosity vs. surface temperature for stellar objects) which represent the sites where protostars first become luminous. The stellar birthline calculations, which are based in part on extrapolations for the low energy $D(p,\gamma)^3He$ S-factor, can be compared with current observational measurements of T-Tauri stars (developing protostars). Considering the large experimental uncertainties involved, the agreement is thought to be good [Sta88].

Another important aspect of $D(p,\gamma)^3He$ burning in protostars concerns the depletion of the primordial deuterium. As it turns out, the amount of primordial deuterium currently present in the universe is a sensitive barometer for our understanding of Big-Bang nucleosynthesis [Rol88]. This is due to the fact that since the era of the Big-

Bang, deuterium is primarily destroyed, not created. If we could measure its present abundance, we could set an upper limit on its primordial abundance. Several astrophysicists have suggested that some of the primordial deuterium which is present in heavy mass protostars could actually survive the $D(p,\gamma)^3He$ protostellar burning process and thus be found in the outer envelopes of heavy mass stars [Hay62,Bod66,Maz80]. These predictions were also based in part on extrapolations for the low energy $D(p,\gamma)^3He$ S-factor.

1.3 Previous $D(p,\gamma)^3He$ Experiment

There is one previously existing $D(p,\gamma)^3He$ experiment which covers the very low energy region, $E_p(lab)<50$ keV. This is the experiment of Griffiths et al [Gri63]. The results of this experiment play a key role in the extrapolation of the $D(p,\gamma)^3He$ S-factor to stellar energies. Our rationale for restudying the $D(p,\gamma)^3He$ reaction over approximately the same energy region as [Gri63] can be seen by examining a graph of the their final results. Figure 1.1 shows the S-factor results of [Gri63] plotted versus incident laboratory beam energy.

The open points in Figure 1.1 are the experimentally derived data points of [Gri63], while the dashed line is a theoretical energy dependence (that of a simplified direct capture model) normalized to the data. The primary results of the [Gri63] experiment were as follows: an extracted total S-factor versus energy; an extracted S-factor value at zero energy, S(0); and an extracted M1 S-factor at zero energy, M1 S(0). Since there is no data actually measured in the very low energy regime of stellar interest ($E_p(lab)<9$ keV), the extrapolation via the dashed line takes on considerable importance. The [Gri63] experiment will be discussed in detail in Chapter 5, but several key points

will now be made. The first is that the data in Figure 1.1 have large error bars, and thus don't allow a very precise determination of the S-factor over the region studied. The second is that the extrapolation to low energies, perhaps the primary result of the [Gri63] experiment, has a large experimental uncertainty. It can easily be argued that one could fit almost any curve through the data points shown in Figure 1.1, including a flat line. This

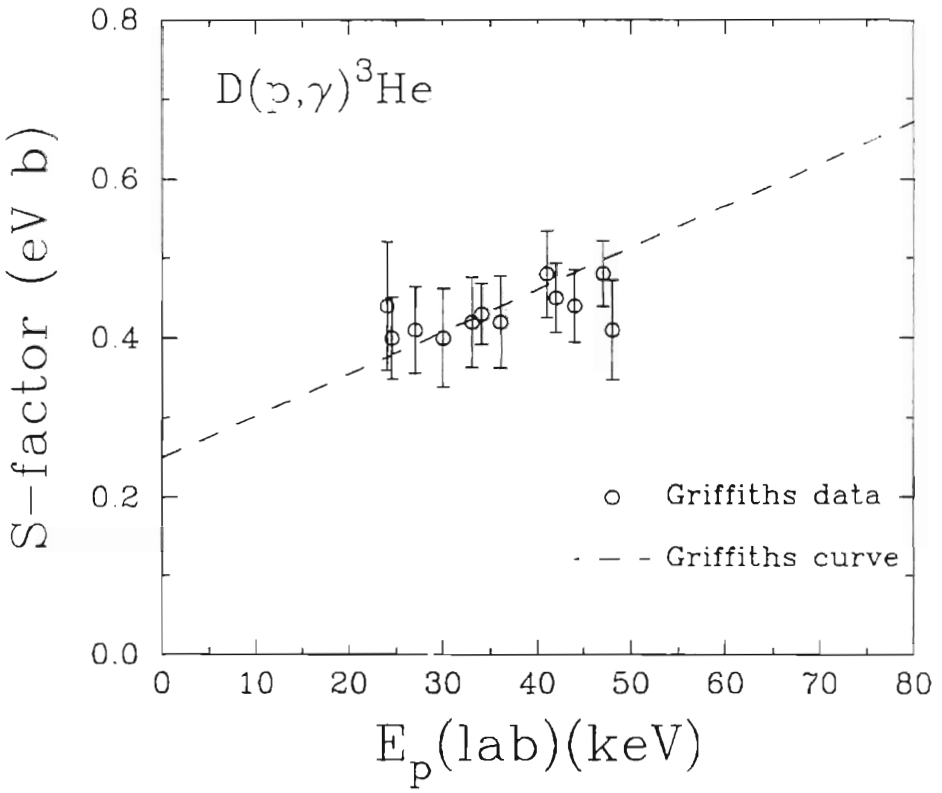

Figure 1.1: The D(p,γ)^{3}He data of Griffiths et al. [Gri63]. The data points were acquired by deconvoluting thick target yields (see Chapter 5). Systematic error is included in the error bars. The dashed curve is a theoretical energy dependence normalized to the data. Note that for this reaction $E_{cm}=(2/3)E_p$.

calls into question the validity of the [Gri63] S-factor extrapolation to zero energy (as shown by the dashed line in Figure 1.1). It would be reassuring to have some empirical evidence for the shape of this theoretical curve.

1.4 Goals of the Current $D(\vec{p},\gamma)^3He$ Experiment

Because of technological advances that have been made in the past 30 years, we felt that we could improve upon the work of [Gri63], and thus extract a more reliable measure of the $D(p,\gamma)^3He$ S-factor at low energies. In particular, our goals for the current experiment were as follows:

1. To measure S-factor data in the energy regime $E_p(lab)<80$ keV which is both higher in quality (i.e. has smaller error bars) and extending lower in energy than the data of [Gri63]. This accurately obtained data can then be directly compared with current three-body calculations [Sch95] in order to gauge the validity of the modern three-body theoretical approach (specifically with regards to the handling of MEC effects). Our new measurements with polarized beam (never done before in this energy region), along with our detailed $\sigma(\theta)$ angular distribution measurements, should also allow a more precise determination of the E1/M1 multipole ratio for $D(p,\gamma)^3He$.

2. To obtain an accurate extrapolation of the S-factor to lower energies than can be experimentally measured. The large error bars and limited energy range of the previous [Gri63] data allowed them to use only a theoretical energy dependence in their extrapolation. We hope to improve on this by using our high quality data to *empirically* determine the energy dependence of the S-factor, and thus perform a more reliable extrapolation down to zero energy. In addition to allowing further

comparison to theoretical three-body calculations [Fri91], our new low energy extrapolation results will give astrophysicists more accurate S-factor values to use in their calculations of stellar and protostellar evolution.

The novel contributions of the current experiment are made possible by two important technological advances that have occurred since the [Gri63] experiment. First of all, polarized proton beams of high intensity and high polarization are now available, and this allows us to measure the vector analyzing power, $A_y(\theta)$, which has never before been done in this low energy regime. The vector analyzing power, which is especially sensitive to E1/M1 interference terms, should play an important role in disentangling of the multipole components, and thus help us extract a reliable value for M1 S(0). As discussed in Chapter 6, the M1 S(0) value is expected to be especially sensitive to MEC effects. The second major advantage that we have over the [Gri63] experiment is that we are able to use a large High Purity Germanium (HPGe) detector which gives exceptionally clean and well resolved spectra (much better than the NaI(Tl) crystal of [Gri63]). It is the high intrinsic resolution of this detector (~4 keV at 5.5 MeV) that will allow us to empirically determine the energy dependence of the $D(p,\gamma)^3He$ reaction by a direct deconvolution of our raw spectra. In this manner, we are able to obtain extrapolations to zero energy which avoid the constraint of a "fixed" energy dependence.

1.5 Overview of Current Experimental Program

The following chapters will discuss all aspects of the present $D(\vec{p},\gamma)^3He$ experiment. A discussion of the experimental set-up and electronics (Chapter 2) will be followed by a discussion of the observables measured and the data analysis techniques used (Chapter 3). The empirical extrapolation to zero energy, accomplished by means of

the "deconvolution" procedure, will be discussed in great detail here. Chapter 4 deals with our measurement of the $D(p,\gamma)^3He$ γ-ray linear polarization. All experimental results acquired, for all observables, will be presented in Chapter 5. Included will be an extraction of the E1/M1 ratio as a function of energy. Chapter 6 will discuss some theoretical calculations that have been done to describe the $D(\vec{p},\gamma)^3He$ reaction, including some very recent three-body calculation results from theory groups at Los Alamos and CEBAF. The results of the theoretical calculations will be compared to the currently acquired data. Chapter 7 will summarize the salient conclusions of the present $D(\vec{p},\gamma)^3He$ study.

Chapter 2

Experimental Techniques and Data Acquisition

Data for the current $D(\vec{p},\gamma)^3He$ experiment were acquired at the Triangle Universities Nuclear Laboratory (TUNL), which is located on the campus of Duke University. The procedure in the $D(\vec{p},\gamma)^3He$ experiment involved extracting an 80 keV beam of polarized protons from the Atomic Beam Polarized Ion Source (ABPIS) [Cle90], and subsequently bending this beam, by means of a dipole magnet, into the low energy capture line (LECAL) beam leg where the target chamber was located. The outgoing γ-rays from the $D(\vec{p},\gamma)^3He$ reaction were detected by an actively and passively shielded High Purity Germanium (HPGe) detector. The proton polarization was periodically measured by diverting the beam through a type FN Tandem Van de Graaff accelerator and on into a proton polarimeter located in a separate beam leg.

The goal of the data acquisition phase of this experiment was to obtain raw $D(\vec{p},\gamma)^3He$ spectra which would allow extraction of the $\sigma(\theta,E)$, $A_y(\theta,E)$, and $P_\gamma(\theta)$ observables (see chapters 3, 4 and 5). The following sections will detail all of the data acquisition procedures that were followed in order to obtain these raw spectra.

2.1 Polarized Proton Beams

The measurement of the $D(\vec{p},\gamma)^3He$ vector analyzing power, $A_y(\theta,E)$, requires an incident beam of vector polarized protons. A vector polarized proton beam is a beam that has been prepared in such a way that there is an excess population in either the $m_I=1/2$ or $m_I=-1/2$ angular momentum sub-state (where I represents the proton spin). In particular, the vector polarization $\vec{P}_\xi$ is defined as

$$\vec{P}_\xi = (N_+ - N_-)\ \hat{\xi}\ , \tag{2.1}$$

where N_+ (N_-) is the fraction of protons which lie in the spin state with projection parallel (anti-parallel) to the quantization axis $\hat{\xi}$. A measurement of the observable $A_y(\theta,E)$ necessitates that $\hat{\xi}$ be oriented in the $\hat{y}$ (or $-\hat{y}$) direction as indicated in Figure 2.1 below.

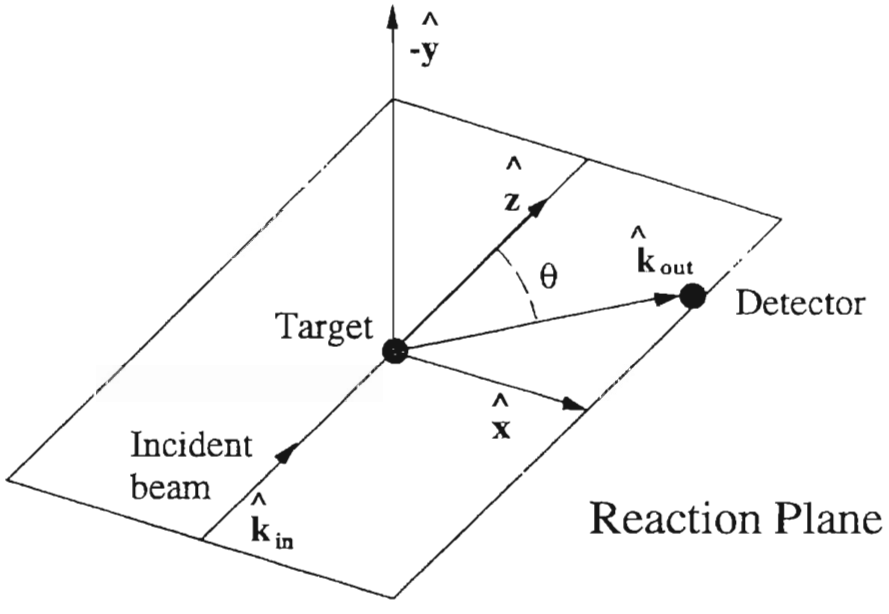

Figure 2.1: Coordinate system for proton polarization.

The choice of axis directions used in Figure 2.1 follows that of the Madison convention [Bar71], where $\hat{k}_{in} \times \hat{k}_{out}$ is in the direction of $\hat{y}$ ($\hat{k}_{in}$ being the incident beam direction and $\hat{k}_{out}$ being the outgoing γ-ray direction), and $\hat{x} \times \hat{y} = \hat{z}$. Measurements of the vector analyzing powers A_x or A_z, which would require $\hat{\xi}$ to be in the $\pm\hat{x}$ or $\pm\hat{z}$ direction respectively, are not pursued, as parity conservation requires that they be zero [Wol49]. Therefore, we only concern ourselves further with vector polarized proton beams which have $\hat{\xi}$ in the $\pm\hat{y}$-direction (i.e. which have polarization $P_{\pm y}$). The next two sub-sections describe the creation and measurement of such beams.

2.1.1 Atomic Beam Polarized Ion Source

The source of polarized proton beams at TUNL is the Atomic Beam Polarized Ion Source (ABPIS) [Cle90]. The ABPIS works by first polarizing the hydrogen atoms in electron polarization and then transferring this polarization to the nucleus by means of radio-frequency (RF) transitions. Once the nucleus has been polarized, the hydrogen atom can then be ionized and accelerated out of the source.

In the ABPIS, the process of producing a beam of polarized protons starts with the introduction of a volume of pure hydrogen gas (H_2). This hydrogen gas is dissociated in an RF discharge, and then allowed to diffuse out of the dissociator chamber and into the region of two Stern-Gerlach type sextupole magnets. Before leaving the dissociator chamber, the beam passes through a cryogenically cooled (~35 K) copper nozzle. This "cold head" serves the purpose of slowing down the beam so that it can spend more time in the polarizing regions which follow. The cold head is coated with high purity nitrogen gas to prevent recombination of the dissociated hydrogen atoms.

Following the dissociator and cold head, the beam enters a region of non-uniform magnetic field created by two Stern-Gerlach type sextupole magnets. These magnets have their field lines aligned such that atoms with electron spin projection m_j=1/2 are bent towards the beam axis direction, while those with m_j=-1/2 are bent out of the beam. Figure 2.2 shows the separation of the electron spin substates that occurs with increasing applied magnetic field. The applied magnetic field on the x-axis is presented in terms of χ, where χ is the ratio of applied magnetic field to the "critical field" (the magnetic field of the proton at the site of the electron). The energy on the y-axis is measured in terms of the zero field splitting, ΔW.

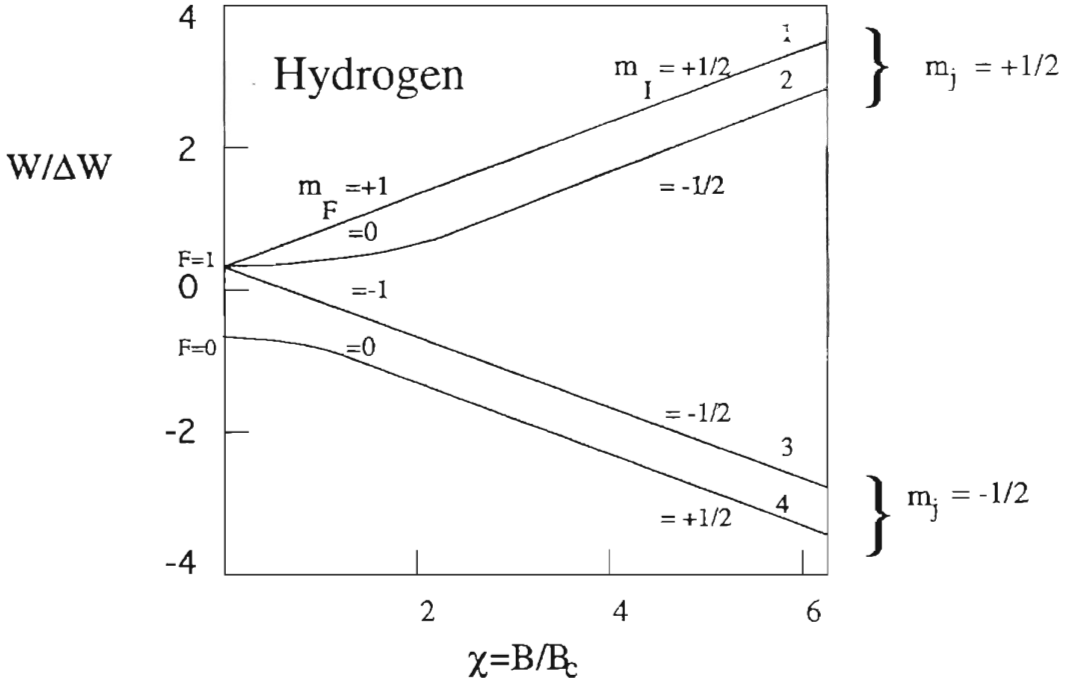

Figure 2.2: The Zeeman and hyperfine structure of hydrogen.

The splitting indicated by the quantum numbers m_j in Figure 2.2 is the separation of the electron spin states (the Zeeman effect), while the splitting indicated by the

quantum numbers m_I is the separation of the hyperfine spin states. The hyperfine structure comes from the interaction between the spin magnetic moment of the nucleus and the orbital magnetic moment of the electron. The total angular momentum for the proton-electron system is represented by F in the Figure.

After exiting the sextupoles, only the m_j=+1/2 states are left. At this point, the beam enters a set of cavities where RF transitions induce population changes among the various hyperfine states in order to produce a nuclear polarization. The technique used is the adiabatic passage method [Hae67], whereby the magnetic moment of an electron (for a selected hyperfine state) is slowly reversed by 180°. In other words, m_j changes from +1/2 to -1/2. In the current experiment, a weak magnetic field (χ close to zero in figure 2.2) is used to induce a transition from hyperfine state 1 to hyperfine state 3. This transition occurs because F is a good quantum number in this region, and it will be conserved in the adiabatic reversal of the electron spin. The RF used in this case has an energy equal to the separation of the m_F states. This procedure leaves states 2 and 3 populated, and thus produces a beam of protons oriented in the m_I=-1/2 direction. In order to produce a beam of protons oriented in the m_I=+1/2 direction, a strong magnetic field (χ around 2) is used to induce the 2 to 4 transition. This is done by using an RF with energy equal to the separation of these two hyperfine states. Note that F is no longer a good quantum number here. This procedure leaves states 1 and 4 populated, and thus creates a beam of protons oriented in the m_I=+1/2 direction. In order to measure the $D(\vec{p},\gamma)^3He$ analyzing power, we utilized a capability of the ABPIS which allows fast spin flipping (at 10 Hz) between these m_I=±1/2 spin states.

Following polarization, the beam in the ABPIS is then ionized in an Electron Cyclotron Resonance (ECR) ionizer cavity in order to allow acceleration out of the source. The resulting positive ions can, if desired, be transformed to negative ions by

passing the beam through an oven of cesium vapor where charge exchange collisions can occur. The usefulness of this feature will be discussed in section 2.1.2. The final section of the ABPIS concerns a Wien-filter spin precessor. As was pointed out at the beginning of section 2.1, we desire that our proton spins be oriented with respect to a quantization axis ($\hat{\xi}$) which lies in either the $\pm\hat{y}$-direction (see figure 2.1). Unfortunately, after exiting the ECR ionizer, the $\hat{\xi}$ of the beam is aligned in the $\hat{z}$-direction. The Wien filter, which consists of a set of crossed $\vec{E}$ and $\vec{B}$ fields, thus plays the important role of changing $\hat{\xi}$ to the orientation desired. Following the Wien filter, the proton beam exits the ABPIS. As a result of a series of acceleration sections in the latter half of the ABPIS, the exiting beam has a lab energy of 80 keV.

The $\pm\hat{y}$ orientation of $\hat{\xi}$ has the added benefit of preventing the possibility of any spin precession in the bending magnet which follows the ABPIS. The bending magnet which follows the source, and allows the beam to be steered into the LECAL beam leg, has its magnetic field in the vertical $\hat{y}$-direction. Since the torque that a magnetic moment feels in a magnetic field is equal to $\vec{\mu} \times \vec{B}$, it is evident that for our beam polarization, $P_{\pm y}$, the torque will be zero, and thus there will be no precession effects.

2.1.2 Proton Beam Polarimeter

Accelerating the Beam

In order to obtain an accurate value for the proton polarization P_y, the beam was periodically tuned into a polarimeter which was located on the high energy side of the TUNL accelerator. This accelerator, a type FN Tandem Van de Graaff, requires negatively charged input beam. The reason for this lies in the nature of the "tandem"

operation of the accelerator, where the word "tandem" here refers to the double acceleration boost an injected beam gets. By raising the central terminal to a high positive voltage (+V), the negative beam is attracted towards the center. Once there, the negative beam encounters a thin Carbon stripping foil which strips the two electrons off and creates a positive ion beam. This positive ion beam is then repulsed from the positive central terminal and out of the accelerator. This completes the double acceleration process whereby the beam has received a net acceleration of 2V.

Although the ABPIS creates positive ions for our low energy $D(\vec{p},\gamma)^3He$ experiment, it can also be made to create negative ions for the purpose of injecting into the tandem accelerator. This is accomplished by charge exchange in a cesium oven (located after the ECR ionizer) whereby the positive hydrogen ions pick up two cesium electrons. This process of changing positive beam to negative beam has an efficiency of about 15 to 20%.

The $^{12}C(p,p_0)^{12}C$ Polarimeter

The polarimeter we used involved the known vector analyzing power for elastic scattering of protons off carbon at E_p(lab)=6.18 MeV and θ_{lab}=40°. The beam energy of 6.18 MeV was chosen on the basis of previous work [Mos65, Ter68, Wil93] which showed that the $^{12}C(p,p_o)^{12}C$ analyzing power was maximum at this energy.

The set-up of the $^{12}C(p,p_o)^{12}C$ polarimeter [Wil93] involved a thin carbon foil, ~5 $\mu g/cm^2$, and two silicon charged particle detectors placed symmetrically at ±40°. The detectors have been carefully collimated with tantalum collimators such that they see only the center of the target. A determination of the proton polarization requires measuring the

left-right asymmetry of the elastically scattered protons. The left-right asymmetry is defined as follows:

$$\text{Asymmetry} = \frac{N_L - N_R}{N_L + N_R} \tag{1.2}$$

In this equation, N_L (N_R) is the number of counts in the left (right) detector for a given amount of incident beam charge deposited on target. The polarization, P_y, of the incident beam is then given by

$$P_y = \frac{\text{Asymmetry}}{A_y} \tag{1.3}$$

where A_y, which has the value -0.851 ± 0.009 [Wil93], is the known vector analyzing power for the $^{12}C(p,p_o)^{12}C$ reaction at E_p(lab)=6.18 MeV and θ_{lab}=40°.

Figure 2.3 shows a schematic of the electronics that were used to process the raw signals from the two solid state detectors.

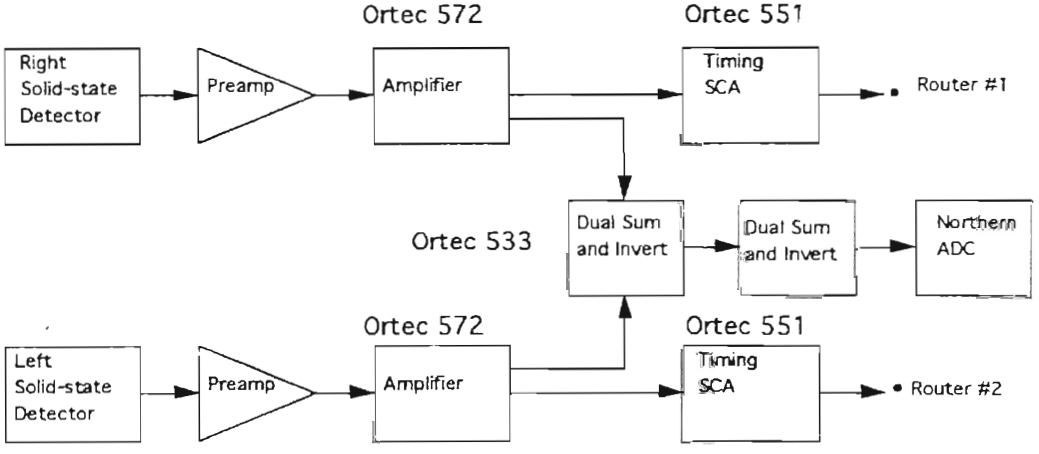

Figure 2.3: The electronics for the proton polarimeter.

Since only one Analog to Digital Converter (ADC) was used, the signals from the two detectors were routed to different locations in the spectrum. This was accomplished by taking the bipolar output from each Ortec 572 amplifier and, after setting the desired thresholds with the Timing Single Channel Analyzer (Timing SCA), using it as a router for the linear signal. Whenever router #1 fires, for example, the Northern ADC processes the linear signal (the unipolar output from the Ortec 572 amplifier) from the right solid state detector, and when router #2 fires, the ADC processes the linear signal from the left solid state detector.

The interface of the ADC with the computer will be described in section 2.4. It should also be pointed out at this juncture that the fast spin flipping capability mentioned in section 2.1.1 can be accommodated in the polarimeter procedure by simply including a few more router signals in the Northern ADC. In this manner, data from the two different spin states can be sent to different regions of the spectrum to simplify analysis.

2.2 Experimental Set-up for $D(\vec{p},\gamma)^3He$

Once a polarized beam (or, in the case of $D(p,\gamma)^3He$, an unpolarized beam) of 80 keV protons was steered into the LECAL beam leg, we were ready to start data acquisition for the $D(\vec{p},\gamma)^3He$ experiment. Before entering the target chamber, the beam passed through a set of horizontal and vertical slits and a tantalum lined collimator. The front of the collimator, which was located about 6 inches upstream of the target, defined a circular on-target beam shape which was about 0.5" in diameter. The experimental method that we followed was to stop the 80 keV proton beam in the target, which in this case was heavy water (D_2O) ice, and then observe the outgoing $D(\vec{p},\gamma)^3He$ γ-rays with a High Purity Germanium (HPGe) detector. The deconvolution of the resulting HPGe

spectra, performed in order to extract the energy dependence of the $D(\vec{p},\gamma)^3He$ reaction, will be discussed in Chapter 3.

Figure 2.4 shows the experimental set-up on the LECAL beam leg. The following subsections will describe the details of this set up. In particular, the topics discussed are: the D_2O ice target; the beam current integration system; and the HPGe detector set up.

2.2.1 D_2O Ice Target

In deciding upon a deuterium target for this $D(\vec{p},\gamma)^3He$ experiment, several options were considered. The idea of using either a deuterated polyethylene or a deuterated titanium target (as did Kramer [Kra92] in his $D(\vec{d},\gamma)^4He$ experiment) was not pursued due to anticipated problems with incident beam implantation. A deuterium gas target, which has been used successfully in higher energy $D(\vec{p},\gamma)^3He$ work (e.g. [Kin83, Gri62], was not deemed feasible at the current low beam energies because of the associated problems with degradation of the incident beam in the gas chamber entrance foil. A gas jet target was simply deemed financially impractical. Thus, following the precedent of Griffiths et al. [Gri63], a D_2O ice target was chosen for the present experiment. The low beam line air pressure (~10^{-6} torr), and the high intensity beam current (~30 μA), was expected to slowly vaporize the outer layers of the D_2O ice target, and thus continuously expose new layers of target material. This was expected to help minimize any problems associated with incident beam implantation.

Since the projected range of 80 keV protons in D_2O ice is only on the order of 1 μm, the idea of using a "thin target" (that is, a target which allows the incident beam to pass completely through it) was not pursued. Instead, we opted to completely stop the 80

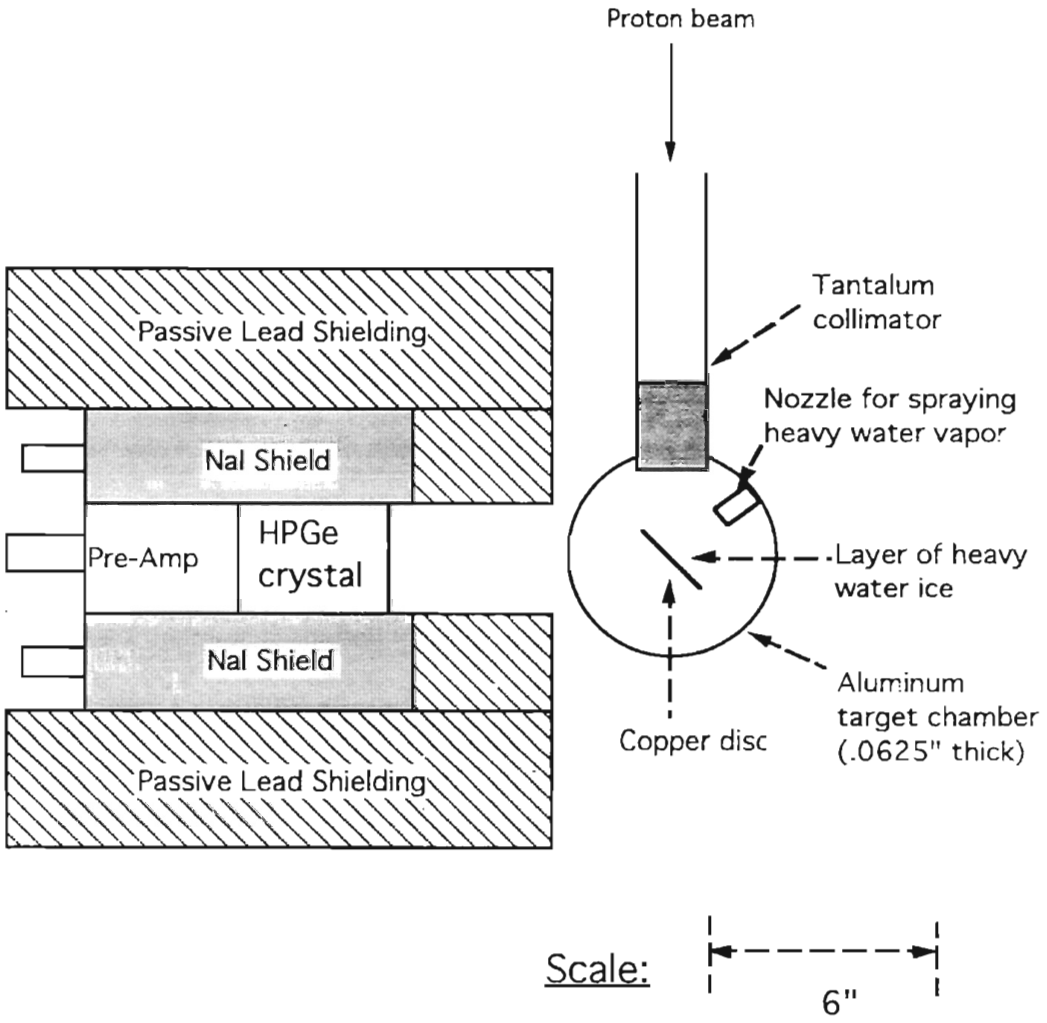

Figure 2.4: Experimental set-up for the D($\vec{p}$,γ)^{3}He experiment at θ_{lab}=90°.

keV beam in the target, thus creating a range of incident beam energies on target from E_p(lab)=80 keV to E_p(lab)=0 keV. This range of incident beam energies created a corresponding range of outgoing γ-ray energies, E_γ=5.49-5.57 MeV (if all outgoing directions are considered), from the $D(\vec{p},\gamma)^3He$ reaction. The procedure for forming the D_2O ice target that we used followed the general method of Griffiths et al. [Gri63]. Figure 2.5 shows a detailed picture of the target and target chamber that was used. The view of the target in figure 2.5 is edge on, and the beam direction is 45° out of the plane of the paper (see figure 2.4 for a better perspective on the beam direction).

The basic procedure of the ice target creation was to let a stream of heavy water vapor freeze on a cold copper surface. The creation of the heavy water vapor stream was created by exposing a flask of liquid heavy water, at room temperature, to the extremely low ambient pressure of the beam line (~10^{-6} torr). Since the vapor pressure of water at room temperature is ~ 20 torr, the water quickly boiled. The resulting steam was then allowed to pass through copper and plastic tubing (as shown in figure 2.5) and onto a copper disk located in the target chamber. The copper disk was attached to a copper cold finger in thermal contact with a reservoir of liquid nitrogen. This kept the temperature of the copper disk at ~77 K, and allowed the heavy water vapor to solidify on the surface in the form of heavy water ice. Deposition for the duration of about 15 minutes produced an ice target approximately 1/2 mm thick.

2.2.2 Beam current integration

In order to measure relative and absolute cross sections, it is necessary to have an accurate method of determining how many protons are incident on the target. This figure

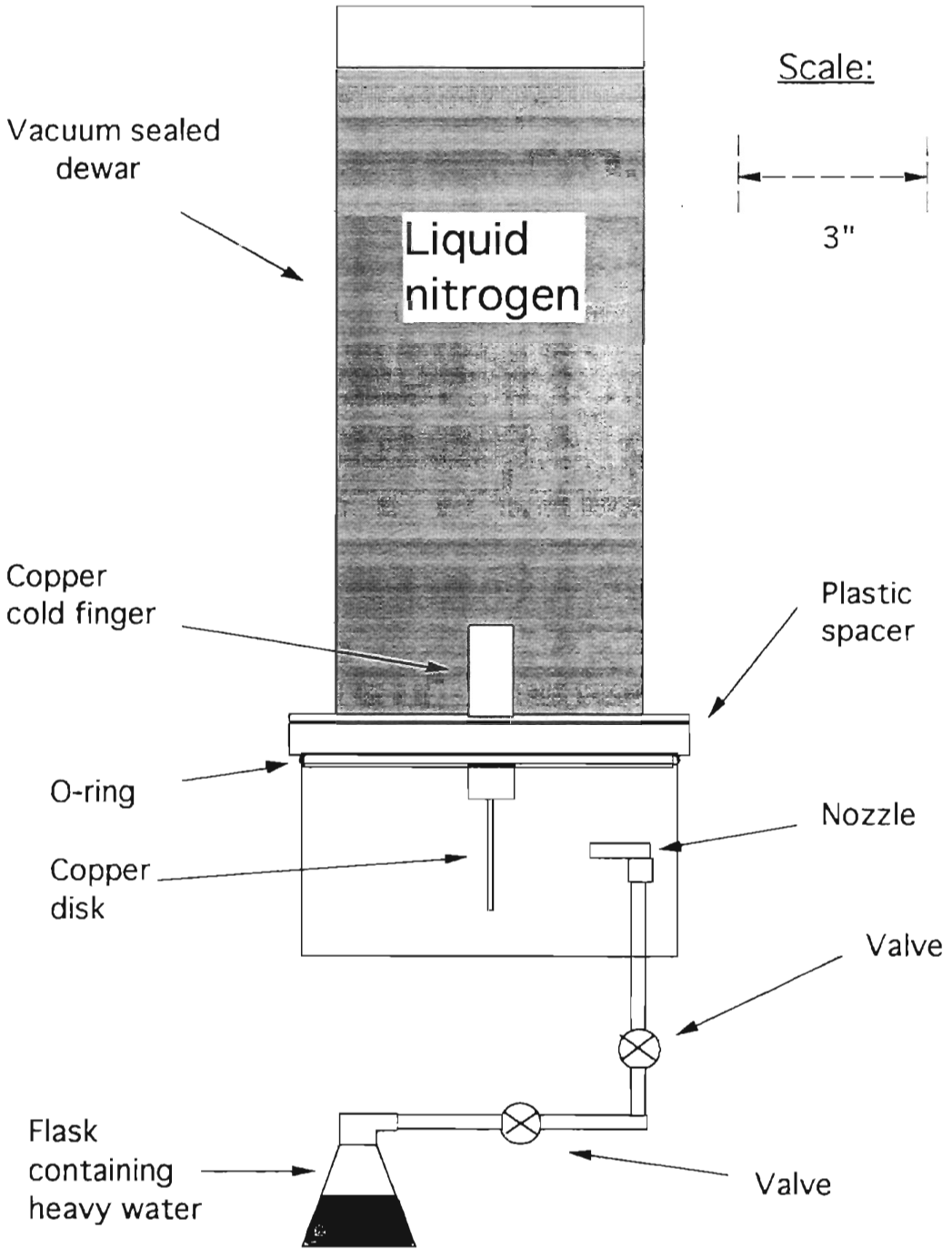

Figure 2.5: The target chamber set-up for the current $D(\vec{p},\gamma)^3He$ experiment. The D_2O ice target was formed by evaporating D_2O vapor onto the cold (~77 K) Cu disk.

was determined by integrating the total charge deposited from the incident proton beam. The integration was carried out using a model 1000 Brookhaven Instruments Corporation current integrator, the precision of which is known to be better than 1%.

One potential problem that can arise with beam current integration is related to the presence of free electrons in the vicinity of the target. In particular, there are two effects that must be taken into account when going about the process of beam integration. The first effect deals with electrons which are knocked off atoms in the collimator (see figure 2.4), or perhaps the upstream slits, and eventually find their way onto the target. These negatively charged electrons will mix in with the positively charged protons, and thus the total charge integrated on target will read somewhat lower than a "true" integration of the proton beam current would indicate. The second effect concerns electrons which are knocked out of the target by the incident proton beam. This process will leave the target with a net positive charge, and thus the total charge integrated on target will read somewhat higher than a "true" integration.

In order to assure proper beam current integration, it is standard procedure to bias the slits, collimator and target to positive voltages in order to "hold in" the negatively charged electrons, and thus prevent spurious beam integration readings. In experiments on most targets, the integrated current will change as the biases are raised (representing the successful suppression of errant electrons). However, this was not the case for the current D_2O ice target. Instead, the integrated current remained constant as biases were raised. This indicates that no secondary electrons were being emitted, and can be understood in light of the high ionization energy of ice as compared with typical metallic targets. This result is in agreement with the observations of [And77]. Based on this finding, the error in beam current integration was assigned the value of 1% (the accuracy of the beam current integrator).

2.2.3 The High Purity Germanium Detector

In order to detect the D($\vec{p}$,γ)^{3}He γ-rays in the current experiment, we opted to use a coaxial High Purity Germanium (HPGe) detector from EG&G ORTEC (Oak Ridge, TN). An HPGe detector is basically a p-n junction with a large reverse bias applied, much like a typical solid state surface barrier detector. The main difference is that significantly larger active volumes are required to detect γ-rays than are required to detect charged particles. The HPGe detector that was used in the current experiment had an active volume of 576 cm^3. This yielded an efficiency of 128% for a 1.33 MeV γ-ray relative to that of a 3" x 3" NaI(Tl) detector (for an on axis source distance of 25 cm). At this energy, the resolution of the HPGe detector was measured at 2.2 keV, a value which is perhaps a factor of 40 better than what one might obtain with a NaI(Tl) scintillator [Kra88].

The decision to use a HPGe detector instead of a NaI(Tl) scintillator in this experiment was based primarily on the superior resolution of the HPGe detector. By stopping the incident beam in the target, a range of outgoing γ-ray energies is created which leads to a broadening of the full energy peak in the spectra by ~50 keV. The high intrinsic resolution of the HPGe, which turns out to be about 4 keV for the D($\vec{p}$,γ)^{3}He γ-rays (see chapter 3), is much less than this width, and thus allows a direct observation of the energy dependence of the D($\vec{p}$,γ)^{3}He reaction. This aspect of an HPGe detector was deemed important enough that the possible higher efficiency which might have been obtainable with a low cost, large volume, NaI(Tl) scintillator was not pursued.

The physical set-up of the HPGe detector is as shown in figure 2.4. The cylindrical canister containing the detector was slipped into a quadrated NaI(Tl) annulus for the purpose of cosmic-ray rejection. This system was then surrounded by 4" of lead

on all sides to further reduce the cosmic ray background. The chassis holding the detectors and lead was mounted securely on several layers of rubber foam, to help protect against microphonics, and bolted to a moveable cart which allowed laboratory angles of θ=0-120° to be reached. In order to reduce thermal noise, the HPGe detector was maintained at 77 K throughout operation by means of a thermal connection to a large liquid nitrogen dewar. The bias applied to the HPGe was +3000 Volts, while each of the four NaI(Tl) segments had their photomultiplier tubes biased to -1400 Volts. The following section describes the electronics used to process signals from the detectors.

2.3 Electronics

Figure 2.6 shows a schematic diagram of the electronics set up that was used in this D($\vec{p}$,γ)^{3}He experiment. The goal of the electronics set up was to perform on-line operations on the raw signals from the HPGe and the NaI(Tl) detectors in order to prepare them for entry into the MicroVAX computer. These on-line operations included amplification of signals, setting discriminator levels, and sorting according to the spin state of the incident proton beam (i.e. spin "up" or spin "down"). Since the data were taken in event-by-event mode, and dumped to magnetic tape for storage, further data analysis operations could be undertaken off-line at a later date.

In particular, there were three specific goals of the electronics set up: the first was to take the HPGe and NaI(Tl) linear signals and prepare them for entry into ADC's (Analog to Digital Converters), which create the desired energy spectra (i.e. histograms of counts vs. γ-ray energy); the second goal was to extract the HPGe and NaI(Tl) scalar signals so that they could be viewed on-line; and the third goal was to process linear and scalar signals from the spin state controller in order to keep track of the spin state of the

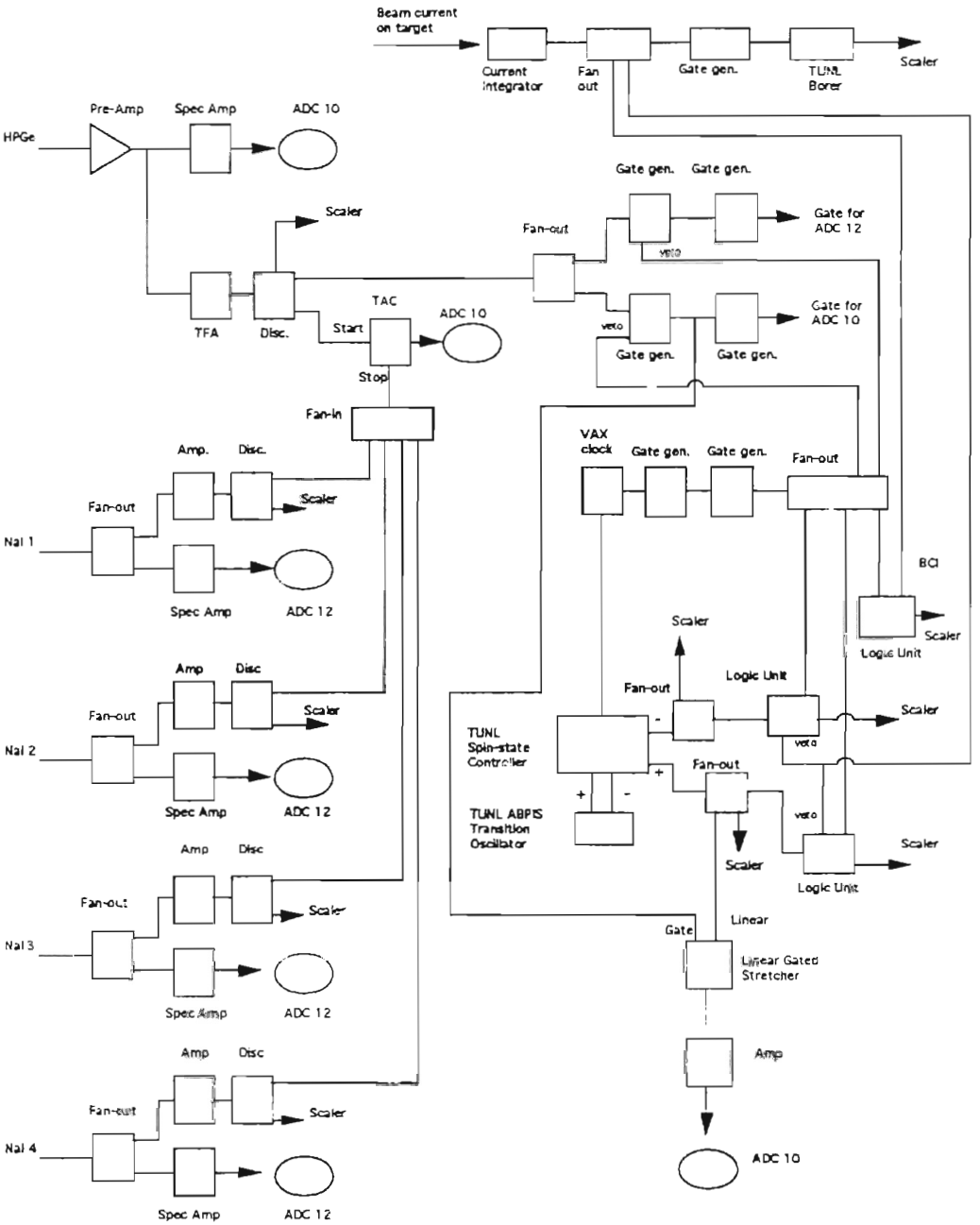

Figure 2.6: Schematic diagram of electronics set-up for the D($\vec{p}$,γ)^{3}He experiment.

incident beam. The details of the electronics set-up are illustrated in figure 2.6. For simplicity, this schematic diagram neglects such devices as inverters and level adapters which performed the function of preparing the proper signal shape (e.g. NIM or TTL) for the logic units that were used.

Following the outline in Figure 2.6, the HPGe signal is first pre-amplified and then fanned out. These two operations are accomplished inside the HPGe canister. These two signals are then sent on low loss cables from the target room to the control room for further processing. One of these signals is treated as a linear signal, and it is sent through a spectroscopy amplifier for shaping and timing before being sent to an ADC. The other HPGe signal is treated as a timing signal, and it will be used to gate the linear signal into the ADC. The raw timing signal is sent through a timing filter amplifier for shaping and amplification, and then on into a discriminator for the purpose of setting an energy threshold (~500 keV in the current experiment). The resulting signal is then used to created the gates for the two ADC's used, TUNL ADC's #10 and #12. ADC #10 handles the HPGe, TAC and spin signals, while ADC #12 handles the 4 NaI segments). Notice that the gates are created using two gate generators in tandem. The first unit is for setting the signal delay (for timing purposes), and the second is for setting the gate width (~10 μs).

As previously mentioned, the HPGe detector is surrounded by four NaI(Tl) segments which serve as an anti-coincidence shield for cosmic ray rejection. Each segment has its linear and timing signals handled separately so that four separate energy spectra can be created. In particular, each NaI(Tl) signal is fanned out into a linear and timing signal. The linear signal is amplified and shaped, and then sent to the ADC. It is important to note that all the ADC's in this experiment are gated by the HPGe signal. In other words, whenever the HPGe discriminator fires (i.e. it receives a signal above

threshold), all the ADC's are read. The NaI(Tl) timing signals are for the specific purpose of creating a TAC (Time to Amplitude Converter) spectrum. As Figure 2.6 shows, the timing signals from each of the segments are amplified, subjected to an energy threshold, and then summed together in a fan-in. The TAC is started with a discriminator signal from the HPGe and stopped with a discriminator signal from any one of the NaI(Tl) segments. Thus, a peak in the TAC spectrum indicates a coincidence between the HPGe and the NaI(Tl) annulus.

A coincidence between the HPGe and NaI(Tl) annulus represents one of two possible events: either it is a single γ-ray (or cosmic ray) which has deposited some of its energy in the HPGe and some of its energy in the annulus; or, it is two unrelated γ-rays (or cosmic rays), one of which has deposited its energy in the HPGe and the other of which has deposited its energy in the NaI(Tl) annulus. While the former event represents a real correlated coincidence, the latter event represents an accidental coincidence which must be accounted for. By looking at the off-TAC peak background, we can get an idea of what the accidental coincidence rate is. This was the primary purpose of the TAC spectrum in this experiment. As it turns out, the very low count rates encountered in the current experiment make the accidental coincidence rate negligible as compared with the real coincidence rate.

The spin state created by the ABPIS is controlled by the TUNL spin-state controller. This allows a fast spin flipping procedure to be undertaken by setting the spin-state controller to flip the incident beam spin state ("+" or "-") every 100 ms. The time rate of the spin flip is controlled by the VAX clock. Approximately 7 ms are required in order to completely "flip" the spin state that the ABPIS creates. Thus, we "blank" (i.e. veto) the ADC gates for 7 ms after each spin flip command is given. As before, the two gate generators in tandem (that are used to create the veto signal) allow,

respectively, a variation of the signal delay and signal width. This veto procedure would thus be expected to create a 7% "electronic" dead time in the ADC (i.e. a dead time that we create via our electronic set up). In practice, this dead time was significantly more, as will now be discussed.

Most runs concerning the absolute cross section were done with unpolarized incident beam, and hence the spin flip electronics discussed above were disconnected. As a result, there was no "electronic" dead time present. The quoted efficiency for the HPGe detector, as presented in Chapter 3, is given for the case of no electronic dead time. However, when running with polarized beam, a large electronic dead time (associated with the spin flip electronics) was present. Rather than the expected 7% dead time, a dead time of 25% was encountered. This was due to an anomaly associated with the Phillips fan out units. As it turned out, if more than one output was taken from a given unit, a change in signal shape occurred which was significant enough so as to affect the operation of the ORTEC ADC's being used. As discussed in Chapter 3, absolute cross sections measured using polarized beams had to take this extra electronic dead time into account. The exact magnitude of this dead time (25%) was easily determined by simply monitoring count rates with and without the spin flip electronics connected.

The beam current integration (BCI) is fed to the TUNL "borer" for the purpose of presetting each experimental run to a given amount of integrated charge (i.e. a given number of protons incident on the target). In order to keep track of the amount of beam in each spin state, the BCI is also fanned out and sent to a number of different logic units. One logic unit keeps track of coincidences between the "+" spin state and the BCI; one logic unit keeps track of coincidences between the "-" spin state and the BCI; and the final logic unit keeps track of coincidences between the veto signal and the BCI. This gives us a breakdown of how much beam we have integrated in each of the three states: "+", "-",

and veto. The spin state of the incident proton beam is recorded for each ADC gate by means of a coincidence requirement (using the linear gated stretcher) between the HPGe discriminator and the "+" spin state. The so-called "spin" spectrum which is created will give counts in a high channel when the beam is in the "+" spin state and will give counts in the zero channel when the beam is in the "-" spin state. This information can be used to sort the γ-ray data according to the incident beam spin state.

The electronics modules that were used in this set up were all from ORTEC, with the following exceptions: the logic modules were from Phillips Scientific; the dual gate generators were from LeCroy; and the scalar units were from Kinetic Systems. Some particular model numbers are as follows. The ADC's were EG&G ORTEC Model AD413A CAMAC Quad 13 bit ADC's, where, as previously described, one gate strobes the four inputs. The spectroscopy amplifiers used were Ortec 672's (for the HPGe) and Ortec 452's (for the NaI(Tl) detectors). The other amplifiers used were Ortec 572's.

2.4 Computer Interface

The digitized ADC signals were fed into a CAMAC crate controller which was in turn connected to a Microprogrammed Branch Driver (MBD). The MBD served as the interface between the electronics set up and the TUNL MicroVAX 3200 computer. Approximately every two seconds the data buffer in the MBD would fill up and it would flush to the MicroVAX. The software running on the MicroVAX was the TUNL XSYS data acquisition package, and it allowed us to view the raw data as γ-ray spectra (i.e. as histograms of counts vs. ADC channel number). Using this data acquisition package, sorting algorithms were written in order to perform the necessary gating procedures, and to create the desired coincidence spectra. In addition to on-line viewing capability, the

data was also stored on magnetic tape in an event-by-event mode. This allowed the possibility of off-line re-sorting of the data at a later date.

In the following chapter, the raw spectra that were acquired will be presented, and the techniques for extracting the $\sigma(\theta,E)$, $A_y(\theta,E)$, and $P_\gamma(\theta)$ observables will be discussed.

Chapter 3

Data Analysis

The $D(\vec{p},\gamma)^3He$ energy spectra acquired with the HPGe detector in this experiment were thick target yield γ-ray spectra which resulted from stopping an E_p(lab)=80 keV beam in the target. The goal of this experiment was to use these thick target yields to extract the polarized and unpolarized observables of the $D(\vec{p},\gamma)^3He$ reaction. In particular, the experimental γ-ray yields acquired with unpolarized incident beam were used to calculate the cross section as a function of angle and energy, $\sigma(\theta,E)$, while the γ-ray yields acquired with polarized incident beam were used to calculate the vector analyzing power as a function of angle and energy, $A_y(\theta,E)$. One $D(\vec{p},\gamma)^3He$ observable that was also extracted in the current experiment, but is not mentioned in this chapter, was the γ-ray polarization, $P_\gamma(\theta)$. All the details of the $P_\gamma(\theta)$ measurements will be described in Chapter 4.

The process of extracting the cross section and analyzing power observables from the raw spectra was carried out using three separate and uncorrelated data analysis methods. The first method involved simply calculating the observables using the unaltered $D(\vec{p},\gamma)^3He$ thick target yields. This method does not attempt to extract the energy dependence of the observables, but only gives the results for the total energy region E_p(lab)=80-0 keV. The next two data analysis methods took advantage of the high HPGe resolution to actually extract the energy dependence of the observables. The first of these methods, hereafter referred to as the binning analysis, involved binning the

acquired thick target spectra into 7 separate energy regions (i.e. E_p(lab)=80-70 keV, 70-60 keV, etc.), and then using these yields to calculate the observables for each energy region. The second method involved a rigorous deconvolution of the raw thick target yield spectra. In this procedure, the intrinsic and kinematic response of the HPGe detector were removed from the spectra, thus allowing a direct extraction of the energy dependence of the yield. In this manner, the energy dependence of the observables could be obtained. While this deconvolution analysis is ostensibly more exact than the binning analysis, it has the limitation that model dependent assumptions are required to carry it out. For this reason, the deconvolution analysis and the model independent binning analysis complement each other.

This chapter begins with a discussion of the raw spectra acquired, and then moves on to discuss each data analysis method in detail, the goal of which is the extraction of the $\sigma(\theta,E)$ and $A_y(\theta,E)$ observables. The final results are presented and discussed in Chapter 5.

3.1 Raw Energy Spectra

The raw $D(\vec{p},\gamma)^3He$ energy spectra in this experiment were acquired with the HPGe detector as shown in Figure 2.4. A quadrated NaI(Tl) annulus, which surrounded the HPGe, was used to veto cosmic rays and Compton scattered events, and was also operated as a Compton polarimeter for the purpose of measuring $P_\gamma(\theta)$ (see Chapter 4). Figure 3.1 shows a typical $D(\vec{p},\gamma)^3He$ energy spectrum acquired with the HPGe at a lab angle of 90°. This spectrum was acquired by stopping an E_p(lab)=80 keV proton beam in a D_2O ice target, and observing the γ-rays which resulted. The energy calibration of

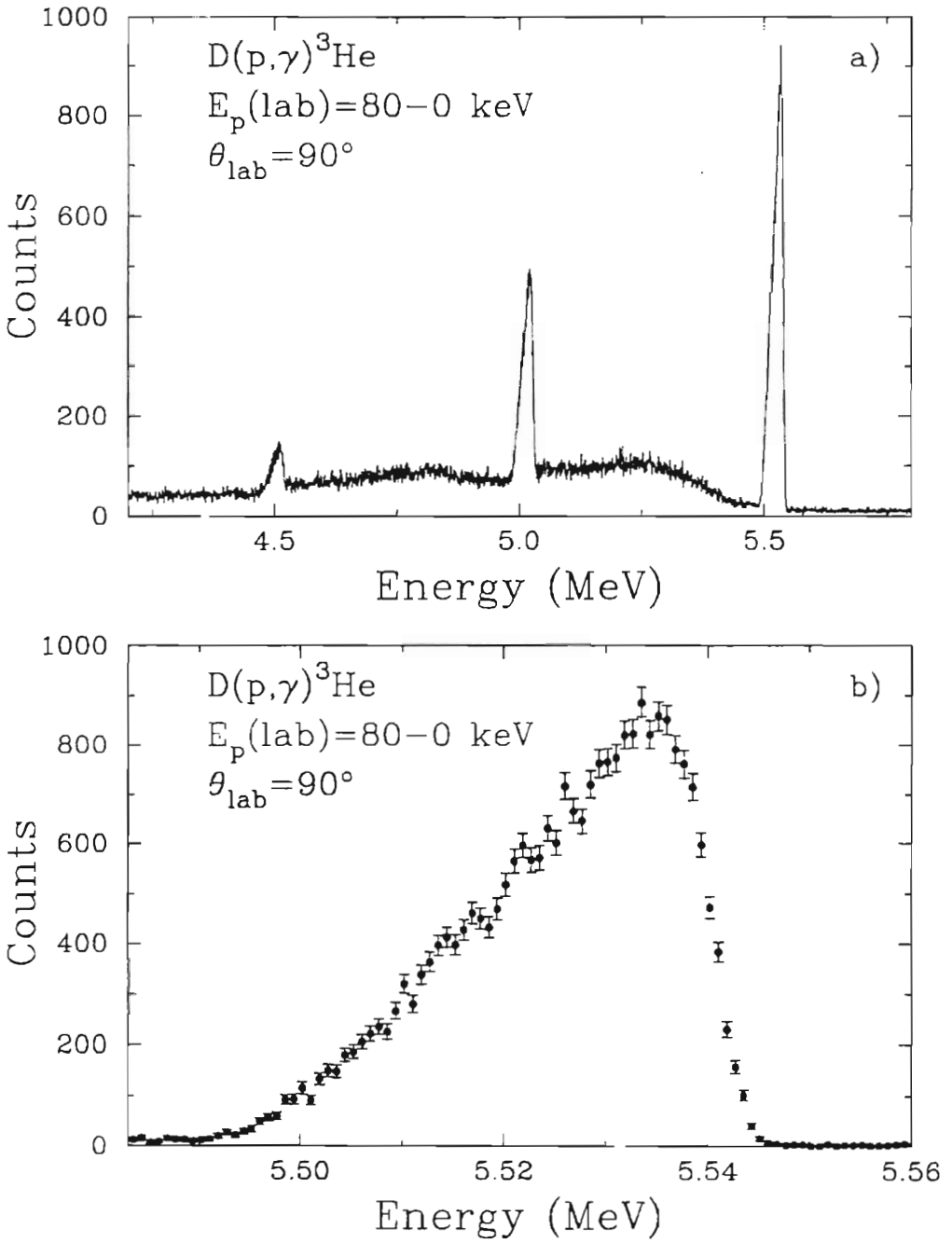

Figure 3.1: Typical D($\vec{p}$,γ)^{3}He spectrum acquired with the HPGe detector, showing (a) the full response and (b) a blow up of the full energy peak.

the x-axis (in keV/channel) was obtained using the energies of known background lines such as radiothorium (2.615 MeV) and potassium-40 (1.460 MeV). Tests using a ^{66}Ga source (see section 3.2) have shown that the energy calibration, from E_γ=1.2-4.8 MeV, can be expected to be linear to within 0.5% (i.e. a calibration in keV/channel derived at 1.1 MeV should be within ±0.5% of that value at 4.8 MeV). Based on a typical calibration of 0.8 keV/channel in an 8K channel spectrum, it can thus be estimated that the absolute energy scale at 5.5 MeV might be in error by as much as 20 keV. We were able to correct for this error to within ±1 keV by realizing that the highest possible energy γ-ray (which can be calculated) lies midway down the sloping high energy edge of the full energy peak. Please see section 3.4 for further discussion of this topic.

Figure 3.1a shows the full response of the HPGe detector to the 5.5 MeV γ-rays from $D(\bar{p},\gamma)^3He$. This spectrum represents the data accumulated in 70 runs, each one taking about 40 minutes. In constructing the summed spectrum, each individual run was corrected for gain shifts by monitoring the position of the known background lines mentioned above. Furthermore, in order to better show the full HPGe response, this spectrum has not been vetoed with the NaI(Tl) anticoincidence shield. The peak on the far right (at 5.5 MeV) is the so called full energy peak which represents complete absorption of the incident γ-ray energy by the HPGe detector. Moving to the left (lower in energy), the next two sharp peaks are the first escape peak, at 5.0 MeV, and the second escape peak, at 4.5 MeV. These peaks represent, respectively, the loss of one or two 511 keV photons from the HPGe. These 511 keV photons arise when, during a γ-ray interaction process, a pair-produced positron (which has lost all of its kinetic energy) annihilates with an electron. The Compton continuum in Figure 3.1a starts with the visible Compton edge at 5.25 MeV and goes on down towards zero energy. The

relatively flat background on the high energy side of the full energy peak is due primarily to cosmic rays.

Figure 3.1b shows a blow-up of the full energy peak. This spectrum has been vetoed with the NaI(Tl) anticoincidence shield in order to eliminate the cosmic ray and Compton backgrounds. The shape of this full energy peak is due to a convolution of the HPGe response function with the $D(\vec{p},\gamma)^3He$ yield function. The large width is due to the fact that this was a thick target yield. In other words, the process of stopping the incident beam in the target created a range of incident proton energies (80-0 keV), and this in turn created a range of outgoing γ-ray energies. This can be seen by the following:

$$E_\gamma \approx Q + \frac{2}{3}E_p \tag{3.1}$$

This equation states that the measured γ-ray energy is approximately equal to the Q-value plus the center-of-mass energy, which in this case is 2/3 times the laboratory proton beam energy. The exact form for this relationship, derived using conservation of relativistic energy and momentum, will be discussed later. Using the approximate relationship of equation 3.1, we can see that for E_p(lab)=80-0 keV, we expect E_γ=5.49-5.54 MeV. The sloping yield on the low energy side of the full energy peak in figure 3.1b is due primarily to the rapidly decreasing cross section with decreasing beam energy (but is also affected somewhat by the changing target thickness as the beam energy decreases).

The anticoincidence procedure between the HPGe and the NaI(Tl) shield was performed on-line by means of computer software. For every HPGe signal received above threshold, the NaI(Tl) spectra were also checked. A simultaneous count in the HPGe and a NaI(Tl) detector indicated a correlated coincidence (accidental coincidences

were negligible). Figure 3.2 below shows a typical spectrum for one of the NaI(Tl) shield segments. The HPGe was at θ_{lab}=90° when this spectrum was acquired.

The NaI(Tl) segments were shielded so that they did not directly see the D_2O target. Only secondary scattered events from the HPGe, in addition to natural background radiation, made it into the NaI(Tl) segments. The cutoff around 200 keV is the energy threshold of the detector, and the small peak (barely visible) at around 500 keV results from the 511 keV photons escaping from the HPGe. This peak was used to energy calibrate this spectrum.

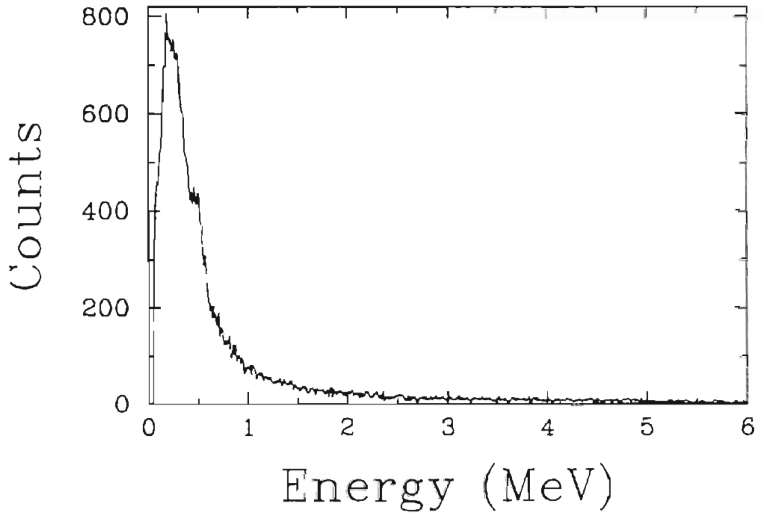

Figure 3.2: A typical NaI(Tl) spectrum from one of the four shield segments.

3.2 Observables Measured

This section discusses the $D(\vec{p},\gamma)^3He$ observables that were measured in this experiment: the differential cross section, $\sigma(\theta,E)$ (and the related differential S-factor,

$S(\theta,E)$); and the vector analyzing power, $A_y(\theta,E)$. A discussion of the γ-ray polarization, $P_\gamma(\theta)$, measurements is deferred until Chapter 4.

3.2.1 Differential Cross Section and S-factor

The laboratory differential cross section for a nuclear reaction, as a function of laboratory detector angle, θ_{lab}, and laboratory beam energy, E_p, is defined as follows:

$$\sigma(\theta_{lab},E_p)=\frac{Y(\theta_{lab},E_p)}{(D)(P)(\varepsilon d\Omega)} \tag{3.2}$$

In Equation 3.2, $Y(\theta_{lab},E_p)$ is the detector yield (typically the full energy peak yield is the one of interest), D is the number of deuterons per cm^2 in the target (i.e. the deuterium areal density), P is the number of protons incident on the target, and $\varepsilon d\Omega$ is the absolute efficiency times solid angle of the detector (only measured for the full energy peak in this experiment). The differential cross section is then given in units of cm^2.

Deuterium Areal Density

The deuterium areal density (D) in equation 3.2 can be calculated from the known stopping cross section, $STP(E_p)$, for protons on D_2O ice as follows:

$$D = dD(E_p)=\frac{2dE_p}{STP(E_p)}, \tag{3.3}$$

where $dD(E_p)$ is the differential deuterium areal density at energy E_p, dE_p is the differential energy loss of the proton beam (at energy E_p) in the D_2O target, and the factor

of 2 is present because there are 2 deuterium atoms in every D_2O molecule. Since the stopping cross section is generally defined in units of eV per 10^{15} molecules per cm^2, dE_p (the energy width under consideration) must be given in units of eV in order to get D in units of 10^{15} deuterons/cm^2.

Stopping Cross Section

The stopping cross section, $STP(E_p)$, for protons on D_2O ice has been measured twice in the low energy region, both times by Wenzel & Whaling [Wen52, Wha52]. The stopping cross section for deuterons on D_2O ice has also been measured once in the low energy region by Andrews & Newton [And77]. Figure 3.3 shows these $STP(E_p)$ values plotted vs. E_p, whereby the data of [And77] have been converted to proton stopping values by using the relationship $E_p=E_d/2$.

Because the error bars for the data points of [Wha52] in Figure 3.3 were not published, they have had error bars assigned to them which are equal to the percentage error of the data of [Wen52] (a subsequent measurement by the same authors). The solid line in Figure 3.3 is an empirical fit the data of [Wha52] and [Wen52] using the form derived by Anderson and Ziegler [A&Z77]:

$$E_p \le 10\ \text{keV}: \quad STP(E_p) = C_1 \sqrt{E_p} \tag{3.4}$$

$$E_p > 10\ \text{keV}: \quad STP(E_p) = \frac{1}{\frac{1}{C_2 E_p^{.45}} + \frac{1}{(C_3/E_p)\ln(1 + C_4/E_p + C_5 E_p)}}.$$

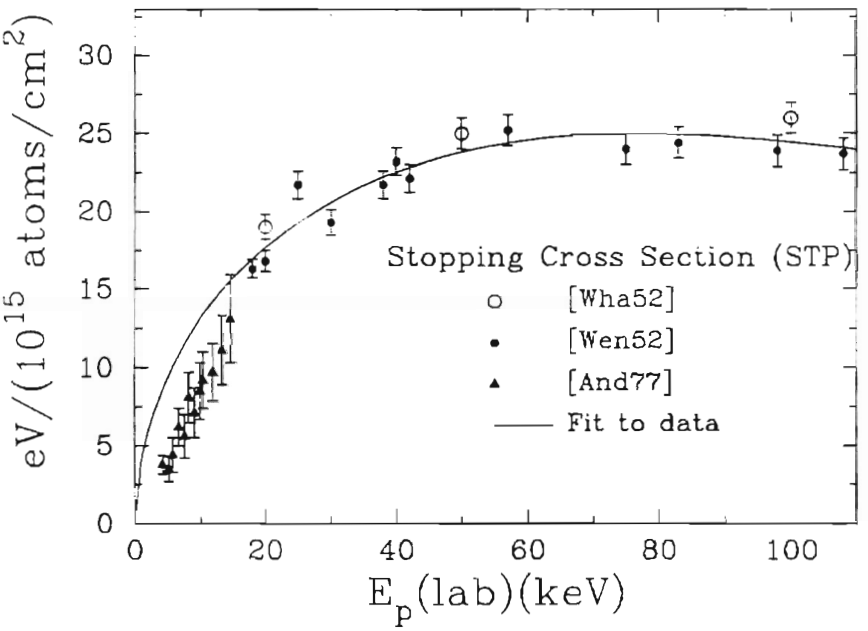

Figure 3.3: The STP(E_p) data for protons stopping on D_2O ice. The solid curve is an empirical fit to the data of [Wha52] and [Wen52] using the form of Equation 3.4.

The empirical form of equation 3.4 was derived by taking into account both theoretical considerations (concerning electronic stopping) and experimental considerations (i.e. fits to all stopping cross section data acquired as of 1977). A constraint was applied to the constants so as to have a continuous curve at 10 keV. The values of the parameters extracted by fitting Equation 3.4 to the [Wha52] and [Wen52] data were: C_1=4.733, C_2=3405, C_3=594, C_4=0.0084. Based on the spread of the [Wha52] and [Wen52] data, a systematic error of 6% was assigned to this curve.

The data of [And77] could not be simultaneously fit to Equation 3.4 along with the other two sets of data, and thus it was not included in the current analysis. The fact that the [And77] data set is about a factor of 2 lower than would be expected based on the other two sets of data indicates one of three possibilities: the energy dependence derived

by [A&Z77] is wrong; there is an unknown systematic error present in the data of [Wha52] and [Wen52]; or there is an unknown systematic error present in the data of [And77]. The first possibility does not seem likely based on the fact that there is no known reason why the energy dependence should change so suddenly around 20 keV. Although the theoretical basis of Equation 3.4 is centered entirely on electronic stopping effects, the neglect of nuclear stopping effects is only thought to be a 1-2% effect at E_p=10 keV [A&Z77], and thus cannot account for the factor of two anomaly which arises in the neighborhood of this energy. The second possibility seems unlikely as well, due to the near corroboration of the [Wha52] and [Wen52] data sets. In light of these arguments, the third possibility (a systematic error in the data of [And77]) is assumed. As will be discussed in section 3.5, the neglect of this data is not expected to strongly affect the extrapolation of results to zero energy. It should also be pointed out at this juncture that empirical stopping power curves extrapolated from higher energy data (e.g. see the TRIM-89 curve in [Mit90]) do not fit any of the low energy data, and thus are not used.

One important point that is worth emphasizing is that the authors of the previous low energy $D(p,\gamma)^3He$ experiment [Gri63] did not use the same set of $STP(E_p)$ data that we are using in the current experiment. In fact, even though the [Gri63] experiment used a D_2O ice target, the [Gri63] authors used $STP(E_p)$ data for H_2O vapor instead of D_2O ice. Their assumption was that the stopping cross section for H_2O vapor should be equivalent to that of D_2O ice. However, our current understanding of low energy stopping cross sections [Thw92,Thw85] now indicates that this is not true. In fact, a difference in stopping cross section of 10-15% should be expected for water in the vapor and solid phases. This effect, whereby the D_2O ice stopping cross section will be 10-15% lower than the H_2O vapor stopping cross section, is referred to as the "physical

state" or "phase" effect. A theoretical description of the physical state effect can be found in papers by Mitterschiffthaler [Mit90] and Xu [Xu85]. The fundamental basis of this effect is that the electrons are more tightly bound in the ice phase than they are in the vapor phase, thus making the stopping cross section (which depends primarily on inelastic electron-proton collisions) smaller in the ice phase. As a result of neglecting this effect (which is considered fairly well established for the case of protons on D_2O ice [Thw92,Thw85]), the [Gri63] S-factor results are expected to be artificially high by 10-15%. This will be discussed further in Chapter 5.

HPGe Efficiency and Solid Angle

The full energy peak efficiency times solid angle ($\varepsilon d\Omega$) of the HPGe detector is another quantity that is needed for the absolute cross section. The technique used to measure this quantity involved placing a radioactive source of known intensity at the exact location of the target, and then, with the HPGe placed in the standard geometry, acquiring a γ-ray spectrum. The radioactive source that was used was the QCD-1 mixed γ-ray standard from Amersham [Am94]. This source emits 11 γ-ray lines from 88 keV to 1.836 MeV, whereby each line has an absolute full energy peak calibration (in counts per second) which is traceable to the National Institute for Standards and Technology (NIST). By analyzing the γ-ray spectrum acquired with this source, it is then possible to obtain the absolute $\varepsilon d\Omega$ value for the full energy peak of the HPGe detector at E_γ=1.836 MeV. Since the Cu target backing and Al target chamber (present during the actual experiment) were included in this $\varepsilon d\Omega$ test, γ-ray absorption effects are automatically taken into account.

As was discussed in section 3.1, the γ-rays from the $D(\vec{p},\gamma)^3He$ reaction have energies in the region around 5.5 MeV, and thus the absolute $\varepsilon d\Omega$ value at 1.836 MeV must be extrapolated upwards. This was accomplished using a ^{66}Ga source [Ald93] which puts out 26 strong γ-ray lines from E_γ=0.83-4.81 MeV. This source, which has a half-life of only 9.5 hours, was created in the TUNL lab by the $^{63}Cu(\alpha,n)^{66}Ga$ reaction using 18 MeV α-particles. Since the relative intensity of the ^{66}Ga γ-ray lines are well known [Ald93], a relative $\varepsilon d\Omega$ curve can then be obtained from the acquired γ-ray spectra. This relative $\varepsilon d\Omega$ curve is then normalized to an absolute scale using the known absolute $\varepsilon d\Omega$ value at 1.836 MeV from the QCD-1 source. The result for the absolute $\varepsilon d\Omega$ curve (for the experimental set up shown in Figure 2.4) is shown in Figure 3.4 along with the normalized ^{66}Ga data.

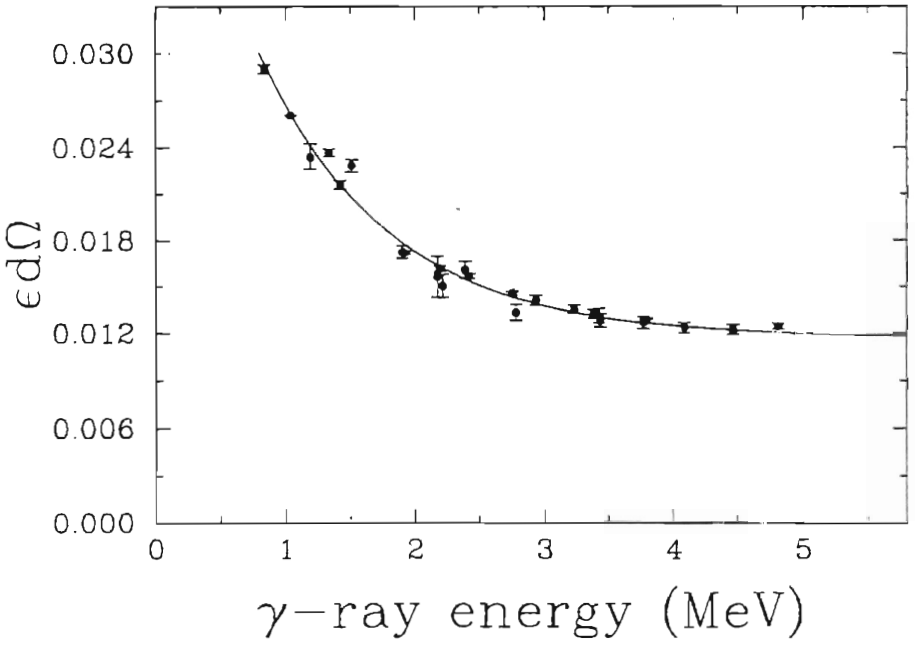

Figure 3.4: The absolute (full energy peak) $\varepsilon d\Omega$ data for the HPGe detector in the configuration of Figure 2.4. The solid line is an empirical fit to the data using equation 3.5.

The data shown in Figure 3.4 was acquired for a geometrical set up similar to that in Figure 2.4 (actually, the same, except that the HPGe lab angle was 60°, not 90° as in the Figure). The source was located at the position of the D_2O ice target (9.06" away from the HPGe on axis). The empirical curve shown in Figure 3.4 has the standard exponential form as suggested by [Kro89]. In particular, Equation 3.5 gives the form that was used:

$$\varepsilon d\Omega = C_1 (C_2 + C_3 \exp(-C_4 E_\gamma)) \qquad (3.5)$$

The values of the parameters extracted from Equation 3.5 are given in the table below:

Extracted Parameters for Equation 3.5

C_1	C_2	C_3	C_4
.000401 ± .000035	29.18 ± 0.48	101.07 ± 3.46	.000993 ± .000036

Table 3.1: Parameter values, for Equation 3.5, obtained by fitting the $\varepsilon d\Omega$ data shown in Figure 3.4

Using the curve of Equation 3.5 along with the parameter values of Table 3.1, it is possible to calculate the expected $\varepsilon d\Omega$ for the full energy peak of the HPGe at E_γ=5.5 MeV. Since the curve is relatively flat at the higher energies, this extrapolation is viewed with considerable confidence. The result is: $\varepsilon d\Omega(5.5\ \text{MeV}) = 0.0119 \pm 0.0007$. This value, the only one of interest for the current experiment, must be corrected for the slight difference in γ-ray absorption (of the target and target chamber) between 1.836 MeV and 5.5 MeV (a 3% increase). It must also be corrected for the fact that the beam spot in the $D(p,\gamma)^3He$ experiment was somewhat larger than the small "hot spot" on the QCD-1

source. This was accomplished by means of a Monte-Carlo simulation (MONTE) in which the exact target-detector geometry was reproduced, and in which the beam spot size could be arbitrarily varied to gauge the effect of its size. The result was a 3% decrease in efficiency. Thus, it is seen that these two small efficiency corrections (corresponding to energy dependent absorption effects and finite target size) cancel out, leaving us with the $\varepsilon d\Omega$ value given above.

By calculating the solid angle at the front face of the HPGe for the given geometry ($d\Omega$=0.101), and calculating the γ-ray absorption effects (in the Al and Cu), the $\varepsilon d\Omega$(5.5 MeV) value of 0.0119 derived above can be shown to indicate an intrinsic photopeak efficiency for the HPGe of ε=0.13 (i.e. 13% of the γ-rays entering the front face of the HPGe end up in the photopeak). This value for ε agrees with a value derived from a Monte Carlo simulation of the target-detector geometry using the EGS4 code [Nel85] (see Appendix A). Because of this agreement, the measured $\varepsilon d\Omega$ value (which is used in subsequent calculations) is viewed with considerable confidence. It must be stressed that the value for the photopeak efficiency, ε, is dependent upon the source-detector distance [Gre66]. For a source very far from the detector, the γ-rays incident on the front face of the detector are all parallel, and this will raise the value of ε somewhat. For a source very close to the detector, ε will be somewhat lower.

Dead Time Corrections

Because of the very low count rates in the current $D(p,\gamma)^3He$ experiment (total HPGe count rate ~60 counts/sec), the observed computer dead time was less than 1% at all times, and thus completely negligible. However, when running with polarized beams, another source of dead time was present that was non-negligible. This other source of

dead time was due to an anomaly in the spin-flip electronics whereby an effective electronic dead time of 25% was present. The source of this dead time is discussed in section 2.3. As a result of this dead time, the absolute cross sections measured with polarized beam were calculated using an effective efficiency times solid angle of: $\varepsilon d\Omega(5.5\ MeV) = (0.75 \times 0.0119) = 0.0089$. It should be stressed that this electronic dead time was present only for the polarized runs.

Counting The Number of Protons on Target

The final quantity that is needed to calculate an absolute cross section, as defined by equation 3.2, is the number of protons incident on target, P. This quantity is determined by integrating the beam current on target, and is discussed in detail in Chapter 2. The quoted accuracy for this procedure is estimated at 1% (as discussed in Chapter 2).

Absolute Cross Section and S-factor

Given an experimental $D(\vec{p},\gamma)^3He$ yield, equation 3.2 can now be used to calculate an absolute $\sigma(\theta)$ (i.e. a differential cross section with a correct absolute scale). In future discussions, the so called "statistical error" of the cross section will refer to the error on the yield only, whereby the so called "systematic error" will refer to the contributing errors of the other parameters which determine the absolute value of the cross section. The systematic error can be calculated by adding the errors associated with the beam current integration (ΔI), the $\varepsilon d\Omega$ value ($\Delta\varepsilon d\Omega$), and the stopping cross section (ΔSTP) in quadrature. Table 3.2 shows the component systematic errors which lead to a total estimated systematic error of 9%.

Systematic Error Components

ΔI	ΔεdΩ	ΔSTP	ΔTotal
1%	6%	6%	9%

Table 3.2: The percentage systematic error components shown along with the total percentage systematic error, ΔTotal, for the cross section and S-factor.

As discussed in Chapter 1, the cross section, $\sigma(\theta,E_{cm})$, and the S-factor, $S(\theta,E_{cm})$, are related by the following equation:

$$\sigma(\theta,E_{cm}) = \frac{S(\theta,E_{cm})}{E_{cm}} e^{-2\pi\eta(E_{cm})} \tag{3.6}$$

In this equation, the Sommerfeld parameter, $\eta(E_{cm})$, is given as follows [Rol88]:

$$2\pi\eta(E_{cm}) = 31.29 \cdot Z_1 \cdot Z_2 \cdot \sqrt{\frac{\mu}{E_{cm}}} = \frac{25.639}{\sqrt{E_{cm}}} \tag{3.7}$$

The Z_1 and Z_2 parameters in Equation 3.7 are the charges on the proton and deuteron respectively, μ is the reduced mass of the deuteron-proton system, and E_{cm} is the center of mass energy in keV.

Angular Distributions

In acquiring angular distributions for $\sigma(\theta)$, and the related $S(\theta)$, corrections must be made to the experimental yields at each laboratory angle in order to normalize the results properly. One such correction is due to varying γ-ray attenuation with HPGe lab angle (θ). This can be seen by examining Figure 3.5. Figure 3.5 shows the geometry of

the Cu disk and D_2O ice target arrangement from a top view (only a small section of the Cu disk is shown). As the HPGe lab angle is changed from 45° to 90°, as shown in the figure, the γ-ray must traverse a thicker portion of the Cu disk. In particular, while the γ-ray at 45° traverses a thickness (t) of 0.0625" of Cu, the γ-ray at 90° must traverse a thickness t = 0.0625"/cos(45°) = 0.0884". The percentage attenuation (AT) of a γ-ray beam is given by the relation

$$AT = 1 - e^{-\mu t}, \tag{3.8}$$

where μ is the γ-ray attenuation coefficient for Cu. Thus, if t_o is the thickness at an HPGe angle of 45° (t_o = 0.0625"), and φ is the angle difference away from θ = 45° (φ = θ - 45°), the percentage attenuation (for the Cu disk) is:

$$AT = 1 - e^{-\mu t_o/\cos(\phi)}. \tag{3.9}$$

Additional γ-ray attenuation occurs in the Al target chamber, but its value is angle independent, and thus need not be included in relative HPGe angle corrections.

Since the absolute efficiency measurement was done at θ = 60°, all yields taken at other HPGe angles had to be corrected for the different γ-ray attenuation. The exact correction factor was calculated using a Monte Carlo simulation program (MONTE) which handled the problem in 3-dimensions and took into account the effect of the finite beam spot size. The thickness of the D_2O ice target, although known from observation to be less than 1mm, was not known to a high degree of accuracy, and was thus neglected in the analysis (i.e. in calculating the angle φ). The justification for neglecting this thickness is simply that the HPGe detector is very far away as compared with t_o, and thus

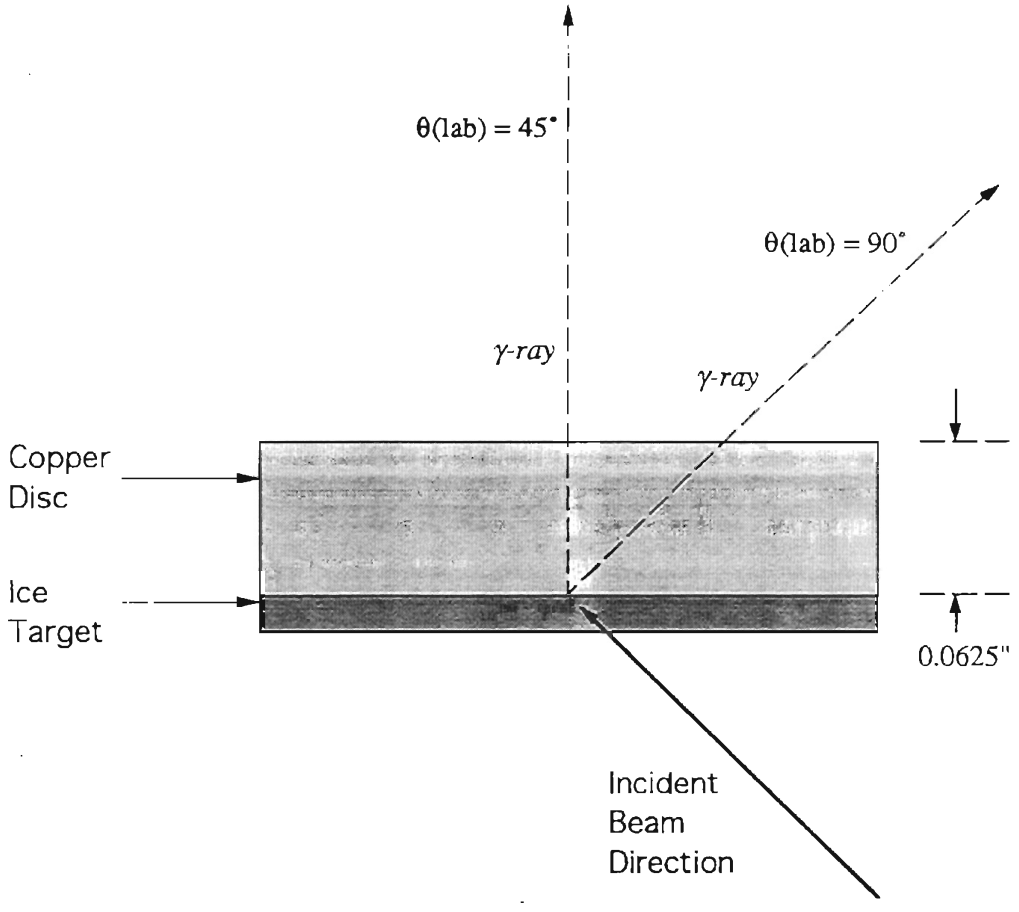

Figure 3.5: The geometry of the Cu disk and D_2O ice target, showing the direction of γ-rays leading to HPGe lab angles of 45° and 90° respectively.

the γ-rays traverse essentially parallel paths through the Cu disk, irrespective of their point of origin. Clearly, then, the γ-ray attenuation is independent of the thickness of the ice target.

When measuring angular distributions, there is one other potentially important correction factor that must be considered: target thickness change (as it relates to changing $D(p,\gamma)^3He$ yield). Since there are no charged particles of adequate energy coming out of the $D(\vec{p},\gamma)^3He$ reaction (for E_p(lab)=0-80 keV) typical target thickness

monitoring with a solid state detector is not possible, and thus the only option is to simply monitor the γ-ray count rate in order to gauge changes in target thickness. Fortunately, no serious problems with D_2O ice target deterioration were encountered. For the majority of experimental runs at a given HPGe angle, the γ-ray count rate remained constant with time. The $D(\vec{p},\gamma)^3He$ count rate was monitored by summing the full energy peak at given time intervals. A typical graph of the count rate vs. time is shown in Figure 3.6. In the event that the count rate started falling (i.e. the target began deteriorating) the affected runs were thrown out, and a new ice target was made. Data acquisition then continued with the new ice target. It was found that an ice target about 0.5mm thick would last several days under about 30μA of proton bombardment.

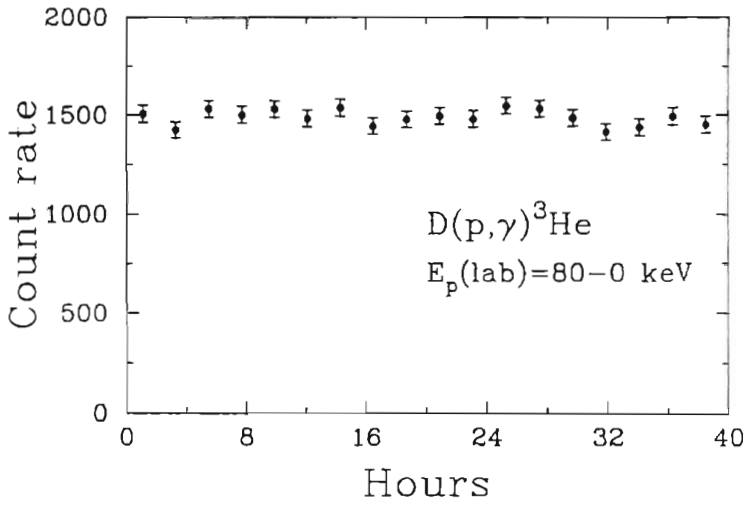

Figure 3.6: The $D(\vec{p},\gamma)^3He$ count rate vs. time for an HPGe lab angle of 60°. The count rate is given in terms of total counts per 2.2 hours of run time. The integrated beam on target, in this case, is a constant function of time.

Other potential correction factors in measuring angular distributions include computer dead time corrections and accidental coincidence corrections. Both of these

factors were negligible in the current $D(\vec{p},\gamma)^3He$ experiment. Computer dead time corrections must be made when the computer dead time is different at different times in an experiment. However, as mentioned before, the low HPGe γ-ray count rate (~60 counts per second above threshold) lead to a computer dead time that was consistently lower than 1%, and thus negligible. Accidental corrections must be made when the background count rate in an anti-coincidence shield (the NaI annulus in the current experiment) causes "good" counts in the main detector (the HPGe) to be accidentally vetoed. Again, the low γ-ray count rate caused the accidental coincidence rate to be negligible. This was seen by comparing the background count rate in the TAC spectrum (see Chapter 2) to the peak count rate in the TAC spectrum.

3.2.2 Vector Analyzing Power

The $D(\vec{p},\gamma)^3He$ yields measured with polarized incident beam allowed the extraction of the vector analyzing power, $A_y(\theta)$. The expression relating the unpolarized yield ($Y_0(\theta)$) and the polarized yield ($Y'(\theta)$) is [Sey79]

$$Y'(\theta) = Y_0(\theta)\,[1 + \vec{P}_\xi \cdot \vec{A}(\theta)], \tag{3.10}$$

where $\vec{P}_\xi$ is the vector polarization (see Equation 2.1), and $\vec{A}$ is the analyzing power vector. In the current experiment, the proton spin quantization axis ($\hat{\xi}$) was aligned in the "up" direction, which, according to Figure 2.1, is the $-\hat{y}$ direction. Thus Equation 3.10 becomes

$$Y'(\theta) = Y_0(\theta)\,[1 - P_{-y}A_y(\theta)], \tag{3.11}$$

where $P_{-y} = N_+ - N_-$ (see Equation 2.1), and, as described in Chapter 2, A_x and A_z are zero. The $A_y(\theta)$ observable was measured by allowing the polarization of the incident beam, P_{-y}, to fast spin flip between two spin states: P^+_{-y} was a polarization state aligned parallel to $\hat{\xi}$ (and thus $N_+ - N_-$ has a positive value); and P^-_{-y} was a polarization state aligned anti-parallel to $\hat{\xi}$ (and thus $N_+ - N_-$ had a negative value). With this information, and Equation 3.11, the following relation for $A_y(\theta)$ is derived,

$$A_y(\theta) = \frac{Y^-(\theta) - Y^+(\theta)}{Y^-(\theta)P^+_{-y} - Y^+(\theta)P^-_{-y}}, \tag{3.12}$$

where $Y^+(\theta)$ and $Y^-(\theta)$ are the $D(\vec{p},\gamma)^3He$ yields associated with an incident beam in a P^+_{-y} or P^-_{-y} spin state respectively. It should be stressed that the parameter P^-_{-y} in Equation 3.12 has a negative value, while P^+_{-y} has a positive value. Taking this into account, we can re-write Equation 3.12 in the more familiar form:

$$A_y(\theta) = \frac{Y^-(\theta) - Y^+(\theta)}{Y^-(\theta)\left|P^+_{-y}\right| + Y^+(\theta)\left|P^-_{-y}\right|}. \tag{3.13}$$

Perhaps the greatest advantage of measuring analyzing power observables (as opposed to measuring only the polarized cross section) is that, as shown in Equation 3.13, they depend on the ratio of yields, not on the absolute magnitude of the yields themselves. Thus, γ-ray attenuation, target thickness changes and other normalization problems, all of which are potentially important in cross section measurements, should have no effect on analyzing power measurements.

3.2.3 Gamma-ray Polarization

In addition to the $\sigma(\theta)$ and $A_y(\theta)$ observables, the $D(\vec{p},\gamma)^3He$ γ-ray polarization observable, $P_\gamma(\theta)$, was also measured. To better describe the details of this complex measurement, a full chapter (Chapter 4) is dedicated to its discussion. Please refer to that chapter for more details.

3.3 Analysis With Thick Target Yields

The accumulated $D(\vec{p},\gamma)^3He$ γ-ray spectra, such as the one shown in Figure 3.1, included all energies from E_p(lab)=80-0 keV, and were acquired for a total of six laboratory angles: 0°, 30°, 60°, 90°, 105° and 120°. One analysis that was done with these accumulated spectra consisted of summing the number of counts from the 2nd escape peak on up through the full energy peak. The cosmic background contribution was measured in a separate run and subtracted. The final background-subtracted γ-ray yield then corresponded to the energy region E_p(lab)=80-0 keV. This yield was then used to calculate $\sigma(\theta)$ (on a relative scale), $A_y(\theta)$, and $P_\gamma(\theta)$ (see Chapter 4). The results for $\sigma(\theta)$ and $A_y(\theta)$ are presented in Chapter 5.

As described in the previous section, corrections were made to account for changing γ-ray attenuation, beam current integration, etc. One additional correction, not previously discussed, is now described. While most of the experimental runs were done with a beam-line collimator included, some of the earlier runs were not. The absence of a beam-line collimator had the effect that the proton beam was focused off-target-center by ~1/4 inch. This caused a slightly different laboratory angle to be seen by the HPGe detector. In all future analysis (i.e. the binning analysis and the deconvolution analysis),

the lab angle quoted is simply the weighted average of the different angles involved (i.e. the angle which is nominally 30° is actually 30.7°). However, in the present thick target yield analysis, the huge amount of data available leads to the conclusion that an exact quotation of angle would be more accurate (i.e. the nominal 30° data is presented as 30.0° and 31.5° data respectively, rather than averaged together). It should be pointed out that while the HPGe lab angle can be calculated to an estimated accuracy of <0.5°, the large geometrical half angle of the HPGe (8.3° at the center of the detector) indicates that the small angle corrections will only be of minimal significance.

3.4 The Binning Analysis

Examining the full energy peak in Figure 3.1b, we can see that the full width is ~50 keV. Since the intrinsic HPGe response function has a resolution of ~4 keV at 5.5 MeV (see section 3.5), it would seem reasonable to assume that we can directly extract the $D(\vec{p},\gamma)^3He$ energy dependence from the spectra by simply dividing the peak into a series of energy bins, and then using these yields to calculate the observables. The exact method followed was to divide the spectra into 7 bins *based on the laboratory beam energy of the incident proton.* Each of the bins had a width of $\Delta E_p(lab)$=10 keV. Figure 3.8 (next page) shows the full energy peak of Figure 3.1b along with the 7 energy bins. The first bin goes from $E_p(lab)$=10-20 keV, the second from $E_p(lab)$=20-30 keV, and so forth on up to the top bin, which is $E_p(lab)$=70-80 keV.

In order to obtain the energy bins in terms of the actual *γ-ray energy*, as shown in Figure 3.8, the relativistic kinematics of the reaction must be worked out in detail. The reason for this is that the approximate formula of Equation 3.1, which relates $E_p(lab)$ to E_γ, is not of sufficient accuracy to allow the determination of E_γ to ±0.5 keV. Equation

3.1 was derived by simply neglecting the ^{3}He recoil, thus assuming that all the energy available in the center of mass (i.e. E_{cm}+Q) goes into the γ-ray energy. While this treatment is adequate for most cases, a more precise value is needed for the present analysis. By considering exact conservation of relativistic energy and relativistic momentum in the lab frame, the following expression for E_γ is derived:

$$E_\gamma = \frac{(E_p + Q)^2 + 2M_r c^2 (E_p + Q) - E_p (E_p + 2M_p c^2)}{2(E_p + Q + M_r c^2 - \cos\theta_\gamma \sqrt{E_p^{\,2} + 2E_p M_p c^2})}, \qquad (3.14)$$

where E_p is the lab beam energy, M_r is the mass of the recoiling ^{3}He particle, M_p is the mass of the proton, Q is the Q-value of the D($\vec{p}$,γ)^{3}He reaction, and θ_γ is the lab angle of the γ-ray with respect to the incident beam axis. Under the assumption that $M_r c^2 \gg Q \gg E_p$, Equation 3.14 can be seen to reduce to Equation 3.1. Using Equation 3.14, the energy bins, formulated in terms of E_p, can now be expressed in terms of E_γ as shown in Figure 3.7. For the binning analysis, we take $\theta_\gamma = \theta_{lab}$ in Equation 3.14.

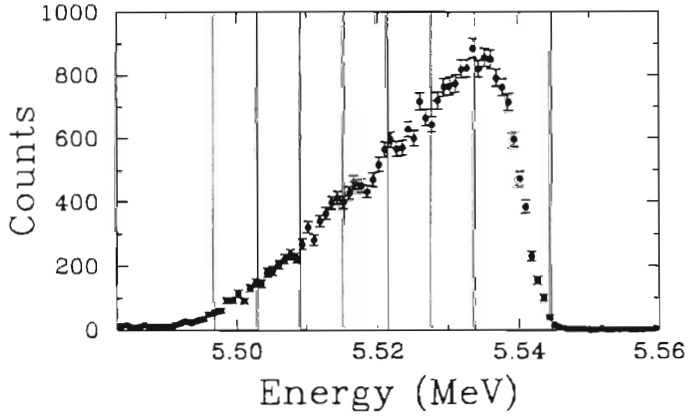

Figure 3.7: The D($\vec{p}$,γ)^{3}He full energy peak for θ_{lab}=90° shown along with the 7 binned energy regions. This is the same full energy peak that was shown in Figure 3.1b.

As was pointed out before, the absolute E_γ energy scale obtained with low energy radioactive sources can be in error by as much as ±20 keV off at 5.5 MeV. Based in part on the results of the deconvolution analysis (to be discussed), it is concluded that the spectrum in Figure 3.7 can be re-scaled to an accuracy of better than ±1 keV based solely on the shape of the full energy peak. The location of the value of E_γ which corresponds to E_p(lab)=80 keV is certain to lie between the peak and the bottom of the high energy edge of the full energy peak, and the results of the deconvolution analysis suggest a central location within this region. Thus, the starting point for the binning process is to estimate the location of this E_p(lab)=80 keV point, and thus set the absolute scale for the x-axis energy calibration in this manner (recall from section 3.1 that the calibration in keV/channel is well known). The location of all seven bins then follows from Equation 3.14. Note that the uppermost bin in Figure 3.7 has been widened to include all the data above E_p(lab)=80 keV (i.e. the γ-ray energy corresponding to E_p(lab)=80 keV). The reason for this is that the process of convoluting the HPGe response function with the $D(\vec{p},\gamma)^3He$ yield has the effect of folding some of the strength from the top bin into the γ-ray region corresponding to E_p(lab)>80 keV. This necessitates widening the top bin in order to obtain the full strength for the E_p(lab)=70-80 keV region.

Once raw binned yields have been acquired for a spectrum, the known cosmic ray background can be subtracted. This background is obtained by monitoring an energy window just above the full energy peak. Another background component that is considered is due to the long, low energy tail of the HPGe response function. Each bin will necessarily lose some of its strength to the lower energy bins because the HPGe response function (described in section 3.5) has a small low energy tail. Based on the analysis described in section 3.5, we can expect a monoenergetic full energy peak to lose 3% of its strength to this tail (for a given energy window). By assuming that each

channel of the full energy peak in Figure 3.7 has a constant tail of this magnitude, we can then derive an estimated form for this background contribution. The absolute strength of this background contribution is obtained by normalizing to the height of the background on the low energy side of the full energy peak (once the cosmic ray background is subtracted). The final form for this background is then subtracted from the yields. As might be expected, this background contribution is negligibly small for all but the lowest few bins. For example, it is a 20% effect for the lowest energy bin, but only a 7% effect for the next higher bin, and considerably smaller thereafter.

Once the background corrected yields are obtained, the cross section and analyzing power can be calculated for each energy bin in the spectrum. After doing this for all angles, we obtain $\sigma(\theta,E)$ and $A_y(\theta,E)$. In order to obtain the $\sigma(\theta,E)$ data, it is necessary to integrate the deuterium areal density (D(E)) over the energy region of interest in order to obtain the proper number of deuterons per cm^2 for each bin. In other words,

$$D(E_{lab} \rightarrow E_{lab}') = \int_{E_{lab}}^{E_{lab}'} dD(E_{lab}) = \int_{E_{lab}}^{E_{lab}'} \frac{2dE_{lab}}{STP(E_{lab})}, \qquad (3.15)$$

where STP(E) is the stopping cross section function. The integrated deuterium areal density for each bin is shown in Table 3.3. A 6% error is assumed for quoted value of D (as previously discussed). The final results for $\sigma(\theta,E)$ and $A_y(\theta,E)$ will presented in Chapter 5.

Deuterium Areal Density

Bin #	Proton lab energy	D = #Deuterons/cm^2
1	10-20 keV	1.29×10^{18}
2	20-30 keV	1.04×10^{18}
3	30-40 keV	9.26×10^{17}
4	40-50 keV	8.62×10^{17}
5	50-60 keV	8.26×10^{17}
6	60-70 keV	8.07×10^{17}
7	70-80 keV	8.01×10^{17}

Table 3.3: Deuterium areal density (D) for each bin in Figure 3.7.

3.5 The Deconvolution Analysis

The goal of the deconvolution analysis was to remove the effects of the HPGe detector response, and the effects of the changing deuterium areal density, from the raw spectra in order to directly view the energy dependence of the D($\vec{p}$,γ)^{3}He S-factor (i.e. cross section). The method chosen to perform the deconvolution procedure was that of a convolution fit to the raw spectra. The steps of this procedure were as follows:

1. Derive a parameterized functional form for the D($\vec{p}$,γ)^{3}He yield.
2. Derive a functional form for the HPGe response function at 5.5 MeV.
3. Convolute the yield function and the HPGe response function together, and

then fit the resulting curve directly to the raw spectra. This will determine the parameters in the yield function, and thus will give us a functional form for the $D(\vec{p},\gamma)^3He$ S-factor.

The following subsections will describe all the details of the above outline. The ultimate goal is to apply this fitting procedure to $D(\vec{p},\gamma)^3He$ spectra obtained with both unpolarized and polarized incident beams. From the spectra obtained with unpolarized incident beams, we hope to extract an S-factor as a function of angle and energy, $S(\theta,E)$. From the spectra obtained with polarized incident beams, we hope to obtain the analyzing power as a function of angle and energy, $A_y(\theta)$.

3.5.1 Parameterized $D(\vec{p},\gamma)^3He$ Yield Function

In order to deconvolute the $D(\vec{p},\gamma)^3He$ spectra (using the present method), it is necessary to make a model dependent assumption about the form of the yield. In this manner, we are able to reduce the number of fitting variables to a small number, and thus have a better chance of obtaining a unique solution. According to Equation 3.2, the $D(\vec{p},\gamma)^3He$ yield can be written as follows:

$$Y(\theta_{lab},E_{lab}) = \sigma(\theta_{lab},E_{lab})\,(D(E_{lab}))\,(P)\,(\varepsilon d\Omega) \qquad (3.16)$$

Since the deuterium areal density (D), the # of protons on target (P), and the efficiency times solid angle ($\varepsilon d\Omega$) are all known (see section 3.2.1), the only unknown in Equation 3.16 is the cross section $\sigma(\theta_{lab},E_{lab})$.

As shown in Equation 3.6, the cross section can be written in terms of the S-factor, $S(\theta,E_{cm})$, where $E_{cm}=(2/3)E_p(lab)$ in this case. In order to simplify the analysis, the following model dependent assumption about $S(\theta,E_{cm})$ is made:

$$S(\theta,E_{cm}) = S_0(\theta) + E_{cm}S_1(\theta) \tag{3.17}$$

In other words, the S-factor is assumed to be linear in the energy region of interest ($E_p(lab)<80$ keV). The $S_0(\theta)$ and $S_1(\theta)$ are parameters to be determined by the convolution fit to the raw spectra (section 3.5.3). The assumption of a linear S-factor seems reasonable based on the wealth of experimental data for low energy, non-resonant, capture reactions (see [Rol88]), which show that the S-factor is typically slowly varying with energy, and that a linear S-factor usually can fit the data quite well (over a small energy region). In addition, it should be pointed out that theoretical treatments of the $D(p,\gamma)^3He$ reaction at low energies (see Chapter 6) predict S-factors which are nearly linear.

Combining Equations 3.6, 3.16, and 3.17, we obtain a final expression for the parameterized $D(\vec{p},\gamma)^3He$ yield:

$$Y(\theta_{lab},E_{lab}) = \frac{S_0(\theta)+E_{cm}S_1(\theta)}{E_{cm}}\, e^{-2\pi\eta(E_{cm})}\,(D(E_{lab}))\,(P)\,(\varepsilon d\Omega) \tag{3.18}$$

3.5.2 HPGe Response Function

In order to be able to remove the effects of the HPGe response function from the raw spectra, it is necessary to have a knowledge of the exact functional form for the HPGe full energy peak response function. The total HPGe full energy peak response

function (R) for the ~5.5 MeV γ-rays from $D(\vec{p},\gamma)^3He$ is actually a convolution of two separate component response functions: an intrinsic response function (I) due to the interaction of a monoenergetic γ-ray with the HPGe crystal; and a so called "kinematic" response function (K), which arises as a result of the finite geometry of the experimental set-up.

Intrinsic HPGe Response Function

The intrinsic HPGe full energy peak response function (I) was studied using a ^{66}Ga source [Ald93] which emits several mono-energetic γ-rays up to 4.8 MeV. The peaks at 3.3, 4.0, 4.4, and 4.8 MeV were fit to a functional form comprised of three components: a primary gaussian, a skewed gaussian, and a smoothed step function (which is the low energy tail). This germanium detector peak fitting recipe follows that of Jorch and Campbell [Jor77], and Emling [Eml86]. The primary gaussian is due to the statistical nature of the charge collection process. The skewed gaussian is thought to be due to incomplete charge collection by the detector. The smoothed step comprising the low energy tail is attributed to the escape of photo-electrons from the detector, and also to Compton scattering background (due to photons which undergo multiple Compton scattering in the detector before escaping, and also due to photons which Compton scatter *into* the detector from outside).

The form of the gaussian component is as shown below

$$\text{Gauss}(E) = A\frac{1}{\sigma\sqrt{2\pi}}\exp\left[-\frac{(E-E_c)^2}{2\sigma^2}\right], \tag{3.19}$$

where A is a constant to assure normalization over a given energy region (in this case, a standard energy window set to encompass the full energy peak), σ is the standard deviation (=FWHM/2.354), and E_c is the centroid of the peak. The form of the skewed gaussian component is obtained by convoluting an exponential tail with a gaussian shape, and is given by the following expression

$$\text{Skew}(E) = B\ \exp\left[\frac{E-E_c}{\beta}\right]\text{erfc}\left[\frac{E-E_c}{\sigma\sqrt{2}}+\frac{\sigma}{\beta\sqrt{2}}\right], \qquad (3.20)$$

where B is a constant to assure normalization over the standard energy region, β is a parameter referred to in the literature as the "skewedness" of the skewed gaussian, and erfc refers to the complement of the error function. And finally, the form of the smoothed step function is obtained by convoluting a pure step function with a gaussian shape, and given by the expression below

$$\text{Step}(E) = C\ \text{erfc}\left[\frac{E-E_c}{\sigma\sqrt{2}}\right], \qquad (3.21)$$

where C is a constant to assure normalization over the standard energy region. The total intrinsic HPGe response function (I) is then a linear combination of these three components, as shown by Equation 3.22:

$$I(E) = (N_{Gauss})\ \text{Gauss}(E) + (N_{Skew})\ \text{Skew}(E) + (N_{Step})\ \text{Step}(E), \qquad (3.22)$$

where N_{Gauss}, N_{Skew}, and N_{Step} represent the fraction of each response component that is present within a given energy region ($N_{Gauss}+N_{Skew}+N_{Step}=1$). It is clear that I(E) is normalized to unity over the standard energy region.

The ^{66}Ga peaks at 3.3, 4.0, 4.4, and 4.8 MeV were fit to a form equal to Equation 3.22 multiplied by a variable height factor. The extracted parameters were then extrapolated to 5.5 MeV (the energy of the D($\vec{p}$,γ)^{3}He γ-ray). The value of the step fraction, N_{Step}, that was used in the final deconvolution was determined by treating it as a free parameter in a series of test fits to D($\vec{p}$,γ)^{3}He spectra. The final 5.5 MeV parameters used were: N_{Step}=.03, N_{Gauss}=.75, N_{Skew}=.22, β=1.72 keV, FWHM=4.2 keV. Figure 3.8 shows the shape of the response function which results from these parameters. On the left side are the three components in their correct relative proportions. On the right is the total intrinsic response function (I), which is the sum of the three component parts. For scale, the FWHM of I is 4.2 keV.

Kinematic HPGe Response Function

Examining Equation 3.14, it can be seen that D($\vec{p}$,γ)^{3}He γ-rays emerging at different lab angles will have different energies. Since the solid angle of the HPGe detector is finite, a range of possible γ-ray energies will be present in the HPGe response function, and this will lead to a widening of the full energy peak. In order to properly fit the shape of the HPGe response function, this kinematic widening must be taken into account. By estimating the HPGe solid angle (i.e. the solid angle subtended by the center of the HPGe detector), the range of possible kinematic γ-ray energies can be obtained. However, in order to determine the shape of the HPGe kinematic response function, it is also necessary to determine the relative strength of each γ-ray energy (i.e. the probability of detection for each γ-ray angle, θ_γ). An initial attempt at determining the relative strengths for each possible θ_γ was undertaken with a "homemade" monte carlo program (MONTE) [Mon95] which calculated the γ-ray path length through the HPGe for each

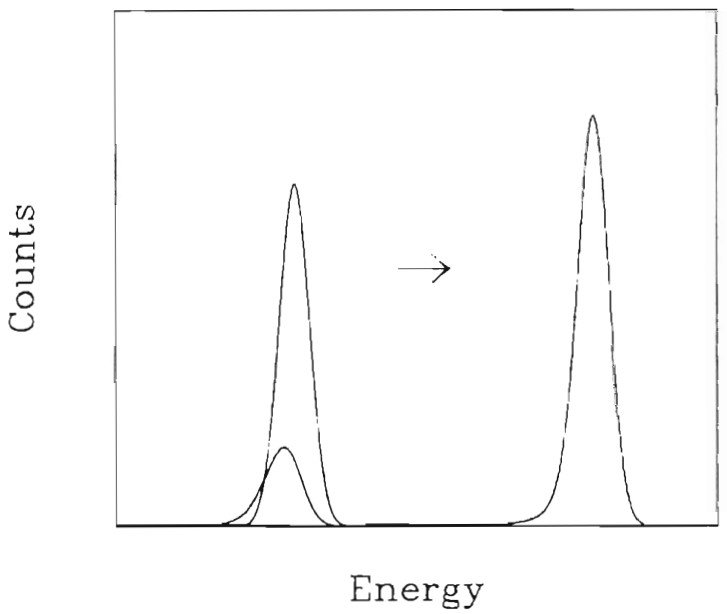

Figure 3.8: The Intrinsic HPGe response function at 5.5 MeV. On the left are the three component parts: the Gaussian, Skew Gaussian, and Step Function parts. On the right is the total intrinsic response function (I), the sum of the parts.

θ_γ, and then used the total absorption coefficient for germanium at 5.5 MeV to calculate the probability of absorption.

One possible problem with this approach is that the present analysis uses only the full energy peak, and not the total HPGe response. Thus, what is truly desired is the full energy peak absorption coefficient. This coefficient depends on the location of the γ-ray interaction within the HPGe (a γ-ray interacting near the HPGe edge is less likely to lead to a full energy peak count), and thus an exact simulation of the γ-ray interaction process is needed. This was accomplished by using the EGS4 code from Stanford [Nel85] instead of the simpler MONTE code. The EGS4 code (EGS stands for Electron-Gamma-Shower) reproduces the γ-ray interaction process in a true-to-life fashion, and allows the user to reliably determine the full energy peak absorption probability for each θ_γ (given a

specific target-detector geometry). The EGS4 code is operated by means of a user-written main program. The main program used in the current case, called GREG, is shown in Appendix A.

For the EGS4 simulation, an isotropically emitting point γ-ray source was assumed to be at the target location, which was 9.125" away from the HPGe front face (on axis). Initial test runs with the MONTE Monte Carlo code showed that several factors were small enough to neglect in determining the kinematic response shape. These factors include the effects of finite target size; the presence of the Cu target disk; and the non-isotropy of the $D(\vec{p},\gamma)^3He$ radiation. For both the MONTE and EGS4 simulations, the HPGe geometry included the on axis "hole" which is present in coaxial Ge detectors (radius=0.2", length=3.79" starting 0.51" behind HPGe front face). The copper contact pin present inside the hole was neglected. The NaI and lead shielding surrounding the HPGe were also neglected in the calculations because they too are not expected to affect full energy peak absorption (appearance in the photopeak requires the initial, and all subsequent, γ-ray interactions to be in the Ge crystal itself). The result of the EGS4 simulation is shown in Figure 3.9.

In Figure 3.9, the HPGe is assumed to be at a lab angle of 90°, as in Figure 2.4. The results of the monte carlo simulations are shown as a function of θ_γ, the γ-ray angle with respect to the incident proton beam direction. The y-axis is the number of counts detected in the full energy peak (normalized such that the sum of all detected counts equals one). The primary difference between the EGS4 result and the initial MONTE result was that the width of the response (i.e. the effective HPGe solid angle for full energy peak events) was somewhat narrower with the EGS4 result than with the MONTE result (which used only the total absorption coefficient). In order to determine the actual

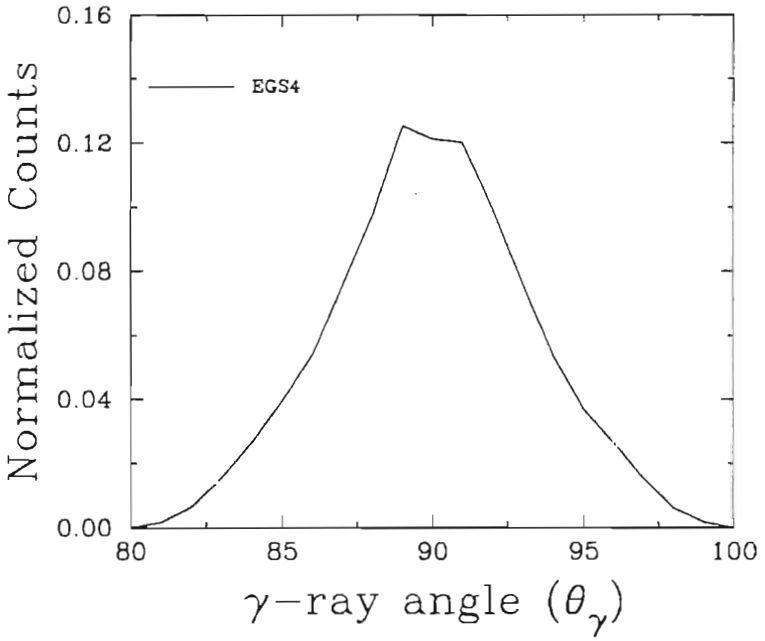

Figure 3.9: The result of the EGS4 monte carlo simulation for an HPGe lab angle of 90°.

HPGe kinematic response that will be viewed in the acquired spectra, the x-axis in Figure 3.9 must be changed from θ_γ to E_γ, and this is done via Equation 3.14. The result is then the kinematic response function (K) as a function of E_γ.

Total HPGe Response Function

The total HPGe response function (R) is then the convolution of the intrinsic response function (I) and the kinematic response function (K) over the energy range of the full energy peak (i.e. R = I * K). The convolution was carried out numerically by means of the computer code FCN_SFACT shown in Appendix B. An example of the total HPGe response function (R) which results from the convolution process is shown in Figure 3.10 by the solid line. This curve is for a convolution corresponding to an

incident beam energy E_p(lab)=80 keV (according to Equation 3.14, E_γ, and thus the shape of the kinematic response function, is a function of the incident beam energy E_p(lab)). The dashed line is the intrinsic response function (I) shown in Figure 3.8. The similarity between the two curves indicates that the kinematic response function plays only a minor role in the determination of the total response function (R). For scale, the FWHM of the dashed curve is 4.2 keV, while the FWHM of the total response function is 4.7 keV.

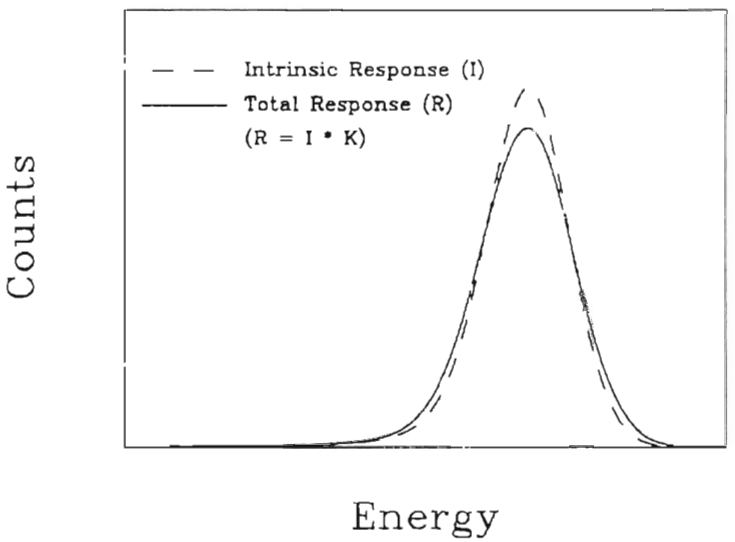

Figure 3.10: The total response function (R) (solid line), for E_p(lab)=80 keV, resulting from the convolution of the intrinsic response function (I) and the kinematic response function (K). The dashed line is the intrinsic response function.

3.5.3 Convolution Fit to Data

Having obtained the total HPGe response function (R), the final step is then to convolute the total response function with the parameterized yield function (Y) given in

Equation 3.18. The resulting curve (= R * Y), after adding in the known cosmic ray background, is then fit directly to the raw D($\vec{p}$,γ)^{3}He spectra in order to determine the $S_0(\theta)$ and $S_1(\theta)$ parameters from Equation 3.18. The fitting procedure was carried out using the MINUIT χ^2 minimization package (Jam77). The user-written code that controlled the MINUIT fitting procedure was FCN_SFACT, the same code which created the parameterized R * Y curve to be fit to the spectra (see Appendix B). In the fitting procedure, three free parameters are assumed: the $S_0(\theta)$ parameter; the $S_1(\theta)$ parameter; and an energy calibration parameter, $C_E(\theta)$. The extraction of the $C_E(\theta)$ parameter, which represents the ADC channel number corresponding to E_p(lab)=80 keV, allows a precise determination of the energy calibration of the raw spectra. This is necessary in order to evaluate the R * Y convolution correctly.

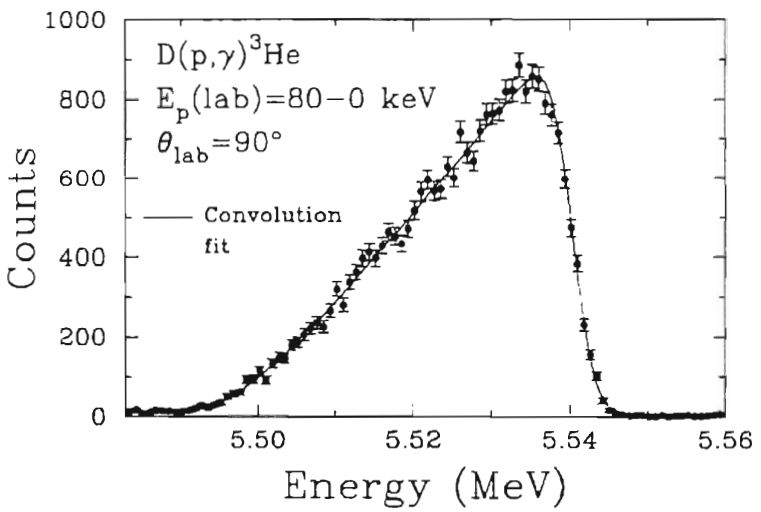

Figure 3.11: The D($\vec{p}$,γ)^{3}He spectra of Figure 3.1b shown along with a convolution fit.

The convolution fitting procedure was carried out for 35 accumulated spectra (corrected for gain shifts) which represented HPGe lab angles of θ = 0°, 30°, 60°, 90°, 105° and 120°. The quality of the fits to the spectra, evaluated in terms of the χ^2 per

degree of freedom (χ^2/ν), were quite good, thus lending credence to the linear S-factor assumption that was used. Figure 3.11 shows the convolution fit to the raw, full energy peak, spectrum of Figure 3.1b. The convolution fit shown has a χ^2/ν of 1.06.

Once the $S_0(\theta)$ and $S_1(\theta)$ parameters have been determined for all of the *unpolarized* spectra, and the results for each lab angle combined, the total $S(\theta,E_{cm})$ factor was calculated by means of Equation 3.17. By tabulating $S_0(\theta)$ and $S_1(\theta)$ results for the *polarized* spectra, the vector analyzing power was calculated by means of Equation 3.13. The results for both of these observables ($S(\theta,E_{cm})$ and $A_y(\theta,E)$) will be presented in Chapter 5.

Chapter 4

Gamma-ray Polarization

In addition to the $\sigma(\theta)$ and $A_y(\theta)$ observables, the γ-ray linear polarization, $P_\gamma(\theta)$, was also measured for $D(p,\gamma)^3He$. Throughout this chapter, only unpolarized incident beams will be considered (for reasons to be discussed). This simplifies matters, since it has been shown [Fer65] that in this case, there should be no circular polarization component in the outgoing γ-radiation. In what follows, the procedure for acquiring the $P_\gamma(\theta)$ data will be discussed. The reason for relegating the $P_\gamma(\theta)$ material to a separate chapter, as opposed to integrating its presentation into Chapter 3, is that the experimental procedure used to acquire the $P_\gamma(\theta)$ data is very different from that used to acquire the $\sigma(\theta)$ and $A_y(\theta)$ data, and hence a detailed presentation is called for. However, it should be emphasized that the greater space allocated for discussion of the $P_\gamma(\theta)$ observable should not imply a greater significance of the $P_\gamma(\theta)$ observable (as compared with the other observables) in obtaining conclusions for this experiment. In fact, as it turns out, the data acquired for the $P_\gamma(\theta)$ observable play a very minor role in the conclusions of the current experiment.

4.1 Definition of $P_\gamma(\theta)$

An excellent discussion of γ-ray linear polarization is contained within the doctoral thesis of J.R. Williams [Wil74], and the interested reader is referred there for a more

detailed discussion on the definitions that follow. For a nuclear reaction initiated by a beam of unpolarized particles, the linear polarization of the outgoing γ-radiation, $P_\gamma(\theta)$, is defined here as follows (it should be noted that other definitions do exist):

$$P_\gamma(\theta) = \frac{J_0(\theta,\phi = 0^\circ) - J_{90}(\theta,\phi = 90^\circ)}{J_0(\theta,\phi = 0^\circ) + J_{90}(\theta,\phi = 90^\circ)}, \tag{4.1}$$

where J_ϕ is the intensity of the outgoing photons which have their electric vector at an angle ϕ with respect to the reaction plane (thus J_0 is the intensity at ϕ=0° and J_{90} is the intensity at ϕ=90°), and θ is the laboratory HPGe detector angle with respect to the incident beam axis. Figure 4.1, below, shows these ϕ directions.

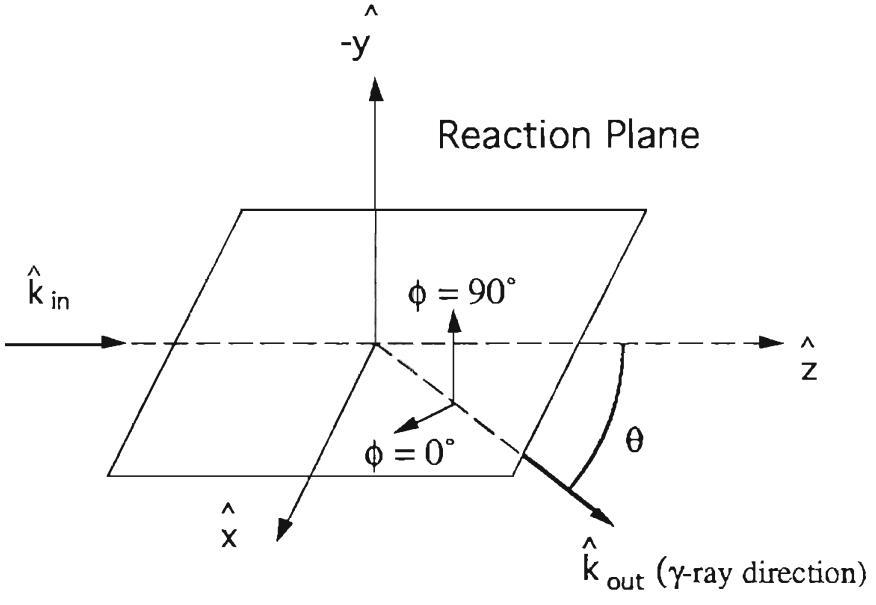

Figure 4.1: The $D(p,\gamma)^3He$ reaction plane (as shown in Figure 2.2) shown along with the ϕ=0° and ϕ=90° directions for the electric vector of the photon.

Clearly, in order to have a linearly polarized γ-ray beam, the J_0 and J_{90} intensities must be unequal. For example, in the event that J_{90} is exactly zero, the γ-radiation would be said to be purely plane polarized in the reaction plane (i.e. all the photon electric vectors have $\phi=0°$). From the standpoint of classical electrodynamics, it is interesting to consider what γ-ray polarization we might expect for $D(p,\gamma)^3He$. The vector potential that results from a classical system of oscillating charges and currents can be expanded into multipole components [Jac75], whereby the lowest order term in this expansion is the electric dipole (E1) term. In the radiation zone, J.D. Jackson [Jac75] has shown that the electric vector of the electric dipole term is in the direction $\hat{E}=(\hat{n}\times\hat{p})\times\hat{n}$, where $\hat{n}$ is the direction of propagation for the γ-radiation, and $\hat{p}$ is the direction of orientation for the radiating proton-deuteron dipole. If we make the reasonable assumption that the dipole is oriented in the reaction plane (along the incident beam direction would seem likely), we see that $\hat{E}$ is also in the reaction plane ($\perp$ to the direction of propagation). This is the case of pure plane polarization with $J_{90}=0$, and thus, according the Equation 4.1, the electric dipole term would be expected to have $P_\gamma(\theta)=1$.

The next higher term in the expansion of the vector potential includes a magnetic dipole (M1) term. I neglect the electric quadrupole term because, as will be shown in Chapter 5, it is not expected to be important in the present study. In [Jac75], it is shown that the electric vector of the magnetic dipole term is $\perp$ to the direction of the electric vector of the electric dipole term. Thus, for pure magnetic dipole radiation, $J_0=0$, and $P_\gamma(\theta)=-1$ might be expected. Actually, since the M1 radiation in the current $D(p,\gamma)^3He$ experiment results from practically pure s-wave capture (see Chapter 5), the proton-deuteron dipole will have no preferred direction in space, and thus we expect $J_0=J_{90}$ and $P_\gamma(\theta)=0$ for M1. Since the γ-radiation from $D(p,\gamma)^3He$ in the current experiment is expected to be largely electric dipole with a certain degree of magnetic dipole mixed in

(see Chapter 5), we expect that the measured $P_\gamma(\theta)$ values will be somewhat less than 1, thus reflecting the mixture of E1 and M1 which is present.

Once the $P_\gamma(\theta)$ observable is measured, the way to determine the relative amounts of E1 and M1 which are present is to expand J_0 and J_{90}, from Equation 4.1, in terms of the complex transition matrix elements by means of the angular correlation formalism discussed in [Wil74] and [LWF59]. However, the final equations which are presented in [Wil74] have been derived for the specific case of isolated resonances, and thus are not directly applicable to radiative capture reactions like $D(p,\gamma)^3He$, which go from continuum states. However, Weller et al. [Wel92] have derived a separate set of equations which are appropriate for nuclear reactions involving continuum states. This paper has organized the polarized photon formalism into a convenient form, and includes a set of tables which give the values for all necessary angular coupling coefficients. Section 4.3 describes the method used to express $P(\theta)$ in terms of the transition matrix elements.

4.2 Previous Measurements of $P_\gamma(\theta)$

Before discussing the current work in measuring the γ-ray linear polarization, $P_\gamma(\theta)$, for the $D(p,\gamma)^3He$ reaction, it is appropriate to review the previous work that has been done. In the low energy regime, this consists of just one previous experiment done in 1952 by D.H. Wilkinson [Wil52]. This experiment used incident protons of 1.1 MeV to initiate the $D(p,\gamma)^3He$ reaction, and then allowed the outgoing γ-rays to photodisintegrate deuterons on a photographic plate. By measuring the angular distribution of the outgoing photoprotons, the γ-ray polarization was determined, and was found to be completely consistent with pure plane polarized E1 radiation.

This conclusion is completely reasonable based on the wealth of experimental $\sigma(\theta)$ data acquired since 1952, which has shown that around 1 MeV, the angular distribution shows a $\sin^2\theta$ shape which is typically associated with E1 radiation (e.g. see [Kin84]). Wilkinson himself provided the following justification: if the spin-orbit coupling in $D(p,\gamma)^3He$ is weak, changes will not be induced in the z-component of the intrinsic spins of the interacting particles, and thus only $\Delta J_z=0$ transitions will arise. According to [Jac75], this condition would lead to a pure $\sin^2\theta$ angular distribution and also pure plane polarization for the γ-rays (i.e. $P(\theta)=1$). The reason that a weak spin-orbit interaction might lead to the restriction $\Delta J_z=0$ can be justified if one assumes a single particle picture for the $D(p,\gamma)^3He$ process (see Chapter 6). In the single particle picture, the incident proton does not interact with the deuteron in the continuum state (i.e. no coupling takes place). In the absence of spin-orbit coupling (or in very weak spin orbit coupling) it can be assumed that in the continuum state (of total angular momentum J) we will have

$$J_z = S_z + l_z, \tag{4.2}$$

and

$$S_z = m_s \hbar \quad \text{and} \quad l_z = m_l \hbar, \tag{4.3}$$

where $\vec{S}$ and $\vec{L}$ are the spin and orbital angular momentum of the proton. Equations 4.2 and 4.3 indicate that for weak spin-orbit coupling, the intrinsic and orbital angular momenta are now quantized with respect to the z-axis (the incident beam direction) instead of the total angular momentum axis. For the $D(p,\gamma)^3He$ reaction, the final state is

^{3}He, which can be well described as an s'=1/2, l '=0 state. For this state, it is clear that $J_z'=S_z'$ since m_l' must be zero, and hence l_z' must be zero. For the continuum state, $J_z=S_z+l_z$. However, since $\vec{L} = \vec{r} \times \vec{p}$ will be $\perp$ to the beam axis, the component of $\vec{L}$ onto the beam axis will be zero (l_z=0). Thus we have

$$\Delta J_z = J_z - J_z' = S_z - S_z'. \tag{4.4}$$

However, since the magnetic dipole moment of the system is proportional to S_z (in the single par le picture), a change in S_z would indicate a change in the magnetic dipole moment ot the system. This would necessitate the presence of magnetic dipole radiation instead of electric dipole radiation. The obvious conclusion is that, for pure E1 radiation, ΔJ_z must be zero!

The assumptions implicit in this argument, while apparently valid at E_p(lab)=1.1 MeV (based on the results oi [Wil52]), may not necessarily be valid at E_p(lab)<80 keV. A re-measurement of the γ-ray polarization in this lower energy regime is thus certainly not redundant and should help point out the changing relative strengths of the E1 and M1 multipoles versus energy.

4.3 TME Expansion for $P_\gamma(\theta)$

The formalism for expressing *photodisintegration* observables in terms of the complex reduced transition matrix elements (TME's) is presented in [Wel92]. However, by using the concept of time reversal invariance for the electromagnetic interaction, it can be shown [Sat58] that the analyzing power, A(θ), for ^{3}He photodisintegration (i.e. ^{3}He(γ,p)D) is exactly equivalent to the γ-ray linear polarization, $P_\gamma(\theta)$, for the inverse

reaction, $D(p,\gamma)^3He$. In this manner, it is possible to use the well organized *photodisintegration* equations of [Wel92] in order to calculate $P_\gamma(\theta)$ for the *photoproduction* reaction $D(p,\gamma)^3He$. The equations in [Wel92] are given in terms of the complex reduced transition matrix elements, R_t, where the subscript "t" refers to the set of quantum numbers {p, L, b, l, s} associated with the transition matrix element R. In particular, p=γ-ray mode ("1"=electric, "0"=magnetic), L=multipolarity of γ-ray, l =orbital angular momentum in the outgoing channel, s=channel spin, and b=total angular momentum=$\vec{l}+\vec{s}$. Thus, using the result for $A(\theta)$ from [Wel92], the following $P_\gamma(\theta)$ expression for $D(p,\gamma)^3He$ is obtained:

$$P_\gamma(\theta) = \frac{-\sqrt{\frac{3}{5}}\sum_{t,t',k'}\left[B_{22}^{k'2}R_tR_{t'}^{'*}P_{k'}^2(\cos\theta)\right]}{\sum_{t,t',k'}\left[\left(B_{00}^{k'0}+\frac{1}{\sqrt{10}}B_{20}^{k'0}\right)R_tR_{t'}^{'*}P_{k'}(\cos\theta)\right]}. \qquad (4.5)$$

In equation 4.5, the R_t are the complex reduced transition matrix elements discussed above, the $P(\cos\theta)$ and $P^2(\cos\theta)$ functions are the Legendre and 2nd associated Legendre polynomials respectively (where θ is the angle of the γ-ray detector with respect to the incident proton beam axis), and the B-coefficients are factors which contain the angular momentum coupling algebra. The exact numerical expression for $P_\gamma(\theta)$ in terms of the transition matrix elements will be worked out in Chapter 5. It should be emphasized that Equation 4.5 gives the γ-ray linear polarization solely for the case of unpolarized incident beam.

The matrix elements used in the $P_\gamma(\theta)$ expansion in Equation 4.5 are the same matrix elements used to express the $\sigma(\theta)$ and $A_y(\theta)$ observables (see Chapter 5). The advantage of measuring the $P_\gamma(\theta)$ observable immediately becomes clear then: it should, in theory, provide an additional constraint in the effort to extract the amplitudes and

phases of the complex matrix elements (Chapter 5). As mentioned earlier, we expect $P_\gamma(\theta)$ to be especially sensitive to the ratio of E1 to M1 radiation.

4.4 Compton Polarimeter

In order to measure $P_\gamma(\theta)$, it is necessary to have a γ-ray detection method which can differentiate between different directions of the γ-ray polarization vector (i.e. the direction of the electric field vector). A standard way of doing this is by means of a Compton polarimeter (e.g. [Wil75], [LWF59]) which takes advantage of the γ-ray polarization sensitivity of the Compton scattering process. The following discussion on Compton polarimeter formalism follows closely the presentation in [Wil75].

The Compton scattering process can be described by Quantum Electrodynamics (QED) as shown by [Eva55]. The expression for the differential cross section, known as the Klein-Nishina formula (first derived by Klein and Nishina [Kle29]), can be written as follows [Eva55,Wil75]:

$$d\sigma(\theta_c,\eta) = \frac{r_0^2}{2}\frac{E_\gamma'^2}{E_\gamma^2}\left[\frac{E_\gamma}{E_\gamma'} + \frac{E_\gamma'}{E_\gamma} - 2\sin^2\theta_c\cos^2\eta\right]d\Omega. \qquad (4.6)$$

In Equation 4.6, $d\sigma$ has been summed over all directions of the polarization of the scattered photon (since the only polarization of interest is the polarization of the incident $D(p,\gamma)^3He$ photon). The symbols used in Equation 4.6 are defined below:

- $r_0 \equiv e^2/(m_e c^2)$ = the "classical electron radius", where m_e is the mass of the electron.
- $d\Omega$ = the solid angle into which the photon is scattered.
- θ_c = the Compton scattering angle (to be distinguished from θ, the HPGe

detector angle).

- η = the angle between the electric vector of the incident photon and the plane containing the Compton scattered photon.
- E_γ is the energy of the incident photon and E_γ' is the energy of the Compton scattered photon.

Using conservation of relativistic energy and momentum for the Compton scattering process, it can be shown that E_γ and E_γ' are related as follows:

$$E_\gamma' = \frac{m_e c^2}{1 + \frac{m_e c^2}{E_\gamma} - \cos\theta_c}. \tag{4.7}$$

From Equation 4.6, it is clear that the differential cross section is a maximum when η is 90° and a minimum when η is 0°. In other words, as discussed by [Wil75], the incident photons are preferentially scattered at right angles to their electric vectors. For example, a photon which has its electric vector in the $D(p,\gamma)^3He$ reaction plane (ϕ=0° in Figure 4.1) will be preferentially scattered in the "up-down" direction (i.e. the $-\hat{y}$ or $\hat{y}$ direction) while a photon with electric vector ϕ=90° will be preferentially scattered in the "left-right" direction. With this in mind, the idea behind a Compton polarimeter is now outlined as follows: the γ-rays from the $D(p,\gamma)^3He$ reaction which Compton scatter in the HPGe crystal are monitored for a left-right/up-down scattering asymmetry. This is accomplished, in the current case, by using the quadrated NaI(Tl) annulus which surrounds the HPGe detector. This annulus consists of four separate NaI(Tl) detectors as shown in Figure 4.2 on the next page.

In Figure 4.2, the direction of $\hat{k}_{out}$, as shown in Figure 4.1, is here going into the page. Since the four NaI(Tl) segments are viewed by separate photomultiplier tubes,

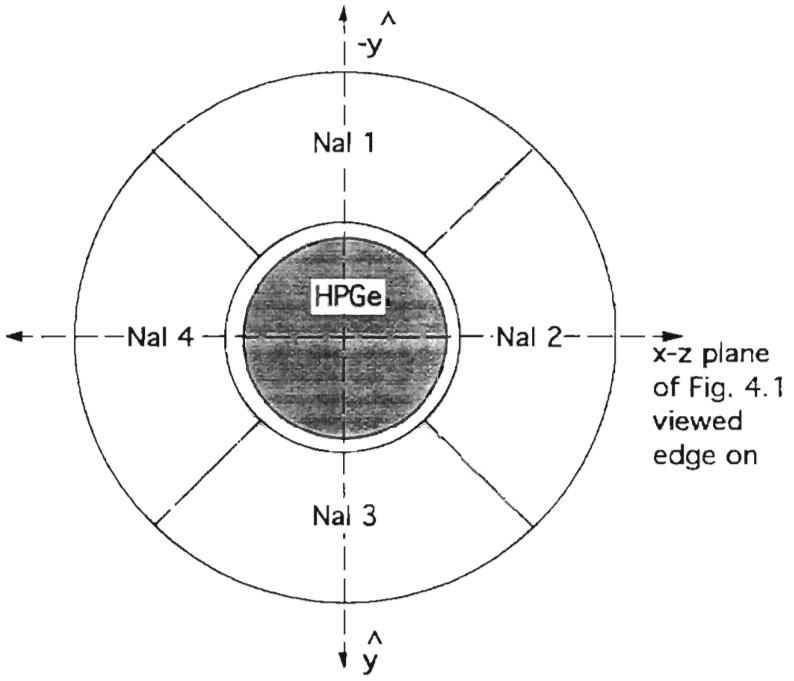

Figure 4.2: The HPGe and annular shield viewed head on. The left-right/up-down Compton scattering asymmetry can be used to determine the γ-ray linear polarization.

and, as shown in Figure 2.8, are sent to separate amplifiers, it is possible to distinguish between the intensity of photons which are scattered up-down (into either NaI 1 or NaI 3 according to Figure 4.2) and the intensity of photons which are scattered left-right (into either NaI 2 or NaI 4). If we call the up-down sum "N_V" and the left-right sum "N_H", we can then define the measured left-right/up-down scattering asymmetry, $A(\theta)$, as:

$$A(\theta) = \frac{N_V - N_H}{N_V + N_H}. \tag{4.8}$$

N_V and N_H can be expressed in terms of J_0 and J_{90} (see Equation 4.1), as follows[Wil75]:

$$N_V = J_0\, d\sigma(\theta_c,\eta=90^\circ) + J_{90}\, d\sigma(\theta_c,\eta=0^\circ) \qquad (4.9)$$
$$N_H = J_0\, d\sigma(\theta_c,\eta=0^\circ) + J_{90}\, d\sigma(\theta_c,\eta=90^\circ)$$

We can substitute Equations 4.9 into Equation 4.8, and, after rearranging terms, we get:

$$A(\theta) = \left(\frac{d\sigma(\theta_c,\eta=90^\circ) - d\sigma(\theta_c,\eta=0^\circ)}{d\sigma(\theta_c,\eta=90^\circ) + d\sigma(\theta_c,\eta=0^\circ)}\right)\left(\frac{J_0 - J_{90}}{J_0 + J_{90}}\right) \qquad (4.10)$$

The second quantity in the parenthesis on the right hand side of Equation 4.10 is just $P_\gamma(\theta)$ from Equation 4.1, while the first quantity in parenthesis on the right hand side of Equation 4.10 is a factor that is called [Wil75] the polarization sensitivity, S. Thus, using these new definitions, we can re-express the experimentally measured asymmetry in Equation 4.10 as:

$$A(\theta) = S \cdot P_\gamma(\theta). \qquad (4.11)$$

Alternatively, we can express $P_\gamma(\theta)$ in terms of $A(\theta)$ and S:

$$P_\gamma(\theta) = \frac{A(\theta)}{S}. \qquad (4.12)$$

Using Equation 4.12, the γ-ray polarization can now be obtained using the measured $A(\theta)$ and a calculated S. In order to calculate an S value, we can use Equation 4.6 to re-write S as a function of E_γ as follows:

$$S(E_\gamma) = \frac{\sin^2\theta_c}{\frac{E_\gamma}{E_\gamma'} + \frac{E_\gamma'}{E_\gamma} - \sin^2\theta_c}. \qquad (4.13)$$

The expression in Equation 4.13 is greatly simplified in the case of a point detector geometry (i.e. the case where the HPGe and NaI(Tl) detectors all have negligible spatial extent). In this case, only θ_C=90° gives a non-zero $S(E_\gamma)$. Using Equation 4.7, Equation 4.13 can be re-written for the point detector geometry:

$$S(E_\gamma) = \frac{1}{\left(\frac{E_\gamma}{m_e c^2}\right) + \left(\frac{m_e c^2}{E_\gamma + m_e c^2}\right)}. \qquad (4.14)$$

Thus, for point detector geometry, it is now possible (using Equations 4.12 and 4.14) to obtain $P_\gamma(\theta)$ for a given $D(p,\gamma)^3He$ γ-ray. The case of finite geometry is typically handled [Wil75] by continuing to use Equation 4.12 for $P_\gamma(\theta)$, but, rather than use Equation 4.14 for S, a new value is *experimentally* determined using the actual polarimeter geometry. The experimental method used to determine $S(E_\gamma)$ is discussed in the next section.

4.5 Polarization Sensitivity

It was necessary to measure scattering asymmetries, $A(\theta)$, for γ-rays of *known* polarization, $P_\gamma(\theta)$, so that Equation 4.12 could be used to determine the polarization sensitivity, $S(E_\gamma)$, for the current set-up. The procedure for obtaining γ-rays of known polarization involves aligning (i.e. orienting with respect to a symmetry axis) a nucleus in an excited state, and then observing the subsequent γ-decay to the ground state. The details are described in subsection 4.5.1. Subsection 4.5.2 describes the procedure for using these γ-rays to measure the polarization sensitivity function at E_γ=1.78 and 4.43 MeV. And finally, sub-section 4.5.3 shows how a value for $S(E_\gamma)$ was obtained at E_γ=5.5 MeV.

4.5.1 Procedure for Obtaining Polarized γ-rays

This subject is discussed in [Wil75]. Other appropriate references include [Lit70] and [Bas72]. Using inelastic nuclear scattering reactions with an unpolarized incident beam and an unpolarized target, it is possible to produce nuclei in excited states which exhibit symmetry about the incident beam axis. This condition of symmetry is described as follows [LWF59]:

$$W(m) = W(-m). \tag{4.15}$$

In this equation, W(m) is the relative population of the m^{th} magnetic sub-state of a nucleus with total angular momentum J. If all the W(m) are equal, the nucleus is isotropically oriented. However, if the magnetic substates are unequally populated (subject to the condition of Equation 4.15), we have the condition of *aligned* nuclear orientation, whereby a single spatial axis (in this case, the beam axis) is specified. This is as opposed to *polarized* orientation, whereby a single direction in space is specified. Gamma-rays emanating from an aligned nucleus will exhibit a certain degree of linear polarization. If the decay scheme is well known, the degree of the γ-ray polarization can be predicted.

As an illustrative example, we consider the case of $^{12}C^*$ produced in the reaction $^{12}C(p,p')^{12}C^*$. Since we are specifically interested in the subsequent γ-decay of $^{12}C^*$ (see subsection 4.5.2), we refer to the reaction as $^{12}C(p,p'\gamma)^{12}C$. In order that the outgoing γ-ray be polarized, it is desired that the magnetic substates of $^{12}C^*$ be unequally populated. This can be arranged by populating a ^{13}N intermediate compound state which will produce an outgoing inelastic proton in a relative s-wave (l=0). Once this is done,

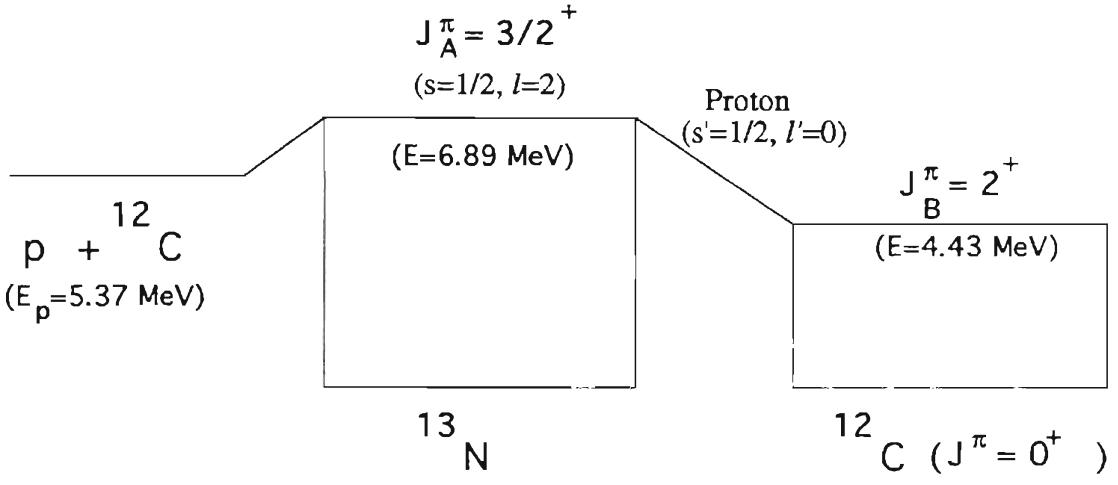

Figure 4.3: The nuclear level scheme for the $^{12}C(p,p'\gamma)^{12}C$ reaction, where J_A is the total angular momentum of the $^{13}N^*$ state and J_B is the total angular momentum of the $^{12}C^*$ state.

alignment of the $^{12}C^*$ state is assured. Figure 4.3 shows the nuclear level scheme for this process. By using a beam energy of E_p(lab)=5.37 MeV, we can populate the E=6.89 MeV, $J^{\pi}=3/2^+$, state of ^{13}N (from conservation of energy, we know that the excitation of ^{13}N is $Q+E_{cm}$, where Q=1.94 MeV in this case). Using conservation of parity, we see that this state is formed by an l=2,s=1/2 proton on ^{12}C. This resonance state then decays by proton emission to $^{12}C^*$, an E=4.43 MeV, $J^{\pi}=2^+$, state in ^{12}C. Conservation of parity shows that the outgoing proton must have l'=0,2,4. From energy conservation, we see that the outgoing proton should have an energy of less than 1 MeV, and thus we conclude that it should be in a relative s-wave (l'=0) since the angular momentum barrier will block the higher l-values. This is significant based on the following consideration. If we write down the equation describing conservation of total angular momentum between the $^{13}N^*$ and $^{12}C^*$ states, we get

$$\vec{s} + \vec{l} = \vec{J}_B + \vec{s}' + \vec{l}'. \tag{4.16}$$

The projections along the symmetry axis must then satisfy

$$m_s + m_l = m_J + m_{s'} + m_{l'}, \tag{4.17}$$

where m_J is the magnetic quantum number of the $^{12}C^*$ state.

Equation 4.17 can be simplified based on two observations. First of all, as mentioned above, $l'=0$, and thus $m_{l'}=0$. Secondly, since $\vec{L} = \vec{r} \times \vec{p}$ is $\perp$ to the symmetry axis, the component of l along the symmetry axis will be zero, and thus $m_l=0$. Therefore, Equation 4.17 is now

$$m_s = m_J + m_{s'}. \tag{4.18}$$

Since both m_s and $m_{s'}$ are $\pm 1/2$, it is immediately clear that only $m_J=-1,0,1$ will satisfy Equation 4.18. Since the values of $m_J=-2$ and 2 are not allowed, we have an aligned nucleus.

The state $^{12}C^*$ will γ-decay to the ^{12}C ground state with the emission of pure E2 radiation. The ^{12}C ground state is J=0, and thus has a magnetic substate of zero. This will produce E2 radiation that is $\Delta m=0,\pm 1$, and thus purely plane polarized (i.e. in theory we have $P_\gamma=1$). This polarized γ-radiation from $^{12}C(p,p'\gamma)^{12}C$ was used to determine the polarization sensitivity function for the Compton polarimeter at $E_\gamma=4.43$ MeV. In addition, the $^{28}Si(p,p'\gamma)^{28}Si$ reaction (also predicted to have $P_\gamma=1$) was used to determine $S(E_\gamma)$ at $E_\gamma=1.78$ MeV. Once $S(E_\gamma)$ is known at $E_\gamma=1.78$ and 4.43 MeV, it can be reliably extrapolated up to the desired energy of $E_\gamma=5.5$ MeV.

In the process of actually determining $S(E_\gamma)$ from the $^{12}C(p,p'\gamma)^{12}C$ and $^{28}Si(p,p'\gamma)^{28}Si$ reactions, the predicted P_γ=1 values were not used in the calculations. Instead, a P_γ value was experimentally measured for each reaction. The reason for doing this is that previous experimental work on these reactions [Wil75,Bas72,Lit70] has shown that P_γ is not exactly equal to 1.0 as predicted. Instead, the results for $^{28}Si(p,p'\gamma)^{28}Si$ indicate $P_\gamma(90°)$~0.8, while the results for $^{12}C(p,p'\gamma)^{12}C$ indicate $P_\gamma(90°)$~0.9. In the following subsection, the current measurements for P_γ will be presented and compared with the results of [Wil75,Bas72,Lit70]. The current results for $S(E_\gamma)$, calculated using the currently measured P_γ values, will then be presented.

4.5.2 Measuring the Polarization Sensitivity

By using the formalism discussed in [Wil75,LWF59], it is possible to express Equation 4.1 in terms of the angular distribution Legendre coefficients. For the case of pure E2 radiation observed at a laboratory angle of 90°, the expression simplifies to

$$P_\gamma(90°) = \frac{\frac{3}{2}a_2 + \frac{5}{8}a_4}{1 - \frac{1}{2}a_2 + \frac{3}{8}a_4}, \qquad (4.19)$$

where a_2 and a_4 are the normalized Legendre polynomial coefficients (see Chapter 5 for a full discussion of Legendre coefficient expansions). Since the $^{12}C(p,p'\gamma)^{12}C$ and $^{28}Si(p,p'\gamma)^{28}Si$ reactions both give pure E2 radiation, the expected value of $P_\gamma(90°)$ can be derived by measuring an angular distribution for the reaction in question, fitting the results to a Legendre coefficient expansion, and using Equation 4.19 to determine $P_\gamma(90°)$. This result is the expected γ-ray polarization. By actually measuring an asymmetry, A(90°), we can then use Equation 4.12 to calculate the polarization

sensitivity, $S(E_\gamma)$. The polarization sensitivity was actually measured at two separate γ-ray energies, as will now be discussed.

The $^{28}Si(p,p'\gamma)^{28}Si$ Experiment

The $^{28}Si(p,p'\gamma)^{28}Si$ reaction was used to measure $S(E_\gamma)$ at E_γ=1.78 MeV. In accordance with the method described in sub-section 4.5.1, the ostensible procedure would be to use the incident proton beam to populate a $J^\pi=3/2^+$ resonance which has sufficient energy to subsequently decay (by proton emission) into the 2^+ excited state of ^{28}Si (E^*=1.78 MeV). This state will then γ-decay to give us the desired E2 photons which should be purely plane polarized. This was achieved by using a proton beam energy of E_p(lab)=3.34 MeV and populating the $J^\pi=3/2^+$ state of ^{29}P at an excitation energy of E^*=5.97 MeV.

The above suggestion, while seeming quite reasonable, was not actually pursued. The reason is that the previous studies of $P_\gamma(90^\circ)$ using $^{28}Si(p,p'\gamma)^{28}Si$ [Wil75,Bas72,Lit70] have all used an E_p(lab)=3.1 MeV beam to populate the $J^\pi=5/2^-$ state in ^{29}P instead of the $J^\pi=3/2^+$ state. The exact reason for this choice of beam energy is not known. Based on the discussion in sub-section 4.5.1, a population of the $J^\pi=3/2^+$ state might seem more logical. However, since the resulting $^{28}Si^*$ γ-ray is pure E2, its polarization can still be determined using Equation 4.19, and the results [Wil75,Bas72,Lit70] have all shown the γ-ray to be highly polarized. Thus, for purposes of comparison to previous results, this same beam energy (E_p(lab)=3.1 MeV) was used in the current experiment.

The actual data taking for this $^{28}Si(p,p'\gamma)^{28}Si$ experiment took place in the TUNL target room which follows the 90°-90° analyzing magnets (top left corner of Figure 2.1).

The target used was a thin layer of ^{28}Si which had been evaporated onto a thin ^{12}C backing. The experimental set-up used was similar to that at shown in Figure 2.5, except that the incident proton beam was allowed to pass through the ^{28}Si target and into a beam dump. In addition to a series of runs taken at a lab angle of 90° (in order to determine A(90°)), an angular distribution of cross-section was acquired at 13 angles between 35° and 150°. By fitting this angular distribution to Legendre coefficients, Equation 4.19 could be used to calculate the expected $P_\gamma(90°)$. Then, using the expected $P_\gamma(90°)$ value and the measured A(90°) value, Equation 4.12 was used to calculate $S(E_\gamma=1.78$ MeV).

Figure 4.4 shows the acquired angular distribution for $^{28}Si(p,p'\gamma)^{28}Si$. In this figure, the full energy γ-ray peaks acquired for each angle (with the HPGe) were summed in order to obtain the data points shown. The solid line is a Legendre polynomial fit to the data where the A_0, A_2, and A_4 coefficients were determined (see Chapter 5).

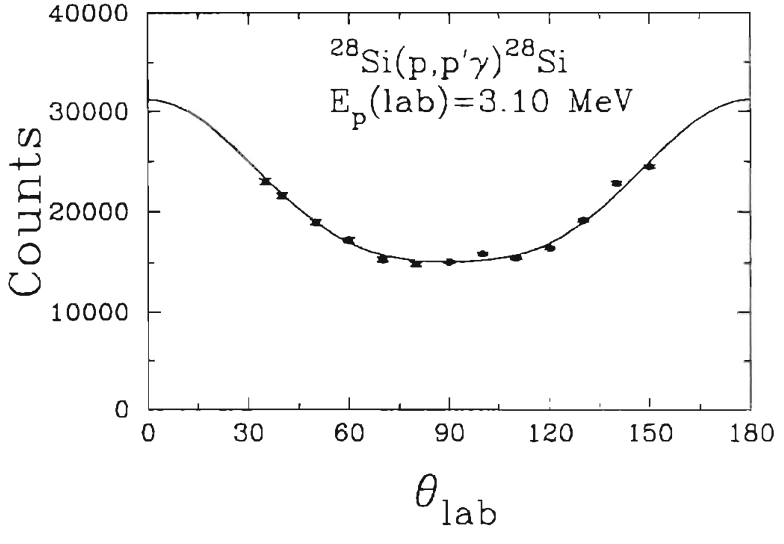

Figure 4.4: Angular distribution of γ-rays for the $^{28}Si(p,p'\gamma)^{28}Si$ reaction. The data points show statistical error only. The solid line is a Legendre fit to the data.

The normalized Legendre coefficients, a_2 and a_4, shown in Equation 4.19 are defined as simply being A_2/A_0 and A_4/A_0. The Legendre fit shown by the solid line in Figure 4.4 indicates the following values: $a_2=0.513\pm0.008$ and $a_4=0.138\pm0.011$. Substituting these values into Equation 4.19, the following γ-ray polarization is obtained for $^{28}Si(p,p'\gamma)^{28}Si$: $P_\gamma(90^\circ)=1.07\pm0.08$. This value includes a 7% systematic error which has been included. The reason for including the 7% systematic error is that $P_\gamma(90^\circ)$ has a theoretical maximum value of 1.0, and thus the result of $P_\gamma(90^\circ)=1.07$ is viewed as 100% polarization in the light of a 7% systematic error. A larger systematic error does not seem likely given the reasonably high quality of the data.

In comparing the present $P_\gamma(90^\circ)$ answer with the previous data, it is seen to be somewhat higher. The references of [Wil75,Bas72,Lit70] give $P_\gamma(90^\circ)=0.80\pm0.03$, 0.74 ± 0.04, and 0.82 ± 0.03 respectively. This discrepancy is not seen as an indicator of an overall constant systematic error in the current procedure due to the fact that the current $^{12}C(p,p'\gamma)^{12}C$ experimental results lie at more of an average value of the previous points. The origin of this discrepancy is of possible future interest, but will not be pursued at the present time.

Along with the HPGe angular distribution data that were acquired for $^{28}Si(p,p'\gamma)^{28}Si$, a set of asymmetry measurements, $A(90^\circ)$, was also obtained by monitoring the Compton scattered γ-rays with the 4 NaI(Tl) segments (see Equation 4.8). The method for acquiring these asymmetry measurements was based on a uniform procedure that was followed throughout the Compton polarimetry process, and this procedure will be discussed in detail in section 4.6. For right now, it will suffice to quote the final result for $^{28}Si(p,p'\gamma)^{28}Si$: $A(90^\circ)=0.107\pm0.002$. Along with the $P_\gamma(90^\circ)$ result previously mentioned, the final value for the 1.78 MeV polarization sensitivity is then $S(1.78)=0.100\pm0.008$.

The $^{12}C(p,p'\gamma)^{12}C$ Experiment

The $^{12}C(p,p'\gamma)^{12}C$ reaction was used to measure $S(E_\gamma)$ at E_γ=4.43 MeV. The rationale for choosing a beam energy of E_p(lab)=5.37 MeV has been well detailed in sub-section 4.5.1. The target consisted of a thin, self-supporting, ^{12}C foil. The target-detector geometry was the same as it was in the $^{28}Si(p,p'\gamma)^{28}Si$ experiment. Figure 4.5 shows the acquired $^{12}C(p,p'\gamma)^{12}C$ angular distribution along with a Legendre polynomial fit (solid line). The normalized Legendre coefficients extracted from this fit were: a_2=0.492±0.013, a_4=-0.239±0.015. Substituting into Equation 4.19, we obtain $P_\gamma(90°)$=0.88±0.04. The previous results from [Wil75,Bas72,Lit70] are, respectively, $P_\gamma(90°)$=0.97±0.02, 0.80±0.06, and 1.10±0.06. Obviously the spread on $P_\gamma(90°)$ for $^{12}C(p,p'\gamma)^{12}C$ is quite large, but the current result is well towards the middle of the spread.

Along with the $^{12}C(p,p'\gamma)^{12}C$ angular distribution data, a set of A(90°) data was also acquired. The final determined value for the asymmetry was A(90°)=0.036±0.002 which was used along with the extracted $P_\gamma(90°)$ value in Equation 4.12 to calculate S. The value obtained for the polarization sensitivity at 4.43 MeV was S(4.43)=0.041±0.003.

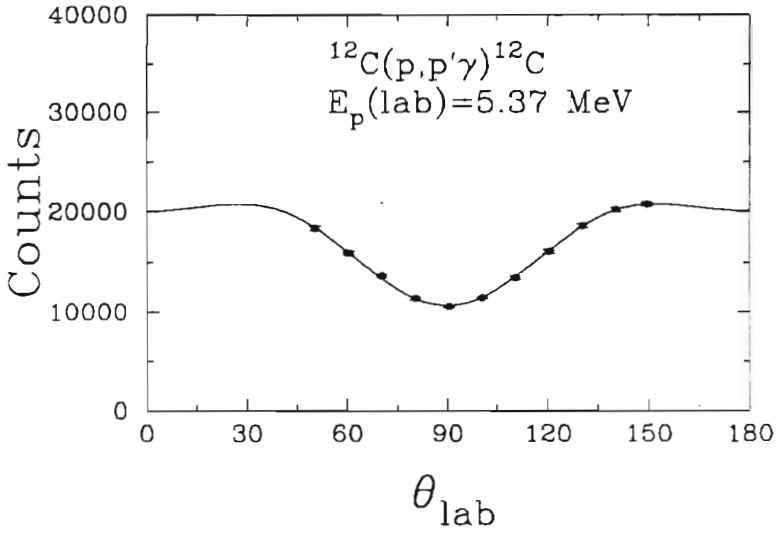

Figure 4.5: Angular distribution of γ-rays for the $^{12}C(p,p'\gamma)^{12}C$ reaction. The data points show statistical error only. The solid line is a Legendre fit to the data.

4.5.3 Extrapolating S to E_γ=5.5 MeV

Now, with values determined for $S(E_\gamma)$ at E_γ=1.78 and 4.43 MeV, it was necessary to extrapolate the value up to E_γ=5.5 MeV (the energy of the γ-ray from $D(p,\gamma)^3He$). The method used here was simply to fit the existing data points to an energy dependent curve. Since the value of $S(E_\gamma)$ is not expected to change rapidly from 4.43 MeV to 5.5 MeV [Wil75], the final extracted value of S(5.5) should not be too sensitive to different energy dependent forms used. Ideally, the best possible energy dependent form would be that resulting from an average of Equation 4.13 over the finite geometry of the detector. However, this complicated procedure was deemed unnecessary for the reason mentioned above. Instead, the energy dependent form used was simply that which would result from a point detector geometry. This energy dependent form was presented in Equation 4.14.

Equation 4.20 below shows the energy dependent form to be used in the fit to the data (C is the overall normalization constant):

$$S(E_\gamma) = \frac{C}{\left(\frac{E_\gamma}{m_e c^2}\right) + \left(\frac{m_e c^2}{E_\gamma + m_e c^2}\right)}. \qquad (4.20)$$

The constant C is a factor that is obtained by fitting Equation 4.20 to the existing $S(E_\gamma)$ data points at E_γ=1.78 and 4.43 MeV. Once this curve has been fit to the data, an S(5.5) value can easily be extracted from Equation 4.20. Figure 4.6 shows the two $S(E_\gamma)$ data points along with a fit to the data using the form of Equation 4.20. The fit was obtained (i.e. the constant C was determined) by minimizing the total χ^2 function. Since the equation for $S(E_\gamma)$ is linear in C, this χ^2 minimization can be done analytically by simply setting $[d(\chi^2)/dC]=0$ and solving for C. The error can then be obtained by finding the increment ΔC for which the total χ^2 function changes by one. The final result is C=0.365±0.019.

As is shown by Figure 4.6, the S data points are fit quite well by the assumed energy dependence. The value extracted for the polarization sensitivity at 5.5 MeV is S(5.5)=0.034±0.0034. A total error of 10% has been assumed for the extracted value based on an estimate for the systematic errors in the Compton polarimetry procedure.

4.6 Acquiring $P_\gamma(\theta)$ data for $D(p,\gamma)^3He$

Once the polarization sensitivity, S, is known at the energy of interest (in this case 5.5 MeV), the task of measuring $P_\gamma(\theta)$ for $D(p,\gamma)^3He$ is thus reduced to measuring a left-right/up-down asymmetry, $A(\theta)$, in the Compton scattering. This section starts with an introduction to the Compton polarimetry data acquisition process, and is then followed by

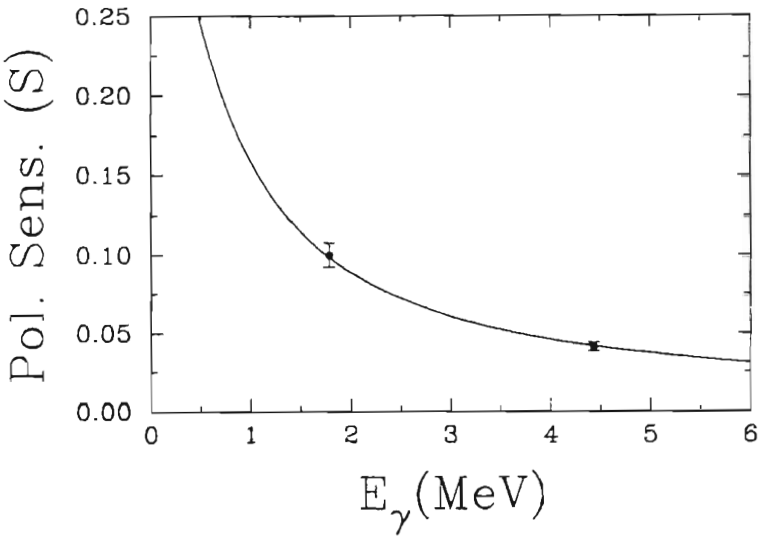

Figure 4.6: Data for the polarization sensitivity function, S, shown along with an empirical fit to the data. The energy dependence of the empirical fit is that of a point detector geometry.

a closer look at the details.

4.6.1 Introduction to the Data Acquisition Process

Since the geometry of the HPGe crystal and the NaI(Tl) annulus is already fixed (see Figures 2.5 and 4.2), the degrees of freedom that we have in acquiring Compton polarimeter data is limited to setting thresholds and summing windows in the two detectors, and also to affecting coincidence requirements on the incoming data. Specifically, the Compton polarimetry process can be outlined as follows. An incoming γ-ray enters the HPGe crystal and Compton scatters into one of the NaI(Tl) segments as shown in Figure 4.2. As discussed in section 2.3, the NaI(Tl) segments are gated by an HPGe signal above a certain energy threshold, and thus we only consider NaI(Tl) events

which are in coincidence with an HPGe event. Experimentally, we can record how much energy is deposited in the HPGe crystal and how much energy is deposited in the particular NaI(Tl) segment. To further reduce background, we only consider events for which the sum of the energy deposited in the HPGe and in the particular NaI(Tl) segment equals the incident γ-ray energy (for $D(p,\gamma)^3He$ this is 5.5 MeV).

Using these coincidence requirements, we can acquire spectra for the four NaI(Tl) segments which should be equivalent to counting the number of Compton scattered γ-rays in the up, down, left, and right directions. In order to eliminate any possible counting asymmetries which might result from slightly different efficiencies or gains in the different NaI(Tl) segments, the annulus shown in Figure 4.2 was rotated in 90° increments after a set number of runs. After three rotations, a single NaI(Tl) segment will have seen all four directions (i.e. up, down, left, and right). This allowed us to measure, simultaneously, an up-down/left-right asymmetry (as defined by Equation 4.8) for each NaI(Tl) segment. The final quoted asymmetry was then determined by a weighted average of the four separate results. This asymmetry, $A(\theta)$, was then used in Equation 4.12 to calculate a $P_\gamma(\theta)$ value.

4.6.2 Experimental Details

One of the important things to be decided in this procedure is where to set the detector thresholds. A useful figure of merit for this procedure can be derived by calculating an expression for the error in the γ-ray polarization. First, we combine Equations 4.8 and 4.12 to obtain:

$$P_\gamma(\theta) = \frac{1}{S}\left(\frac{N_V - N_H}{N_V + N_H}\right). \tag{4.20}$$

Then, we write down the expression for the error:

$$\Delta P_\gamma(\theta) = \sqrt{\frac{4N_H^2(\Delta N_v)^2 + 4N_V^2(\Delta N_H)^2}{(N_V + N_H)^4 S^2} + \frac{1}{S^4}(\Delta S)^2\left(\frac{N_V - N_H}{N_V + N_H}\right)^2}. \quad (4.21)$$

By assuming that $N_V \approx N_H = N$, and $(\Delta N_V)^2 \approx (\Delta N_H)^2 = N$, where N is the number of Compton scattered γ-rays recorded, the expression in Equation 4.21 simplifies to:

$$\Delta P_\gamma(\theta) \approx \frac{1}{\sqrt{2NS^2}} \quad (4.22)$$

Equation 4.22 indicates that by maximizing the quantity NS^2, we can minimize the error on $P_\gamma(\theta)$. Since the number of counts, N, at a particular Compton scattering angle, θ_c, is proportional to the Compton cross section, $d\sigma/d\theta_c$, we can associate the quantity $(d\sigma/d\theta_c)S^2$ with a figure of merit to be maximized. The $d\sigma/d\theta_c$ quantity of interest can be calculated from the Klein-Nishina formula (Equation 4.6), whereby the following proportionality can be obtained (absolute numbers are not needed):

$$\frac{d\sigma}{d\theta_c} \propto \frac{E_\gamma'^2}{E_\gamma^2}\left[\frac{E_\gamma}{E_\gamma'} + \frac{E_\gamma'}{E_\gamma} - \sin^2\theta_c\right]\sin\theta_c \quad (4.23)$$

The relation in (4.23) has been obtained by averaging Equation 4.6 over η and then integrating over ϕ. As we acquire data, we obviously want to minimize the error in $P_\gamma(\theta)$, and therefore we want to maximize the figure of merit, $(d\sigma/d\theta_c)S^2$. Figure 4.7 below shows the figure of merit plotted versus θ_c, the Compton scattering angle in the HPGe.

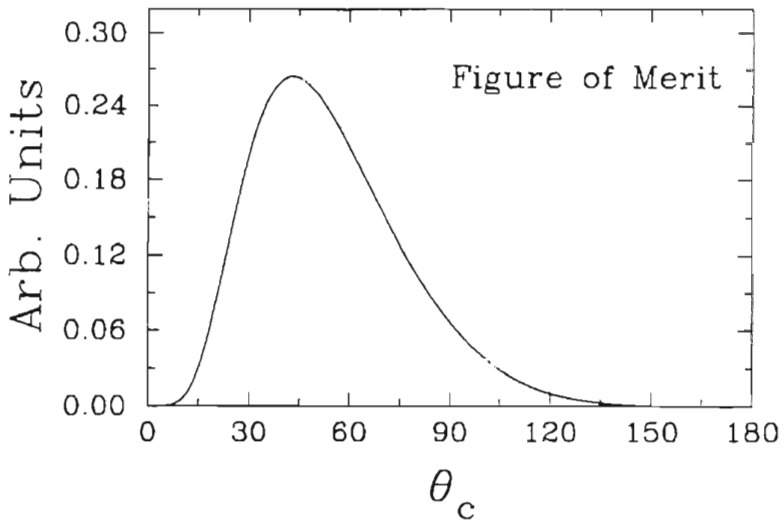

Figure 4.7: The figure of merit, $(d\sigma/d\theta_c)S^2$, for a 5.5 MeV γ-ray plotted vs. θ_c.

Figure 4.7 shows that the ideal Compton polarimeter, for a 5.5 MeV γ-ray, would be designed so as to encompass the Compton scattering range from θ_c~10° to θ_c~135°. In order to translate this angular range into a more tractable experimental quantity, we can express the figure of merit in terms of E_{recoil}, the energy deposited in the HPGe crystal by the Compton scattered γ-ray. For a γ-ray of energy E_γ, $E_{recoil}=E_\gamma-E_\gamma'$ with E_γ' as defined by Equation 4.7. Based on this relation, the angular range defined as θ_c~10° to θ_c~135° (for a 5.5 MeV γ-ray) becomes E_{recoil}~0.8 MeV to E_{recoil}~5.2 MeV. The figure of merit plotted vs. E_{recoil} is shown in Figure 4.8.

Based on Figure 4.8, it would appear that from about 0.8 MeV up to near the "Compton Edge" at 5.2 MeV would indeed be an appropriate range of HPGe energies to include. With this in mind, an energy window was set (during off-line sorting of the data) so as to encompass the HPGe energy region from 0.6 MeV-5.26 MeV. This, in effect, constituted the HPGe threshold for the Compton polarimetry process. Since, for a 5.5 MeV γ-ray, the energy deposited in the HPGe plus the energy deposited in the

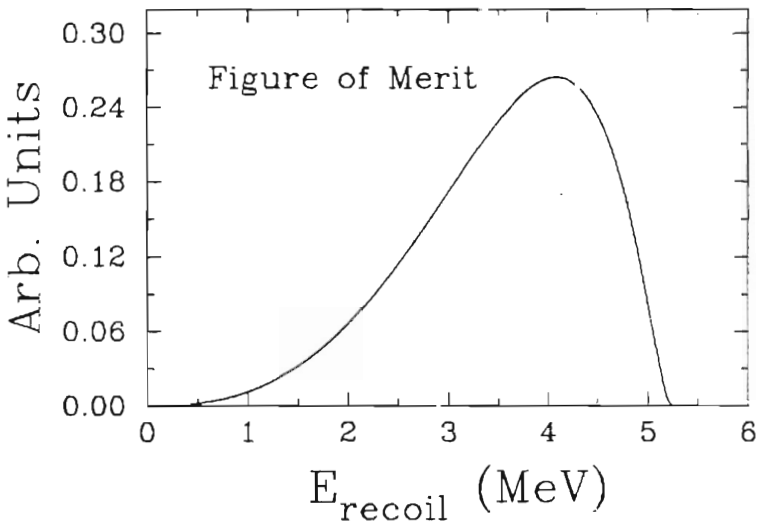

Figure 4.8: The figure of merit, $(d\sigma/d\theta_c)S^2$, for a 5.5 MeV γ-ray plotted vs. E_{recoil}, the energy deposited in the HPGe by the Compton scattered γ-ray.

NaI(Tl) annulus should equal 5.5 MeV, the threshold in the NaI(Tl) annulus was set (in off-line sorting) to be 240 keV.

In addition to setting thresholds appropriately, the summed energy criterion, whereby the HPGe and NaI(Tl) energies (acquired in coincidence) sum to the original γ-ray energy of 5.5 MeV, was further enforced by creating a summed energy spectrum for the HPGe+NaI(Tl) set-up. This spectrum, an example of which is shown in Figure 4.9, allowed us to consider only the events for which the total deposited energy was 5.5 MeV, and thus we were able to greatly reduce the "accidental" coincidences.

The summed energy spectrum shown in Figure 4.9 shows three large peaks. The peaks at 1.46 MeV and 2.615 MeV are natural background peaks (^{40}K and radiothorium), while the peak at 5.5 MeV corresponds to the $D(p,\gamma)^3He$ peak of interest. A gate was set around this 5.5 MeV peak. Applying this gate to the NaI(Tl) coincidence spectrum, we can create a final spectrum which should include only Compton

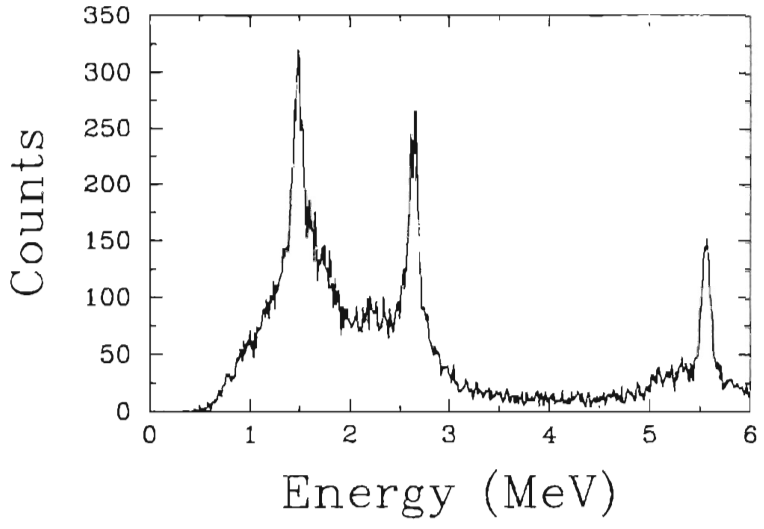

Figure 4.9: A summed energy spectrum, for $D(p,\gamma)^3He$ at $\theta_{lab}=90^\circ$, representing the total energy deposited in the HPGe+NaI(Tl) set up.

scattered events. An example of this final NaI(Tl) spectrum is shown in Figure 4.10 superimposed upon the initial NaI(Tl) coincidence spectrum (before the application of the summed energy criterion). The higher curve in Figure 4.10, which reaches up to 325 counts, is the initial NaI(Tl) coincidence spectrum, while the lower curve, most noticeable between 0 and 1 MeV, is the final NaI(Tl) spectrum representing Compton scattered events only. For the final NaI(Tl) spectrum, events which fired more than one NaI(Tl) segment have been rejected. Furthermore, any events associated with the 1st and 2nd escape peaks in the HPGe have been vetoed out of the final NaI(Tl) spectrum. This is done to get rid of the effects dealing with the 511 keV photons which are emitted from the HPGe in these events.

The final NaI(Tl) spectra can then be summed for each NaI(Tl) segment, thus allowing an extraction of the relative number of Compton scattered γ-rays into each segment. These yields are then used to calculate the asymmetries as has been discussed.

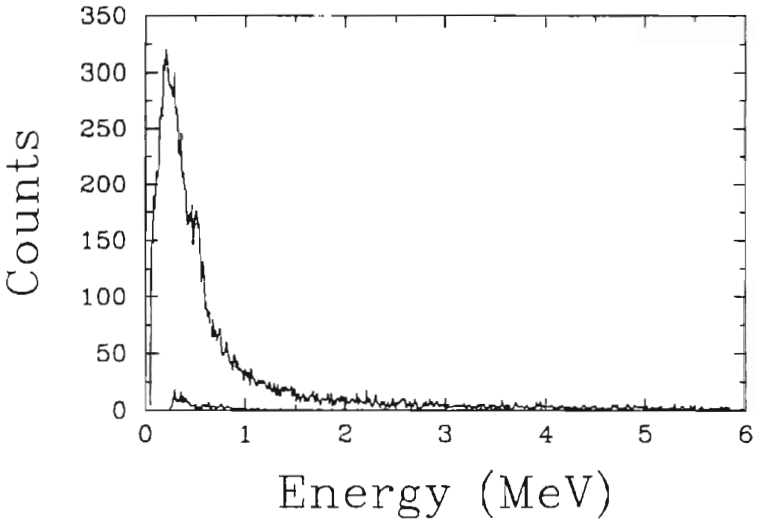

Figure 4.10: A coincidence energy spectrum (higher curve), for one NaI(Tl) segment, acquired for $D(p,\gamma)^3He$ at $\theta_{lab}=90^\circ$. The lower curve is the final NaI(Tl) spectrum (noticeable between 0 and 1 MeV) representing Compton scattered events only.

Since the asymmetries depend on ratios of yields, the systematic error is thought to be negligible (thus the error on $A(\theta)$ will be primarily statistical in nature). The final results for $P_\gamma(\theta)$ $(=A(\theta)/S)$ will be presented in Chapter 5.

Chapter 5

Experimental Results

In this chapter, the experimental results for the current $D(\vec{p},\gamma)^3He$ experiment will be presented. This will include results for the $\sigma(\theta)$, $S(\theta)$, $A_y(\theta)$ and $P_\gamma(\theta)$ observables extracted in the following (separate) data analysis methods: the thick target yield analysis; the binning analysis; and the deconvolution analysis. Also discussed in this chapter will be the techniques for parameterizing the data: the Legendre polynomial expansion, and the transition matrix element expansion. The discussion of these expansions will lead off this chapter, and will be followed by a presentation of the results from the various analysis methods. A comparison of the current data with the previous low energy data of [Gri63] and [Bai70] will then conclude this chapter.

5.1 The Legendre Polynomial Expansions

5.1.1 Definitions

Using an angular correlation formalism, such as the one used in [Fer65], the $\sigma(\theta)$ and $A_y(\theta)$ observables can be expanded in terms of the transition matrix elements (see section 5.2). These expansions can be simplified by grouping all of the factors involving the transition matrix elements into the Q_k, a_k, and b_k coefficients:

$$\sigma(\theta) = \sum Q_k A_k P_k(\cos\theta) = A_0 \sum_{k=0} Q_k a_k P_k(\cos\theta) \qquad (5.1)$$

where $Q_0=a_0=P_0=1.0$, and

$$\sigma(\theta)A_y(\theta) = A_0 \sum_{k=1} Q_k b_k P_k^1(\cos\theta). \qquad (5.2)$$

In Equations 5.1 and 5.2, $\sigma(\theta)$ is the unpolarized cross section, $A_y(\theta)$ is the vector analyzing power, the a_k, b_k are the normalized Legendre polynomial coefficients (which are dimensionless), the Q_k are the finite geometry attenuation factors, and the P_k (P_k^1) are the Legendre (1st associated Legendre) polynomials respectively. Due to a Clebsch-Gordan coefficient which arises in the definitions of the a_k and b_k coefficients (see section 5.2), the sum over k values is restricted to $|L'-L| \le k \le |L'+L|$, where L is the multipolarity of the γ-ray being considered. The A_0 coefficient is the absolute cross section normalization constant which contains the correct cross section units. The unnormalized Legendre coefficients (A_k, B_k) are related to the normalized Legendre coefficients by this factor of A_0: $A_k=A_0a_k$; and $B_k=A_0b_k$. It should also be noted, for future reference, that if Equation 5.1 is integrated over all angles ($d\Omega=\sin\theta d\theta d\phi$), the result is:

$$\sigma_T = \int \sigma(\theta) d\Omega = 4\pi A_0, \qquad (5.3)$$

where σ_T is the angle integrated cross section.

By examining Equation 4.5, it is clear that in addition to the $\sigma(\theta)$ and $A_y(\theta)$ observables, the $P_\gamma(\theta)$ observable can be expressed in terms of Legendre polynomials as follows:

$$P_\gamma(\theta) = \frac{\sum Q_k F_k P_k^2(\cos\theta)}{\sum Q_k G_k P_k(\cos\theta)}. \qquad (5.4)$$

5.1.2 The Q_k Coefficients

The original derivation of these coefficients is in [Ros53], although a good discussion is also contained in [Fer65]. According to [Fer65]:

$$Q_k = J_k/J_0, \qquad (5.5)$$

where

$$J_k = \int_0^\pi \varepsilon(\beta) P_k(\cos\beta) d(\cos\beta), \qquad (5.6)$$

β being the angle with respect to the HPGe symmetry axis and $\varepsilon(\beta)$ being the probability for γ-ray detection (i.e. the efficiency) at that angle. According to Equations 5.5 and 5.6, the Q_k coefficient for a given Legendre polynomial can be viewed as the weighted average of that Legendre polynomial over the extent of the detector. In this case, the weighting factor is the probability of detection for a γ-ray which enters the HPGe detector at an angle β with respect the HPGe symmetry axis.

The simplest method for calculating the Q_k coefficients is the method of [Ros53], whereby the probability of γ-ray detection is calculated by using the γ-ray linear attenuation coefficient, τ (units=cm^{-1}). Knowing the path length through the HPGe at an angle β, $x(\beta)$, one can express the probability for γ-ray detection, $\varepsilon(\beta)$, as follows:

$$\varepsilon(\beta) = 1 - e^{-\tau x(\beta)}. \qquad (5.7)$$

Because of its simplicity, Equation 5.7 is often the preferred expression in the calculation of the Q_k coefficients. Unfortunately, Equation 5.7 gives a probability for detection which includes the total HPGe response function, whereas we are typically only interested in the full energy component (i.e. γ-rays which deposit all their energy in the HPGe). The probability for full energy absorption is dependent not only upon path length, $x(\beta)$, but also upon the position of the initial interaction, and thus its calculation is more complicated. The question then arises as to how closely Equation 5.7 can approximate the case of full energy absorption (of interest in the current experiment).

In order to test the validity of using equation 5.7 for the current HPGe geometry, a monte carlo simulation (the EGS4 code described in section 3.5.2) was used to calculate the Q_k coefficients. By launching 100,000 γ-rays from the target center, the $P_k(\cos\beta)$ value was recorded for each γ-ray detected at angle β. Then, by following the method of [Bru94], the Q_k coefficients were calculated using the following expression:

$$Q_k = \frac{1}{N}\sum_{i=1}^{N} P_k(\cos\beta_i), \tag{5.8}$$

where N is the total number of detected events. By calculating the Q_k coefficients using Equation 5.8, the values were seen to agree with the values obtained with Equation 5.7 to within 1%. This good agreement can be understood in light of the fact that the Q_k coefficients are very close to one for the current HPGe geometry (e.g. Q_2=0.99), and thus the shortcomings of approximate methods are not so apparent.

5.1.3 Extracting the Legendre Coefficients

This subsection describes the procedure for extracting the Legendre coefficients from a set of $\sigma(\theta)$ and $A_y(\theta)$ data. Since Equations 5.1 and 5.2 are linear in the coefficients, the values for a_k, b_k can be extracted using the following method [Cml94]: set the first derivative of the χ^2 function (for either $\sigma(\theta)$ or $\sigma(\theta)A_y(\theta)$) to zero and then solve for the coefficients. In this manner we obtain a solution which minimizes the total χ^2 function. For example, the χ^2 function for the $\sigma(\theta)$ equation can be written as:

$$\chi^2 = \sum_t \frac{\left(A_0 \sum_k Q_k a_k P_{k,t} - \sigma_t \right)^2}{\left(\Delta\sigma_t \right)^2}, \tag{5.9}$$

where the t subscript refers to the lab angle θ, and the σ_t, $\Delta\sigma_t$ values are simply the cross section and error at the angle indexed by t. Taking the derivative with respect to a_m, and setting the result to zero, we obtain:

$$\sum_k \sum_t \left(a_k \right) \left(\frac{A_0 P_{k,t} P_{m,t}}{(\Delta\sigma_t)^2} \right) = \sum_t \left(\frac{\sigma_t P_{m,t}}{(\Delta\sigma_t)^2} \right). \tag{5.10}$$

Equation 5.10 can be written in a more compact form by using matrix notation:

$$\mathbf{a}B = \mathbf{c}, \tag{5.11}$$

where **a** is the vector of a_k coefficients, B is the (k,m) indexed matrix in the second set of parenthesis in Equation 5.10, and **c** is the (m) indexed vector on the right hand side of Equation 5.10. Clearly, we can solve for the a_k coefficients as follows:

$$\mathbf{a} = \mathbf{c}B^{-1}, \tag{5.12}$$

where B^{-1} refers to the inverse of the matrix B.

We now look at the errors associated with the a_k coefficients. If we rename the matrix B^{-1} as the matrix D, we can expand Equation 5.12 as shown below:

$$a_k = \sum_m \sum_t \frac{\sigma_t P_{mt}}{(\Delta\sigma_t)^2} D_{mk}. \tag{5.13}$$

The variances in the a_k coefficients, $(\Delta a_k)^2$, are then given by

$$(\Delta a_k)^2 = \sum_{m,m'} D_{mk} \left[\sum_{t,t'} \frac{P_{mt} P_{m',t'}}{(\Delta\sigma_t)(\Delta\sigma_{t'})} \right] D_{m'k}, \tag{5.14}$$

where the Δa_k are the errors in the a_k coefficients. Since the errors at different angles are uncorrelated, we can simplify Equation 5.14 to

$$(\Delta a_k)^2 = \sum_{m,m'} D_{mk} \left[\sum_{t} \frac{P_{m,t} P_{m',t}}{(\Delta\sigma_t)^2} \right] D_{m'k} \tag{5.15}$$

By comparison with Equation 5.10, it is realized that the quantity in parenthesis in Equation 5.15 is simply $\frac{1}{A_0} D^{-1}_{m,m'}$, and thus Equation 5.15 becomes

$$(\Delta a_k)^2 = \frac{1}{A_0} \sum_{m,m'} D_{m,k} \delta_{m,k} = \frac{D_{kk}}{A_0}. \tag{5.16}$$

Thus we have shown that the errors on the a_k coefficients can be derived from the diagonal elements of the D matrix.

The procedure for obtaining the values and errors for the b_k coefficients is similar to the one just described for the a_k coefficients. However, the Legendre coefficients in Equation 5.4 are not determined by this procedure, but must be determined by a parameter search. This is because the observable, $P_\gamma(\theta)$, is not linear in the coefficients.

5.2 Transition Matrix Element Expansions

5.2.1 Introduction

The Legendre polynomial expressions presented in the previous section were obtained from transition matrix element expansions. One good example of such expansions can be found in [Fer65]. A more concise set of expansions (as far as current use is concerned), which includes specific equations for all polarized observables, can be found in [Sey79]. This latter set of equations was used in the present analysis to express all of the observables in terms of the transition matrix elements. It should be pointed out that the notation used in [Sey79] is slightly different than the notation presented above (i.e. the current notation). In particular, the current a_k coefficients are equivalent to the $\bar{a}_k$ coefficients presented in [Sey79]. Alternatively, the current A_k, B_k coefficients presented in section 5.1.1 are equivalent to the a_k, b_k coefficients in [Sey79].

The matrix element expansions in [Sey79] are presented in terms of complex, reduced transition matrix elements: $R=|R|e^{i\phi}$, where $|R|$ is the matrix element amplitude and ϕ is the phase. These matrix elements are identified by their continuum quantum numbers in the channel spin coupling scheme. In this coupling scheme, the particle spins in a continuum state are combined vectorially to give a total "channel spin", s, and then the channel spin is combined vectorially with the relative orbital angular momentum, l, to

give a total angular momentum for the state, J. A particular matrix element (going from the continuum state to a final bound state) is then uniquely identified by specifying the mode and multipolarity of the transition (e.g. E1, M1) along with J, *l*, and s.

Using the equations derived in [Sey79], the unnormalized Legendre coefficients presented in section 5.1.1 are expanded in terms of matrix elements as follows:

$$A_0 = \sum (2J+1)|R|^2, \tag{5.17}$$

$$A_k = \sum (\cdots\cdots) \mathrm{Re}[RR'^*], \tag{5.18}$$

$$B_k = \sum (\cdots\cdots) \mathrm{Re}[iRR'^*], \tag{5.19}$$

where the sums are over the different combinations of matrix elements which are possible (i.e. RR'*), along with their associated quantum numbers. The (·····) symbol refers to a cofactor which is dependent upon the quantum numbers of the two interfering matrix elements, and is explicitly defined in [Sey79]. In the case of Equation 5.17, this cofactor has reduced to 2J+1 (as shown). The main thing to note from Equations 5.17, 5.18 and 5.19 is that the A_k coefficient expansion includes a factor which is linear in Re(RR'*), and is thus proportional to cos(ϕ-ϕ'), while the B_k expansion includes a factor which is linear in Re(iRR'*), and is thus proportional to sin(ϕ-ϕ'). By examining Equations 5.1 and 5.2, we see that this indicates that σ(θ) will be proportional to the cosine of the phase differences between pairs of interfering transition matrix elements, while $A_y(\theta)$ will be proportional to the sine of these phase differences.

5.2.2 Transition Matrix Elements for $D(p,\gamma)^3He$

In order to determine what transition matrix elements (TME's) are present in the $D(\vec{p},\gamma)^3He$ reaction, it is appropriate to consider the angular momentum coupling that is taking place. Figure 5.1 shows a diagram representing the radiative capture process for $D(\vec{p},\gamma)^3He$. The proton ($J^\pi=1/2^+$) and deuteron ($J^\pi=1^+$) couple together to form a variety of possible continuum states. These continuum states then decay by γ-ray emission to the ^3He ground state ($J^\pi=1/2^+$).

All possible combinations of continuum quantum numbers (six in total) are shown in Figure 5.1. Given the very low incident beam energy in this experiment (E_{lab}=0-80 keV), one would expect relative s-wave capture (l=0) to dominate. However, Figure 5.1 shows that p-wave terms (l=1) have also been considered. One reason for this is that there are no s-wave E1 transitions, and thus to include E1, we must allow for p-wave terms. As was discussed in Chapter 4, E1 is the first (and most dominant) term in the expansion of the electromagnetic field, and its inclusion will be shown to be extremely important in fitting the data. Assignment of the γ-ray mode (E or M) and multipolarity (L) for a matrix element is done by determining which EL and ML multipoles can satisfy both conservation of angular momentum and conservation of parity for the reaction in question. Recall that the parity of an electric multipole (EL) is $(-1)^L$, while the parity of a magnetic multipole (ML) is $(-1)^{L+1}$. The parity of the continuum state (P) is simply $P=\pi_p\pi_D(-1)^l$, where π_p and π_D are the intrinsic parities of the proton and deuteron (both +), and the $(-1)^l$ term is the parity arising from the relative orbital angular momentum of the two particles. Since the parity of the final ^3He ground state is known (+), conservation of parity can be applied to determine the allowed transitions. The result is a total of 9 possible matrix elements for the reaction.

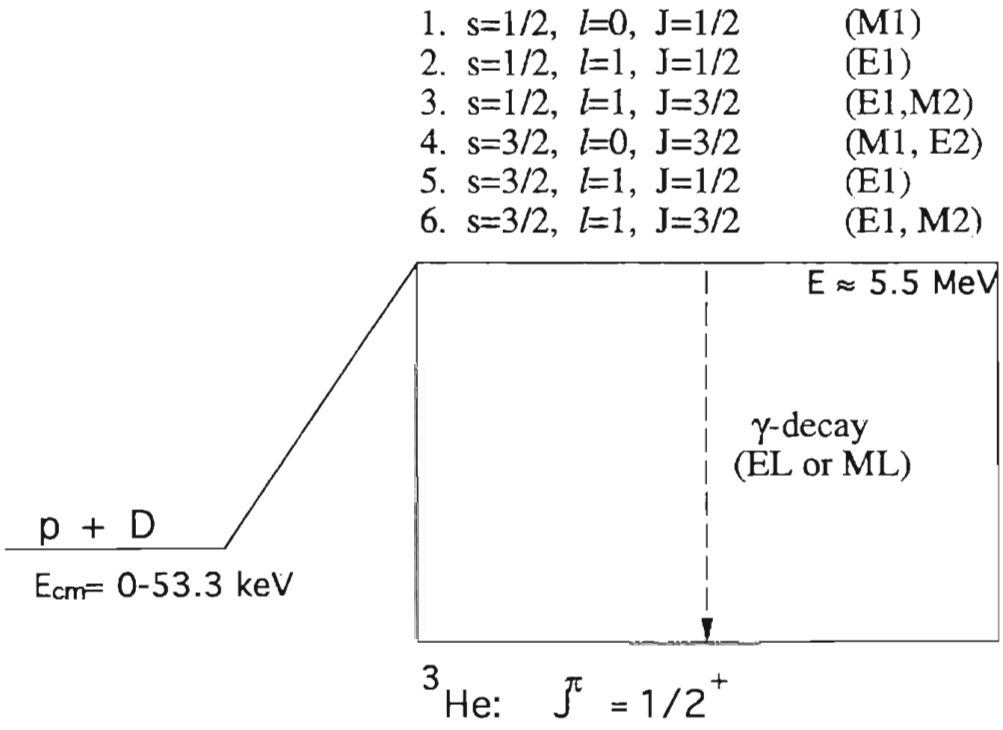

Figure 5.1: Angular momentum coupling diagram for D($\vec{p}$,γ)^{3}He. The possible channel spin values are $s^{\pi}=1/2^+$ or $3/2^+$. The relative orbital angular momentum, l, has been restricted to s-wave and p-wave capture only.

5.2.3 Constraining the fit

In a transition matrix element (TME) fit to the data, the nine possible D($\vec{p}$,γ)^{3}He matrix elements shown in Figure 5.1 will yield 17 free parameters (9 amplitudes and 8 relative phases). Trying to find a unique fit with this number of free parameters would be extremely difficult, if not impossible. Fortunately, there are many reasonable assumptions that we can make which will greatly reduce the number of free parameters in the TME analysis.

The first assumption we make is to assume a certain structure for the ^{3}He ground state: we assume it to be describable by a p+D cluster model. In this picture, equivalent to the assumption used in the direct capture model (see Chapter 6), the proton and deuteron move about each other in either a relative s-wave or a relative d-wave (no p-wave due to parity considerations). Since the s-wave is lower in energy, it should be expected to dominate. Estimates of the D-state probability of ^{3}He typically center around 9% [Vet85,Wel88]. Since the electric multipole operators are expected to be spin independent to a large degree, we need only consider electric transitions which have $\Delta s=0$ (where Δs in this case is the change in channel spin between the continuum and final states). Since the S-state of ^{3}He must have channel spin 1/2 (in order to satisfy angular momentum coupling), we need only consider electric matrix elements which have s=1/2 when considering transitions to the ^{3}He S-state. This indicates that we can neglect all E2 transitions to the S-state. The $\Delta s=0$ E1 and E2 transitions to the D-state are also neglected due to the small D-state percentage.

The next assumption we make is to neglect M2 transitions. This is reasonable based on the results of single particle shell model calculations for γ-decay transition rates in heavy nuclei (the well known Weisskopf estimates [Eis85]). These calculations predict that M2 should only be the fourth strongest term in the expansion of the electromagnetic field, following E1,M1, and E2. Based on these results, and the fact that M2 in this reaction is all p-wave, it seems quite reasonable to neglect it when compared with the other (allowed) transitions.

Making the above assumptions (i.e. removing all M2 transitions, along with the s=3/2 E1 and E2 transitions, from Figure 5.1), we are left with four matrix elements: two p-wave E1 terms; and two s-wave M1 terms. In particular, the Table 5.1 shows the four matrix elements which are under consideration in the current analysis.

The dominant TME's

s	l	J	E1 or M1	Abbreviation
1/2	0	1/2	M1	$^2S_{1/2}$
3/2	0	3/2	M1	$^4S_{3/2}$
1/2	1	1/2	E1	$^2P_{1/2}$
1/2	1	3/2	E1	$^2P_{3/2}$

Table 5.1: The four matrix elements which are under consideration in the current TME analysis for $D(\vec{p},\gamma)^3He$. The abbreviation used is $^{2s+1}l_J$.

As it turns out, a further constraint was necessary in order to obtain unique fits with this set of matrix elements. This final constraint involved setting the J=1/2 and J=3/2 E1 amplitudes and phases equal to each other. This final constraint is equivalent to assuming a pure $\sin^2\theta$ angular distribution for the E1 transitions, and is the assumption made by the authors of [Gri63]. As discussed in section 4.2, this is the case where the spin-orbit coupling is negligible. Some important consequences of using this equal amplitude and phase constraint will be discussed in subsection 5.2.4.

5.2.4 Performing the TME fit

Using Equations 5.17, 5 18 and 5.19, along with the equations given in [Sey79], we can derive the following exact matrix element expansions for the A_k and B_k coefficients in $D(\vec{p},\gamma)^3He$ (using the matrix elements listed in Table 5.1 with no constraints applied):

$$A_0 = 2\left|{}^2P_{1/2}\right|^2 + 4\left|{}^2P_{3/2}\right|^2 + 2\left|{}^2S_{1/2}\right|^2 + 4\left|{}^4S_{3/2}\right|^2, \tag{5.20}$$

$$A_1 = -4\left|{}^2P_{1/2}\right\|{}^2S_{1/2}\left|\cos(\phi_{s_{1/2}} - \phi_{p_{1/2}}) + 4\right|{}^2P_{3/2}\left\|{}^2S_{1/2}\right|\cos(\phi_{s_{1/2}} - \phi_{p_{3/2}}),$$

$$A_2 = -4\left|{}^2P_{1/2}\right\|{}^2P_{3/2}\left|\cos(\phi_{p_{3/2}} - \phi_{p_{1/2}}) - 2\right|{}^2P_{3/2}\Big|^2,$$

$$\begin{aligned} B_1 = {} & -1.333\left|{}^2P_{1/2}\right\|{}^2S_{1/2}\left|\sin(\phi_{s_{1/2}} - \phi_{p_{1/2}}) - 1.333\right|{}^2P_{1/2}\left\|{}^4S_{3/2}\right|\sin(\phi_{s_{3/2}} - \phi_{p_{1/2}}) \\ & -0.667\left|{}^2P_{3/2}\right\|{}^2S_{1/2}\left|\sin(\phi_{s_{1/2}} - \phi_{p_{3/2}}) - 6.667\right|{}^2P_{3/2}\left\|{}^4S_{3/2}\right|\sin(\phi_{s_{3/2}} - \phi_{p_{3/2}}) \quad , \end{aligned}$$

$$B_2 = -0.667\left|{}^2P_{1/2}\right\|{}^2P_{3/2}\left|\sin(\phi_{p_{3/2}} - \phi_{p_{1/2}}).\right.$$

In the case of the $P_\gamma(\theta)$ observable, Equation 4.5 can be used to derive the following expansions for the F_k and G_k coefficients in Equation 5.4 (with the same set of matrix elements as in Equation 5.20):

$$F_2 = 1.0\left|{}^2P_{1/2}\right\|{}^2P_{3/2}\left|\cos(\phi_{p_{3/2}} - \phi_{p_{1/2}}) + 0.5\right|{}^2P_{3/2}\Big|^2, \tag{5.21}$$

$$G_0 = \left|{}^2P_{1/2}\right|^2 + 2\left|{}^2P_{3/2}\right|^2 + \left|{}^2S_{1/2}\right|^2 + 2\left|{}^4S_{3/2}\right|^2,$$

$$G_1 = \left|{}^2P_{3/2}\right\|{}^2S_{1/2}\left|\cos(\phi_{s_{1/2}} - \phi_{p_{3/2}}) - \right|{}^2P_{1/2}\left\|{}^2S_{1/2}\right|\cos(\phi_{s_{1/2}} - \phi_{p_{1/2}}),$$

$$G_2 = -\left|{}^2P_{3/2}\right|^2 - 2\left|{}^2P_{1/2}\right\|{}^2P_{3/2}\left|\cos(\phi_{p_{3/2}} - \phi_{p_{1/2}}),\right.$$

where the F_0 and F_1 coefficients are zero in this case.

Using Equations 5.20 and 5.21, along with Equations 5.1, 5.2 and 5.4, we can fit the acquired data for all observables simultaneously in order to obtain the amplitudes and phases of the contributing matrix elements. The process of fitting the equations to the data can be carried out by using the MINUIT minimization package [Jam77] to minimize the total χ^2 fit to the data by means of a parameter search. The number of free parameters in these fits will be seven (four amplitudes and three relative phases). However, if the final constraint discussed in subsection 5.2.3 is also applied (i.e. if the E1 amplitudes and phases are set equal to each other), the number of free parameters is reduced by four. This can be seen by examining Equations 5.20 and 5.21, where it becomes apparent that by setting the E1 amplitudes and phases equal to each other, we make the ratio of the $^2S_{1/2}$ and $^4S_{3/2}$ terms essentially arbitrary, and thus reduce the number of free parameters by four instead of two. What we are left with is three free parameters: an M1 s-wave amplitude (S); an E1 p-wave amplitude (P); and a relative phase (Δ). In the case of the equal amplitude and phase assumption, the Legendre coefficients of Equations 5.20 and 5.21 can be re-written as:

$$A_0 = 6|P|^2 + 6|S|^2, \tag{5.22}$$

$$A_1 = 0,$$

$$A_2 = -6|P|^2,$$

$$B_1 = -10|P||S|\sin\Delta,$$

$$B_2 = 0,$$

and,

$$F_2 = 1.5|P|^2, \tag{5.23}$$

$$G_0 = 3|P|^2 + 3|S|^2,$$

$$G_1 = 0,$$

$$G_2 = -3|P|^2.$$

With the equal amplitude and phase assumption, Equations 5.22 and 5.23 can be used, along with Equations 5.1, 5.2 and 5.4, in order to determine the P, S and Δ parameters for a given set of data. The MINUIT code is still used to do the fitting. However, it should be pointed out that if we restrict our analysis to the $\sigma(\theta)$ and $A_y(\theta)$ observables (i.e. if we don't consider $P_\gamma(\theta)$), as is the case in the binning analysis, Equation 5.22 can be solved exactly for the P, S, and Δ parameters in terms of the Legendre coefficients, and thus a χ^2 minimization using MINUIT is not necessary.

5.3 Thick Target Yield Results

In this section, we present the thick target yield results along with Legendre and TME fits. Table 5.2 shows the acquired thick target yield data. Since no absolute cross section has been calculated from this data, the errors shown are statistical only. Figure 5.2 gives a graphical picture of the acquired thick target yield data along with Legendre fits to each observable. The results are summarized in Table 5.3.

Thick target yield results

θ_{cm}	$\sigma_{cm}(\theta)$ (arb.units)	$A_y(\theta)$	$P_\gamma(\theta)$
120.2	0.769 ± 0.023	0.089 ± 0.014	0.79 ± 0.30
105.2	0.918 ± 0.007	----------	----------
91.0	1.000 ± 0.009	0.085 ± 0.006	1.06 ± 0.23
61.7	0.825 ± 0.015	----------	----------
60.4	----------	0.095 ± 0.010	0.79 ± 0.27
60.2	0.805 ± 0.006	----------	----------
31.6	0.386 ± 0.012	----------	----------
30.8	----------	0.124 ± 0.011	0.56 ± 0.21
30.1	0.358 ± 0.007	----------	----------
1.5	0.157 ± 0.004	----------	----------
0.0	0.157 ± 0.003	----------	----------

Table 5.2: The acquired D($\vec{p}$,γ)^{3}He data for the thick target yield analysis (E_p=80-0 keV) shown vs. θ_{cm} (evaluated at E_p=80 keV). The $\sigma(\theta)$ data has been normalized to 1.0 at θ_{cm}=91° (i.e. arbitrary units). The error bars shown are statistical only. Note that at these energies, $\sigma_{cm}(\theta)=\sigma_{lab}(\theta)$ to better than 1% accuracy.

Legendre fit

a_1	a_2	b_1	b_2	G_0	G_1	G_2	F_2
.066 ± .014	-.86±.02	.12±.01	.005±.004	.98±.15	-.07±.2	-.52±.35	.41±.06

Table 5.3: The Legendre coefficients extracted by fitting the $\sigma(\theta)$, $A_y(\theta)$ and $P_\gamma(\theta)$ thick target yield data. The fits, in this case, are done independently.

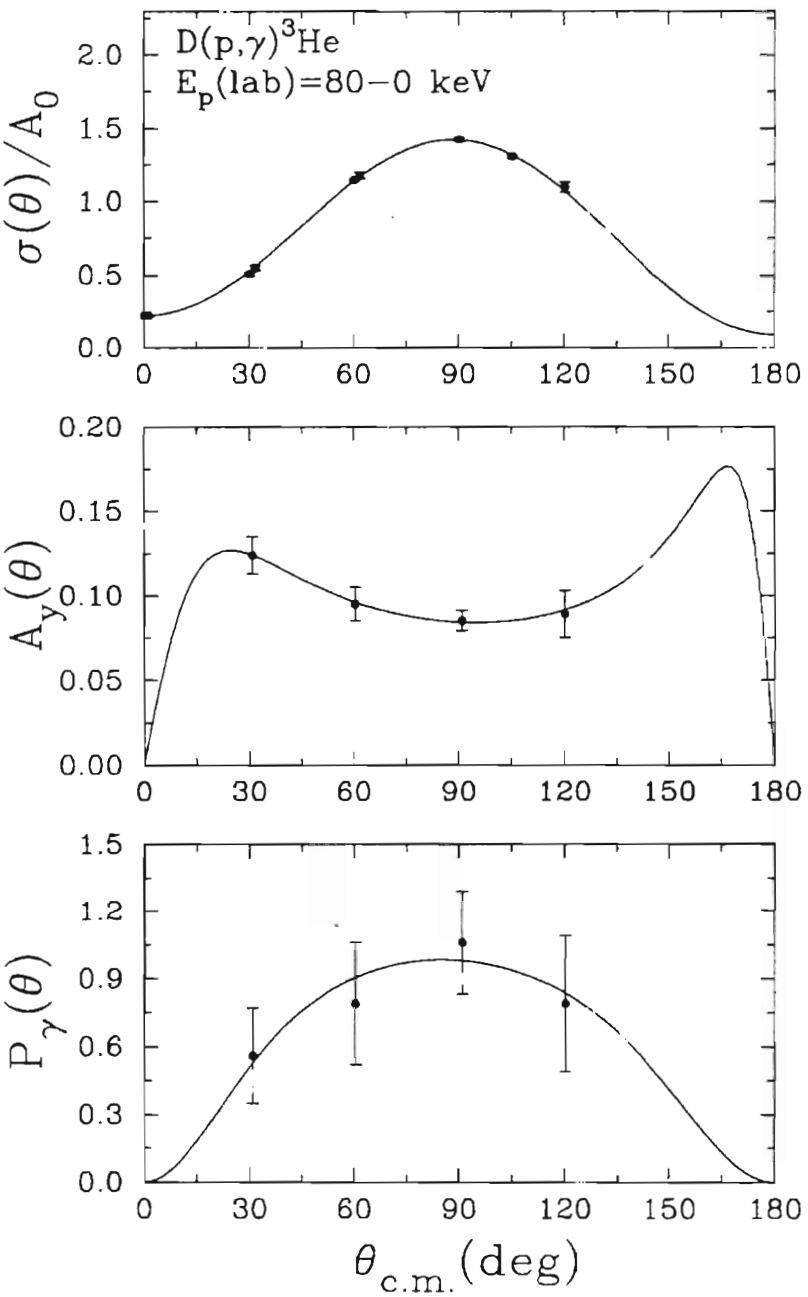

Figure 5.2: The acquired thick target yield data for D($\vec{p}$,γ)^{3}He. The solid lines are Legendre fits to the data (done separately for each observable).

Figure 5.3 shows the same set of $D(\vec{p},\gamma)^3He$ thick target yield data shown along with a TME fit. This fit has been done simultaneously to all the observables by using Equations 5.22 and 5.23. These equations use the equal amplitude and phase assumption. Among its other consequences, this assumption necessitates that $\sigma(\theta)\sim\sin^2\theta+\text{constant}$ (i.e. that the cross section be symmetric about 90°). The implementation of the equal amplitude and phase constraint was necessary in order to obtain a unique solution. If the data shown in Figure 5.3 were fit with Equations 5.20 and 5.21 (i.e. no equal amplitude and phase constraint), numerous solutions could be found which, although all having the same χ^2 per degree of freedom (χ^2/ν=0.83), gave total M1 fractions varying from 2-13%. In addition, the ratios of the two M1 amplitudes determined in these fits were completely arbitrary (as were the ratios of the two E1 amplitudes). By using the equal amplitude and phase assumption instead, exact solutions could be obtained for an M1 s-wave amplitude, S, an E1 p-wave amplitude, P, and a relative phase, Δ. Table 5.4 shows the results of the TME fit shown in Figure 5.3.

TME fit

ν	χ^2/ν	P	S	Δ (deg.)	% M1
14	1.49	0.308±0.001	0.160±0.001	10.4±0.5	20.4±0.3

Table 5.4: The results of the TME fit to the thick target $D(\vec{p},\gamma)^3He$ data using the equal amplitude and phase assumption (Figure 5.3). All observables are included in this fit. With 17 data points and 3 varied parameters, there are 14 degrees of freedom in this fit.

Although the equal amplitude and phase assumption seems to give a reasonable fit to the data (as shown in Figure 5.3), the χ^2/ν value is larger than in the unconstrained fits (1.49 as compared with 0.83), and thus the question to ask at this point is how confident

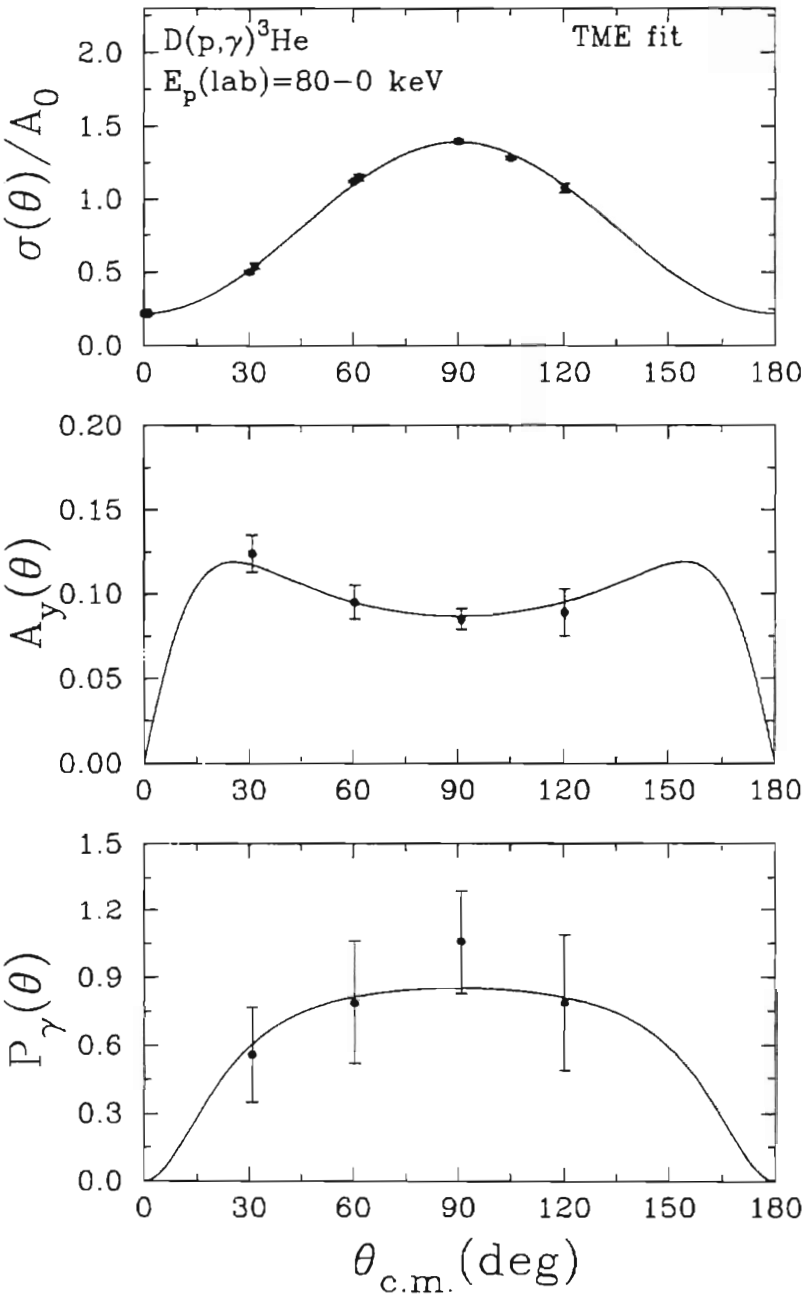

Figure 5.3: The thick target yield data for D($\vec{p}$,γ)^{3}He along with a TME fit (solid line). This TME fit, done simultaneously to all the observables, used the set of matrix elements in Table 5.1 along with the equal amplitudes and phases constraint.

are we in using this assumption? By means of confidence limit tables for the χ^2 distribution [Bev69], we see that for $\nu = 14$ we expect a χ^2/ν of 1.49 or worse about 10% of the time. Thus one could argue that our equal amplitude and phase assumption is within the realm of reason. Another justification for the equal amplitude and phase assumption comes from considering the data shown in Figure 5.4. In this figure, the current binned data from E_p(lab)=30-40 keV (E_{cm}=20-26.7 keV) are compared with recently acquired data from the p(d,γ)^{3}He reaction over the energy regime E_{cm}=16.6-26.7 keV [Ric95]. These two reactions complement each other in the sense that, in the center of mass,$\theta_{pd}=180^\circ-\theta_{dp}$. This allows forward angles in the p(d,γ)^{3}He reaction to be compared to back angles in the D(p,γ)^{3}He reaction (which are typically hard to measure experimentally). Combining these data sets, as shown in Figure 5.4 (plotted vs. D(p,γ)^{3}He center of mass angle), we see that the data are roughly consistent with a symmetric distribution. The solid line is a Legendre fit to the data (with no constraints), and the symmetric character of the data is made quite clear by this fit. This result gives us additional confidence in the equal amplitude and phase assumption since one of the primary predictions of this assumption is a symmetric angular distribution.

The constrained TME fit shown in Figure 5.3, which gives an M1 fraction of ~20%, included the $P_\gamma(\theta)$ data in the fitting. From looking at the raw $P_\gamma(\theta)$ data, it is clear that they indicate a predominately E1 solution (a predominately M1 solution would have $P_\gamma(\theta)$ closer to zero). However, as it turns out in this case, the $P_\gamma(\theta)$ data play no special role in constraining the TME fit results. This is because the $\sigma(\theta)$ data and $A_y(\theta)$ data alone necessitate a predominately E1 solution (when using the matrix elements in Table 5.1). Since the error bars on the $P_\gamma(\theta)$ data are much larger than the $\sigma(\theta)$ or $A_y(\theta)$ data, all possible solutions present with just the $\sigma(\theta)$ and $A_y(\theta)$ data are also possible once the $P_\gamma(\theta)$ data has been added in. Thus, the role that the $P_\gamma(\theta)$ observable plays in

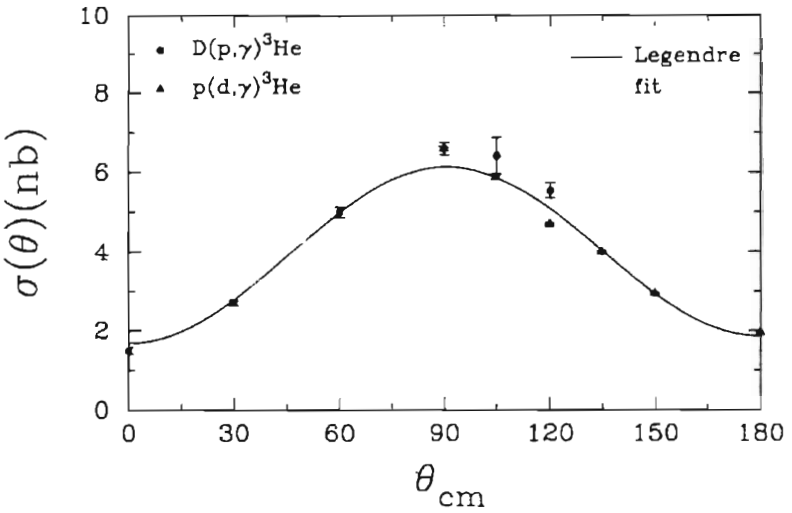

Figure 5.4: $D(p,\gamma)^3He$ data in the energy region E_{cm}=20-26.7 keV, and $p(d,\gamma)^3He$ data in the energy region E_{cm}=16.6-26.7 keV, are plotted vs. θ_{cm} for $D(p,\gamma)^3He$. The solid line, which is a Legendre fit to all the data, shows the symmetric character of the angular distribution.

the current TME analysis is primarily one of improving statistical accuracy by way of providing additional data to be fit. The large error bars on the $P_\gamma(\theta)$ data make its contribution to the results extremely small in the current case.

This relative insensitivity of the results to the $P_\gamma(\theta)$ data would change in the event that other matrix elements were considered. For example, if the three possible d-wave M1 terms are also included in the fit (the $^2S_{1/2}$, $^4S_{1/2}$, and $^4S_{3/2}$ TME's), and all constraints are relaxed, the $P_\gamma(\theta)$ data becomes much more important. Figure 5.5 clearly demonstrates the importance of the $P_\gamma(\theta)$ data in this case. The dashed line in Figure 5.5 represents a fit obtained using only the $\sigma(\theta)$ and $A_y(\theta)$ data, while the solid line represents a fit which included the $P_\gamma(\theta)$ data. It should be pointed out that these two fits were obtained using exactly the same set of matrix elements (2 E1 and 5 M1 TME's) and

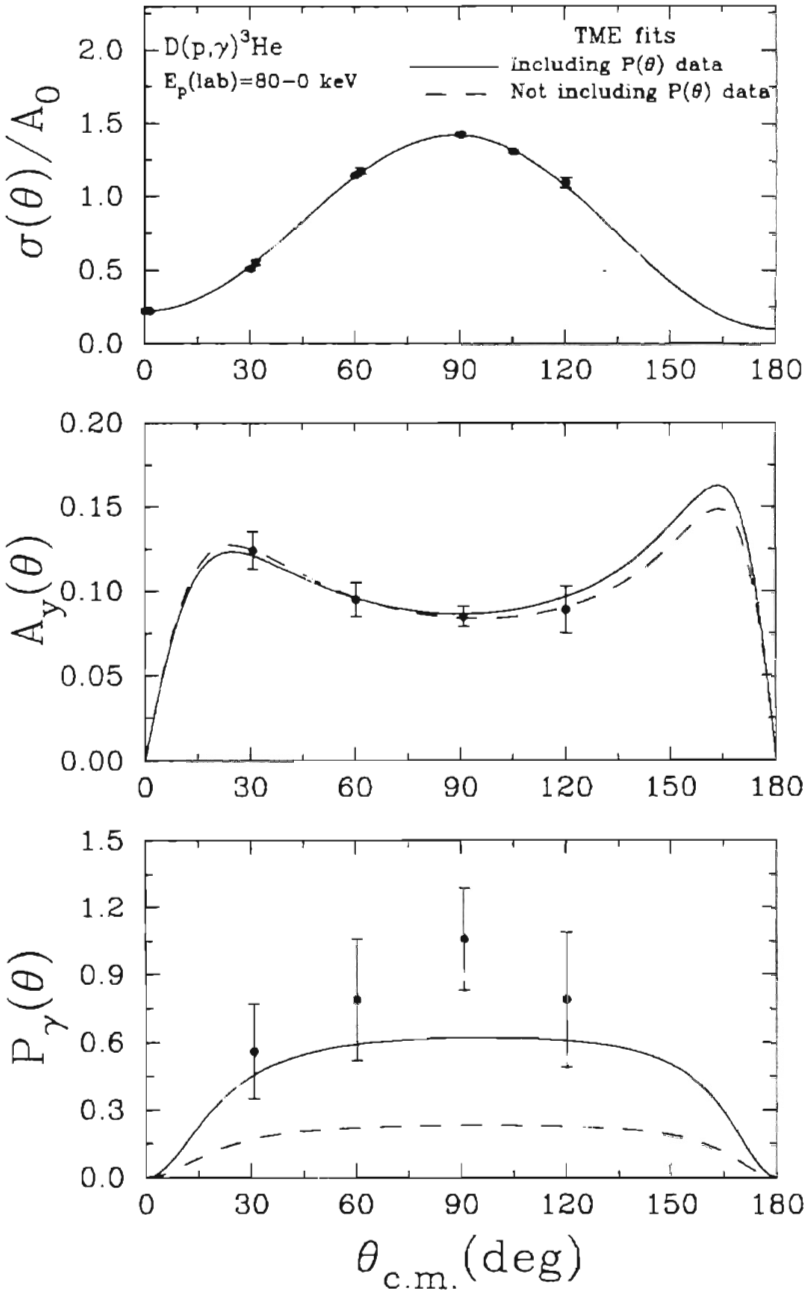

Figure 5.5: The thick target yield data for D($\vec{p}$,γ)^{3}He shown along with two TME fits. Both of the fits use the matrix elements from Table 5.1 (with no constraints) *along with the three d-wave M1 terms* mentioned in the text. The solid line (M1=27%) includes the P(θ) data in the fitting, while the dashed line (M1=45%) does not.

exactly the same set of starting values for the amplitudes and phases. This emphasizes the fact that the only difference between the two fits is the inclusion of the extra observable ($P_\gamma(\theta)$) in the fit represented by the solid line.

By examining Figure 5.5, it is clear that the two fits are practically indistinguishable *based on the $\sigma(\theta)$ and $A_y(\theta)$ data*, but with the inclusion of the $P_\gamma(\theta)$ data, the solid line is clearly the preferred fit. This discrimination between the two fits is significant from a physics standpoint, because the dashed line predicts an M1 fraction of $45 \pm 0.7\%$, while the preferred solid line predicts an M1 fraction of $27 \pm 0.2\%$. The inclusion of the $P_\gamma(\theta)$ data has thus, in this case, helped discriminate between two possible solutions which otherwise would have been indistinguishable. Of course, we can use reasonable arguments to neglect d-wave capture in the first place (the centrifugal barrier). It should also be pointed out that the solutions obtained using this set of seven matrix elements are not unique, and thus are not quantitatively useful in the current analysis. The only reason for considering this fit is to demonstrate a possible use for the $P_\gamma(\theta)$ observable in a hypothetical set of circumstances.

5.4 Results from the Binning Analysis

In this section, the results for the $D(\vec{p},\gamma)^3He$ binning analysis are presented. The results will be presented in terms of the center-of-bin beam energies, $\overline{E}_p(lab)$. The goal of this section is to demonstrate the energy dependence of the $\sigma(\theta,E)$ and $A_y(\theta,E)$ observables. Since the $P_\gamma(\theta)$ data was only analyzed for the whole 0-80 keV region, no $P_\gamma(\theta)$ data will discussed in this section.

Tables 5.5 and 5.6 show the results from the binning analysis presented as a function of θ_{lab} and $\overline{E}_p(lab)$. The reason for presenting the data as a function of $\overline{E}_p(lab)$

$\sigma_{cm}(\theta,E)$, in nb, as a function of θ_{lab} and $\overline{E}_p(lab)$

θ_{lab}	15 keV	25 keV	35 keV	45 keV	55 keV	65 keV	75 keV
1°	0.20 ± 0.03	0.66 ± 0.05	1.28 ± 0.08	1.62 ± 0.10	2.09 ± 0.11	2.32 ± 0.12	2.43 ± 0.13
31°	0.29 ± 0.03	1.10 ± 0.04	2.31 ± 0.06	3.65 ± 0.08	5.27 ± 0.09	6.43 ± 0.10	7.64 ± 0.11
60°	0.48 ± 0.03	2.07 ± 0.08	4.26 ± 0.11	7.15 ± 0.16	10.5 ± 0.2	14.0 ± 0.2	16.1 ± 0.2
91°	0.52 ± 0.03	2.38 ± 0.08	5.63 ± 0.13	9.62 ± 0.17	13.5 ± 0.2	17.4 ± 0.3	21.1 ± 0.3
105°	-------	-------	5.50 ± 0.39	9.61 ± 0.63	12.0 ± 0.8	16.1 ± 1.0	18.9 ± 1.2
120°	0.46 ± 0.04	1.90 ± 0.09	4.74 ± 0.16	8.02 ± 0.22	11.7 ± 0.3	14.7 ± 0.3	16.1 ± 0.3

Table 5.5: The $\sigma_{cm}(\theta,E)$ results for the $D(\vec{p},\gamma)^3He$ binning analysis presented as a function of θ_{lab} and $\overline{E}_p(lab)$. The error bars are statistical only. Since $\sigma_{cm}=\sigma_{lab}$ to within 1% accuracy, we henceforth refer to σ_{cm} as simply σ.

$A_y(\theta,E)$

θ_{lab}	15 keV	25 keV	35 keV	45 keV	55 keV	65 keV	75 keV
31°	.147 ± .138	.125 ± .061	.216 ± .043	.129 ± .034	.124 ± .029	.126 ± .026	.158 ± .024
60°	.183 ± .154	.138 ± .068	.087 ± .047	.096 ± .037	.077 ± .031	.094 ± .028	.072 ± .026
91°	.116 ± .075	.164 ± .039	.106 ± .025	.069 ± .020	.079 ± .017	.081 ± .015	.092 ± .014
120°	.260± .200	.220 ± .094	.032 ± .059	.115 ± .047	.116 ± .039	.070 ± .036	.120 ± .035

Table 5.6: The $A_y(\theta,E)$ results for the $D(\vec{p},\gamma)^3He$ binning analysis presented as a function of θ_{lab} and $\overline{E}_p(lab)$.

is simply to provide easy reference for the experimentalist. To obtain the results as a function of E_{cm}, use the relation $E_{cm}=(2/3)\overline{E}_p$. The reason for presenting the data as a function of θ_{lab} instead of θ_{cm} is that θ_{cm} depends on the beam energy, and thus a

presentation in terms of θ_{lab} saves considerable space. It should be emphasized, however, that all analysis (i.e. Legendre fits and TME fits) were done using the exact values of θ_{cm} at each bin energy.

Figures 5.6-5.12 show graphically the acquired $D(\vec{p},\gamma)^3He$ data for the binning analysis. For each figure, the $\sigma(\theta)$ data (in nanobarns) is plotted along with the $A_y(\theta)$ data. The energy bins are identified by the center-of-bin beam energy, $\overline{E}_p(lab)$. For the $\sigma(\theta)$ data, only the statistical error has been shown (as discussed in Chapter 3, the estimated systematic error is 9%). The solid lines shown in Figures 5.6-5.12 are TME fits to the data with the matrix elements in Table 5.1. These TME fits *include* the equal amplitude and phase constraint. The dashed lines in Figures 5.6-5.12 are Legendre fits to the data. Figure 5.13 shows graphically the acquired Legendre coefficients for $D(\vec{p},\gamma)^3He$. Table 5.7 summarizes the results of the Legendre analysis. The extracted b_2 coefficient was consistent with zero, and is not shown. The total angle integrated cross section is defined as $\sigma_T=4\pi A_0$, and the results for σ_T are shown in Table 5.8.

Legendre Coefficients vs. Energy

	15 keV	25 keV	35 keV	45 keV	55 keV	65 keV	75 keV
A_0 (nb)	.425 ± .022	1.79 ± .049	4.26 ± 0.08	7.14 ± 0.11	10.2 ± 0.13	12.9 ± 0.2	14.7 ± 0.2
a_1	.027 ± .120	.063 ± .063	-.12 ± .04	-.11 ± .04	-.10 ± .03	-.055±.027	.024 ± .026
a_2	-.560±.112	-.72 ± .06	-.60 ± .04	-.67 ± .03	-.69 ± 0.03	-.77 ± .03	-.86 ± 0.02
b_1	.185 ± .081	.223 ± .043	.122 ± .027	.107 ± .022	.115 ± .018	0.11 ± 0.02	0.13 ± 0.02

Table 5.7: The Legendre coefficients extracted from the $D(\vec{p},\gamma)^3He$ binning analysis. The energy shown is the center-of-bin beam energy, $\overline{E}_p(lab)$. The errors on A_0 are statistical only.

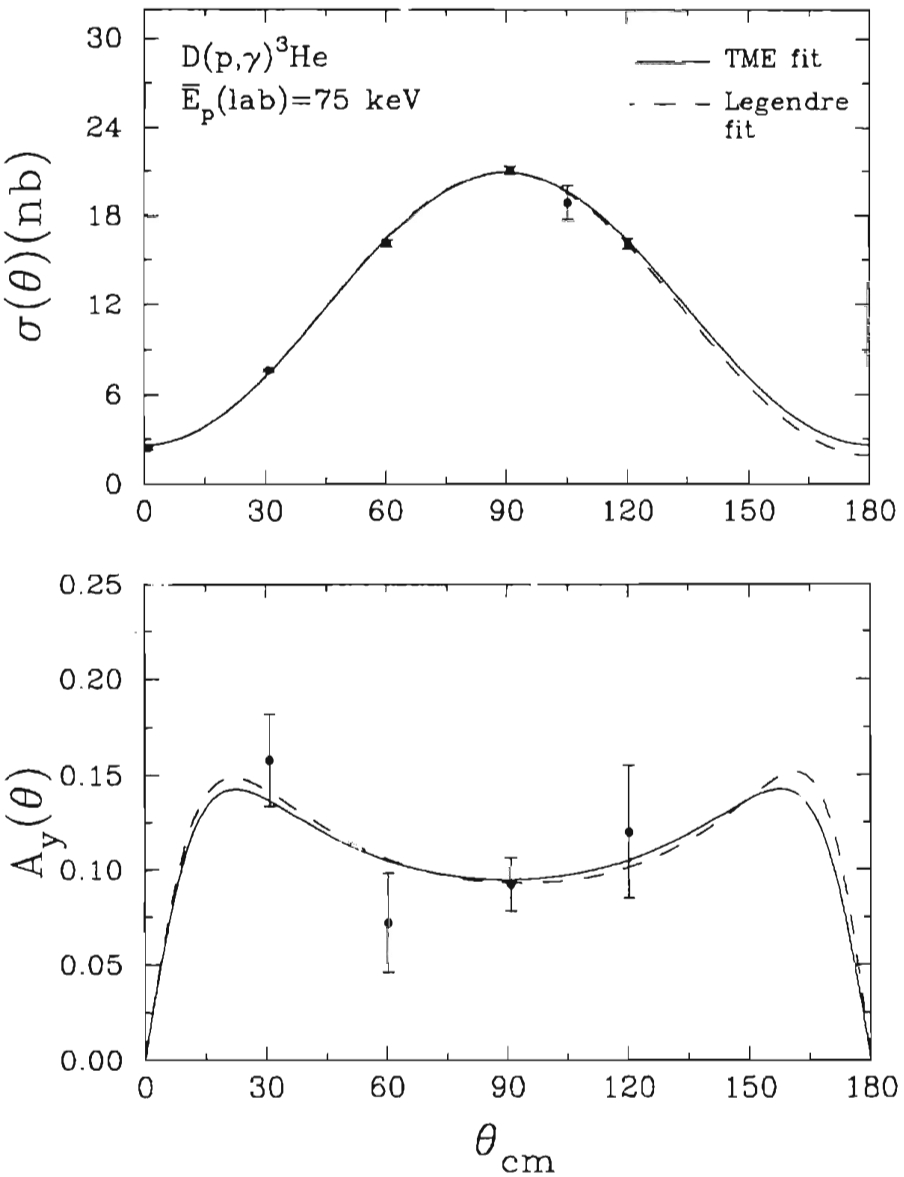

Figure 5.6: The binned D($\vec{p}$,γ)^{3}He data at $\bar{E}_p$(lab)=75 keV. The dashed line is a Legendre fit while the solid line is a simultaneous TME fit to both observables (the equal amplitude and phase assumption is used).

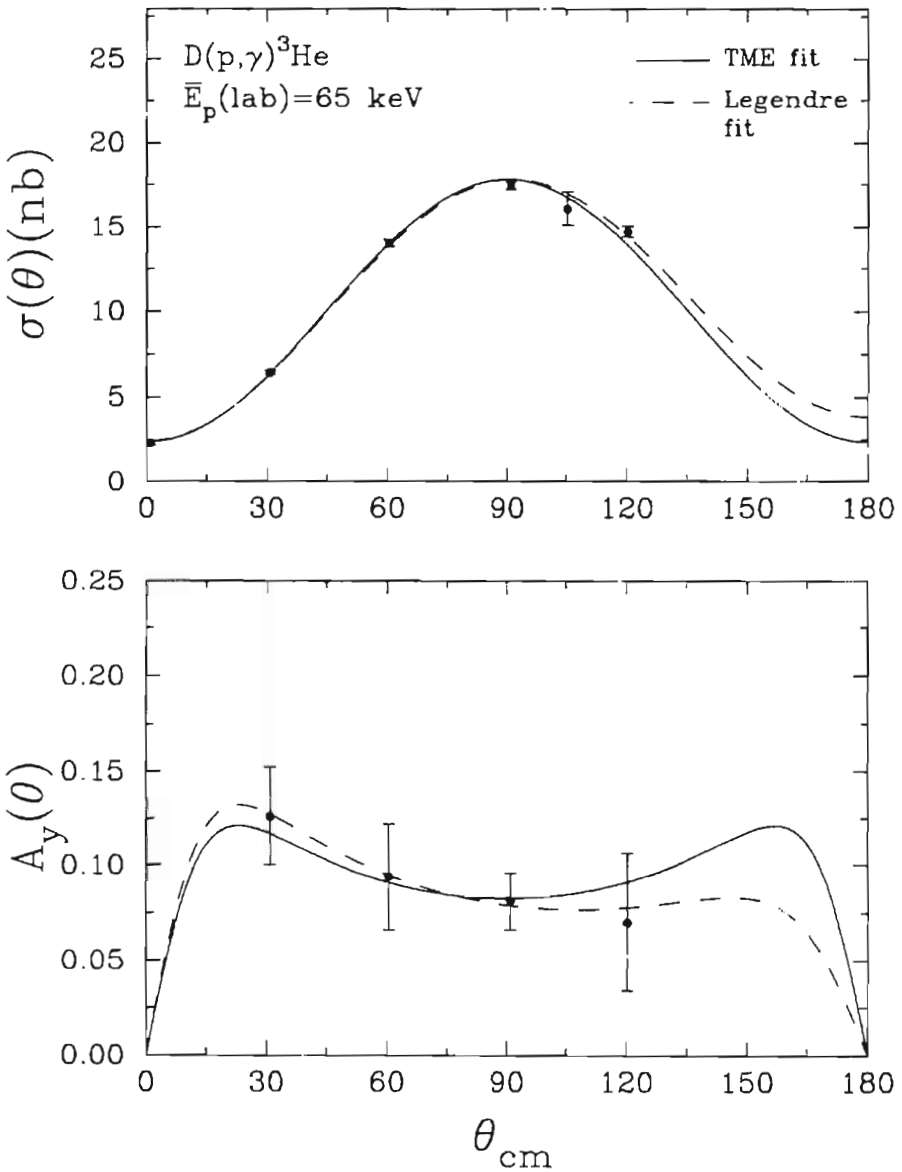

Figure 5.7: The binned D($\vec{p}$,γ)^{3}He data at $\overline{E}_p$(lab)=65 keV. The dashed line is a Legendre fit while the solid line is a simultaneous TME fit to both observables (the equal amplitude and phase assumption is used).

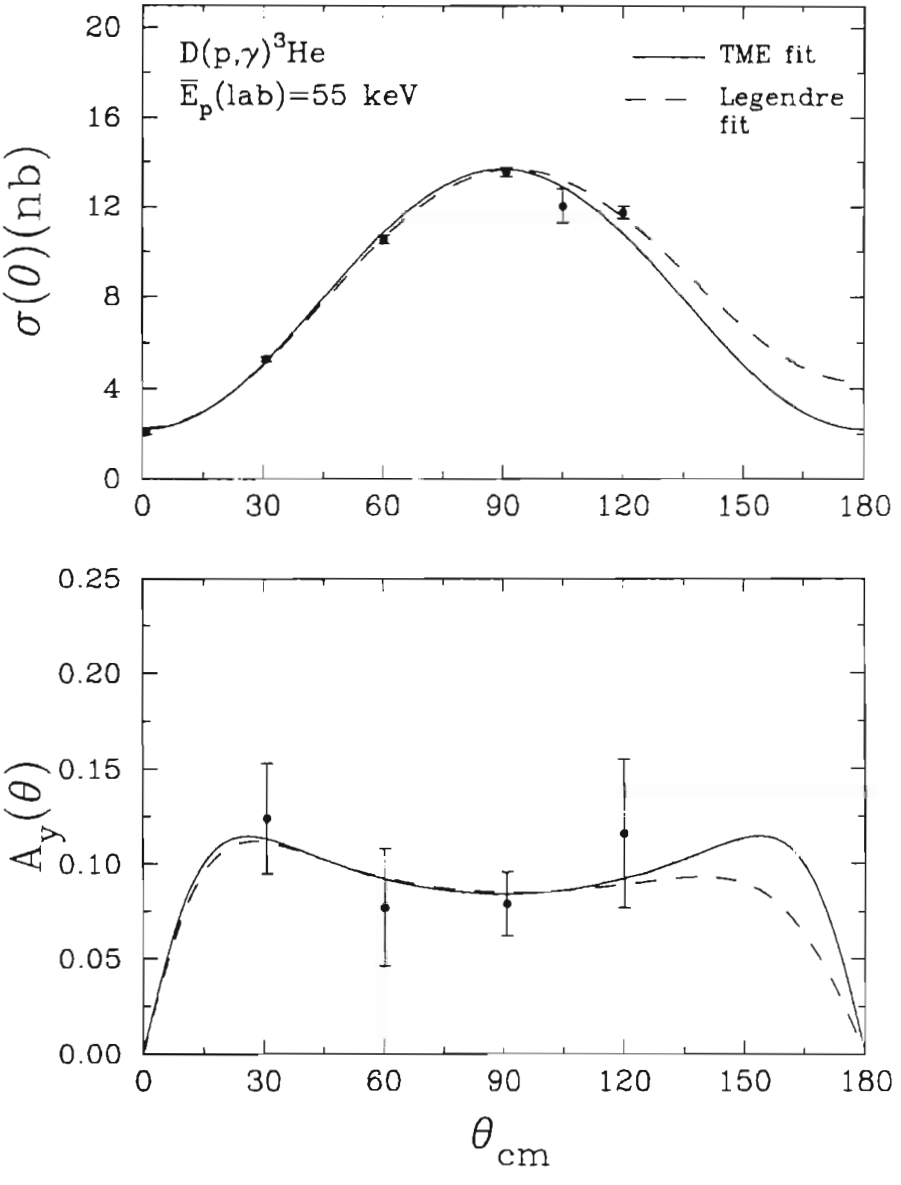

Figure 5.8: The binned D($\vec{p}$,γ)^{3}He data at $\bar{E}_p$(lab)=55 keV. The dashed line is a Legendre fit while the solid line is a simultaneous TME fit to both observables (the equal amplitude and phase assumption is used).

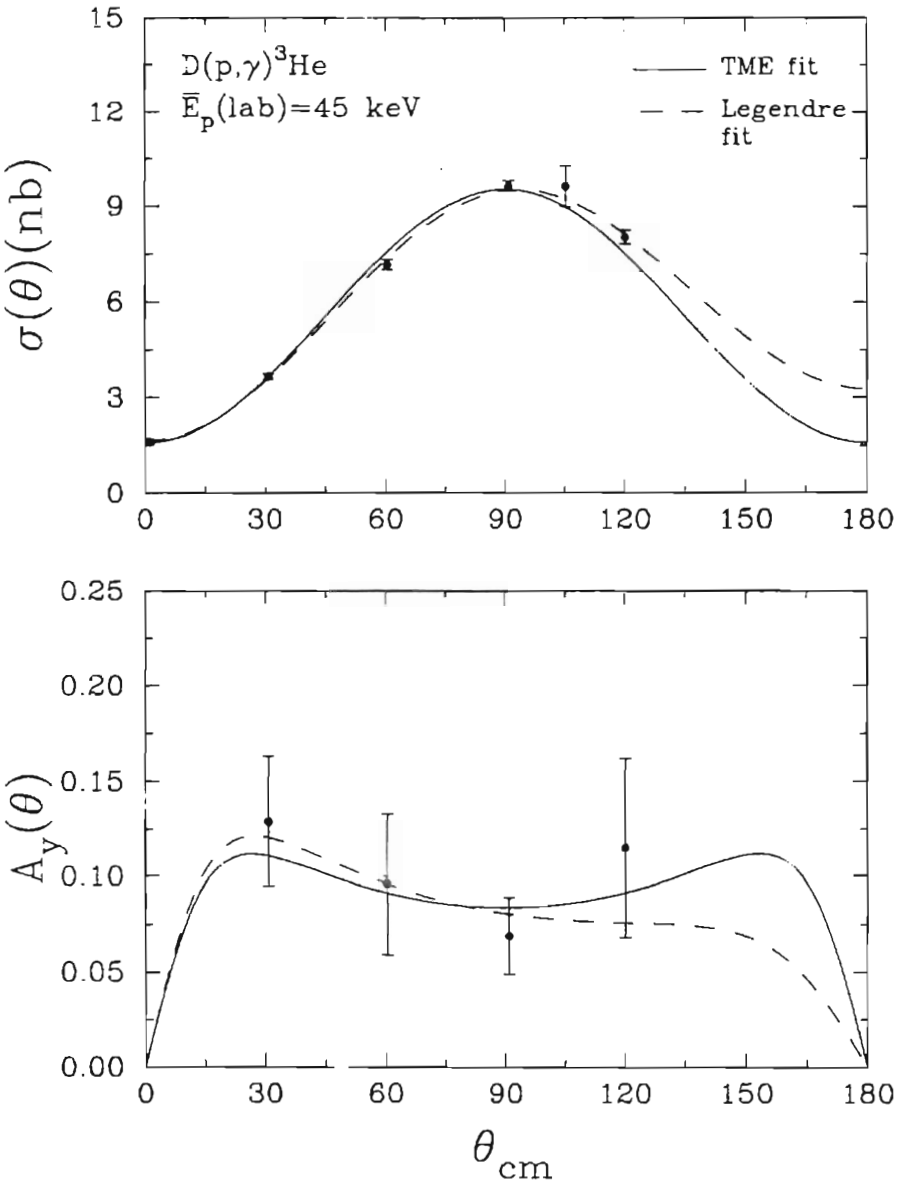

Figure 5.9: The binned D($\vec{p}$,γ)^{3}He data at $\overline{E}_p$(lab)=45 keV. The dashed line is a Legendre fit while the solid line is a simultaneous TME fit to both observables (the equal amplitude and phase assumption is used).

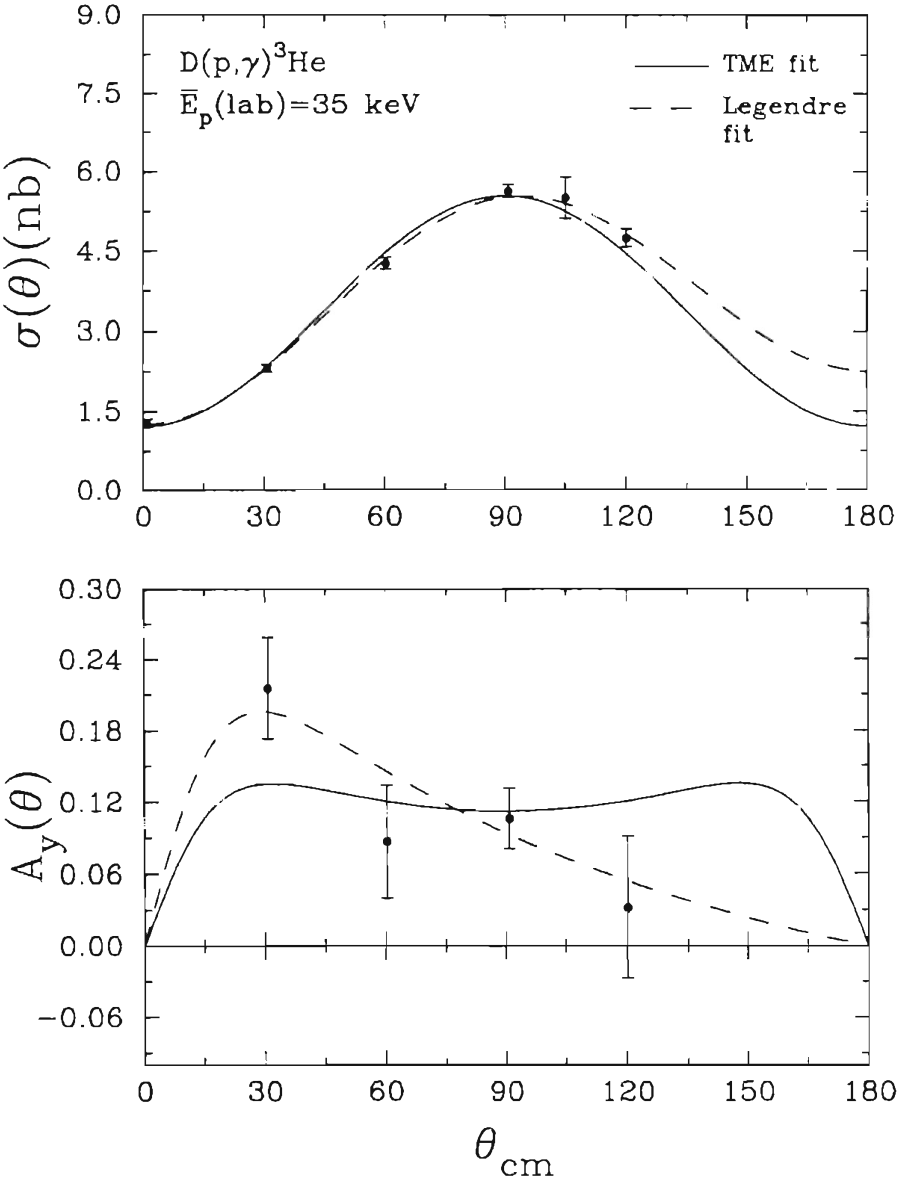

Figure 5.10: The binned D($\vec{p}$,γ)^{3}He data at $\overline{E}_p$(lab)=35 keV. The dashed line is a Legendre fit while the solid line is a simultaneous TME fit to both observables (the equal amplitude and phase assumption is used).

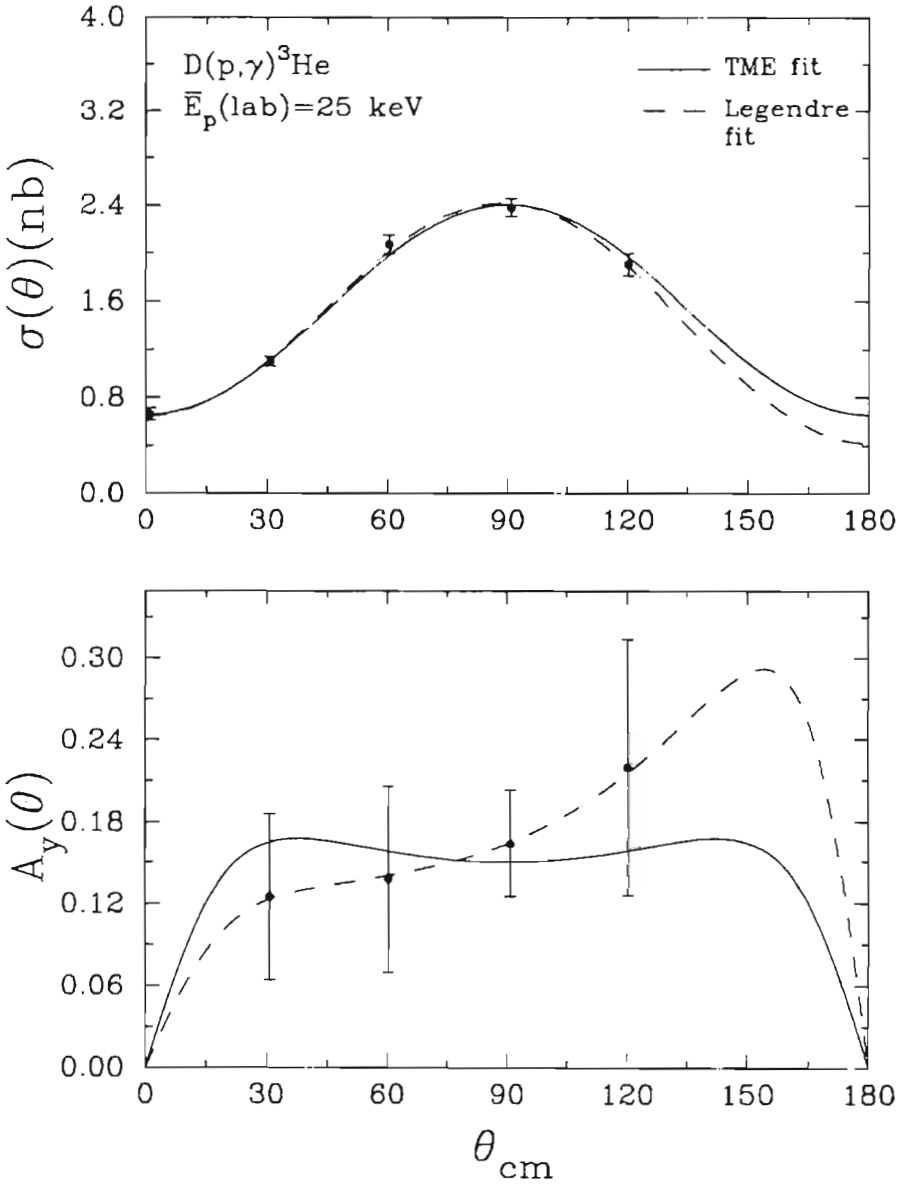

Figure 5.11: The binned D($\vec{p}$,γ)^{3}He data at $\overline{E}_p$(lab)=25 keV. The dashed line is a Legendre fit while the solid line is a simultaneous TME fit to both observables (the equal amplitude and phase assumption is used).

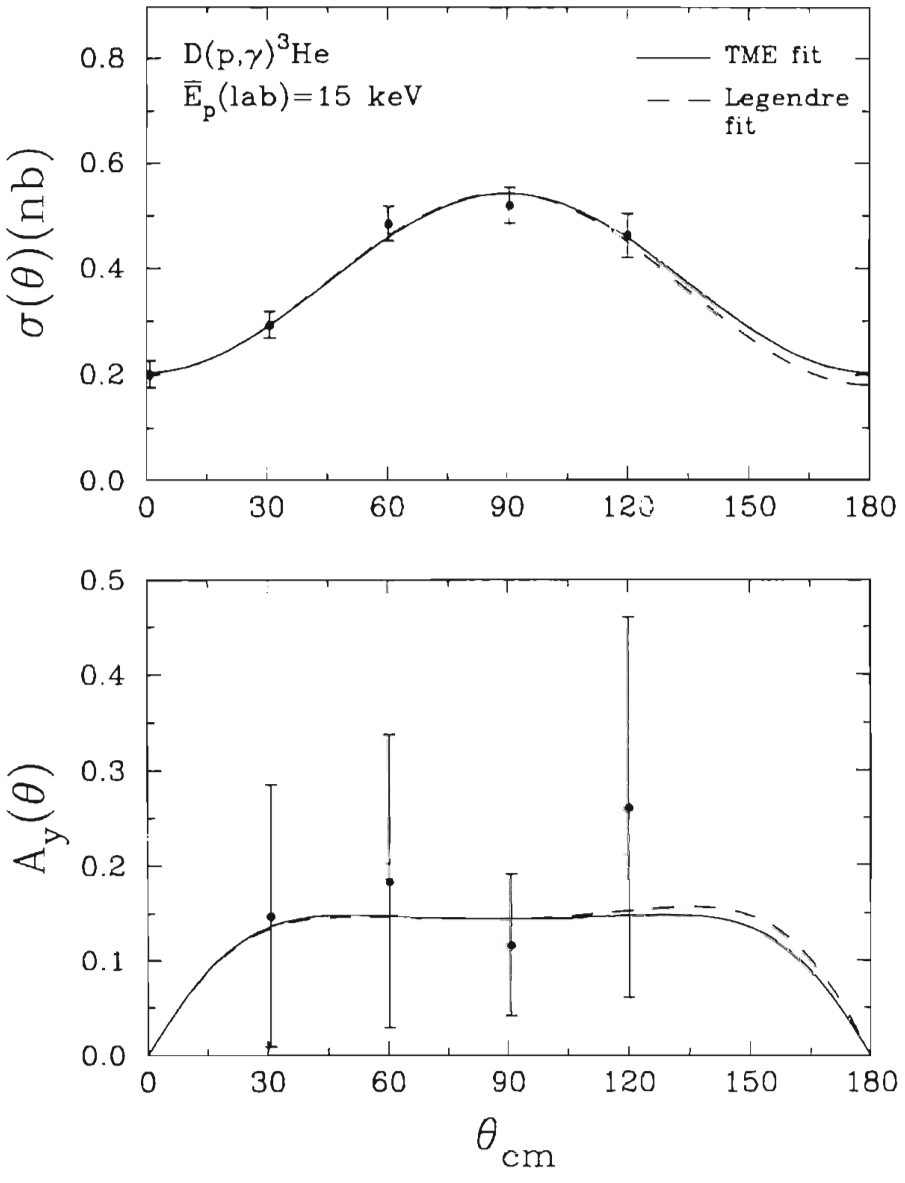

Figure 5.12: The binned D($\vec{p}$,γ)^{3}He data at $\overline{E}_p$(lab)=15 keV. The dashed line is a Legendre fit while the solid line is a simultaneous TME fit to both observables (the equal amplitude and phase assumption is used).

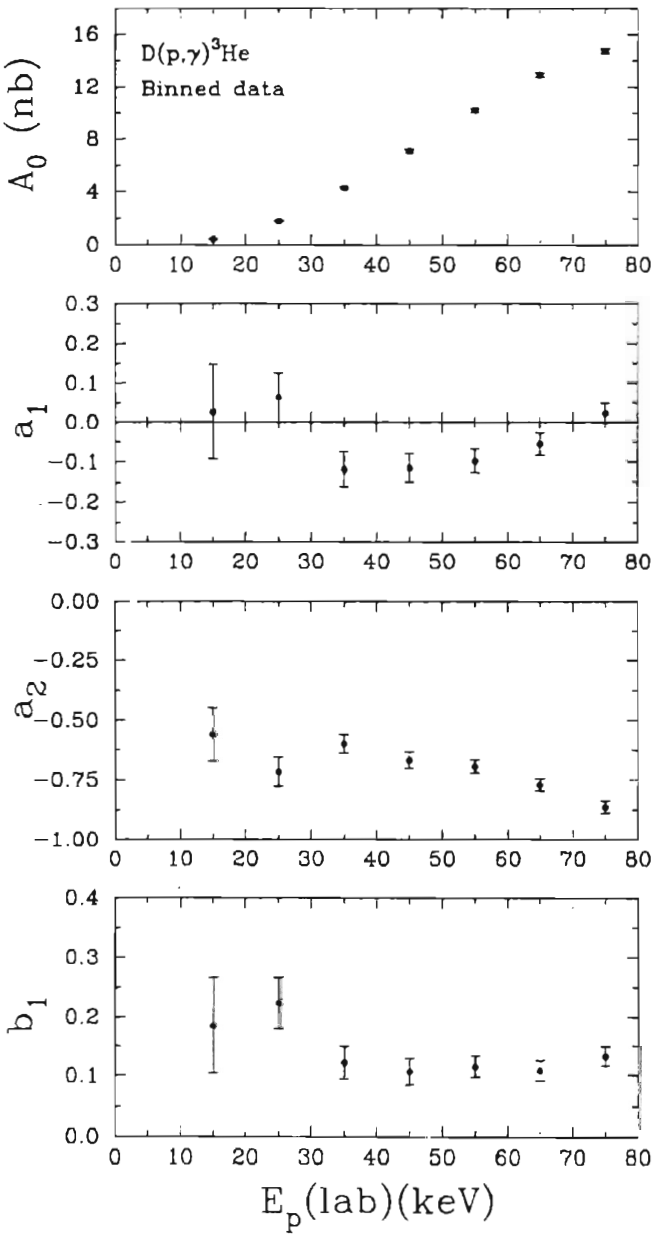

Figure 5.13: The extracted D($\vec{p}$,γ)^{3}He Legendre coefficients as a function of energy. The data for each energy bin are plotted at the center-of-bin beam energy, $\overline{E}_p$(lab).

σ_T extracted from Legendre fits

	15 keV	25 keV	35 keV	45 keV	55 keV	65 keV	75 keV
σ_T (nb)	5.34 ± 0.28	22.5 ± 0.6	53.5 ± 1.0	89.7 ± 1.4	128.2 ± 1.7	162.1 ± 2.0	184.7 ± 2.1

Table 5.8: The σ_T results calculated from the A_0 coefficients in Table 5.6. Again, only statistical error is shown.

The results of the TME analysis on the binned data (the solid lines in Figures 5.6-5.12) are shown in Tables 5.9 and 5.10. The TME results presented in Table 5.9 are: the degrees of freedom, ν; the χ^2/ν value; the E1 P and M1 S amplitudes; the relative phase, Δ; and the M1 fraction of the total cross section. The results presented in Table 5.10 are the total cross section, σ_T, and the component E1 and M1 cross sections, σ_{E1} and σ_{M1} (where $\sigma_T=\sigma_{E1}+\sigma_{M1}$). It will be noted that, in some cases, a very small discrepancy (no larger than a few %) exists between the σ_T values determined from the Legendre and TME analyses. When this occurs, the value extracted from the Legendre fit is taken to be more accurate (because no constraints are applied in the Legendre fits).

Figure 5.14 shows graphically the M1 fraction of σ_T vs. beam energy. The binned data points have been plotted at the $\overline{E}_p$(lab) values shown in Table 5.9. The figure shows the M1 fraction increasing steadily as one goes down lower in energy, indicating that the M1 fraction at threshold (E=0) is at least 50%, and perhaps higher. The focus of the deconvolution analysis (the results of which follow) was to accurately determine this M1 fraction, and σ_{M1}, at E=0. Figure 5.15 shows graphically the E1 and M1 cross sections (σ_{E1} and σ_{M1}) as given in Table 5.10. The solid and dashed curves in Figure 5.15 are to guide the eye. The very sharp energy dependence of the E1 cross section is clearly displayed in this graph.

Amplitudes and rel. phase from TME analysis

	15 keV	25 keV	35 keV	45 keV	55 keV	65 keV	75 keV
ν	6	6	7	7	7	7	7
χ^2/ν	0.27	0.55	2.21	2.19	2.94	1.47	1.77
P	.196±.010	.445±.010	.700±.010	.947±.010	1.14±.01	1.32±.01	1.44±.01
S	.182±.010	.325±.010	.440±.011	.499±.012	.584±.013	.602±.013	.632±.014
Δ	12.7±5.2	14.5±2.7	11.7±1.9	9.7±1.6	10.0±1.4	10.7±1.33	12.7±1.29
% M1	46.5±3.6	34.7±1.6	28.3±1.1	21.7±0.8	20.8±0.7	17.2±0.6	16.2±0.5

Table 5.9: Some of the results from the TME analysis on the D($\vec{p}$,γ)^{3}He binned data. The energies shown are center-of-bin energies in the lab frame. The P and S amplitudes are in $\sqrt{nb}$. The Δ phase difference is in degrees. The M1 fraction is expressed as a percentage. No systematic errors are included in the error bars.

σ_{E1} and σ_{M1} from TME analysis

	15 keV	25 keV	35 keV	45 keV	55 keV	65 keV	75 keV
σ_T (nb)	5.39 ± 0.30	22.9 ± 0.6	51.5 ± 0.9	86.3 ± 1.2	123.5 ± 1.5	159.6 ± 1.6	186.0 ± 1.9
σ_{E1} (nb)	2.88 ± 0.27	14.9 ± 0.8	36.9 ± 1.6	67.6 ± 2.6	97.8 ± 3.5	132 1 ± 4.8	155.9 ± 5.0
σ_{M1} (nb)	2.51 ± 0.24	7.94 ± 0.42	14.6 ± 0.6	18.7± 0.7	25.7 ± 0.9	27.5 ± 1.0	30.1 ± 1.0

Table 5.10: The σ_T, σ_{E1}, and σ_{M1} values from the TME analysis on the D($\vec{p}$,γ)^{3}He binned data. The error bars are statistical only.

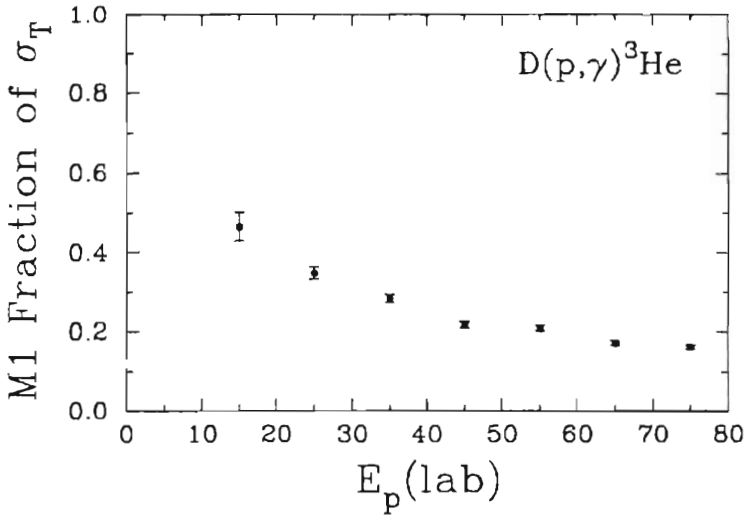

Figure 5.14: The M1 fraction of σ_T vs. beam energy as extracted from the TME analysis on the binned data (Table 5.9).

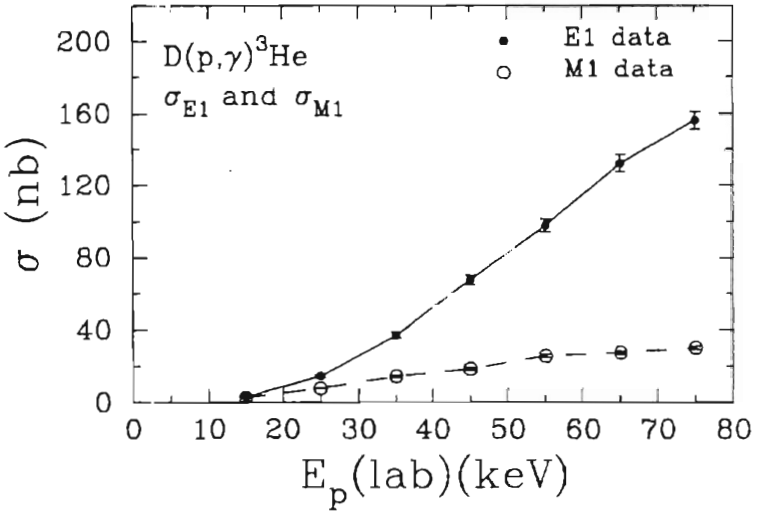

Figure 5.15: The σ_{E1} and σ_{M1} data as extracted from the TME analysis on the binned data (Table 5.10). The solid and dashed curves through the data points are to guide the eye.

5.5 Deconvolution Results

Each accumulated $D(\vec{p},\gamma)^3He$ γ-ray spectrum acquired, of which there were 35 in total, was deconvoluted separately. The significant results of this process are the $S_0(\theta)$ and $S_1(\theta)$ parameters which can be used to calculate the differential S-factor at all energies: $S(\theta,E_{cm})=S_0(\theta)+S_1(\theta)E_{cm}$. The final results for these parameters (a weighted average of all measurements made at each angle) are shown in Table 5.11. The absence of any deconvolution results for the $\theta_{lab}=0^\circ$ data is due to the fact that not enough data was acquired at 0° to allow a reliable deconvolution. The spectral shape was simply not well enough determined. Table 5.12 shows the results for $A_y(\theta,0)$ (i.e. the analyzing power at E=0) extracted from the deconvolution fits to the polarized $D(\vec{p},\gamma)^3He$ data.

Extracted $S_0(\theta)$ and $S_1(\theta)$ parameters

	$S_0(\theta)$ (eVb)	$S_1(\theta)$ (eVb/keV)
$\theta_{lab}=31^\circ$	0.0082 ± 0.0004	$1.48 \times 10^{-4} \pm 0.18 \times 10^{-4}$
$\theta_{lab}=60^\circ$	0.0119 ± 0.0003	$3.93 \times 10^{-4} \pm 0.26 \times 10^{-4}$
$\theta_{lab}=91^\circ$	0.0137 ± 0.0006	$5.62 \times 10^{-4} \pm 0.37 \times 10^{-4}$
$\theta_{lab}=105^\circ$	0.0143 ± 0.0015	$4.86 \times 10^{-4} \pm 1.0 \times 10^{-4}$
$\theta_{lab}=120^\circ$	0.0106 ± 0.0008	$4.66 \times 10^{-4} \pm 0.55 \times 10^{-4}$

Table 5.11: The extracted $S_0(\theta)$ and $S_1(\theta)$ parameters, for the $D(\vec{p},\gamma)^3He$ deconvolution analysis, which are needed to calculate the CM S-factor: $S(\theta,E_{cm})=S_0(\theta)+S_1(\theta)E_{cm}$.

Extracted A_y at E=0

	$\theta_{lab}=30^\circ$	$\theta_{lab}=60^\circ$	$\theta_{lab}=90^\circ$	$\theta_{lab}=120^\circ$
$A_y(\theta)$	0.254 ± 0.056	0.355 ± 0.096	0.174 ± 0.061	0.181 ± 0.199

Table 5.12: The vector analyzing power at E=0 as extracted from the $D(\vec{p},\gamma)^3He$ deconvolution analysis.

By using Tables 5.11 and 5.12, the differential S-factor and analyzing power can be plotted at E=0. The total S-factor at E=0, S(0), can be extracted by integrating $S(\theta,0)$ over all angles:

$$S(0) = \int S(\theta,0)d\Omega \qquad (5.24)$$

This integration is easily carried out by first fitting the data to a Legendre polynomial series: $S(\theta,0) = A_0' \sum_{k=0} Q_k a_k' P_k(\cos\theta)$. The total S(0) value is then: $S(0)=4\pi A_0'$. Extracting the E1 and M1 components can be accomplished by TME fitting the same S(0) data. Figure 5.16 shows the S(0) data along with a TME fit (solid line) and a Legendre fit (dashed line). Again, the error bars shown are statistical only. The results of the TME and Legendre fits are shown in Tables 5.13, 5.14, and 5.15.

Legendre Coefficients at E=0

A_0' (eV b)	a_1'	a_2'	b_1'	b_2'
0.0108 ± 0.0004	0.093 ± 0.077	-.537 ± 0.081	0.251 ± 0.067	0.061 ± 0.040

Table 5.13: The Legendre coefficients extracted from the fit to the data in Figure 5.16. The A_0' value shown indicates an S(0) value of 0.136 ± 0.005 eV b. The coefficients in this table include statistical error and errors from the deconvolution procedure.

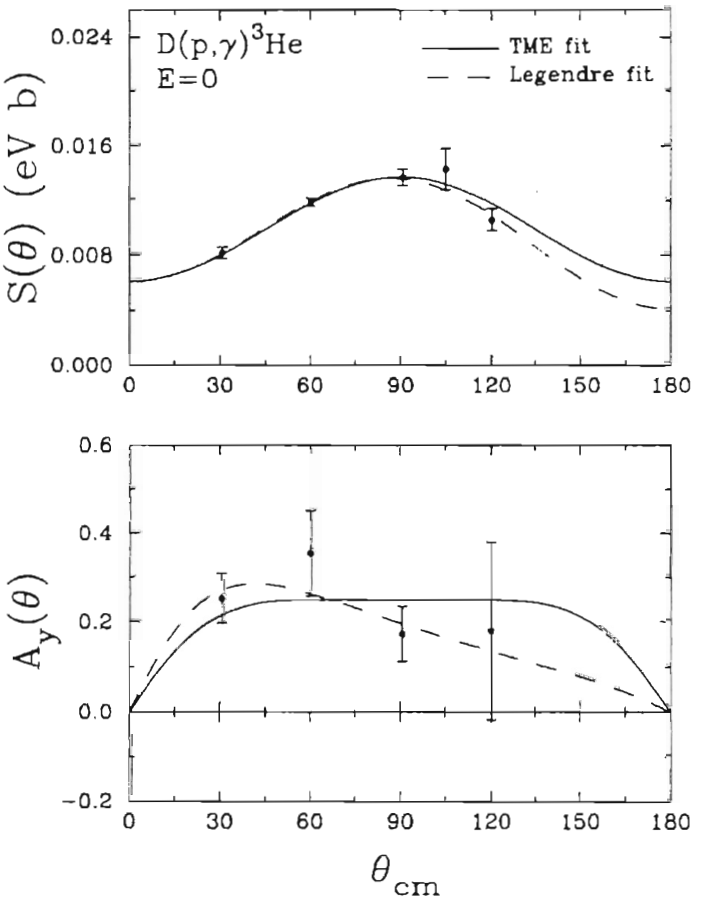

Figure 5.16: The deconvolution results for E=0 shown along with a TME fit (solid line) and a Legendre fit (dashed line). The TME fit used the matrix elements of Table 5.1 along with the equal amplitude and phase assumption.

TME fit at E=0

ν	χ^2/ν	P	S	Δ	% M1
6	1.04	.0293 ± .0016	.0317 ± .0015	21.7 ± 3.6	53.8 ± 3.9

Table 5.14: The results from the TME fit to the data in Figure 5.16. P and S are given in $\sqrt{\text{eV}\cdot\text{b}}$, Δ is in degrees, and the M1 fraction is written as a percentage.

E1 S(0) and M1 S(0) from TME fit

Total S(0) in eV b	M1 S(0) in eV b	E1 S(0) in eV b
0.141 ± 0.008	0.076 ± 0.007	0.065 ± 0.006

Table 5.15: The results for E1 S(0) and M1 S(0) from the TME analysis to the data shown in Figure 5.16. The errors shown include statistical errors and errors from the deconvolution procedure, but do not include systematic error.

If we include the known 9% overall systematic error, the following experimental result for M1 S(0) is obtained:

$$\text{M1 S(0)} = 0.076 \pm 0.010 \text{ eV b.} \tag{5.25}$$

This result can be compared directly to theoretical calculations which have been done [Fri91] (see Chapter 6). It should be emphasized that the experimental result shown in Equation 5.25 is dependent upon the equal amplitude and phase assumption used in the TME analysis. However, based on our results plotted in Figures 5.6-5.12, and the result plotted in Figure 5.16, the equal amplitude and phase assumption seems very reasonable. For example, by applying confidence limit tables for the χ^2 distribution [Bev69] to the TME results of the binning analysis (Table 5.9), it can be seen that all the TME fits lie within two standard deviations of the center of the χ^2 distribution. In fact, two of the fits in Table 5.9 lie within 1 standard deviation of the center. Our confidence in applying the equal amplitude and phase assumption at E=0 comes from the fact that the TME fit in Figure 5.16 (described in Table 5.14) lies well within one standard deviation of the center of the χ^2 distribution. In more quantitative terms, the $\nu = 6$ and $\chi^2/\nu = 1.04$ parameters

(regarding the TME fit in Figure 5.16) indicate that 40% of the time one would expect a *worse* fit than the one which we have obtained.

Besides the M1 S(0) value, another deconvolution result that is of interest is the total S-factor as a function of energy. This can be obtained by integrating $S(\theta,E_{cm})=S_0(\theta)+S_1(\theta)E_{cm}$ over all angles:

$$S(E_{cm}) = \int S_0(\theta)d\Omega + E_{cm}\int S_1(\theta)d\Omega = S_0' + E_{cm}S_1' \qquad (5.26)$$

In Equation 5.26, the integrations can simply be done by Legendre fitting the $S(\theta,E_{cm})$ data (the Legendre fitting procedure has no constraints). Of course, the first integration has already been done, and thus we know that $S_0'=S(0)=0.136 \pm 0.005$ eV b. The second integration is done by Legendre fitting the $S_1(\theta)$ data in Table 5.11. The result is: $S_1'=0.0050 \pm 0.0004$ eV b/keV. Therefore, the result for the angle integrated S-factor is:

$$S(E_{cm}) = 0.136 + (0.0050)E_{cm}, \qquad (5.27)$$

with errors as indicated above. This relation, from the deconvolution analysis, is plotted in Figure 5.17 along with results derived from the binning analysis. While the solid line in Figure 5.17 is Equation 5.27, the data points are S-factor points which have been calculated from the σ_T values in Table 5.8 (i.e. from the results of the binning analysis). It can be seen from the Figure that the deconvolution results agree fairly well with the binning results over the range of the data points. The systematic error has been included on the binned data points in order to give a feeling for the total expected error on the determined S-factor.

Figure 5.18 shows the deconvolution results for $A_y(90°)$ as compared with the results from the binning analysis. A slow rising trend with decreasing beam energy would seem to be indicated for this observable (perhaps indicating the increasing importance of M1 as the energy is lowered). The fairly good agreement in Figure 5.16 between the binning and deconvolution results is, again, worth noting.

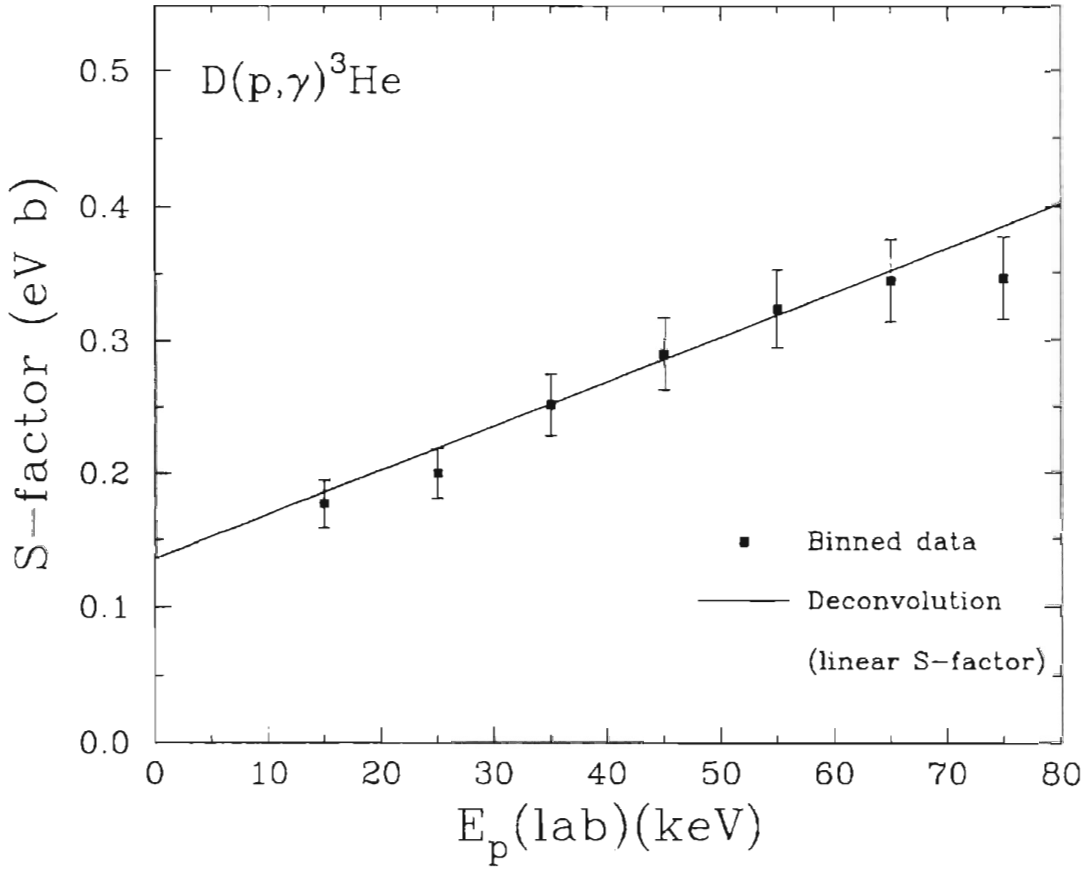

Figure 5.17: The deconvolution results (solid line) and binning results (data points) for the D($\vec{p}$,γ)^{3}He S-factor.

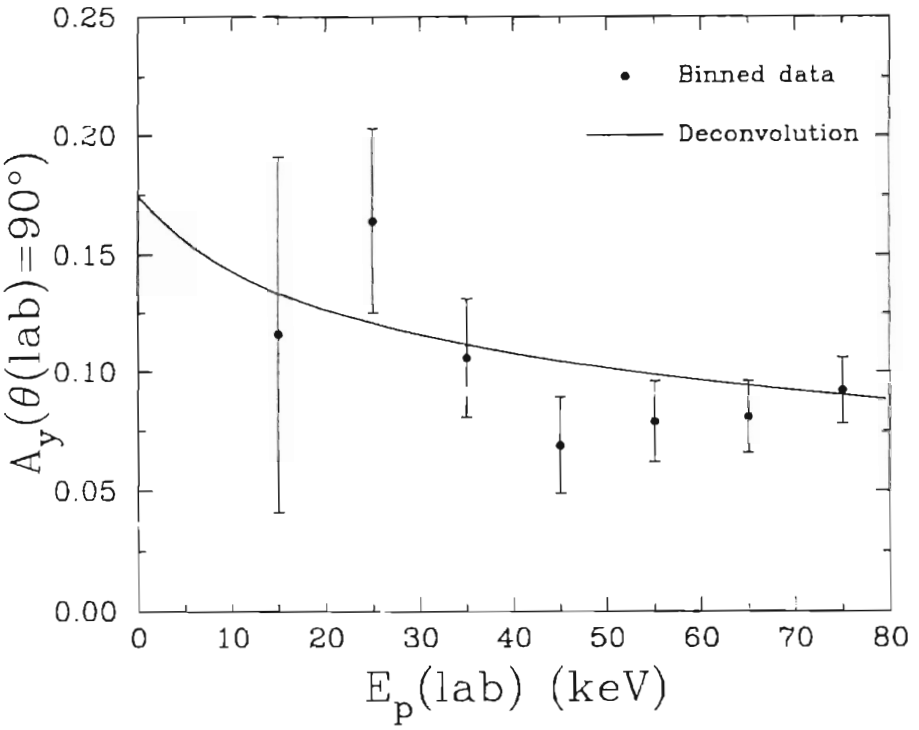

Figure 5.18: The vector analyzing power at 90° as a function of energy. Both the deconvolution results (solid line) and the binning results (data points) are shown.

5.6 Summary of Current Experimental Results

The primary experimental results of this $D(\vec{p},\gamma)^3He$ experiment can be summarized as follows:

1. The total S-factor at zero energy,S(0), has been extracted:

   $S(0) = 0.136 \pm 0.005 \pm 0.012$ eV b. The two errors specified are the statistical and 9% systematic errors respectively. These errors are added in quadrature to produce the total error.

2. The E1 S(0) and M1 S(0) components have also been determined:

M1 $S(0) = 0.076 \pm 0.007 \pm 0.007$ eV b

E1 $S(0) = 0.065 \pm 0.006 \pm 0.006$ eV b

3. The E1 and M1 cross section components have also been determined over the energy range E_p(lab)=15-75 keV as shown in Figure 5.15 and Table 5.10.
4. The total S-factor as a function of energy (over the region E_p(lab)=80-0 keV, or equivalently, E_{cm}=53.3-0 keV) has been determined:

   $S(E_{cm}) = 0.136 + (0.0050)E_{cm}$ eV b, where the total error, including the systematic component, is: $\Delta S(E_{cm}) = \sqrt{1.75\times10^{-4} + 3.63\times10^{-7} E_{cm}^2}$.

In Chapter 6, which follows, the results presented in this chapter will be compared to theoretical calculations in order to gauge the validity of various nuclear reaction models. In particular, the question to be addressed is this: can current three-body calculations accurately describe our $D(\vec{p},\gamma)^3He$ results?

5.7 Comparison to Previous Experimental Results

In the very low energy region, E_p(lab)<50 keV, only one previous experimental study of $D(p,\gamma)^3He$ has been made. This was by Griffiths et al. [Gri63], who measured cross sections (and, equivalently, S-factors) from E_p(lab)=24-48 keV. Figure 5.19 shows the current $D(p,\gamma)^3He$ binned S-factor data (solid points) along with the data of [Gri63] (open points). Both sets of data points include systematic error. The solid line in Figure 5.19, as in Figure 5.17, is the current deconvolution result for the total S-factor. The dashed line is the theoretical energy dependence assumed by [Gri63] normalized to their data. This assumed energy dependence of [Gri63], which was also used to deconvolute their data, is derived from a direct capture calculation they did for the

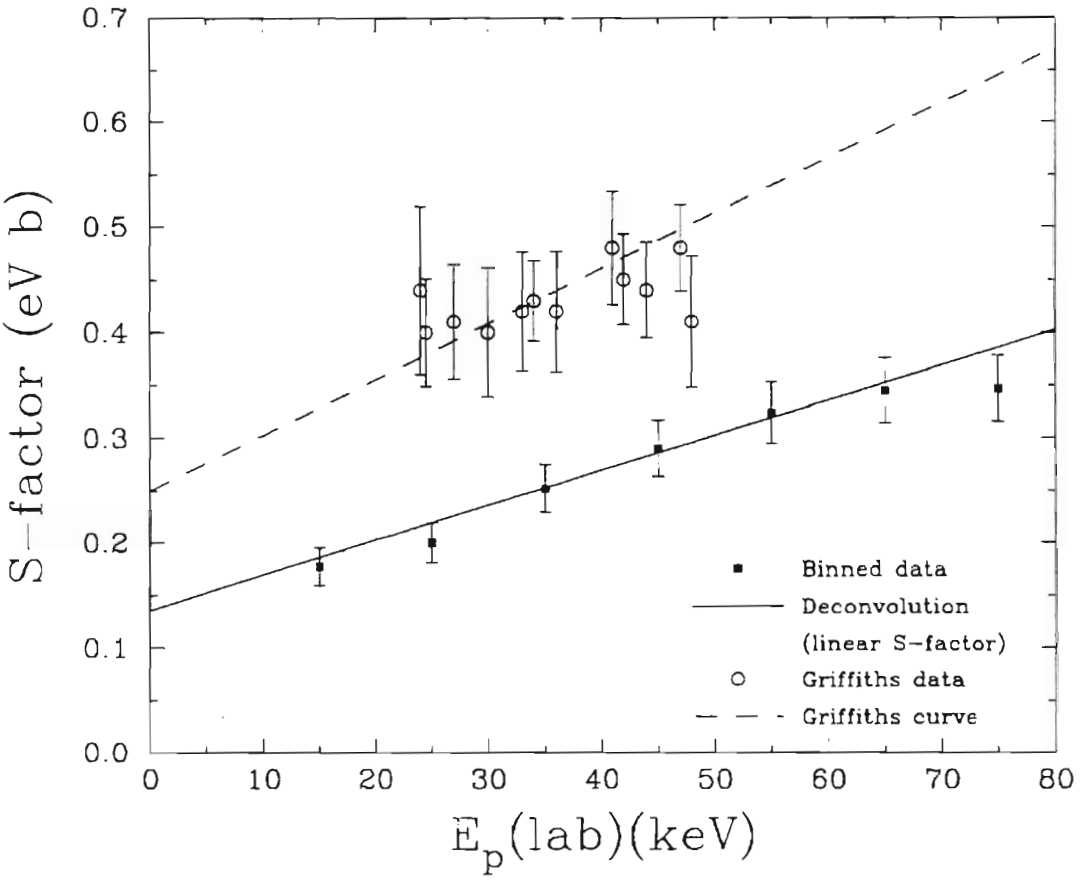

Figure 5.19: The current D(p,γ)^{3}He results (solid points and solid line) shown along with the data of [Gri63] (open points and dashed line).

D(p,γ)^{3}He reaction. The result of this direct capture calculation was a linear S-factor shape which was then normalized to their data by an overall multiplicative constant.

It is apparent from Figure 5.19 that the current D(p,γ)^{3}He S-factor results are approximately 40-45% lower than the results of [Gri63] throughout the energy region. Furthermore, it is also apparent that the energy dependence of the S-factor that we have empirically determined differs, somewhat, from the assumed theoretical energy dependence of [Gri63]. In order to gauge this effect quantitatively, let's consider the exact result of [Gri63] for $S(E_{cm})$:

$$S(E_{cm}) = 0.25 + (0.0079)E_{cm}\ \text{eV b}, \qquad (5.28)$$

where the error quoted for the constant term was ±0.04 eV b.

In obtaining the relationship shown in Equation 5.28, Griffiths et al. used an S_1/S_0 ratio that was entirely theoretical in nature. The total S-factor was then arrived at by using the form $S(E_{cm})=S_0(1+(S_1/S_0)E_{cm})$ to normalize to their [Gri63] data. The theoretical S_1/S_0 ratio of [Gri63] was 0.0316 keV^{-1}. The current S_1/S_0 ratio (extracted from our present data) is 0.0368 ± 0.0033 keV^{-1} (statistical error only). This would seem to indicate that the theoretical energy dependence used by [Gri63] is not adequate. We will explore this issue further in Chapter 6. If we use the theoretical S_1/S_0 ratio of [Gri63] and normalize the resulting S-factor expression to our S(0) result (effectively, we multiply Equation 5.28 by a factor of 0.544), we obtain:

$$S(E_{cm}) = 0.136 + (0.0043)E_{cm}\ \text{eV b}, \qquad (5.29)$$

where the difference in slope (0.0043 eVb/keV as compared with the current result of 0.0050 eVb/keV) is again apparent.

Another result of the [Gri63] experiment was to decompose the total S-factor into E1 and M1 components. This can be compared, over the energy range E_p(lab)=80-0 keV, with the results of the current experiment. Figure 5.20 shows, along with the [Gri63] results, the current results for the E1 and M1 S-factors (as derived from the E1 and M1 cross sections shown in Table 5.10). The current E1 and M1 S-factors extracted at E=0 (by means of the deconvolution analysis) are also included. The results of [Gri63] in Figure 5.20 have again been multiplied by the normalizing factor of 0.544. As shown

in Figure 5.20, although the energy dependence of the current data is close to the energy dependence assumed by [Gri63], it does not exactly match it.

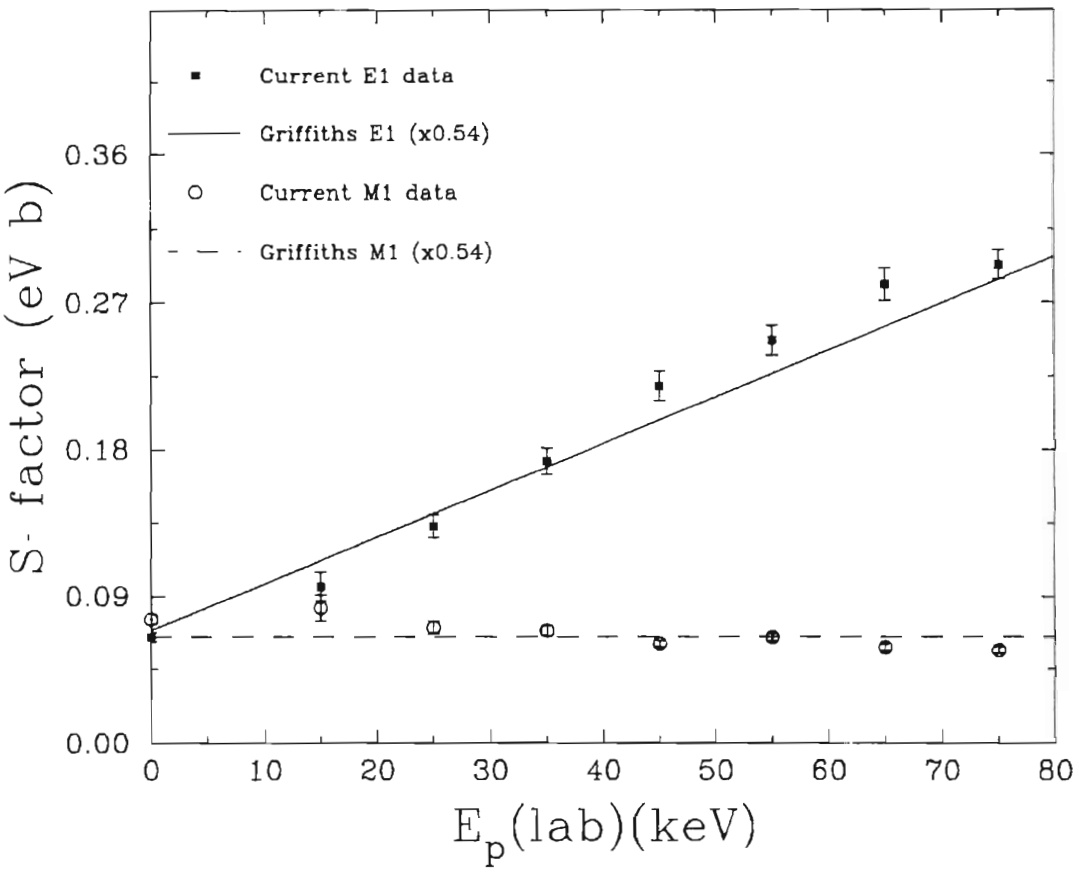

Figure 5.20: The extracted E1 and M1 $D(p,\gamma)^3He$ S-factors for both the current experiment (solid and open data points) and the experiment of [Gri63] (solid line and dashed line). The [Gri63] results have been multiplied by a normalizing factor of 0.544. The data points shown include only statistical error.

Given that both the absolute magnitude and energy dependence of the current results are different than the [Gri63] results, it is necessary to understand the discrepancy.

First of all, we will address the more difficult issue relating to the difference in absolute magnitude between the two data sets. Based on the [Gri63] paper, no obvious signs of experimental error exist. Possible sources of error that could lead to a mistake in the absolute $\sigma(E)$ and $S(E)$ determinations include: beam current integration error; error in detector efficiency measurement; and error in stopping cross section (STP(E)) values. Actually, as discussed in Chapter 3, the [Gri63] authors did make a mistake on the issue of STP(E) values. Since they used the STP(E) values for H_2O vapor instead of D_2O ice, we can expect that their absolute S-factor values will be artificially high by as much as 15%. Unfortunately, this does not completely account for the discrepancy with the current data, since another 35% lowering of the [Gri63] values is still needed. One other possible effect that could have caused the authors of [Gri63] to overestimate their yields is related to the severe target deterioration problem which they encountered (the effect of this deterioration was that their $D(p,\gamma)^3He$ yields fell rapidly with time). They attempted to correct for this problem by extrapolating yields back to "zero time". A slight overestimation of the "true" yield is certainly possible in this procedure, but it remains uncertain whether or not this could translate into such a large effect as would be necessary in order to account for the discrepancy.

On the issue of energy dependence, there is no question that the current measurement should be more accurate. Due to our high detector resolution, we actually observe the energy dependence in our spectra. By deconvoluting these spectra, we can obtain an accurate empirical value for S(E). On the other hand, the energy dependence of [Gri63] was entirely theoretical in nature. Clearly the current approach (made possible by the improvement in technology between 1963 and 1995) is the preferred one.

Also relating to the issues of energy dependence and absolute magnitude for the S-factor is the fact that the [Gri63] authors did not measure accurate angular distributions

for the cross section as we did. Instead, they assumed a certain shape based on rough measurements. Uncertainty in the angular distributions could certainly have caused uncertainty in their extracted total cross sections and S-factors. Also, due to the fact that the angular distribution helps determine the E1/M1 ratio, it is certainly possible that a poor knowledge of the angular distribution could affect the extrapolated energy dependence. However, as we have shown, their assumption of $\sigma(\theta)\sim(\sin^2\theta$ + constant) has been shown to be a fairly accurate representation of the angular distribution. This assumption of [Gri63] is exactly equivalent to our assumption of equal amplitudes and phases for the E1 terms (in our TME fitting procedure). With this in mind, we conclude that a poor knowledge of the angular distribution is not the cause of the discrepancy.

In order to determine which data set is right, it is worthwhile to extrapolate the extracted energy dependencies to slightly higher energies, and to gauge the agreement with previously acquired data. The data set of [Bai70] extends from E_p(lab)~57 keV-1.1 MeV. However, due to the fact that the bin widths in this "thin target" experiment were quite large (and thus the exact "center-of-bin" beam energies measured were somewhat uncertain), a direct comparison with the current results, or the results of [Gri63], is difficult. Rather, we look to a higher energy "thin target" result at E_{cm}=183.3 keV, which is that of [Gri62]. The S-factor extracted here was S(183.3)=1.18±0.13 eVb. This value has recently been confirmed by Lijun Ma et. al. [Ma95]. Our S-factor curve, when evaluated at E_{cm}=183.3 keV, gives: S(183.3)=1.05±0.11 eVb, which agrees within error bars with the measured data point of [Gri62]. The S-factor curve of [Gri63] gives S(183.3)=1.70 ± 0.04 eVb, far overestimating the measured data point. While this result cannot be used to disprove the measurements of [Gri63], it can be used to give some degree of confidence in the current results. This is based on the fact that for

energies well below the Coulomb barrier, a mechanism for rapid change in the energy dependence is not readily apparent (assuming the absence of resonant structure).

Chapter 6

Theory

An experimental study of the $D(p,\gamma)^3He$ reaction at low energies offers an excellent opportunity to test our current understanding of the nuclear three-body problem. In particular, as discussed in Chapter 1, the following aspects of three-body nuclear physics are of current interest to theorists:

1. Two-body nucleon-nucleon (NN) potentials in the three-body system: It has long been wondered just how accurately one can describe the three-body system by using only two-body NN potential models. In order to solve certain problems, three-body forces are sometimes included.

2. The Coulomb interaction: The handling of the Coulomb interaction for three bodies is of sufficient difficulty that until this year (1995), only calculations at E=0 had been done. The three body nature of the Coulomb interaction for $D(p,\gamma)^3He$ can be seen by realizing that the Coulomb field of the proton in the scattering state will charge polarize the deuteron, and thus distort its shape.

3. Meson Exchange Currents (MEC's): The nuclear force is thought to be transmitted by virtual meson exchange. In radiative capture reactions, this exchange current can interact with the electromagnetic field of the γ-ray, and thus create noticeable effects on the reaction cross section. An exact treatment of MEC's is thus necessary in order to describe $D(p,\gamma)^3He$. The opportunity to learn more about MEC's is of particular interest in the current experiment.

In what follows, we will present some very recent three-body calculations that have been done for $D(p,\gamma)^3He$. These calculations, done by theoretical groups at Los Alamos and CEBAF, have sought to take into account all of the three-body aspects mentioned above. The primary question to be addressed, then, is simply this: how well do these modern calculations describe our currently acquired $D(p,\gamma)^3He$ data (which are the most accurate $D(p,\gamma)^3He$ data to date in the very low energy region)? In the process of answering this question, we will seek to learn more about the validity of the current theoretical three-body approach.

However, before we look at the $D(p,\gamma)^3He$ reaction from an exact three-body point of view, it is worthwhile to first look at it from the point of view of an effective two-body model. One might think that because the current energy regime of interest ($E_p(lab) \leq 80$ keV) is well below the deuteron breakup threshold of 2.2 MeV, a two body model of the radiative capture process might be valid. One such model, which treats the deuteron as a point particle (both in the continuum and in the bound states), is known as the direct capture model. By performing a direct capture calculation for $D(p,\gamma)^3He$, and then comparing the results to our experimental data, we will see that although this simple model does an adequate job in some respects, it is deficient in others. The shortcomings of the direct capture model will provide us with the motivation we need in order to pursue the framework of an exact three-body calculation.

6.1 The Direct Capture Model

6.1.1 Introduction

The direct capture model is a two body model used to describe non-resonant radiative capture reactions. Both the projectile and the target nucleus are assumed to be point particles with no internal structure. By means of an electromagnetic interaction, the projectile is assumed to undergo a transition from an initial continuum state (represented by a distorted plane wave) to a final single particle bound state (a standing wave). A photon is emitted in the process. The timescale for this transition is on the order of the nuclear transit time (~10^{-22} seconds), and hence the name "direct" capture.

In describing the direct capture process, the extreme single particle picture is often used. In this picture, the target nucleus is assumed to be a spectator, and does not participate in the interaction. The angular momentum coupling scheme used to describe this process can be outlined as follows: in the initial state, where there is no interaction between the projectile and target nucleus, the spin of the projectile, $\vec{s}_p$, couples with the relative orbital angular momentum, $\vec{l}$, to form a total single particle angular momentum, $\vec{j}$. Because the projectile and target are assumed to be non-interacting, there is no coupling between $\vec{j}$ and the spin of the target, $\vec{s}_t$. In the final state, the spin of the projectile couples with the bound state orbital angular momentum, $\vec{l}\,'$, to form a single particle angular momentum, $\vec{j}'$. This single particle angular momentum then couples with the target spin, $\vec{s}_t$, to form a well defined state of total angular momentum J' (i.e. the so called "residual nucleus", which, for the current experiment, is ^{3}He).

A good discussion of the direct capture formalism can be found in [Chr61,Bai67,Rol73,Laf82]. The first three of these references actually use the channel

spin coupling scheme (described in Chapter 5) instead of the j-j coupling scheme used here. The basic equations used to describe the direct capture process are the same for both schemes. The only difference lies in the treatment of the angular momentum part of the problem. The current discussion follows closely the presentation given in [Laf82].

The Hamiltonian (H) for the direct capture process can be written as follows:

$$H = H^0 + H', \tag{6.1}$$

where H' is the Hamiltonian associated with the interaction of the projectile with the electromagnetic field of the γ-ray, and H^0 is the Hamiltonian associated with the kinetic and potential energies of the particle along with the energy of the free electromagnetic field. Since H^0 involves nuclear interactions associated with the strong force coupling constant ($\approx$1) while H' involves electromagnetic interactions associated with the electromagnetic coupling constant ($\approx$1/137), it is clear that the electromagnetic transition rate may be calculated by means of perturbation theory. Using first order time dependent perturbation theory, it is possible to derive the well known Fermi's Golden Rule:

$$W_{fi} = \frac{2\pi}{\hbar}|T_{fi}|^2 \rho_f \ , \tag{6.2}$$

where the unreduced matrix element T is defined as:

$$T_{fi} = \langle \Psi_f | H' | \Psi_i \rangle. \tag{6.3}$$

In Equation 6.2, W_{fi} is the transition rate between the initial and final states, which have wavefunctions Ψ_i and Ψ_f respectively, and ρ_f is the density of final states. The differential cross section for this process is simply defined as:

$$\frac{d\sigma_{if}}{d\Omega} = \frac{W_{fi}}{\Phi_i} , \tag{6.4}$$

where Φ_i is the flux of incident particles. The incident flux is defined as $\Phi_i=n_iv_i$, where n_i is the particle density of the incident beam and v_i is the velocity of the incident particles with respect to the target nucleus. If we take the arbitrary normalization volume in this calculation (used to calculate ρ_f and Φ_i) to be 1, we then obtain: $\Phi_i=v_i$. By averaging Equation 6.4 over the initial spin projections (those of $\vec{s}_p$ and $\vec{s}_t$, where s_p and s_t are the spins of the incident and target particles respectively), summing over the final spin projections (those of $\vec{J}'$, where J' is the spin of the residual nucleus), and summing over the circular polarization states of the photon (C), we can then obtain the total direct capture differential cross section:

$$\frac{d\sigma}{d\Omega} = \frac{2\pi}{\hbar v_i}\rho_f \frac{1}{(2s_p+1)(2s_t+1)} \sum_{\substack{m_p,m_t \\ m_{j'},C}} \left|\left\langle \Psi_f \left| H \right| \Psi_i \right\rangle\right|^2 , \tag{6.5}$$

where m_p, m_t and $m_{j'}$ are the magnetic substates of $\vec{s}_p$, $\vec{s}_t$ and $\vec{J}'$.

6.1.2 The Continuum Wavefunction

In order to evaluate the direct capture cross section given in Equation 6.5, we need forms for the initial (or continuum) wavefunction, Ψ_i, the final (or bound state)

wavefunction, Ψ_f, and the electromagnetic operator, H'. This subsection will focus on the continuum wavefunction. The continuum wavefunction is formed by the product of a nuclear wavefunction (describing the target nucleus) and a distorted plane wave describing the projectile. The form of the nuclear wavefunction is not important, since it will be the same in both the continuum and final states (i.e. there is assumed to be no interaction between the projectile and target). The distorted plane wave is generated by solving the Schrödinger equation for an empirically derived optical model potential. In particular, an optical model potential is defined to have the following form:

$$V(r) = -V_0 f(a_0,r_0,r) + i4a_d V_d \frac{d}{dr} f(a_d,r_d,r) + \left(\frac{h}{m_\pi c}\right)^2 V_{so} \frac{1}{r}\frac{d}{dr} f(a_{so},r_{so},r)\,\vec{L}\cdot\vec{S} \qquad (6.6)$$
$$+ V_c(r_c)\,,$$

where V_0 is the central potential strength, V_d the imaginary potential strength, V_{so} the spin orbit potential strength, and V_c the Coulomb potential for a uniformly charged sphere or radius r_c. The function f(a',r',r) is a Woods-Saxon form factor:

$$f(a',r',r) = \frac{1}{1+\exp\left(\frac{r - r' A^{1/3}}{a'}\right)}\,, \qquad (6.7)$$

where A is the mass of the target nucleus (in a.m.u). The purpose of the imaginary potential is to account for the absorptive processes in the $D(p,\gamma)^3He$ scattering (i.e. the inelastic strength). Since the current experiment was performed well below the deuteron breakup threshold, there are no significant inelastic channels available (only radiative capture), and thus we expect the imaginary potential to be negligibly small.

The V_0, V_d, V_{so}, r_0, a_0, r_d, a_d, r_{so}, a_{so}, and r_c parameters in Equation 6.7 are fixed by experimental studies of p-d scattering. In particular, the optical model parameters of Guss [Kin83], acquired for $^2H(n,n)^2H$ scattering at E_n=14 MeV, have been used. The spin-orbit parameters were acquired by measuring the analyzing power of this reaction. The Coulomb radius used in the current case is from [Dev72], who studied $^2H(p,p)^2H$ at higher energies. The Guss parameters were chosen for the current work in order to be consistent with $D(p,\gamma)^3He$ direct capture calculations by [Kin83] and [Vet85] (which were done at somewhat higher energies), and also for other reasons to be discussed later. Since the parameters were measured at much higher energies than the current work (no experimental scattering data exists at the very low energies of the current experiment), they were assigned an energy dependence based on global parameters for light ion scattering [Kin83]. The sensitivity of the calculation to the choice of optical model parameters will be discussed later.

Table 6.1 shows the parameter set of Guss that was used. It will be noted that the parameters shown predict a finite imaginary potential, V_d, at zero energy. This might seem somewhat unphysical based on the argument previously given. However, the potential shown is actually small enough such that it has almost a negligible effect on the calculation (setting V_d to zero changes the predicted cross section by only 2%). As it turns out, the Coulomb potential is by far the dominant term in Equation 6.6, the rest of the terms being only very small perturbations. For this reason, it is correct to refer to the continuum state wavefunction as a "Coulomb distorted" plane wave.

Optical Model Parameters

Parameter	Value
V_0 (MeV)	90.75 - 0.4871 E_p
r_0 (fm)	1.153
a_0 (fm)	0.454
V_d (MeV)	4.54 + 0.1E_p
r_d (fm)	1.104
a_d (fm)	0.691
V_{so} (MeV)	2.408 - 0.0331E_p
r_{so} (fm)	1.049
a_{so} (fm)	1.119

Table 6.1: Optical model parameters used to generate the scattering state wavefunctions for the current D(p,γ)^{3}He calculation. E_p is the proton beam energy, and was set to 80 keV in order to calculate the optical model parameters that were used.

6.1.3 The Bound State Wavefunction

Once the continuum state wavefunction has been calculated, the next step is to calculate the bound state wavefunction. The bound state wavefunction is formed by the product of a nuclear wavefunction (representing the target nucleus), a pure single particle wavefunction representing the bound projectile, and a quantity $\sqrt{S_{l',j'}}$, where $S_{l',j'}$ is the spectroscopic factor associated with the final state (i.e. the probability of finding the projectile in a pure single particle final state with orbital angular momentum l' and total single particle angular momentum j'). In the case of D(p,γ)^{3}He, we know that ^{3}He has a

spin and parity of $J^{\pi}=1/2^{+}$, where J' is the total angular momentum of the final state. In order to conserve parity and angular momentum in the j-j coupling scheme, we see that l' is restricted to be either 0 (an S-state) or 2 (a D-state), and that j' is restricted to be 1/2 or 3/2. Based on energy considerations, we might expect the S-state to be the dominant partial wave of the ground state wavefunction. This is, in fact, true. Studies have shown that the S-state comprises approximately 91% of the ^{3}He ground state wavefunction, with the D-state comprising the remaining 9% [Vet85]. With this in mind, the possible spectroscopic factors for the current direct capture calculation have been set as follows: $S_{0,1/2}=.91$, $S_{2,3/2}=.09$.

The pure single particle wavefunction for the bound state was calculated by simply solving the Schrödinger equation for a real Woods-Saxon potential which included Coulomb and spin-orbit terms. The radius (r), diffuseness (a), and well depth (V) parameters that were used were the same as in the continuum state (as shown in Table 6.1) with one notable exception: the real well depth (V_0) was searched upon until a value could be found which matched the p+d binding energy (5.5 MeV). In constructing the bound state wavefunction, the form of the wavefunction was constrained to have a node at zero and infinity. The radial part of the bound state wavefunction that was used is shown graphically in Figure 6.1.

6.1.4 The Electromagnetic Operator

The Hamiltonian, H', for the interaction of the proton-deuteron system with the electromagnetic field is given by:

$$H' = -\frac{1}{c}\int \vec{J}(\vec{r})\cdot\vec{A}(\vec{r})d\vec{r} \ , \qquad (6.8)$$

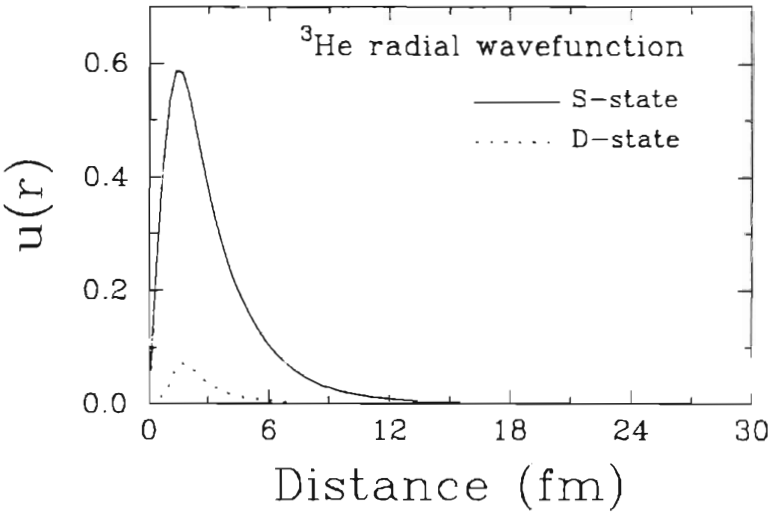

Figure 6.1: The two body radial wavefunction for ^{3}He that was used in the direct capture calculation. Both the S and D state wavefunctions are shown (the appropriate spectroscopic factor has been included, as discussed in the text).

where $\vec{J}$ is the nuclear current density, $\vec{A}$ is the vector potential in the radiation gauge, and $\vec{r}$ is the relative position vector of the two particles. This Hamiltonian can be expanded into multipoles. For the current analysis, we keep the electric dipole (E1) and magnetic dipole (M1) terms. Preliminary calculations done which included the E2 terms showed them to be completely insignificant. In particular, they were found to be about four orders of magnitude lower than the E1 terms for transitions to the S-state, and about 1 order of magnitude lower than the E1 terms for transitions to the D-state. In the current analysis, the calculation of the E1 terms was simplified by replacing the nuclear current density by the charge density (Siegert's theorem), while calculation of the M1 terms was simplified by neglecting the exchange currents. Furthermore, the relatively low energy of the photon (5.5 MeV) implies kr«1 (if we take r~1 fm), and thus the long wavelength

approximation is valid. With these simplifications, the radial part of the M1 operator is simply unity, while the radial part of the E1 operator is given by r.

6.1.5 Calculating the Observables

Knowing the initial and final state wavefunctions, and also the operator H', we are now ready to evaluate the matrix elements in Equation 6.5, and thus determine the direct capture cross section (and also the predicted vector analyzing power). The evaluation of the matrix elements, and the determination of the cross section, is carried out using the computer code HIKARI (Kin83). In particular, the integral of H' over the initial and final state wavefunctions proceeds as follows: the angular dependence of H' is extracted from the integral in the form of angular coupling coefficients and Legendre polynomials, and we are then left with a radial integral. This radial integral is evaluated numerically to produce the resulting matrix elements. The limits set for the radial integral were 0 to 100 fm. As can be seen from Figure 6.1, the bound state wavefunction will be completely negligible at the upper limit of this region (i.e. at 100 fm).

The matrix elements associated with transitions to the ^{3}He S-state and D-state are calculated separately (using the appropriate spectroscopic factors mentioned above). The results from these separate calculations can then be combined to give the actual observables. In order to do this, a set of Legendre polynomial coefficients is extracted from each set of matrix elements. These two sets of Legendre coefficients can then be used to calculate $\sigma(\theta)$ and $A_y(\theta)$ (see Equations 5.1 and 5.2) for the S-state and D-state transitions respectively. The total differential cross section can then be written as:

$$\sigma(\theta) = \sigma_S(\theta) + \sigma_D(\theta) = A_{0,S}\sum a_{k,S}P_k(\cos\theta) + A_{0,D}\sum a_{k,D}P_k(\cos\theta), \qquad (6.9)$$

where $\sigma_S(\theta)$ and $\sigma_D(\theta)$ are the S-state and D-state differential cross sections, and $A_{0,S}$, $a_{k,S}$, $A_{0,D}$, $a_{k,D}$ are the associated Legendre coefficients for transitions to the S-state and D-state respectively.

Equation 6.9 can be re-written in the form:

$$\sigma(\theta) = A_0' \sum a_k' P_k(\cos\theta), \tag{6.10}$$

where

$$A_0' = A_{0,S} + A_{0,D}, \tag{6.11}$$

and

$$a_k' = \frac{a_{k,S}A_{0,S} + a_{k,D}A_{0,D}}{A_{0,S} + A_{0,D}}. \tag{6.12}$$

By means of Equation 6.10, we see that the total a_k' coefficients are simply a weighted average of the a_k coefficients obtained from the S-state and D-state calculations respectively. A similar relation exists for the b_k coefficients. Using these relations, we are now in a position to calculate the predicted $\sigma(\theta)$ and $A_y(\theta)$ observables.

6.1.6 Direct Capture Results

The observables were calculated over the energy range E_p(lab)=15-75 keV so as to correspond with the range of the acquired binned data (see Chapter 5). As it turns out,

the only matrix elements of any significance over the entire calculated energy range were the p-wave E1 terms. At first glance, this may seem like a somewhat surprising result since we would expect that as we go very low in energy, the s-wave terms (i.e. the M1 strength) should become quite significant. However, by examining the details of the calculation, the reason for the null M1 strength becomes apparent. Since the radial part of the M1 operator is unity, the evaluation of the M1 matrix element is reduced to calculating an overlap between the initial and final state radial wavefunctions. Since the potentials used to determine the continuum and final state wavefunctions were practically identical, we would expect that the radial wavefunctions for continuum and final states of similar l and j should be orthogonal, thus making the overlap vanish. This would make the M1 s-wave to S-state transition zero, and thus greatly "quench" the M1 strength. As is turns out, HIKARI predicts a negligible strength for all the other M1 transitions as well (including M1 transitions to the ^{3}He D-state).

However, it is well known, from rigorous three-body calculations (to be discussed), that significant M1 strength does in fact exist in the D(p,γ)^{3}He reaction at low energies. In the next sub-section, the prediction of zero M1 strength by HIKARI will be used to demonstrate a serious shortcoming of the two-body direct capture model. However, for the time being, let us examine the HIKARI results for the E1 capture. Table 6.2 shows the total calculated E1 cross section for capture to the S-state and to the D-state respectively. The total E1 cross section, σ(E1), is then: $\sigma(E1)=\sigma_S(E1)+\sigma_D(E1)$. It should be stressed that no arbitrary normalization was added to these calculations, and the values shown in Table 6.2 represent absolute predictions (in nanobarns) for the E1 cross section for D(p,γ)^{3}He.

Direct Capture Calculation

E_p(lab)	σ(E1) to S-state	σ(E1) to D-state	σ(E1) total
15 keV	3.89 nb	0.004 nb	3.9 nb
25 keV	18.2 nb	0.17 nb	18.4 nb
35 keV	41.3 nb	0.39 nb	41.7 nb
45 keV	70.4 nb	0.66 nb	71.1 nb
55 keV	103.7 nb	0.97 nb	105 nb
65 keV	139.2 nb	1.31 nb	141 nb
75 keV	176.5 nb	1.65 nb	178 nb

Table 6.2: Direct capture calculation for the $D(p,\gamma)^3He$ E1 cross section using the HIKARI computer code. All allowed E1 transitions were included (see Figure 5.1). The total cross section was calculated as follows: $\sigma(E1) = \sigma_S(E1) + \sigma_D(E1)$.

Figure 6.2 shows (by the solid line) the total σ(E1) values from Table 6.2 plotted versus beam energy. Also plotted on Figure 6.2 are the σ_{E1} results extracted from the current $D(p,\gamma)^3He$ data (Table 5.10 in Chapter 5). Clearly, the agreement between theory and data is remarkably good. This success of the direct capture model in describing the E1 cross section can be understood in terms of the extranuclear nature of the radiative capture process at low energies. At the very low bombarding energies of the current experiment, the transition matrix elements will be most sensitive to that part of the ^3He wavefunction which lies outside the boundaries of the nucleus. Because of this, the calculated observables should not depend on the details of the bound state wavefunction for small r (i.e. less than a few fm), and thus the inadequacies of using a simple model are not revealed. In addition to the good description of the absolute magnitude of the E1

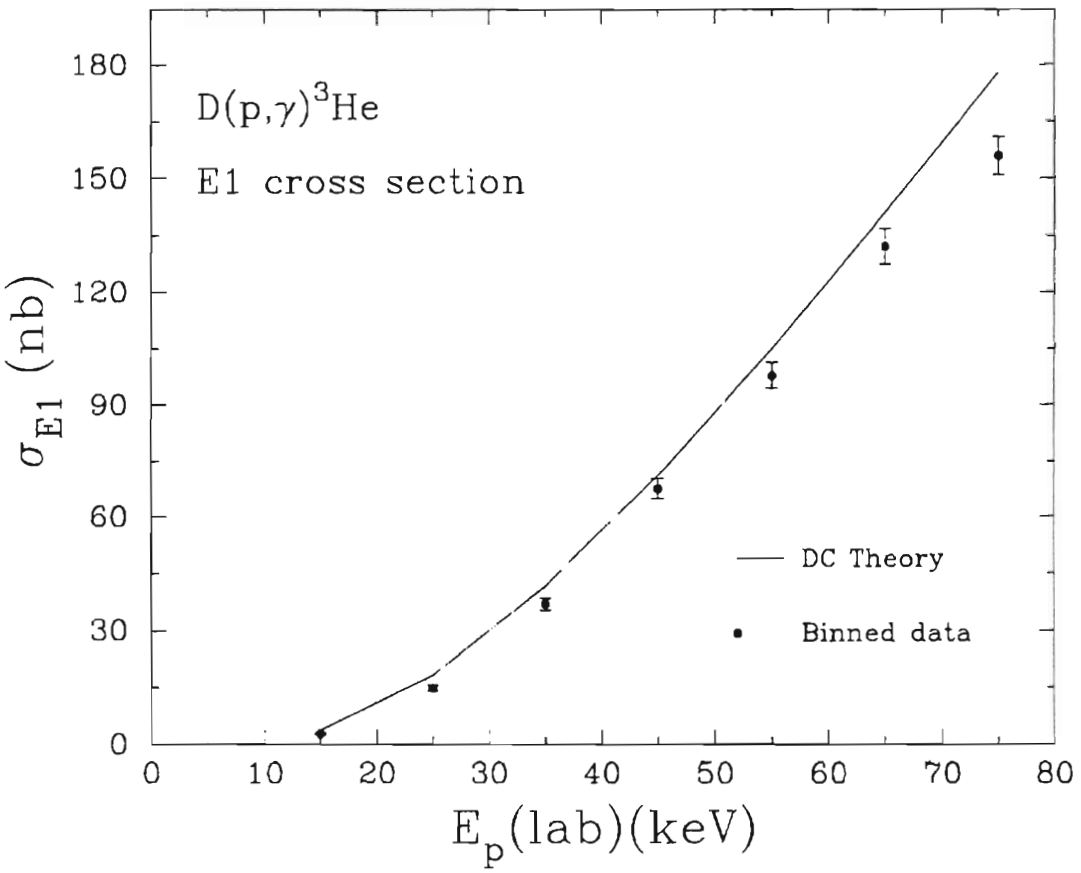

Figure 6.2: The results of the direct capture (DC) calculation for the $D(p,\gamma)^3He$ E1 cross section, shown along with the acquired data from Table 5.10. The error bars do not include the 9% systematic error. No arbitrary normalization is applied to the theory.

cross section, HIKARI correctly predicts the shape of the E1 angular distribution as well: $\sigma(\theta)\sim\sin^2\theta$. This shape is consistent with what was seen in the experimentally derived angular distributions (Chapter 5), where the data was fit very well by assuming a $\sin^2\theta$ E1 part and a constant M1 part (the TME analysis). The predicted shape arises from the fact that the E1 amplitudes and phases are assumed to be equal.

Upon examining the good agreement between theory and data in Figure 6.2, it is natural to wonder just how dependent this calculation is upon the optical model

parameters that were used. In order to test this sensitivity, the optical model parameters of Guss (the ones used in Figure 6.2) were replaced by the optical model parameters of DeVries [Dev72], who studied $^2H(p,p)^2H$ from 17-46.3 MeV. The calculation done with this set of parameters yielded an E1 cross-section which was about 20% lower than the curve shown in Figure 6.2. However, some possible problems with using the [Dev72] parameters in the current experiment should be pointed out. First of all, the [Dev72] data was acquired at higher energies than the Guss data, and thus was further away in energy from the region of current interest. Secondly, the energy dependence of the [Dev72] parameters was based on data from 17-46.3 MeV, while the Guss energy dependence came from global values. For these reasons, the more recent data of Guss should perhaps be considered preferable for use in a low energy direct capture calculation. The good agreement between the resulting calculation and the current data confirms these suspicions.

However, even though the E1 cross section is described quite well by the present calculation, the description of the other observables fares somewhat worse. Since the predicted M1 cross section is zero, the predicted total cross section is significantly less than the corresponding total cross section data points. This is shown in Figure 6.3, where the predicted total cross section (solid line) is plotted along with the measured total cross section (the binned data results from Table 5.7). It is also noted from Figure 6.3 that the energy dependence predicted by the direct capture model is also somewhat incorrect. This is in accordance with the results of the [Gri63] direct capture calculation discussed in section 5.7.

As was previously mentioned, the shape of the angular distribution is quite well represented, but clearly, based on Figure 6.3, we would expect that the calculated values of the $\sigma(\theta)$ will be too low. Figure 6.4 shows the predicted $\sigma(\theta)$ at E_p(lab)=75 keV

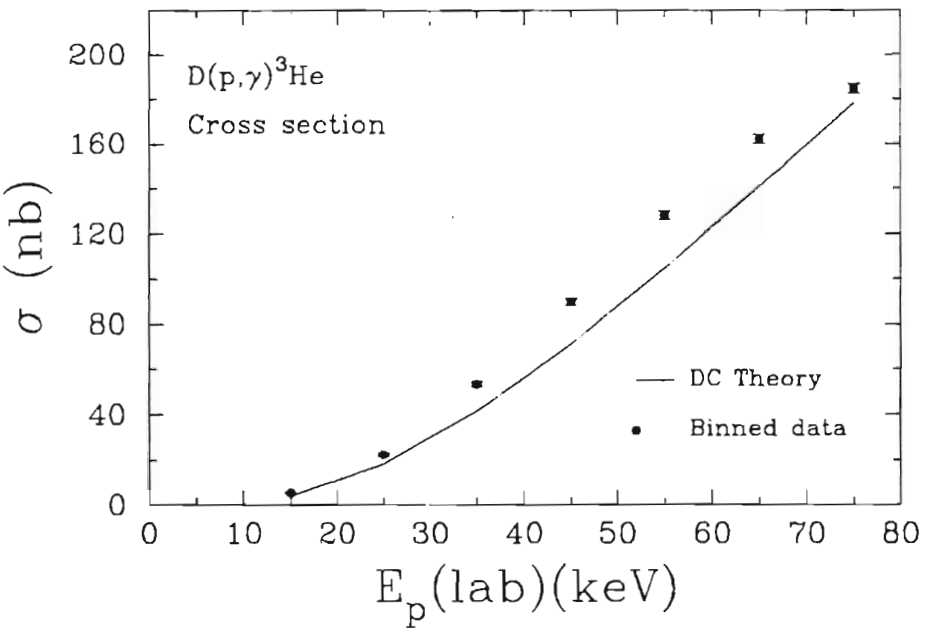

Figure 6.3: The direct capture (DC) results for the $D(p,\gamma)^3He$ total cross section are plotted along with the experimental binned data points from Table 5.8 (from the Legendre polynomial analysis of the raw data). The experimental systematic error is not shown.

(solid line) shown along with the raw binned data from Table 5.5. While the agreement at central angles is actually remarkably good, the discrepancies at lower angles shows that the isotropic component of the cross section is not well represented.

Furthermore, the fact that the M1 component is zero will make the predicted analyzing power practically zero. By examining the expressions in Equation 5.20, it is clear that the B_1 coefficient will be zero when M1 is zero, and therefore the only way to get a finite analyzing power is to have a phase splitting between the two E1 terms (a finite B_2 coefficient). This can arise, to a small extent, from the spin-orbit potential that was included in the calculation. Figure 6.5 shows the predicted $A_y(\theta)$ at $E_p(lab)$=75 keV shown along with the raw binned results from Table 5.6. Clearly, the agreement here is quite bad.

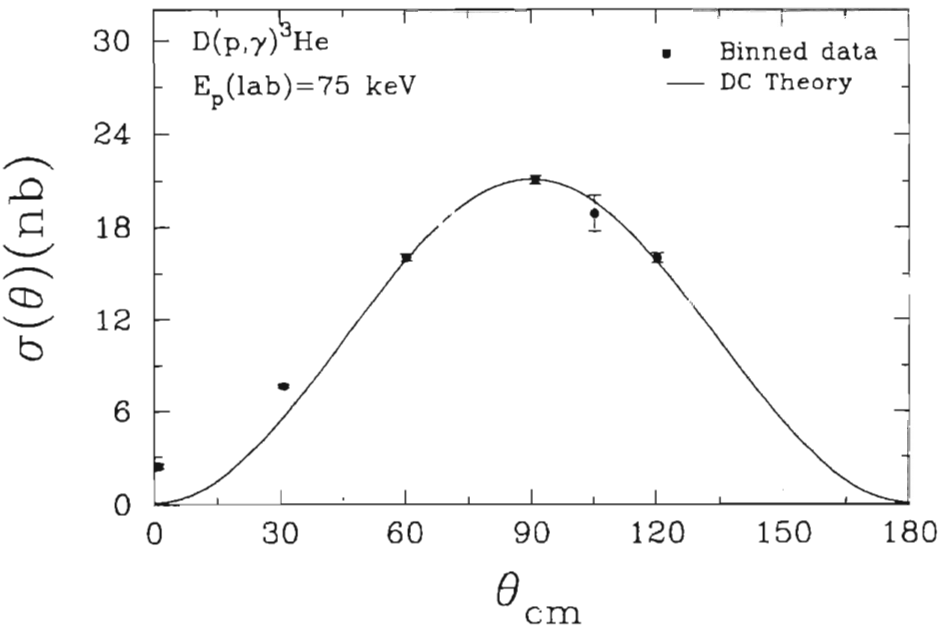

Figure 6.4: The direct capture (DC) results for $\sigma(\theta)$ at E_p(lab)=75 keV are shown (solid line) along with the raw binned data from Table 5.5 (shown without systematic error).

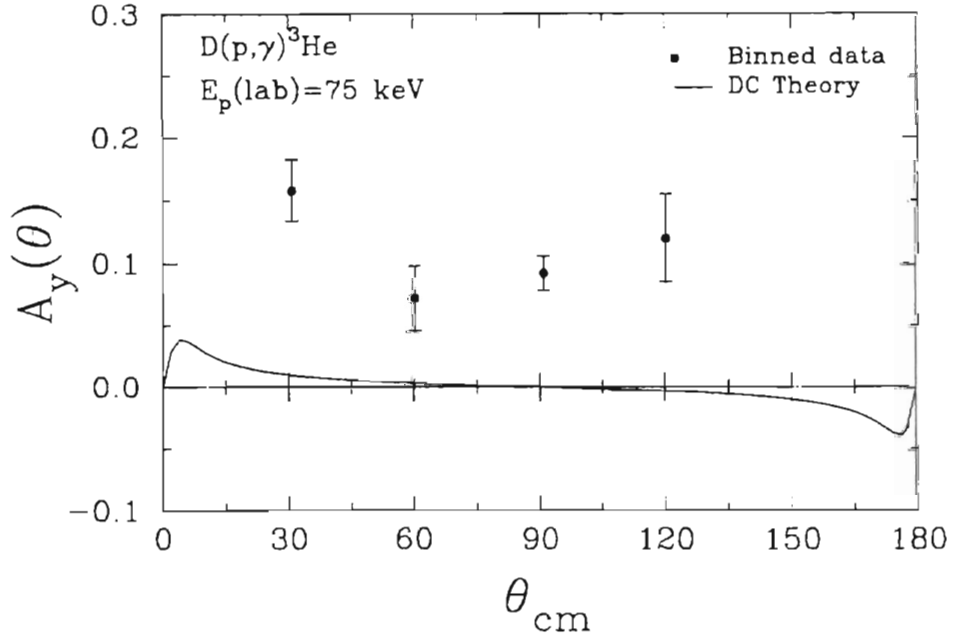

Figure 6.5: The direct capture (DC) results for $A_y(\theta)$ at E_p(lab)=75 keV (solid line) shown along with the experimental binning results from Table 5.6.

6.1.7 Discussion

It is interesting to see that the direct capture model works as well as it does. In fact, the absolute magnitude and energy dependence of the experimentally extracted E1 data is predicted remarkably well (Figure 6.2), as is the central part of $\sigma(\theta)$ (Figure 6.4). However, there are some notable discrepancies: the absolute magnitude and energy dependence of the total cross section is not well predicted (Figure 6.3); the isotropic component of $\sigma(\theta)$, as represented by the acquired data points at small angles, is not well reproduced; and, in what is perhaps the worst disagreement between theory and experiment, the vector analyzing power is completely misrepresented.

As is turns out, the blame for all these disagreements can be readily assigned to the failure of the direct capture model in predicting the M1 contribution. Even a small amount of s-wave M1 would allow a significant $A_y(\theta)$ strength to be present (see the expression for the B1 coefficient in Equation 5.20), and thus allow agreement with the $A_y(\theta)$ data. Inclusion of M1 could also resolve the discrepancy with regards to the cross section data, both in absolute magnitude and shape. This can again be seen by examining Equation 5.20. The reason that the direct capture model is unable to properly account for the presence of M1 can be understood by realizing two major deficiencies associated with a two body treatment of $D(p,\gamma)^3He$: the lack of correct antisymmetrization in accordance with the Pauli principle; and the lack of exchange contributions in the electromagnetic operators.

To address the first point, the direct capture model cannot correctly antisymmetrize the wavefunctions because one of the "identical" particles (a proton) is locked up in the deuteron (which is treated as a point particle). It turns out that this fact has important consequences with regards to M1 transitions to the S-state of ^3He. As was

first pointed out by Schiff [Sch37] and Verde [Ver50], and discussed nicely by [Don67], the dominant S-state component of the ^{3}He ground state wavefunction can be expressed in terms of spatially symmetric, antisymmetric, and mixed symmetry pieces as shown below:

$$\Psi_{He}(\text{S-state}) = \varphi^s\mu^a + \varphi^a\mu^s + \varphi'\mu'' + \varphi''\mu'. \tag{6.13}$$

In Equation 6.13, Ψ_{He}(S-state) is the S-state of ^{3}He, φ^a and φ^s are the antisymmetric and symmetric spatial wavefunctions, μ^a and μ^s are the antisymmetric and symmetric spin-isospin functions, and the primed functions are states of mixed symmetry. It will be noted that the symmetric-antisymmetric combinations in Equation 6.13 are enforced by the Pauli principle, which requires an antisymmetric total wavefunction. It has been shown (see discussion in [Kin83]) that the spatially symmetric piece of Ψ_{He}(S-state), φ^s, is the dominant S-state component.

The importance of the expansion in Equation 6.13 is simply this: Schiff [Sch37] and Verde [Ver50] have shown that μ^a is an eigenfunction of the magnetic dipole (M1) operator in the impulse approximation. In the impulse approximation (used in the direct capture model) the M1 operator is taken to be the sum of the magnetic moment operators of the free nucleons (in other words, the M1 operator in the impulse approximation neglects exchange currents). If we assume (for now) that the impulse approximation is completely valid, the fact that μ^a is an eigenfunction of the M1 operator indicates the following: s-wave M1 capture to the symmetric S-state, φ^s, should be zero. This is due to the orthogonality of the initial and final state wavefunctions (as is true for the direct capture model). *However*, the really important fact is this: M1 capture can still proceed to the ^{3}He S-state via capture to the mixed symmetry components, φ' and φ''! This extra

M1 strength, not present in the direct capture model predictions, is a direct result of exact three-body antisymmetrization (not included in a simple two body approach). Its inclusion will help resolve the disagreement between theory and experiment.

It also important to consider the second of the two direct capture model "deficiencies" that were initially mentioned: the lack of exchange contributions in the transition operators. A description of the nuclear force in terms of meson exchange is thought to be valid at low energies, and these currents will have a strong effect on the magnetic dipole operator. The effect is so as to increase the M1 cross section [Fri91]. Meanwhile, the explicit inclusion of meson exchange should not affect calculations dealing with the E1 operator. The reason for this is that the effects of meson exchange are already included in the E1 operator by means of Siegert's theorem [Laf82]. Thus it is clear that the inclusion of meson exchange currents will also help resolve the disagreement between theory and experiment.

6.1.8 Previous Direct Capture Work

In Chapters 1 and 5, the previous $D(p,\gamma)^3He$ direct capture calculation of [Gri63] was referred to. Perhaps the most obvious difference between the current $D(p,\gamma)^3He$ direct capture calculation, and the direct capture calculation of [Gri63], is that the [Gri63] results show a large M1 cross section (and S-factor) being present. The reason for this is simply that the [Gri63] authors did not directly calculate the M1 component, but instead derived its value by estimating the E1/M1 ratio that would be present, and by taking into account the difference in centrifugal barrier penetrabilities for the E1 and M1 components (E1 is predominantly p-wave capture, while M1 is predominantly s-wave capture). The

direct capture calculation of [Gri63] is essentially equivalent to the detailed direct capture calculation presented in T.W. Donnelly's Ph.D. thesis [Don67].

The primary differences between the direct capture calculation in [Don67], and the present calculation, are:

1. The current calculation involves a more realistic nuclear potential (Woods-Saxon shape instead of square-well).

2. The absolute scale for the current E1 cross section prediction is based entirely on the chosen form for the potential and the associated optical model parameters (from elastic scattering data). No arbitrary normalization to the acquired $D(p,\gamma)^3He$ data was necessary in the current case. However, this was not the case for the [Gri63] and [Don67] calculations. On pages 18 and 23 of [Don67], it is clearly stated that parameters were adjusted in order to fit the then existing $D(p,\gamma)^3He$ data of [Gri63] at low energies and of [Gri62] and others at higher energies, even when this meant disagreement with the elastic scattering data. It should also be pointed out that the M1 strength included in the [Don67] calculation is effectively treated as a free parameter (similar to [Gri63]), and is adjusted to fit the data. These two facets of the [Don67] calculation are sometimes overlooked (e.g. [Tom67]).

3. In the current work, polarization observables (i.e. the vector analyzing power) were computed. The calculation of [Don67] dealt only with the unpolarized cross section. Clearly, our current result for $A_y(\theta)$, shown in Figure 6.5, gives as strong a motivation as any other for the need to explicitly take into account the M1 strength.

Other direct capture calculations, by other authors, have also been performed for $D(p,\gamma)^3He$. However, these other calculations [Kin83,Vet85] were done at much higher

energies, and thus will not be discussed here. Instead, having now motivated the need for an exact three body treatment of the $D(p,\gamma)^3He$ process, we will now discuss the recent three-body calculations that have been performed.

6.2 Three-Body Calculations

As explained in section 6.1, a three body treatment of $D(p,\gamma)^3He$ which correctly takes into account the Pauli principle and the meson exchange currents is necessary. An exact three-body treatment must also properly take into account issues associated with three-body unitarity. Additional topics of interest are related to proper handling of the Coulomb interaction and to the validity of two body nucleon-nucleon (NN) potential models in the three-body system. The two $D(p,\gamma)^3He$ calculations that will be discussed here are a three-body Faddeev calculation at thermal energies (E~0) [Fri91], and a three-body variational calculation in the energy regime E_p(lab)=80-0 keV [Sch95].

6.2.1 Faddeev Calculation

In 1991, Friar et al. (Los Alamos and Univ. of Iowa) completed a set of three-body calculations for the $D(p,\gamma)^3He$ S-factor at thermal energies (essentially zero energy). In these calculations, the Faddeev technique, using the AV14 [Wir84] and RSC [Rei68] NN potentials, was employed to determine the bound and scattering states. Since realistic NN potential models always end up underbinding the ^3He nucleus, three-body forces [Coo79,Coe83] were included in the calculation. The electromagnetic operator was then used to calculate the transition rates and S-factor (however, only M1 transitions were considered). The novel aspects of this calculation involved a rigorous three-body

treatment of the MEC effects (never before done for the $D(p,\gamma)^3He$ reaction), and a rigorous treatment of the Coulomb effect. With regards to the handling of the MEC effects, the standard "seagull", "pion", and "Δ-isobar" exchange diagrams are included ([Fri91] and references therein). These MEC diagrams, which are shown in Figure 6.6, represent (respectively) the following interactions: a γ-ray, nucleon, and pion all interacting at a single localized point; a γ-ray and pion interacting at a non-localized point; and a γ-ray and nucleon interacting so as to produce an excited state (a Δ-isobar) which then decays by pion emission.

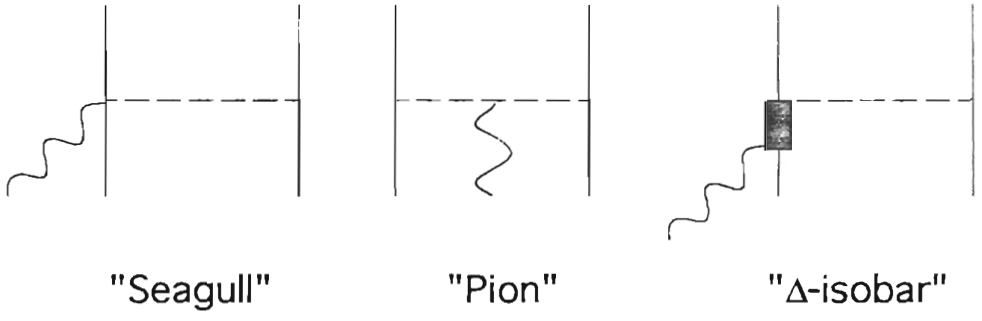

Figure 6.6: The dominant MEC diagrams considered in the Faddeev calculation.

In what follows, the basic tenants of the Faddeev technique will be outlined, and then the results of the [Fri91] calculation will be presented.

The Faddeev Technique

The goal of the Faddeev technique is to solve the three-body (or, in general, the n-body) Schrödinger equation for a given potential. For the case of $D(p,\gamma)^3He$, the realistic NN potential used had a Coulomb component added on. The Faddeev technique is often

referred to as an "exact" technique, in the sense that we actually solve the equations analytically to get the wavefunctions. The specific case of nucleon-deuteron scattering is handled in [Che91]. Other nice overviews are in [Pic92,Fri92]. To set the stage for the current discussion on the three-body Faddeev approach, let's first consider the case of solving the Schrödinger equation for two-bodies.

In order to solve the Schrödinger equation for the two-body bound state, we first reduce to an effective one-body problem by transforming to the center of mass [Fri91]. Then, by applying the appropriate boundary conditions (E<0, well behaved wavefunction), we can obtain the solution. For the two-body scattering state, it is usually convenient to put the Schrödinger equation in integral form. This form, known as the Lippmann-Schwinger equation, is given as [Pic92]:

$$\Psi = \phi + G_0 V \Psi, \tag{6.14}$$

where,

$$G_0 = \lim_{\varepsilon \to 0} \left[\frac{1}{E - T + i\varepsilon} \right]. \tag{6.15}$$

In Equations 6.14 and 6.15, Ψ is the total wavefunction, T is the kinetic energy operator, E is the energy, V is the potential, and ϕ is a plane wave. The ε parameter in Equation 6.15 is introduced to handle the singularity that occurs when E=T (i.e. when V=0). By defining G_0 as we have in Equation 6.15, the right hand term in Equation 6.14 now goes to zero when V=0, thus giving $\Psi=\phi$ as we would expect (i.e. the "free particle" solution). Equation 6.14 can be solved numerically to yield a unique solution.

While the techniques just discussed work well for the two body system, they do not apply, in general, to the three-body system. Foldy and Tobocman [Fol57] have shown that unique solutions to Equation 6.14 do not exist for the three-body scattering system. The problem is that the two-body boundary conditions in Equation 6.14 are not properly specified for the three-body scattering state. The difficulty lies in dealing with the rearrangement channels which are possible in three-body scattering. This issue was addressed by Faddeev in his landmark paper in 1960 [Fad60], and he proposed the following solution. First, consider the three-body Schrödinger equation which is [Fri92]:

$$(E - T - V_{12} - V_{13} - V_{23})\Psi(\vec{x}, \vec{y}) = 0, \tag{6.16}$$

where V_{ij} is the potential between particles i and j, and $\vec{x}$ and $\vec{y}$ are the Jacobi coordinate variables (assuming equal mass particles) defined below:

$$\vec{x} = \vec{r}_2 - \vec{r}_3 \ , \tag{6.17}$$

and

$$\vec{y} = \frac{1}{2}(\vec{r}_2 + \vec{r}_3) - \vec{r}_1. \tag{6.18}$$

Now, we make the following decomposition of the total wavefunction:

$$\Psi(\vec{x}, \vec{y}) = \psi_1(\vec{x}_1, \vec{y}_1) + \psi_2(\vec{x}_2, \vec{y}_2) + \psi_3(\vec{x}_3, \vec{y}_3), \tag{6.19}$$

where the Faddeev wavefunctions, ψ_i, are all defined to have the same form (they just have different arguments). The arguments $\vec{x}_1$ and $\vec{y}_1$ in Equation 6.19 are defined to be the Jacobi coordinates defined in Equations 6.17 and 6.18, while the arguments $\vec{x}_i, \vec{y}_i$ are obtained from cyclic permutations of $\vec{x}_1, \vec{y}_1$. In this manner, it is then clear that each Faddeev wavefunction deals with one of the three possible rearrangement channels specified by a given $\vec{x}_i, \vec{y}_i$.

By substituting Equation 6.19 into Equation 6.16, we obtain the following set of equations [Fri92]:

$$\begin{aligned} (E-T)\psi_1 &= V_{23}(\psi_1 + \psi_2 + \psi_3), \\ (E-T)\psi_2 &= V_{13}(\psi_1 + \psi_2 + \psi_3), \\ (E-T)\psi_3 &= V_{12}(\psi_1 + \psi_2 + \psi_3). \end{aligned} \tag{6.20}$$

These equations are known as the Faddeev equations. The beauty of the Faddeev equations is that we have now reduced the three-body problem to a series of two-body problems which we can (in principle) solve. To obtain solutions for the three-body scattering state, we now apply the appropriate boundary conditions directly to the two-body Faddeev wavefunctions. We no longer need to concern ourselves with the rearrangement boundary conditions because they are already taken into account in Equations 6.20 [Fri92]. The Faddeev equations can also be used to solve the bound state three-body system by simply applying the appropriate boundary conditions to the Faddeev wavefunctions.

The practical process of solving the Faddeev equations involves expanding the Faddeev wavefunctions in terms of angular momentum "channels" [Che91]:

$$\psi_i(\vec{x}_i,\vec{y}_i)=\sum_\alpha \frac{\psi_\alpha(x_i,y_i)}{x_i y_i}|\alpha\rangle, \tag{6.21}$$

where each channel wavefunction, $|\alpha\rangle$, is specified by the angular momentum quantum numbers of a two particle system (in particular, the two particles separated by x_i), and the angular momentum quantum numbers of the remaining "spectator" particle (the particle which is a distance y_i from the center of mass of the other two particles). These channel wavefunctions are properly anti-symmeterized as required by the Pauli principle. By inserting the expansion in Equation 6.21 into the top Faddeev equation in Equation 6.20, and then projecting the resulting equation out onto channel $|\alpha'\rangle$, we obtain the following set of coupled equations:

$$\sum_\alpha \langle\alpha'|(E-T)|\alpha\rangle \frac{\psi_\alpha(x_1,y_1)}{x_1 y_1} = \sum_\alpha \langle\alpha'|V_{23}|\alpha\rangle \left[\frac{\psi_\alpha(x_1,y_1)}{x_1 y_1} + \frac{\psi_\alpha(x_2,y_2)}{x_2 y_2} + \frac{\psi_\alpha(x_3,y_3)}{x_3 y_3} \right]. \tag{6.22}$$

The important thing to note about Equation 6.22, in the context of the current discussion, is that the potential V_{23} has been effectively expanded into channels. Since the potential under current consideration has a Coulomb component, this means that the Coulomb potential must be expanded into channels. Unfortunately, the Coulomb expansion is only very slowly convergent [Kie94], and thus significant problems arise when the expansion in Equation 6.21 is truncated at too low a channel. In fact, in the $D(p,\gamma)^3He$ Faddeev calculation of [Fri91] (the one of current interest), the correct determination of the Coulomb strength required significant help from variational methods (to be discussed).

For further details on the bound state calculations presented in [Fri91], the interested reader is referred to [Fri83]. For further details on the continuum state calculations, the reader is referred to [Che91].

Results for $D(p,\gamma)^3He$ Faddeev calculation

The primary result of the $D(p,\gamma)^3He$ Faddeev calculation of [Fri91], at least as it pertains to the current experiment, was a theoretical M1 S(0) value. This theoretical result was M1 $S(0) = 0.108 \pm .004$, and is plotted in Figure 6.7 along with the experimentally extracted values. The solid line in Figure 6.7 is the theoretical prediction, the dashed lines are the theoretical error bars, the open data point is the experimentally determined value of Griffiths, and the solid data point is the result extracted from the current experimental results (see Table 5.15). Both data points include systematic error.

There are two immediate observations that one can make based on Figure 6.7. The first is that the current data point has significantly smaller error bars than the previous data point of [Gri63]. The second is that the current data point lies below the theoretical prediction by about 30%, while the previous data point actually agrees with the theoretical prediction within error bars. The conclusions that one can draw from Figure 6.7 are varied. It will be noticed that if the [Gri63] data point is scaled down by 10-15%, in accordance with the STP(E) correction discussed in Chapters 3 and 5, the agreement with theory is remarkably good. This would perhaps indicate that the [Gri63] data is perhaps more reliable than the current result due to its excellent agreement with theory. Of course, due to the large error bars on the [Gri63] result, it is difficult to substantiate this claim. In fact, as discussed in Chapter 5, we have every reason to believe that our extracted M1 S(0) value is more accurate (as stated by our error bars) than the result of [Gri63].

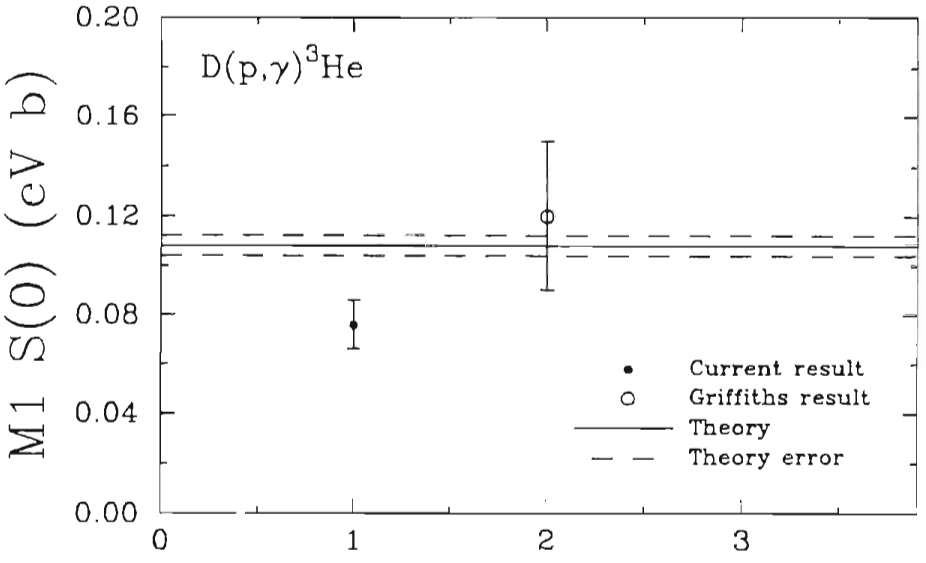

Figure 6.7: The theoretical result for M1 S(0) from the Faddeev calculation of [Fri91] (solid line) is shown along with the experimentally acquired data points. The horizontal axis of this figure is in arbitrary units. The data points include systematic error.

The large disagreement with theory is thus a mystery. In order to find the cause of this disagreement, one possible path to take would be to vary the components of the theoretical calculation (i.e. MEC effects, NN potentials, Coulomb effects, etc.) in order to gauge their sensitivity to the final result, and thus perhaps find a culprit (e.g. the MEC effects are too weak, etc.).

Unfortunately, the calculation having been done several years ago, such a procedure cannot be attempted. However, it should be pointed out that the MEC strength for the [Fri91] calculation was fixed so as to agree with the well established results for n-d capture [Jur82], and thus would be expected to be correct to a good degree of accuracy. The validity of the [Fri91] calculation is further strengthened by the experimental results of [Pet91]. The experiment of [Pet91] dealt with muon catalyzed p-d fusion. It has been well known since the 1950's that a negatively charged muon, if present, can "catalyze"

the p-d fusion process, and thus greatly enhance the p-d reaction rate. As it happens, the muon usually "sticks" to the resulting ^{3}He nucleus, and thus cannot "catalyze" many reactions (because of this, the hopes of using muon catalyzed fusion as a commercial energy source have not been realized). The tie-in of the [Pet91] experiment with the current discussion is that Friar et al., using the same theoretical framework as for the D(p,γ)^{3}He case, also calculated muon catalyzed fusion reaction rates. These theoretical results [Fri91] are in good agreement with the muon catalyzed fusion data of [Pet91], and thus lend strong support to the [Fri91] results for D(p,γ)^{3}He.

With the above arguments in mind, the possibility of a ~30% systematic error in the current experimental procedure must be addressed. As discussed in Chapter 5, the current experimental M1 S(0) value shown in Figure 6.7 was extracted from the raw data by extrapolating results to zero energy, and then performing a transition matrix element analysis (which required several assumptions) in order to obtain the M1 component of the total S-factor. A 30% error in this procedure (in addition to errors already discussed) is certainly possible, although not expected. In light of this, what is really needed is a theoretical calculation that predicts observables which were actually measured. In other words, a calculation which predicts the *total* S-factor instead of just the M1 component would be much easier to compare directly with our experimental data. Fortunately, the next calculation we discuss *does just this!* We now turn our attention to this calculation.

6.2.2 Variational Calculation

In April, 1995, Schiavilla et al. (CEBAF and Pisa, Italy) completed a variational calculation for the D(p,γ)^{3}He reaction in the energy region E_p(lab)=80-0 keV [Sch95]. In this calculation, the Rayleigh-Ritz variational principle [Del72] was used to determine the

bound state, while the Kohn variational principle [Del72] was used to determine the scattering state. The AV14 NN potential [Wir84] was employed in these calculations. In addition, in order to properly bind the ^{3}He nucleus, a three-nucleon force was added (the UrbannaVIII TNF [Wir91]). The electromagnetic operator (in the E1,M1,E2,M2 multipoles) was then used to determine the transition rates and observables (which, in this case, included the *total* S-factor and $A_y(\theta)$). Explicit MEC effects were also included in the calculation [Sch92,Wir91], whereby the novel aspect here was a new method for handling the Δ-isobar degrees of freedom

The biggest advantage of a variational calculation, as compared with a Faddeev calculation, is the fast convergence of the associated partial wave expansion. The reason for this is that the potentials in a variational calculation are not expanded into channels as they are in a Faddeev calculation (only the wavefunctions are expanded). This is a particular advantage when dealing with the Coulomb potential, where the very slow convergence of the expansion can lead to significant series truncation errors.

The following discussion will outline the variational technique. Following this, the current $D(p,\gamma)^3He$ results will be presented.

The Variational Technique

The basic idea of the variational technique is to assume a parameterized form for the desired wavefunction, Ψ (either continuum or bound state). This wavefunction is then inserted into a functional, $F[\Psi]$, which is defined to be stationary with regards to variations of all relevant parameters. Thus, the following equations define the variational principle [Del72]:

$$\frac{\partial F[\Psi]}{\partial \rho_i} = 0, \tag{6.23}$$

where the ρ_i are the parameters being varied.

Clearly, the first task in a variational calculation is to identify an appropriate functional, $F[\Psi]$. For the case of the ^{3}He bound state, we can use the Rayleigh quotient, $E[\Psi]$, which is defined as follows [Bra89]:

$$F[\Psi] = E[\Psi] = \frac{\langle \Psi | H | \Psi \rangle}{\langle \Psi | \Psi \rangle}, \tag{6.24}$$

where H is the three-body Hamiltonian. By substituting Equation 6.24 into Equation 6.23, and using the known form for H, we can solve for the parameters ρ_i, and thus determine the ground state eigenfunctions.

However, in the current variational calculation, the aforementioned equations were not directly solved. Instead, an approximate scheme, known as the Rayleigh-Ritz variational method, was employed. This method is based on the following important inequality [Del72]:

$$E[\Psi] \geq E_0, \tag{6.25}$$

where E_0 is the ground state eigenvalue.

This inequality can be derived as follows (see [Bra89]). First, we expand the assumed wavefunction, Ψ, in terms of the eigenfunctions of H, ϕ_m:

$$|\Psi\rangle = \sum_m a_m |\phi_m\rangle, \tag{6.26}$$

where it is understood that

$$H|\phi_m\rangle = E_m|\phi_m\rangle. \tag{6.27}$$

By substituting Equation 6.26 into Equation 6.24, we obtain:

$$E[\Psi] = \frac{\sum_m |a_m|^2 E_m}{\sum_m |a_m|^2}. \tag{6.28}$$

By now subtracting the quantity E_0 from both sides, Equation 6.28 can be written as [Bra89]:

$$E[\Psi] - E_0 = \frac{\sum_m |a_m|^2 E_m}{\sum_m |a_m|^2} - \frac{\sum_m |a_m|^2 E_0}{\sum_m |a_m|^2} = \frac{\sum_m |a_m|^2 (E_m - E_0)}{\sum_m |a_m|^2}. \tag{6.29}$$

Since E_0 is, by definition, the lowest energy eigenvalue (i.e. it is the ground state eigenvalue), we see that the right hand side of Equation 6.29 is always greater than or equal to zero, and thus we have proved Equation 6.25.

Equation 6.25 is important because it indicates that the functional $E[\Psi]$ gives an upper bound for the possible values of E_0. This idea is exploited in the Rayleigh-Ritz method, whereby we perform a Monte-carlo search in parameter space in order to find the parameter values which minimize the $E[\Psi]$ functional. Once we have minimized $E[\Psi]$, we have determined all the ρ_i, and hence we have determined Ψ.

For the $D(p,\gamma)^3He$ calculation under current consideration [Sch95], the calculation of the bound state wavefunction is discussed in [Kie93,Kie94]. The first step was to expand the ground state wavefunction in Faddeev components just like in Equation 6.19.

Each Faddeev wavefunction, ψ_i, was then channel expanded into a product of angular (Y_α) and radial (Φ_α) functions as shown below:

$$\psi_i(\vec{x}_i,\vec{y}_i) = \sum_\alpha \Phi_\alpha(x_i,y_i)Y_\alpha(jk,i), \tag{6.30}$$

where x_i and y_i are the Jacobi coordinates, (jk,i) stands for the angular momentum coupling of the three particles (j, k and i), and where the total wavefunction (Ψ) is properly anti-symmetrized with respect to the Pauli principle.

The radial wavefunction is then expanded into correlated hyperspherical harmonics [Kie93,Kie94]:

$$\Phi_\alpha(x_i,y_i) = \rho^{\ell_\alpha+L_\alpha}F_\alpha(x_i)\left[\sum_K u_K^\alpha(\rho)P_K\right], \tag{6.31}$$

where ρ is the hyperradius, the $F_\alpha(x_i)$ are the correlation functions, the $u_K^\alpha(\rho)$ are the hyperradial functions, and the P_K are the hyperspherical polynomials. All of these quantities are defined in [Kie93]. The "unknown" quantities are the hyperradial functions, $u_K^\alpha(\rho)$, which are determined by means of the Rayleigh-Ritz technique as discussed above. Using this method, the ^{3}He binding energy can be predicted to within 1%.

The continuum wavefunction, for the current calculation, was determined by means of the Kohn variational principle [Del72]. This method is essentially the same as the Rayleigh-Ritz method, except that a different functional, $F[\Psi]$, is used. The continuum wavefunction can be written as follows [Kie94]:

$$\Psi = \Psi_C + \Psi_A, \tag{6.32}$$

where Ψ_C is the "core" wavefunction, important at small internuclear separation, and Ψ_A is the "asymptotic" wavefunction, important at large internuclear separation. The "core" wavefunction is decomposed into Faddeev components, where each component has a form similar to Equation 6.30. The "asymptotic" wavefunction is also decomposed into Faddeev components, $\Omega_{LSJ}(\vec{x}_i,\vec{y}_i)$, which are written as follows:

$$\Omega_{LSJ}(\vec{x}_i,\vec{y}_i) = \Omega^R_{LSJ}(\vec{x}_i,\vec{y}_i) + \sum_{L'S'} R^{SS'}_{LL'}\Omega^I_{L'S'J}, \tag{6.33}$$

where each Ω_{LSJ} function is expanded as a product of deuteron and two-body Coulomb scattering wavefunctions [Kie94]. The Ω^R_{LSJ} and Ω^I_{LSJ} refer to functions which use the regular and irregular Coulomb functions respectively. As stated in [Kie94], the matrix elements $R^{SS'}_{LL'}$ give the relative weight between the regular and irregular components. The subscript L is the relative orbital angular momentum of the deuteron and proton, the subscript S is the channel spin (see Chapter 5), and J is then the vector sum of L and S.

The total continuum state wavefunction (corresponding to an asymptotic state LSJ) can then be written as follows [Kie94]:

$$\Psi_{LSJ} = \sum_{i=1,3}\left[\psi_C(\vec{x}_i,\vec{y}_i) + \Omega^R_{LSJ}(\vec{x}_i,\vec{y}_i) + \sum_{L'S'} R^{SS'}_{LL'}\Omega^I_{L'S'J}(\vec{x}_i,\vec{y}_i)\right], \tag{6.34}$$

where the "unknown" parameters are the hyperradial functions in ψ_C and the $R^{SS'}_{LL'}$ matrix elements. These unknowns are determined by finding the stationary values of the following functional, F[Ψ]:

$$F[\Psi] = R^{SS'}_{LL'} - \left\langle \Psi_{L'S'J}\left|\frac{M}{2\sqrt{3}\hbar^2}(H-E)\right|\Psi_{LSJ}\right\rangle, \tag{6.35}$$

where, as defined in [Kie94], H is the Hamiltonian and E is the total energy. This procedure constitutes the Kohn variational principle.

Results for $D(p,\gamma)^3He$ Variational Calculation

The $D(p,\gamma)^3He$ variational calculation of [Sch95] has several very nice features which make comparison with experiment very fruitful. First of all, the total S-factor, S(E), was calculated over the entire energy range E_p(lab)=80-0 keV, and could thus be compared directly to the data (i.e. no extraction of multipole components necessary). Secondly, the [Sch95] calculation gives the vector analyzing power $A_y(\theta)$ at E_p(lab)=25 keV, and this can also be compared directly to the data. And thirdly, the [Sch95] calculation included tests whereby the MEC strength was probed. This was done by doing two sets of calculations for every theoretical data point: one calculation done with the full electromagnetic operator; and one calculation done with only the impulse approximation (IA) operators. Since the IA operators completely neglect exchange current effects, a comparison of the IA result to the full result yields an indication of the MEC contribution to the observable. Issues relating to the Coulomb effect (treated exactly), and the three-body forces (needed to correctly bind ^3He), are also significant in the calculation, but these sensitivities were not gauged.

Figure 6.8 shows, by the dashed line, the full [Sch95] theoretical result for the total $D(p,\gamma)^3He$ S-factor. The data points in Figure 6.8 are the same ones that were shown in Figure 5.17, whereby the solid data points are the current experimental results, and the open data points are the results of [Gri63]. The solid line in Figure 6.8 is the current experimental deconvolution result which is discussed in Chapter 5, whereby the dotted line is a calculation done using the IA operators. It can be seen from Figure 6.8

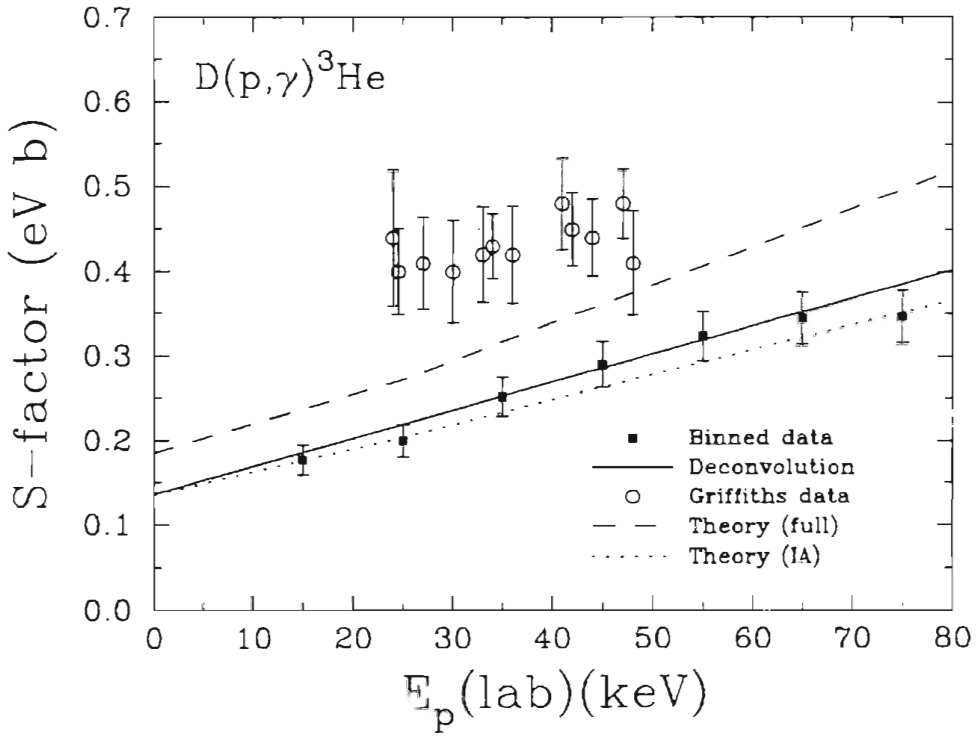

Figure 6.8: The full theoretical result from [Sch95] for the $D(p,\gamma)^3He$ S-factor (dashed line), shown along with experimental results. The dotted line is a calculation done using the impulse approximation (IA) operator. Systematic error is included in the data points.

that the calculation done with the IA operators agrees fairly well with the current data, where as the full calculation does not (it is consistently 20-30% too high). In fact, at zero energy, the calculated IA value agrees exactly with the current S(0) result extracted from our data. It should be pointed out that even if the [Gri63] data points are corrected for their erroneous STP(E) values (i.e. the [Gri63] S-factor points in Figure 6.8 should be lowered by 10-15% across the energy region), they still lie above the full calculation of [Sch95]. This indicates that the [Sch95] calculation is in disagreement with both data sets.

In addition to the total S-factor, the [Sch95] group also calculated $A_y(\theta)$ at E_p(lab)=25 keV, and the E1 and M1 S-factors vs. energy. Figure 6.9 shows the vector analyzing power calculation of [Sch95] along with the current experimental data for this observable. The agreement between the data and the full calculation is quite good in this case, lending strong support to the importance of MEC effects in calculating the observables. However, in Figure 6.10, which shows the calculated E1 S-factor along with the current experimentally derived values, the discrepancy between theory and data is again quite clear with the full calculation being significantly off in absolute magnitude. As in Figure 6.8, we note that the IA result agrees remarkably well with the acquired data.

Based on the results shown in Figures 6.8 and 6.10, it could be concluded that the MEC's are perhaps not handled properly in the calculation. In particular, it would appear that the MEC strength is too strong, and thus creates an overprediction of the total S-factor by 20-30% over the energy region considered. Actually, this conclusion is in excellent agreement with the fact that the same authors of the [Sch95] calculation also calculated the $D(n,\gamma)^3H$ thermal cross section [Viv95] (using the same theoretical prescription), and obtained a value which was 25% higher than the experimental result. In particular, the [Viv95] result was 0.636 nb, while the experimental result was 0.508 $\pm$0.015 nb [Jur82]. In addition, the authors of [Sch92] have shown that the $^3He(n,\gamma)^4He$ thermal cross section is also overpredicted using the same theoretical prescription of [Sch95,Viv95]. The blame for this overprediction has been assigned to uncertainties in the explicit MEC description [Sch92].

The above conclusion concerning the overprediction of the MEC strength in the [Sch95] calculation must be reconciled with the results shown in Figure 6.9, which demonstrate that the MEC strength is necessary to fit the data. Given that the $A_y(\theta)$ data

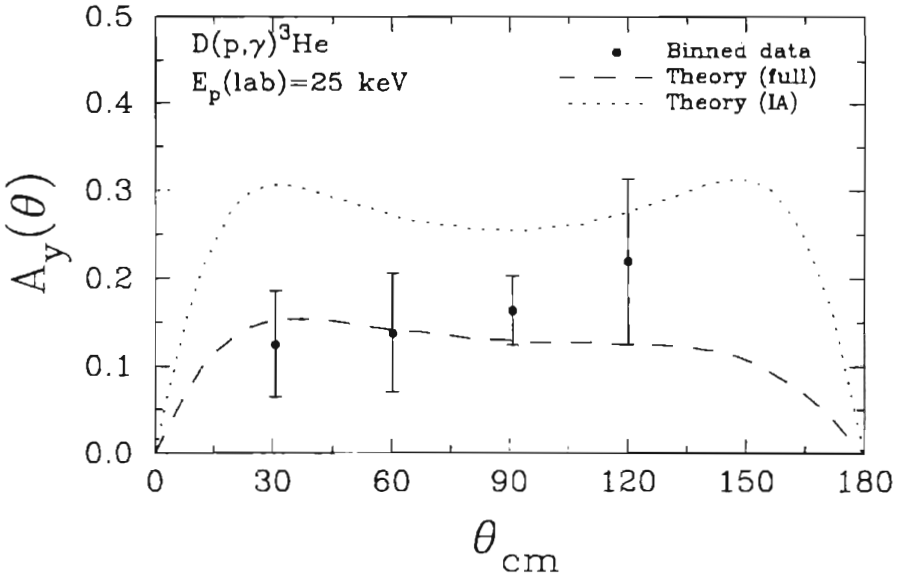

Figure 6.9: The [Sch95] prediction for the vector analyzing power, at 25 keV, shown along with the current experimental results.

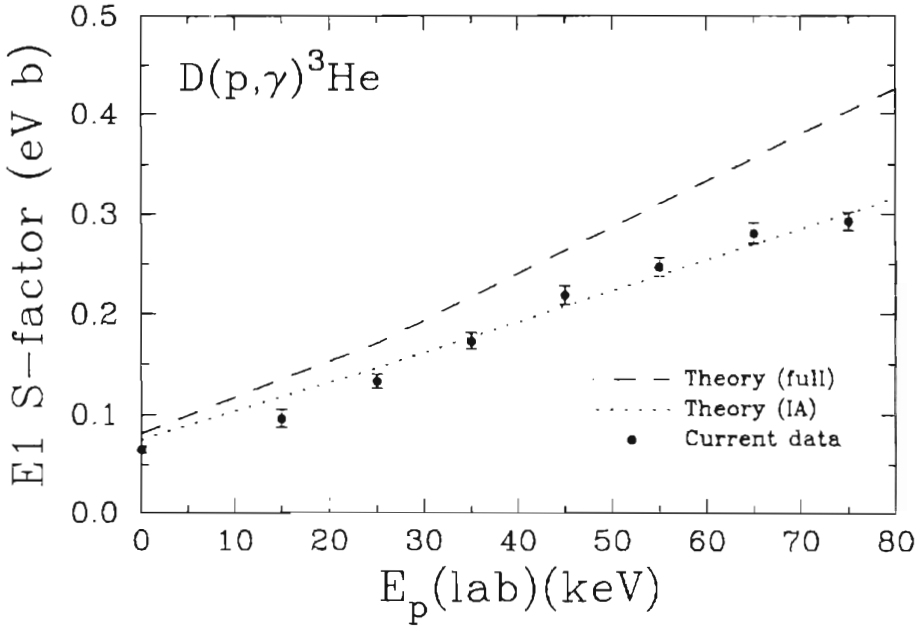

Figure 6.10: The [Sch95] prediction for the E1 S-factor, shown along with the currently acquired experimental data. Systematic error is not included in the data points.

is expected to be virtually free from systematic error (see Chapter 3), we must assign considerable importance to this result. Further calculations from the [Sch95] group are expected in the near future [Viv95], and we hope that these new results will help resolve this issue regarding the accuracy of the current theoretical approach.

6.3 Theoretical Conclusions

The two-body direct capture model does a remarkable job in qualitatively approximating both the magnitude and energy dependence of the experimental $D(p,\gamma)^3He$ E1 cross section (Figure 6.2), and also the general magnitude and shape of the angular distribution (Figure 6.4). However, it should be emphasized that the quantitative agreement is not very precise. The disagreement of the direct capture model with the results of the total cross section is more striking, whereby both the absolute magnitude and energy dependence are not verified by the data (Figure 6.3). Perhaps the most serious shortcoming of the direct capture model involves its prediction of the vector analyzing power (Figure 6.5), which is not even close to the data. All of these shortcomings can be ascribed primarily to the incorrect treatment of M1 by the direct capture model.

The extent to which modern three-body calculations improve the description of M1 is somewhat uncertain based on the current results. The three-body calculation of [Sch95] does an excellent job in clearing up the discrepancy with regards to the $A_y(\theta)$ observable. The [Sch95] result for this observable, shown in Figure 6.9, shows a strong sensitivity to the MEC effects, and the good agreement with data appears to verify the predicted MEC magnitude. Unfortunately, the predicted total S-factor results of both [Fri91] and [Sch95], shown in Figures 6.7, 6.8 and 6.10, overpredict the data by 20-

3)% over the energy regime of interest. This result, taken in tandem with the fact that the IA calculations appear to match the S-factor data quite well, might perhaps be an indication that the MEC prescription currently being used [Sch92] is incorrect to some degree. An unknown overall systematic error involving the current S-factor data could possibly solve some of the discrepancies between theory and data, but is thought to be unlikely based on the discussions in section 5.7. We await further theoretical results [Viv95] to help resolve this issue.

As a final note, we point out that the energy dependence predicted by the full [Sch95] S-factor calculation actually agrees, within error bars, with the currently extracted value of 0.0050 eV b/keV (Equation 5.27), *if the [Sch95] result is corrected for the difference in absolute scale.* We will address this issue in Chapter 7.

Chapter 7

Conclusions

This brief chapter will serve to summarize the salient conclusions of the current experimental study of $D(\vec{p},\gamma)^3He$. The primary goal of the current study has been to acquire accurate data on the $D(\vec{p},\gamma)^3He$ observables over the energy regime E_p(lab)=80-0 keV ($E_{cm}=(2/3)E_p$). In particular, the observables acquired were the cross section, $\sigma(\theta)$, the astrophysical S-factor, $S(\theta,E)$, the vector analyzing power, $A_y(\theta,E)$, and the γ-ray linear polarization, $P_\gamma(\theta)$. In the case of the $\sigma(\theta)$, $S(\theta,E)$ and $A_y(\theta,E)$ observables, an empirical deconvolution technique was used to extrapolate results down to zero energy. In the case of the $P_\gamma(\theta)$ observable, data were acquired only for the entire summed energy regime, and no effort was made to extract an energy dependence. The acquired S-factor and analyzing power data were then compared to theoretical predictions.

7.1 Summary and Discussion of Results

All experimental results pertaining to the current $D(\vec{p},\gamma)^3He$ study are contained in Chapter 5. This includes a parameterization of all of our data in terms of Legendre coefficients (through k=2) and complex transition matrix elements (for the matrix elements shown in Table 5.1). In the case of the transition matrix element (TME) fit, an equal amplitude and phase assumption for the two contributing E1 matrix elements was necessary in order to extract unambiguous results. Based on our acquired angular

distributions (Figures 5.6-5.12), we have concluded that this assumption, which is equivalent to assuming a symmetric $\sin^2\theta$+constant shape for $\sigma(\theta)$, is valid over the energy range E_p(lab)=80-0 keV. This is a significant result in the sense that it verifies the assumed shape of $\sigma(\theta)$ that was used in the data analysis of the previous $D(p,\gamma)^3He$ experiment of [Gri63] (they assumed this form without measuring accurate angular distributions).

The primary result of the TME analysis on our data is the extraction of E1 and M1 S-factor components over the energy region studied. Our results for these components are shown in Figure 7.1 as the solid and open data points respectively. These data points were obtained from a TME analysis to the complete $S(\theta)$ and $A_y(\theta)$ data set at each energy. Although no data was directly measured at E=0, an extrapolated data set was acquired there by evaluating, at zero energy, the $S(\theta,E)$ and $A_y(\theta,E)$ functions obtained from the deconvolution analysis. The curves shown in Figure 7.1 are the results of the direct capture calculation presented in [Gri63] which have been normalized to the current results (in particular, the [Gri63] curves are multiplied by a factor of 0.54 in order to match our extracted S(0) value). In the [Gri63] calculation, the energy dependence of the S-factors comes solely from effects related to tunneling through the centrifugal barrier. These effects are clearly present in the E1 S-factor in Figure 7.1 due to the fact that, for $D(p,\gamma)^3He$ in the low energy region, the E1 capture is thought to be pure p-wave (the $\sin^2\theta$ part of the angular distribution). On the other hand, the M1 capture is thought to be pure s-wave (the isotropic part of the angular distribution), and thus the null centrifugal barrier produces no energy dependence.

By comparing the [Gri63] curves with our data, it is clear that while the direct capture energy dependence of [Gri63] is adequate in some respects, it does not precisely match (within error bars) the E1 and M1 energy slopes indicated by our results. This

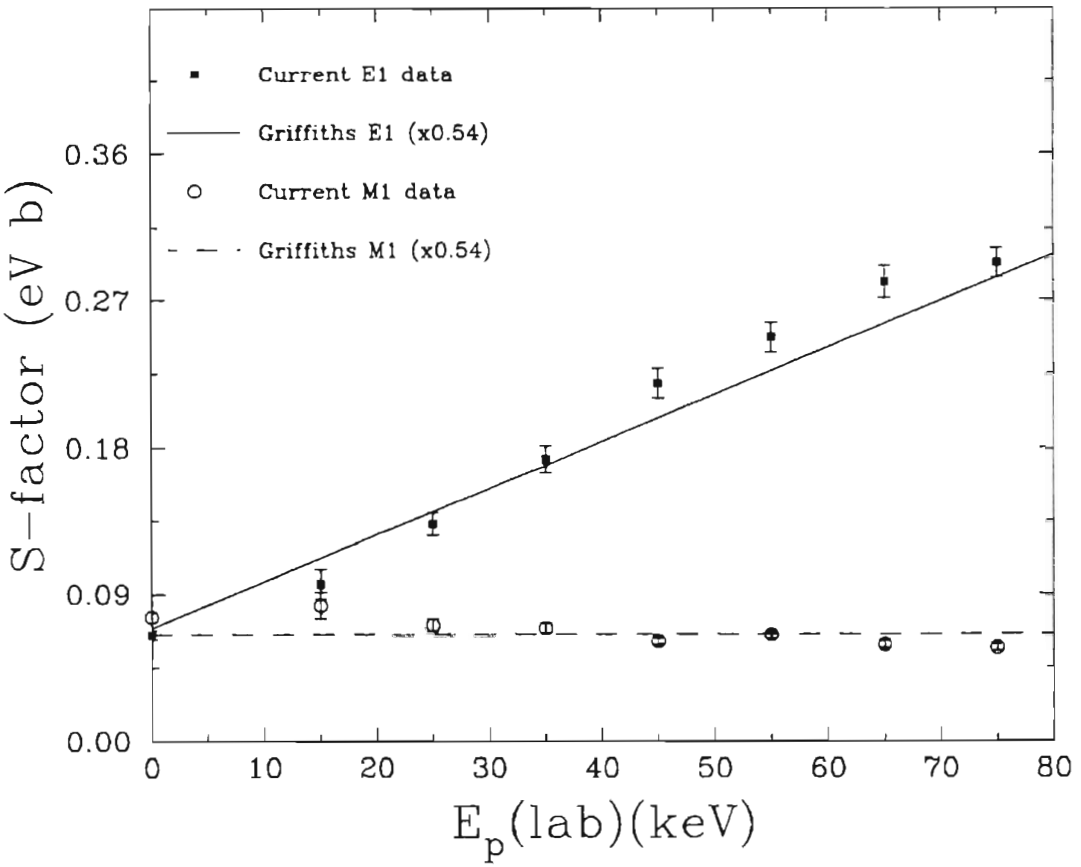

Figure 7.1: The E1 and M1 D($\vec{p}$,γ)^{3}He S-factor results for the current experiment, as extracted from the TME analysis, are shown by the data points (systematic error is not included). The curves shown are the results of the [Gri63] direct capture calculation which have been normalized so as to agree with the currently extracted value for S(0).

is taken to be evidence of an inadequacy in the direct capture model. In order to gauge quantitatively the inadequate energy dependence of the direct capture model, we have extracted a parameterized form for the total S-factor directly from our raw spectra (via the deconvolution analysis). Our result is:

$$S(E_{cm}) = S_0 + E_{cm}S_1, \tag{7.1}$$

$$S_0 = 0.136 \pm 0.005 \pm 0.012 \text{ eV b},$$

$$S_1 = 0.0050 \pm 0.0004 \pm 0.0005 \text{ eV b/keV},$$

where the first error quoted is the statistical error and the second error quoted is the 9% overall systematic error. This result for the form of the total $D(p,\gamma)^3He$ S-factor is shown in Figure 7.2 by the solid line. The solid data points in Figure 7.2 are the results of the current binning analysis at each measured energy, while the open data points in Figure 7.2 are the previously measured data points of [Gri63]. The direct capture result from [Gri63] is shown (normalized to the [Gri63] data) as the dashed line.

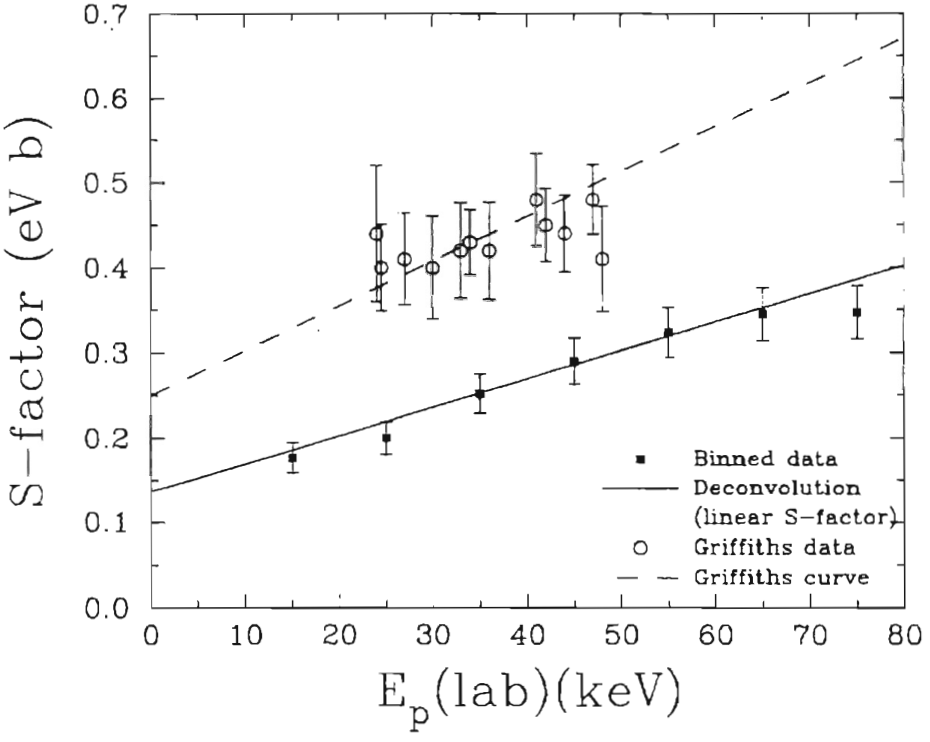

Figure 7.2: Current results for the total $D(p,\gamma)^3He$ S-factor (the solid points and solid line) are shown along with the [Gri63] data (open points). Systematic error is included. The dashed curve is the [Gri63] direct capture calculation normalized to the [Gri63] data.

As was pointed out in Chapter 5, the theoretical energy dependence of [Gri63] is S_1/S_0=0.0316 keV^{-1}. The current experimentally derived energy dependence, as shown in Figure 7.2, is S_1/S_0=0.0368 ± 0.0033 keV^{-1}, which is different outside of error bars from the [Gri63] result. While the difference in energy dependence with the theoretical energy dependence of [Gri63] is interesting, perhaps the most striking conclusion to be drawn from Figure 7.2 is related to the difference in absolute scale between the data points of [Gri63] and the current data points. In fact, the current results lie about 40-45% lower than the [Gri63] results over the entire energy region studied. It should be pointed out (as we did in Chapter 3) that because the authors of [Gri63] used incorrect stopping cross sections in analyzing their data (they used values for protons on H_2O vapor instead of protons on D_2O ice), the [Gri63] results in Figure 7.2 should be scaled down by 10-15% over the energy region studied (due to the so called "Physical state effect" in the stopping cross sections). However, even if we correct the [Gri63] data for this effect, they still lie well above the current results.

It is also interesting to compare our current S-factor results with the results of recent three-body calculations. One such comparison is shown in Figure 7.3, where the current total S-factor data (solid points and solid line) are shown along with the theoretical results of [Sch95]. The dashed line is the full theoretical result, while the dotted line is a theoretical result obtained by *neglecting the effect of meson exchange currents (MEC's).* In other words, the calculation represented by the dotted line was done with the impulse approximation (IA) operators. Although the full [Sch95] calculation shown does not exactly represent a linear S-factor, it is nearly linear. If we calculate an approximate slope of the full calculation using the theoretical E=0 and E_p(lab)=80 keV points, we obtain a theoretical S_1/S_0 value of 0.0346 keV^{-1}. This value agrees, within error bars, with the current experimental result of S_1/S_0=0.0368 ± 0.0033 keV^{-1}.

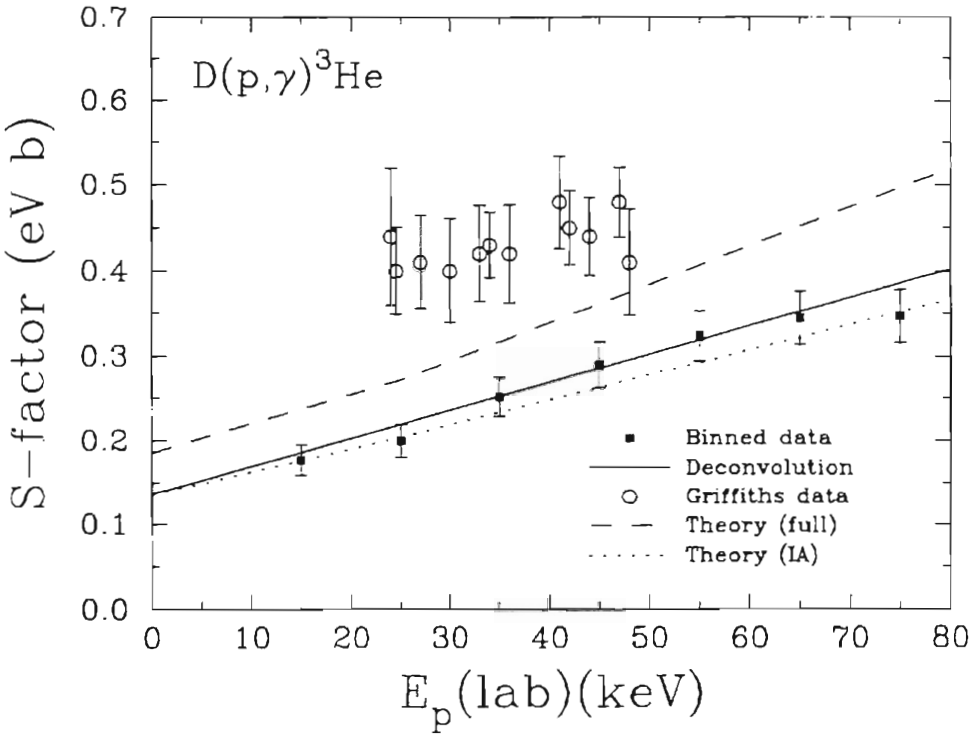

Figure 7.3: The theoretical calculations of [Sch95] which include (dashed line) and don't include (dotted line) the MEC effects. The solid line and solid points are the current results, while the open points are the results of [Gri63]. Systematic error is included.

The difference in absolute scale between the full theoretical calculation and the current experimental results is worth noting. The fact that the IA calculation agrees fairly well with the data, while the full calculation overpredicts the data by ~25%, is interesting to note. It should be pointed out that even if we correct the [Gri63] data for the ~12% stopping cross section anomaly, we still see that the [Gri63] data will exceed the full calculation by 10-15%. By comparison of the full S-factor calculation with our data, we conclude that the MEC strength in this theoretical prescription [Sch92,Sch95] is possibly too high. This has been previously suggested [Sch92,Viv95]. The fact that the full [Sch95] calculation actually matches our analyzing power data very well (Figure 6.9) is

an anomaly that is not understood at present. We await further calculations to help resolve this discrepancy [Viv95].

7.2 Astrophysical Implications

Prior to the current experiment, the results of [Gri63] were the only existing $D(p,\gamma)^3He$ data points in the very low energy region (E_p(lab)<50 keV). In light of our new results, which suggest an S(0) factor almost a factor of two below the accepted value of [Gri63] value of S(0)=0.25±0.04, it is instructive to explore the possible astrophysical consequences.

Based upon the discussion in Chapter 1, a factor of two change in the $D(p,\gamma)^3He$ reaction rate would not be expected to affect energy production in the solar proton-proton chain. This is due to the fact that $D(p,\gamma)^3He$ follows the weakly interacting $p+p\rightarrow D+e^+\nu$ in the sequence of events, and thus is effectively bottlenecked by ~18 orders of magnitude. However, despite its relative unimportance in stellar energy production, the discussion in Chapter 1 clearly indicates the importance of $D(p,\gamma)^3He$ in the evolution of low mass protostars (whereby primordial deuterium, instead of solar generated deuterium, is burned). The effect that a lower $D(p,\gamma)^3He$ S-factor would have on the protostellar calculations of [Sta88] is a topic which would now appear to merit further study. It would also be interesting to redo the protostellar calculations of [Maz80,Bod66,Hay62] using the revised $D(p,\gamma)^3He$ S-factor. These calculations predict that undepleted primordial deuterium could possibly exist in the outer envelopes of high mass stars. At least one of the calculations [Hay62] indicates an inverse relationship between the $D(p,\gamma)^3He$ S-factor and the timescale for nuclear burning. Although current protostellar theory argues against finding undepleted primordial deuterium in stars

[Gal95], our new measurements could potentially have a bearing on further discussion of this topic.

7.3 Final Comments

The results of this $D(\vec{p},\gamma)^3He$ experiment have demonstrated how current methods can make a significant improvement in the studies of nuclear reactions below the Coulomb barrier. In the current case, the use of a high purity germanium detector and polarized beams have allowed us to extract the energy dependence and multipole components of the $D(p,\gamma)^3He$ reaction with significantly better accuracy than has been possible before. Our results show that the direct capture model, while still doing an adequate job from a qualitative standpoint, has not been able to predict either the absolute magnitude or the energy dependence of our $D(p,\gamma)^3He$ data (to within experimental error). Recent three-body calculations [Fri91,Sch95] also show discrepancies with the current data.

Based on the above observations, we conclude that continued study of low energy nuclear reactions, from both an experimental and theoretical perspective, should be pursued in the future.

Appendix A

Code Used for Calculating the HPGe Kinematic Response Function

What follows is the user-written main program, GREG.MOR, associated with the EGS4 simulation system [Nel85]. It is written in the MORTRAN programming language. The process being simulated is that of a γ-ray interacting with the HPGe crystal of the current experiment (the exact geometry is used). The γ-ray is launched in a random direction from a point emitting γ-ray source. The solid angle for γ-ray emissions is chosen so as to completely illuminate the front face of the HPGe. For each launch, the energy deposited in the crystal, and the direction of the initial launch, is recorded. The output of this program is a plot such as the one shown in Figure 3.9. By simply recording the number of full energy peak counts and the total number of γ-rays launched, this program can also be used to obtain a value for the intrinsic photopeak efficiency, ε (see section 3.2).

```
%L
%E
!INDENT M 4;  "INDENT MORTRAN LISTING BY 4 PER NESTING LEVEL"
!INDENT F 2;  "INDENT FORTRAN OUTPUT BY 2 PER NESTING LEVEL"
"*************************************************************************"
"                                        "
"            **************                      "
"            *          *                  "
"            * GREG.MOR *                    "
```

```
"              *        *                    "
"              **************                 "
"                                           "
"*************************************************************************"

"-------------------------------------------------------------"
"STEP 1:  USER-OVERRIDE-OF-EGS4-MACROS                       "
"-------------------------------------------------------------"
REPLACE {$MXMED} WITH {1}   "only 1 medium in the problem(default 10)"
REPLACE {$MXREG} WITH {5}   "only 5 geometric regions (default 20)"
REPLACE {$MXSTACK} WITH {15}"less than 15 particles on stack at once  "
REPLACE {$EBIN} WITH {55}
REPLACE {$BWIDTH} WITH {.1}
"DEFINE A COMMON TO PASS INFORMATION TO THE GEOMETRY ROUTINE
HOWFAR"
REPLACE {;COMIN/GEOM/;} WITH {;COMMON/GEOM/Z3,Z2,z1,R1,R2,ITEST;}
"DEFINE A COMMON FOR SCORING IN AUSGAB"
REPLACE {;COMIN/SCORE/;} WITH {;COMMON/SCORE/EHIST;}
"DEFINE COMMON FOR BINNING STUFF"
COMMON/BINS/EBIN($EBIN);
INTEGER RESULT(300);
CHARACTER LINE(48);

"    THE FOLOWING RANDOM NUMBER GENERATOR NEEDS TO BE USED ON
A VAX"
"    REMOVE THIS MACRO DEFINITION ON AN IBM MACHINE SINCE THE
EGS4 "
"    DEFAULT WORKS THERE                                    "
REPLACE {;COMIN/RANDOM/;} WITH {;COMMON/RANDOM/IXX,IXXX;}
REPLACE {$RANDOMSET#;} WITH
{IXX=IXX*663608941;{P1}=0.5 + IXX*0.23283064E-09;IXXX=IXXX+1;}
;COMIN/BOUNDS,GEOM,MEDIA,MISC,THRESH,RANDOM,SCORE/;
"     THE ABOVE EXPANDS INTO A SERIES OF COMMON STATEMENTS"

"-------------------------------------------------------------"
"STEP 2 PRE-HATCH-CALL-INITIALIZATION                        "
"-------------------------------------------------------------"
$TYPE MEDARR(24) /$S'GERMANIUM',15*' '/; "PLACE MEDIUMN ARRAY"
"                  $S IS A MORTRAN MACRO TO EXPAND STRINGS"
"                  $TYPE IS INTEGER (F4) OR CHARACTER*4(F77)"
DO I=1,24[MEDIA(I,1)=MEDARR(I);]"THIS IS TO AVOID A DATA STATEMENT
FOR"
"                       A VARIABLE IN COMMON"
"                  $S IS A MORTRAN MACRO TO EXPAND STRINGS"
"                  $TYPE IS INTEGER (F4) OR CHARACTER*4(F77)"

/MED(1),MED(4),MED(5)/=0; /MED(2),MED(3)/=1; " VAC IN 1,4,5 ;GE IN 2,3"
ECUT(2)=.61;
PCUT(2)=0.011;
```

```
%E
"-------------------------------------------------------------------"
"STEP 3  HATCH-CALL                                                 "
"-------------------------------------------------------------------"
;OUTPUT;('1START SIM1'//' CALL HATCH TO GET CROSS-SECTION DATA'/);
CALL HATCH;"   PICK UP CROSS SECTION DATA"
;OUTPUT AE(1)-0.511, AP(1);
(' KNOCK-ON ELECTRONS CAN BE CREATED AND ANY ELECTRON
FOLLOWED DOWN TO'
/T40,F8.3,' MeV KINETIC ENERGY'/
 ' BREM PHOTONS CAN BE CREATED AND ANY PHOTON FOLLOWED DOWN
TO',
/T40,F8.3,' MeV '/);"NOTE, AE VALUES CAN OVER-RIDE ECUT VALUES"

"-------------------------------------------------------------------"
"STEP 4  INITIALIZATION-FOR-HOWFAR                                  "
"-------------------------------------------------------------------"
Z3=33.93;   "far boundary plane"
Z1=23.01;   "NEAR BOUNDARY PLANE"
R2=4.1275;  " DETECTOR RADIUS"
Z2=24.30;
R1=0.51;
"-------------------------------------------------------------------"
"STEP 5  INITIALIZATION-FOR-AUSGAB                                  "
"-------------------------------------------------------------------"

"-------------------------------------------------------------------"
"STEP 6  DETERMINATION-OF-INCIDENT-PARTICLE-PARAMETERS              "
"-------------------------------------------------------------------"
"DEFINE INITIAL VARIABLES FOR 5.5 MEV BEAM OF PHOTONS"

IQIN=0;"            INCIDENT CHARGE - PHOTONS"
EIN= 5.5;"          INCIDENT ENERGY"
/XIN,YIN,ZIN/=0.0;"    INCIDENT AT ORIGIN"
IRIN=1;"            STARTS IN REGION 1"
WTIN=1.0;"          WEIGHT = 1 SINCE NO VARIANCE REDUCTION USED"
IXX=123456789;  "     RANDOM NUMBER INITIALIZE"
"-------------------------------------------------------------------"
"STEP 7  SHOWER-CALL                                                "
"-------------------------------------------------------------------"
DO JJ=1,300[RESULT(JJ)=0];
NCASE=300000; "INITIATE THE SHOWER NCASE TIMES"
DO ITEST=1,NCASE [
$RANDOMSET RN1;
$RANDOMSET RN2;
W1=SIN(RN1*0.175);
TH1=W1/SIN(0.175);  "RANDOM NUMBER BETWEEN ZERO AND ONE."
"                    THIS NUMBER IS WEIGHTED IN A SIN FASHION."
THETA=TH1*0.175;   "ANGLE FROM Z-AXIS IN RADIANS.  THIS ANGLE,"
"                   WITH RANGE FROM ZERO TO TEN DEGREES,"
```

```
"                        IS WEIGHTED SO AS TO GIVE EQUAL PROBABILITY"
"                        FOR ALL DIRECTIONS IN 3-D SPACE."
PHI=RN2*6.2831854;     "ANGLE FROM X-AXIS IN RADIANS"
UIN=SIN(THETA)*COS(PHI);
VIN=SIN(THETA)*SIN(PHI);
WIN=COS(THETA);
"PSI=ATAN(VIN/WIN)*57.295779;ANGLE OFF HPGE AXIS IN REACTION
PLANE,"
PSI=ACOS(-VIN)*57.295779;"ANGLE W/RESPECT TO BEAM AXIS"
 EHIST=0.0;  "ZERO ENERGY DEPOSITED IN THIS HISTORY"
 CALL SHOWER(IQIN,EIN,XIN,YIN,ZIN,UIN,VIN,WIN,IRIN,WTIN);
"  ;OUTPUT; (' ----------',/)"

 "INCREMENT BIN CORRESPONDING TO ENERGY DEPOSITED IN THIS
HISTORY"

 IBIN= MIN0 (IFIX(EHIST/$BWIDTH + 0.999),$EBIN);
 IF(IBIN.NE.0) [EBIN(IBIN)=EBIN(IBIN)+1;]
 IF(IBIN.EQ.55)[
  NUMC=NUMC+1;
  IANG=NINT(PSI);
  RESULT(IANG)=RESULT(IANG)+1;
"   Q1=Q1+P0(1,WIN);"
"   Q2=Q2+P0(2,WIN);"
 ]
]

"-------------------------------------------------------------"
"STEP 8   OUTPUT-OF-RESULTS                                   "
"-------------------------------------------------------------"

"PICK UP MAXIMUM BIN FOR NORMALIZATION"

"BINMAX=0.0;"
"DO J=1,$EBIN ["
"  BINMAX=MAX(BINMAX,EBIN(J));"
"   OUTPUT J,EBIN(J);(' EBIN(',I3,')= ',F12.5);"
"]"

"OUTPUT EIN,ZBOUND; (' RESPONSE FUNCTION'/' FOR A',F8.2,"
" ' MeV PENCIL BEAM OF PHOTONS ON A 'F7.2,' cm THICK SLAB OF NAI'"
" /T6,'ENERGY  COUNTS/INCIDENT PHOTON');"

"DO J=1,48 ["
"   LINE(J)=' ';  BLANK ENTIRE ARRAY"
"]"

"DO J=1,$EBIN ["
"   ICOL=IFIX(EBIN(J)/BINMAX*48.0+0.999);"
"   IF(ICOL. NE. 0)[LINE(ICOL)='*';]"
```

```
  "LOAD OUTPUT ARRAY AT DESIRED LOCATION"
"   OUTPUT $BWIDTH*J,EBIN(J)/FLOAT(NCASE),LINE;"
"    (F10.2,F10.4,48A1); "
"   IF(ICOL. NE. 0)[LINE(ICOL)=' ';]  REBLANK"
"]"
DO JJJ=80,100[
  OUTPUT JJJ,RESULT(JJJ);(I6,I6);
]
"Q1TOT=Q1/NUMC;"
"Q2TOT=Q2/NUMC;"
"OUTPUT Q1TOT,Q2TOT;(F10.5,F10.5);"
STOP;END;"END OF TUTOR3 MAIN ROUTINE"

%E
"*************************************************************************"
"                                                                         "
SUBROUTINE AUSGAB(IARG);
"                                                                         "
" In this AUSGAB routine for TUTOR3, we score the energy deposited       "
" in the detector region, region 2.  For IARG=0, an electron or          "
" photon step is about to occur and we score the energy deposited, if    "
" any.  Note that only electrons deposit energy during a step, and       "
" due to our geometry, electrons only take steps in region 2.  But       "
" there is no need to check this here.  For IARG=1,2 and 4, par-         "
" ticles have been discarded for falling below various energy cut-       "
" offs and all their energy is deposited locally (in fact EDEP is the    "
" particles K.E.).  This only happens in region 2.  For IARG=3, we       "
" are discarding the particle since it is in region 1 or 3, so we do     "
" not score its energy.  EHIST keeps track of the total energy depos-    "
" ited during each history.  In the main routine it is zeroed at the     "
" start of each history and binned at the end of each history.           "
"*************************************************************************"

;COMIN/EPCONT,SCORE,STACK/;
"WE USE EDEP FROM EPCONT, AND EHIST FORM SCORE"
IF(IARG.LE.2 .OR. IARG.EQ.4) [EHIST=EHIST+EDEP;]
"OUTPUT EDEP,EHIST,IARG;('AUSGAB----'/' EDEP,EHIST,IARG',2F12.5,I4);"
RETURN;END;"END OF AUSGAB"


"*************************************************************************"
"                                                                         "
SUBROUTINE HOWFAR;
"                                                                         "
"   HOWFAR FOR USE WITH TUTOR3 (SAME AS TUTOR1)                           "
"                                                                         "
"*************************************************************************"
COMIN/STACK,EPCONT,GEOM/;
" "
"    COMMON STACK CONTAINS X,Y,Z,U,V,W,IR,NP(STACK POINTER) "
```

```
"    COMMON EPCONT CONTAINS IRNEW, USTEP, IDISC "
"    COMMON GEOM CONTAINS Z2,Z1,rhob- defines boundaries "
" "

";OUTPUT  NP,X(NP),Y(NP),Z(NP),U(NP),V(NP),W(NP),IR(NP);"
"('NP X Y Z: ' I4,3F12.5,/,'U V W:          ',3F12.5,/,'IR:      ',I4);"
"OUTPUT ZBOUND,USTEP; (' ZBOUND,USTEP: ',2F12.5,/);"
""
""
"REGION LOOP"
IF(IR(NP).EQ.5)[
   IDISC=1;
   RETURN;"TERMINATE THIS HISTORY: IT IS OUTSIDE THE DETECTOR"
] "END OF IR EQ 5"

ELSEIF(IR(NP).EQ.4)["IN THE HOLE"
   IF(W(NP).GT.0.0)["GOING FORWARD"
    ZVAL=(Z3-Z(NP))/W(NP);
    A=U(NP)**2+V(NP)**2;
    B=2*(U(NP)*X(NP)+V(NP)*Y(NP));
    C=X(NP)**2+Y(NP)**2-R1**2;
    IF (A.EQ.0.0)["MOTION ALONG Z-AXIS"
     IF (ZVAL.GT.USTEP)[RETURN;"VALID STEP"]
     ELSE[USTEP=ZVAL+.000001;IRNEW=5;RETURN;]
    ]
    FAC=B*B-4*A*C;
    IF(FAC.LT.0.0)["NO INTERSECTION"
     RHOVAL=1000.0;]
    ELSE["INTERSECTION"
     RHOVAL1=(-B+SQRT(FAC))/(2*A);
     RHOVAL2=(-B-SQRT(FAC))/(2*A);
     IF(RHOVAL1.LE.0.0)[RHOVAL1=1000.0;]
     IF(RHOVAL2.LE.0.0)[RHOVAL2=1000.0;]
     RHOVAL=MIN(RHOVAL1,RHOVAL2);]
    STEPVAL=MIN(ZVAL,RHOVAL);
    IF (STEPVAL.GT.USTEP)[RETURN;"VALID STEP"]
    ELSE[
      USTEP=STEPVAL+.000001;
      IF (RHOVAL.LT.ZVAL) ["HIT SIDE"
       IRNEW=3;
       RETURN;]
      ELSE["HIT BACK, REGION 5"
        IRNEW=5;
        RETURN;]
    ]
   ] "END OF W GT 0"

   IF(W(NP).EQ.0.0)["NO Z COMPONENT"
    A=U(NP)**2+V(NP)**2;
    B=2*(U(NP)*X(NP)+V(NP)*Y(NP));
```

```
 C=X(NP)**2+Y(NP)**2-R1**2;
 IF (A.EQ.0.0)["NO MOTION!";IDISC=1;RETURN;]
 FAC=B*B-4*A*C;
 IF(FAC.LT.0.0)["NO INTERSECTION"
  RHOVAL=1000.0;]
 ELSE["INTERSECTION"
  RHOVAL1=(-B+SQRT(FAC))/(2*A);
  RHOVAL2=(-B-SQRT(FAC))/(2*A);
  IF(RHOVAL1.LE.0.0)[RHOVAL1=1000.0;]
  IF(RHOVAL2.LE.0.0)[RHOVAL2=1000.0;]
  RHOVAL=MIN(RHOVAL1,RHOVAL2);]
 STEPVAL=RHOVAL;
 IF (STEPVAL.GT.USTEP)[RETURN;"VALID STEP"]
 ELSE[
   USTEP=STEPVAL+.000001;
   IRNEW=3;
   RETURN;]
] "END OF W EQ 0"

IF(W(NP).LT.0.0)["GOING BACKWARDS"
 ZVAL=(Z2-Z(NP))/W(NP);
 A=U(NP)**2+V(NP)**2;
 B=2*(U(NP)*X(NP)+V(NP)*Y(NP));
 C=X(NP)**2+Y(NP)**2-R1**2;
 IF (A.EQ.0.0)["MOTION ANTI-ALONG Z-AXIS"
  IF (ZVAL.GT.USTEP)[RETURN;"VALID STEP"]
  ELSE[USTEP=ZVAL+.000001;
  IRNEW=2;RETURN;]
 ]
 FAC=B*B-4*A*C;
 IF(FAC.LT.0.0)["NO INTERSECTION"
  RHOVAL=1000.0;]
 ELSE["INTERSECTION"
  RHOVAL1=(-B+SQRT(FAC))/(2*A);
  RHOVAL2=(-B-SQRT(FAC))/(2*A);
  IF(RHOVAL1.LE.0.0)[RHOVAL1=1000.0;]
  IF(RHOVAL2.LE.0.0)[RHOVAL2=1000.0;]
  RHOVAL=MIN(RHOVAL1,RHOVAL2);]
 STEPVAL=MIN(ZVAL,RHOVAL);
 IF (STEPVAL.GT.USTEP)[
  RETURN;]
 ELSE[
   USTEP=STEPVAL+.000001;
   IF (RHOVAL.LT.ZVAL) ["HIT SIDE"
     IRNEW=3;
     RETURN;]
   ELSE["HIT FRONT, REGION 2"
     IRNEW=2;
     RETURN;]
 ]
```

```
   ] "END OF W LT 0"
  ] "END OF IR EQ 4"

ELSEIF(IR(NP).EQ.3)["WE ARE IN THE GE ANNULUS, REGION 3"
   IF(W(NP).GT.0.0)["GOING FORWARD"
    ZVAL=(Z3-Z(NP))/W(NP);
    A=U(NP)**2+V(NP)**2;
    B=2*(U(NP)*X(NP)+V(NP)*Y(NP));
    C=X(NP)**2+Y(NP)**2-R1**2;
    IF (A.EQ.0.0)["MOTION ALONG Z-AXIS"
     IF (ZVAL.GT.USTEP)[RETURN;"VALID STEP"]
     ELSE[USTEP=ZVAL+.000001;IRNEW=5;RETURN;]
    ]
    FAC=B*B-4*A*C;
    IF(FAC.LT.0.0)["NO INTERSECTION"
     RHOVAL=1000.0;]
    ELSE["INTERSECTION WITH INNER CYL"
     RHOVAL1=(-B+SQRT(FAC))/(2*A);
     RHOVAL2=(-B-SQRT(FAC))/(2*A);
     IF(RHOVAL1.LE.0.0)[RHOVAL1=1000.0;]
     IF(RHOVAL2.LE.0.0)[RHOVAL2=1000.0;]
     RHOVAL=MIN(RHOVAL1,RHOVAL2);]
    C=X(NP)**2+Y(NP)**2-R2**2;
    FAC=B*B-4*A*C;
    IF(FAC.LT.0.0)["NO INTERSECTION WITH OUTER CYL"
     SVAL=1000.0;]
    ELSE["INTERSECTION WITH OUTER CYL"
     SVAL1=(-B+SQRT(FAC))/(2*A);
     SVAL2=(-B-SQRT(FAC))/(2*A);
     IF(SVAL1.LE.0.0)[SVAL1=1000.0;]
     IF(SVAL2.LE.0.0)[SVAL2=1000.0;]
     SVAL=MIN(SVAL1,SVAL2);]
    TVAL=MIN(SVAL,RHOVAL);"TVAL IS DISTANCE TO NEAREST BNDRY"
    STEPVAL=MIN(ZVAL,TVAL);
    IF (STEPVAL.GT.USTEP)[RETURN;]
    ELSE[
      USTEP=STEPVAL+.000001;
      IF (ZVAL.LE.TVAL) ["HIT BACK"
       IRNEW=5;
       RETURN;]
      ELSE["HIT INNER CYL OR OUTER CYL"
       IF (SVAL.LT.RHOVAL)["HIT OUTER CYL"
        IDISC=1;
        RETURN;]
       ELSE["HIT INNER CYL"
        IRNEW=4;
        RETURN;]
      ]
    ]
   ] "END OF W GT 0"
```

```
IF(W(NP).EQ.0.0)["NO Z COMPONENT"
 A=U(NP)**2+V(NP)**2;
 B=2*(U(NP)*X(NP)+V(NP)*Y(NP));
 C=X(NP)**2+Y(NP)**2-R1**2;
 IF (A.EQ.0.0)["NO MOTION";IDISC=1;RETURN;]
 FAC=B*B-4*A*C;
 IF(FAC.LT.0.0)["NO INTERSECTION"
  RHOVAL=1000.0;]
 ELSE["INTERSECTION WITH INNER CYL"
  RHOVAL1=(-B+SQRT(FAC))/(2*A);
  RHOVAL2=(-B-SQRT(FAC))/(2*A);
  IF(RHOVAL1.LE.0.0)[RHOVAL1=1000.0;]
  IF(RHOVAL2.LE.0.0)[RHOVAL2=1000.0;]
  RHOVAL=MIN(RHOVAL1,RHOVAL2);]
 C=X(NP)**2+Y(NP)**2-R2**2;
 FAC=B*B-4*A*C;
 IF(FAC.LT.0.0)["NO INTERSECTION WITH OUTER CYL"
  SVAL=1000.0;]
 ELSE["INTERSECTION WITH OUTER CYL"
  SVAL1=(-B+SQRT(FAC))/(2*A);
  SVAL2=(-B-SQRT(FAC))/(2*A);
  IF(SVAL1.LE.0.0)[SVAL1=1000.0;]
  IF(SVAL2.LE.0.0)[SVAL2=1000.0;]
  SVAL=MIN(SVAL1,SVAL2);]
 TVAL=MIN(SVAL,RHOVAL);"TVAL IS DISTANCE TO NEAREST BNDRY"
 STEPVAL=TVAL;
 IF (STEPVAL.GT.USTEP)[RETURN;]
 ELSE[
   USTEP=STEPVAL+.000001;
   IF (SVAL.LT.RHOVAL)["HIT OUTER CYL"
      IDISC=1;
      RETURN;]
   ELSE["HIT INNER CYL"
      IRNEW=4;
      RETURN;]
 ]
] "END OF W EQ 0"

IF(W(NP).LT.0.0)["GOING BACKWARDS"
 ZVAL=(Z2-Z(NP))/W(NP);
 A=U(NP)**2+V(NP)**2;
 B=2*(U(NP)*X(NP)+V(NP)*Y(NP));
 C=X(NP)**2+Y(NP)**2-R1**2;
 IF (A.EQ.0.0)["MOTION ANTI-ALONG Z-AXIS"
  IF (ZVAL.GT.USTEP)[RETURN;"VALID STEP"]
  ELSE[USTEP=ZVAL+.000001;IRNEW=2;return;]
 ]
 FAC=B*B-4*A*C;
 IF(FAC.LT.0.0)["NO INTERSECTION"
```

```
      RHOVAL=1000.0;]
     ELSE["INTERSECTION WITH INNER CYL"
      RHOVAL1=(-B+SQRT(FAC))/(2*A);
      RHOVAL2=(-B-SQRT(FAC))/(2*A);
      IF(RHOVAL1.LE.0.0)[RHOVAL1=1000.0;]
      IF(RHOVAL2.LE.0.0)[RHOVAL2=1000.0;]
      RHOVAL=MIN(RHOVAL1,RHOVAL2);]
     C=X(NP)**2+Y(NP)**2-R2**2;
     FAC=B*B-4*A*C;
     IF(FAC.LT.0.0)["NO INTERSECTION WITH OUTER CYL"
      SVAL=1000.0;]
     ELSE["INTERSECTION WITH OUTER CYL"
      SVAL1=(-B+SQRT(FAC))/(2*A);
      SVAL2=(-B-SQRT(FAC))/(2*A);
      IF(SVAL1.LE.0.0)[SVAL1=1000.0;]
      IF(SVAL2.LE.0.0)[SVAL2=1000.0;]
      SVAL=MIN(SVAL1,SVAL2);]
     TVAL=MIN(SVAL,RHOVAL);"TVAL IS DISTANCE TO NEAREST BNDRY"
     STEPVAL=MIN(ZVAL,TVAL);
     IF (STEPVAL.GT.USTEP)[RETURN;]
     ELSE[
       USTEP=STEPVAL+.000001;
       IF (ZVAL.LE.TVAL) ["HIT FRONT"
         IRNEW=2;
         RETURN;]
       ELSE["HIT INNER CYL OR OUTER CYL"
         IF (SVAL.LT.RHOVAL)["HIT OUTER CYL"
           IDISC=1;
           RETURN;]
         ELSE["HIT INNER CYL"
           IRNEW=4;
           RETURN;]
       ]
     ]
    ] "END OF W LT 0"

] "END OF IR EQ 3"


ELSEIF(IR(NP).EQ.2)["WE ARE IN THE detector, CHECK THE GEOMETRY"
    IF(W(NP).GT.0.0)["going forward"
                "find length of step in this direction"
                "that would hit back z plane"
       ZVAL=(Z2-Z(NP))/W(NP);
""
"      NOW FIND LENGTH OF STEP IN THIS DIRECTION THAT WOULD HIT"
"      SIDE OF DETECTOR"
""
       CALL PLNDIS(X(NP),Y(NP),U(NP),V(NP),R2,DIST,VECNORM);
""
```

```
"           DIST- DISTANCE TO WALL IN PLANE OF CONSTANT Z"
"           VECNORM- NORM FOR UNIT VECTOR PROJECTED INTO PLANE"
""
""
    RHOVAL=DIST;
    STEPVAL=MIN(ZVAL,RHOVAL);
    IF (STEPVAL.GT.USTEP) [
    RETURN; "STEPSIZE LEGAL"]
""
    ELSE["           STEPSIZE TOO LARGE"
      USTEP=STEPVAL+.000001;
      IF (RHOVAL.LE.ZVAL) ["HIT SIDE"
       IDISC=1;
       RETURN;]
      ELSE["HIT BACK, EITHER REGION 3 OR 4"
        XNEW=X(NP)+U(NP)*USTEP;
        YNEW=Y(NP)+V(NP)*USTEP;
        ZR=SQRT(XNEW**2+YNEW**2);
        IF (ZR.LT.R1) ["HIT REGION 4"
         IRNEW=4;
         RETURN;]
        ELSEIF(ZR.EQ.R1)["HIT REGION 3 OR 4"
          SCOS=U(NP)*X(NP)+V(NP)*Y(NP);
          IF(SCOS.LE.0.0)[
           IRNEW=4;RETURN;]
         ELSE[IRNEW=3;RETURN;]
        ]
        ELSE[
         IRNEW=3;
         RETURN;]
      ]
    ]
  ]             "END OF W(NP) GT 0"
""
"  w(NP) LT 0 LOOP"
""
  ELSEIF(W(NP).LT.0)[ "       gOING BACKWARDS"
            "FIND LENGTH OF STEP IN THIS DIRECTION"
            "THAT WOULD HIT FRONT Z PLANE"
    ZVAL=(Z1-Z(NP))/W(NP);
""
"    NOW FIND LENGTH OF STEP IN THIS DIRECTION THAT WOULD HIT"
"    SIDE OF DETECTOR"
""
    CALL PLNDIS(X(NP),Y(NP),U(NP),V(NP),R2,DIST,VECNORM);
""
"           DIST- DISTANCE TO WALL IN PLANE OF CONSTANT Z"
"           VECNORM- NORM FOR UNIT VECTOR PROJECTED INTO PLANE"
""
    RHOVAL=DIST;
```

```
""
     STEPVAL=MIN(ZVAL,RHOVAL);
     IF (STEPVAL.GT.USTEP) [
     RETURN; "STEPSIZE LEGAL"]
""
     ELSE["          STEPSIZE TOO LARGE- THIS TIME"
"                  MUST DETERMINE WHICH REGION ENTERED"
       USTEP=STEPVAL+.000001;
       IF(RHOVAL.LE.ZVAL)[  "ENTERED REGION 1"
          IDISC=1;
          RETURN;
       ]
       ELSE["          ENTERED REGION 1"
          IDISC=1;
          RETURN;
       ]
     ]
  ]          "END OF W(NP) LT 0"
""
"  w(NP) EQ 0 LOOP"
""
  ELSEIF(W(NP).EQ.0)["    NO Z COMPONENT"
     DX=X(NP)*X(NP)+Y(NP)*Y(NP);
     CALL PLNDIS(X(NP),Y(NP),U(NP),V(NP),R2,DIST,VECNORM);
     STEPVAL=DIST;
     IF(STEPVAL.GT.USTEP)[
     RETURN;  "STEPSIZE OKAY"]
     ELSE["              STEPSIZE TOO LARGE"
       USTEP=STEPVAL+.000001;
       IDISC=1;
       RETURN;
     ]
  ]"          END OF W(NP) EQ 0"
]"            END OF IR EQ 2"
ELSEIF(IR(NP).EQ.1)["REGION 1  - IN FRONT OF DETECTOR"
  IF(W(NP).LE.0) [IDISC=1; "BAG PARTICLES IN THIS REGION UNLESS "
                 "MOVING FORWARD"
     RETURN;
  ]
  ELSE["    MOVING FORWARD"
""
"    BAG PARTICLES UNLESS MOVING SUCH THAT THEY WILL HIT
DETECTOR"
""
     ZVAL=(Z1-Z(NP))/W(NP);
     CALL PLNDIS(X(NP),Y(NP),U(NP),V(NP),R2,DIST,VECNORM);
""
     IF((U(NP)**2+V(NP)**2).GT.0)["  PARTICLE NOT PARALLEL TO Z"
     RHOVAL=DIST;
       IF(ZVAL.LE.RHOVAL) ["  WILL HIT DETECTOR"
```

```
            IF(ZVAL.LE.USTEP)["STEP TOO LARGE"
               USTEP=ZVAL+.000001;
               IRNEW=2;
               RETURN;
            ]
            ELSE [RETURN;   "STEP NOT TOO LARGE"]
         ]
         ELSE["  BAG IF NOT AIMED AT DETECTOR"
            IDISC=1;
            RETURN;
         ]
""
      ]
      ELSE[  "PARALLEL TO Z -- WILL HIT"
         IF(ZVAL.LE.USTEP)["STEP TOO LARGE"
            USTEP=ZVAL+.000001;
            IRNEW=2;
            RETURN;
         ]
            ELSE [
            RETURN;   "STEP NOT TOO LARGE"]
      ]   "END OF PARALLEL TO Z"
   ]   "END OF MOVING FORWARD"
]"      END OF IR 1"
END;"END OF SUBROUTINE HOWFAR"




SUBROUTINE PLNDIS(X,Y,U,V,RHOB,DIST,VECNORM);

     A=U**2+V**2;
     B=2*(U*X+V*Y);
     C=X**2+Y**2-Rhob**2;
     FAC=B*B-4*A*C;
     IF(A.LE.0.0)[DIST=1000.0;RETURN;]
     IF(FAC.LT.0.0)["NO INTERSECTION"
       dist=1000.0;]
     ELSE["INTERSECTION"
       RHOVAL1=(-B+SQRT(FAC))/(2*A);
       RHOVAL2=(-B-SQRT(FAC))/(2*A);
       IF(RHOVAL1.LE.0.0)[RHOVAL1=1000.0;]
       IF(RHOVAL2.LE.0.0)[RHOVAL2=1000.0;]
      dist=MIN(RHOVAL1,RHOVAL2);]
RETURN;
END;    "SUBROUTINE PLNDIS"
""
```

```
"""
%E

    real function p0(L,x);

"     Calculates Legendre polynomials"

    IF ( L .eq. 0 ) [
      p0 = 1.;]
    ELSEIF ( L .eq. 1 )[
      p0 = x;]
    ELSEIF ( L .eq. 2 )[
      p0 = 0.5*(3.0*x*x - 1.);]
    ELSEIF ( L .eq. 3 )[
      p0 = 0.5*(5.0*x*x*x - 3.*x);]
    ELSEIF ( L .eq. 4 )[
      p0 = ((35.0*x*x - 30.0)*x*x + 3.0)/8.0;]
    ELSE[
      p0 = 0.;]
    RETURN;
    END;
```

Appendix B

The Deconvolution Computer Code

What follows is the computer code FCN_SFACT, written in VAX Fortran77, that was used to deconvolute the raw D($\vec{p}$,γ)^{3}He full energy peak spectra (such as the one shown in Figure 3.1b). This code operates as a subroutine of the MINUIT fitting program [Jam77]. FCN_SFACT requires the following input files: a file containing the raw spectral data (in a channel vs. counts format); a file containing information about the spectral data, such as energy calibration, lab angle of the detector, etc.; a file containing the kinematic response function of the HPGe at 5.5 MeV (calculated using the EGS4 code shown in Appendix A); and a file containing starting values for all the free parameters. The free parameters determined by this code were SP0, SP1, and CENTR. The SP0 and SP1 values are related to the S-factor, $S(E_{cm})$, as follows: $S(E_{cm})=SP0(1+E_{cm}SP1)$. Thus, it is clear that $S_0=SP0$ and $S_1=(SP0)(SP1)$, with S_0 and S_1 as defined in Chapter 5. The parameter CENTR determines the location (in spectral channel) of the γ-rayenergy which corresponds to $E_p(lab)=80$ keV.

```
      Subroutine FCN(npar,G,F,X,iflag)
C
C                 FCN_SFACT.FOR
C
C     ********************ASSUME S-FACTOR SHAPE**********************
C
C     This program is for deconvoluting HPGe spectra. It has been
C     written specifically for the d(p,g)3He experiment, but, with
C     a few changes, should be adaptable to any capture reaction.  It
C     works by assuming a functional form for the cross section, and then
C     fitting the data to a series of response functions whose amplitudes
C     follow the cross section form. The fitting is done by MINUIT.
C     This program operates as a subroutine which is called by the MINUIT
C     code.
C     The functional form assumed for the yield is:
C       Y=(dE/stp(Elab))*(SP0*(1.0+SP1*Ecm)/Ecm)*ex1
C     where:
C       ex1=exp(-25.639/sqrt(Ecm))
C       dE is the energy width (Ep) of each channel
C     and stp is the stopping cross section.
C
C     The deuterium areal density is actually 2*dE/stp(E).  This
C     factor of 2 does not appear in the expression for Y because
C     it has been absorbed into the value of SP0.
C
C     -Greg Schmid, 9/94
C
C     ---------------------------------------------------------
C
C     This version has been modified to allow the convolution
C     of the the intrinsic HPGe response function with the kinematic
C     response.  The HPGe response function consists of three parts:
C       1. A gaussC       2. A skewed gaussian
C       3. A smoothed step function
C     These three components are convoluted with the kinematic
C     response to produce the final response function.  This final
C     response function is then used to deconvolute the full energy
C     peak.
C
C     The input parameters from the cards.info file are:
C       X(1)=SP0
C       X(2)=SP1
C       X(3)=centroid of highest energy response function
C       X(4)=Fraction of step
C       X(5)=Ratio of Skew/gauss
C       X(6)=Beta*cal
C
C     -Greg Schmid, 9/94
C
```

```
      real sigma,pi,zero,str2(21)
      real ichan(21),ichan2(21),iang(21),iang2(21),rkin(21),str(21)
       real*8 G(100),X(100),F,werr(100),U(100),xnam(100),max,nu
C
      character*50 Amonte
      common/greg/data(200),error(200),tchisq,NDATA,IWID
      common/greg2/bkgd,theta,cal,ener(100),nfree
      common/greg3/FWHM,str3(100,21),rmonte(30),dE(100)
      common/greg4/R1(100,200),R2(100,200),R3(100,200)
      common/parext/U,xnam,werr,max,nu
C
C
      pi=3.1415927
      zero=0.0
C
C
       go to (10,20,30,40,50,60) iflag
   10 continue
       open(unit=1,name='infos.dat',status='old')
C
C     The variable cal is the spectrum calibration in
C     keV per channel.
C
      read(1,*)cal
C
C     Enter # of data points in spectrum to be fit:
C
      read(1,*)NDATA
C
C     The following is equal to the number of amplitudes.
C
      read(1,*)IWID
C
C     HPGe angle:
C
      read(1,*)theta
C
C     Now enter the number of cosmic bkgd counts per channel.
C
      read(1,*)bkgd
C
C     The following is the montecarlo output file which contains
C     angle vs. detector response.
C
      read(1,91)Amonte
   91 format(A50)
C
      close(unit=1)
```

```
C
C ******Detector resolution set at 4.2 keV at 5.5 MeV******
C
      FWHM=4.2/cal
C
C ***********************************************************
C
C     Now read in Monte*.out file:
C
C
      open(unit=11,name=Amonte,status='old')
      do 31 k=1,21
      read(11,*)iang(k),rmonte(k)
   31 continue
      close(unit=11)
C
C
C     Now calculate the exact Ep energy at each centroid #:
C
C     First, I calculate the gamma ray energy for Ep=0.0
C
      call eptog(0.0,theta,egamlow)
C
      Eplab=79.7        !This is the top Ep energy
C
      tener=Eplab
      call eptog(Eplab,theta,Egamma)
      do 32 l=IWID,1,-1
      Egamma=Egamma-cal
      if (l.gt.1)then
      call gtoep(egamma,theta,Eplab)
      ener(l)=(Eplab+tener)/2.0
C     dE is the energy width in Ep(lab) for the lth channel
      dE(l)=1000*(tener-Eplab)   !dE is stored in units of eV
      tener=Eplab
      else
      Eplab=0.0
      ener(l)=(Eplab+tener)/2.0
      dE(l)=1000.0*(tener-Eplab)
      tener=0.0
      endif
   32 continue
C
C
C ********** Calculate kinematic response function***********
C
C     The result is read into the array str3(100,21)
C
      nangle=int(theta+.5)
C
```

```
C
C    Now I loop over the number of centroids:
C
     do 71 icent=1,IWID,1
     Ep=ener(icent)
C
C
     call grkin2(Ep,theta,iang2,rkin)
C
C    Determine energy of central angle
     do 72 l=1,21
     if (iang2(l).eq.nangle)then
      const=rkin(l)
     endif
  72 continue
C    Now find the energy difference between central
C    angle and surrounding angles.  Once this is done,
C    The energies are changed to channels.
     do 73 l=1,21
     funct=rmonte(l)
     energy=rkin(l)
     ediff=energy-const
     chan=(ediff)/cal
C    Roundoff chan to nearest integer value
     if (chan.ge.0.0)then
     ichan(l)=int(chan+.5)
     endif
     if (chan.lt.0.0)then
     ichan(l)=int(chan-.5)
     endif
C
     str(l)=funct
  73 continue
C    If there is more than one response at one channel
C    I then add the responses at that channel to
C    obtain a total response at that channel
     tot1=0.0
     do 74 j=-10,10
     jjj=11+j
     do 75 l=1,21
     if (ichan(l).eq.j)then
      tot1=tot1+str(l)
     endif
  75 continue
     str2(jjj)=tot1
     tot1=0.0
  74 continue
C    Now normalize the resulting response function.
     total=0.0
     do 76 l=1,21
```

```
      total=total+str2(l)
    76 continue
       do 77 l=1,21
      str3(icent,l)=str2(l)/total
    77 continue
    71 continue
C
C
C
C     Read in data:
C
       open(unit=20,status='old')
      do 33 l=1,NDATA
        read(20,*)chan,data(l),error(l)
    33 continue
      close(unit=20)
      return
C
    20 continue
      return
C
    30 continue
C
C     Fitting done!  Output results:
C
      fr3=X(4)                !This is the step fraction
      rat=X(5)               !This is the ratio frac2/frac1
      fr1=(1-fr3)/(1+rat)       !This is the gaussian fraction
      fr2=fr1*rat             !This is the skew gaussian fraction
      ST=1.0-(frac1+frac2)
       open(unit=10,name='fits.out',status='new')
       open(unit=95,name='plots.out',status='new')
      write(10,81)' Reduced chi-squared is: ',Tchisq/nfree
       write(10,*)' '
       write(10,82)' SP0 is: ',X(1),' +/- ',werr(1)
       write(10,83)' SP1 is: ',X(2),' +/- ',werr(2)
      write(10,84)' The top centroid is: ',X(3),' +/- ',werr(3)
      write(10,85)' The step fraction is: ',X(4),' +/- ',werr(4)
      write(10,87)' The ratio skew/gauss is ',X(5),' +/- ',werr(5)
      write(10,88)' Beta is: ',X(6)/cal
    81 format(A25,F5.2)
    82 format(A8,F9.2,A5,F9.2)
    83 format(A8,F7.4,A5,F7.4)
    84 format(A22,F7.2,A5,F7.2)
    85 format(A23,F7.4,A5,F7.4)
    87 format(A25,F7.4,A5,F7.4)
    88 format(A10,F7.2)
      call calcresp(ener,theta,X,IWID,rmonte,iang,cal,FWHM,
     &            str3,NDATA,R1,R2,R3)
      do 99 l=1,NDATA
```

```
      call sumresp(dE,R1,R2,R3,ener,NDATA,IWID,l,X,tresp)
      funct=tresp+bkgd
      write(95,*)l,funct
   99 continue
      return
C
   40 continue
C
C     Now calculate each component of the response function,
C     R1,R2,R3.  Each component has a full response at each
C     centroid (up to 100 possible centroids), and has a maximum
C     of 200 possible points for each full response.  Thus, each
C     response function will be a 100x200 matrix (200 possible points
C     for each of 100 possible full response functions).  I will
C     create the matricies such that the first index is the
C     centroid # of the response (a first index of IWID corresponds to
C     a beam energy of Ep=79.7-(dE(IWID)/2) keV), and the second index
C     is related to the channel number under consideration.  The second
C     index will range from 1 to NDATA.
C
C
      call calcresp(ener,theta,X,IWID,rmonte,iang,cal,FWHM,
     &              str3,NDATA,R1,R2,R3)
C
C
C     Calculate the chi-squared function for Minuit to minimize:
C
C
      tchisq=0.0
      izdat=0
      nfree=0
      do 35 l=1,NDATA
      call sumresp(dE,R1,R2,R3,ener,NDATA,IWID,l,X,tresp)
C
C     Now add cosmic bkgd to sum.
C
      funct=tresp+bkgd
      if (data(l).gt..1)then
      chisq=((funct-data(l))/(error(l)))**2
      tchisq=tchisq+chisq
      else
      izdat=izdat+1
      endif
   35 continue
      nfree=NDATA-izdat-3
      F=tchisq
      return
C
   50 continue
      return
```

```
C
  60 continue
     return
C
     end
C
C    This is the end of the main program.  What follows are
C    the functions and subroutines that are also used:
C

     subroutine sumresp(dE,R1,R2,R3,ener,NDATA,IWID,ichan,X,tresp)
C
C    This subroutine sums all the response functions at a certain
C    channel (ichan).  In other words, this subroutine calculates
C    the total contribution, at a certain channel (ichan), from all
C    the response functions which are centered at channels
C    ICENT=1 thru ICENT=IWID.  Each response function consists of
C    three parts:  A gaussian; a skewed gaussian; and a smoothed
C    step function.  Each of these components is convoluted with
C    the kinematic response function.
C
C    X is the vector which contains the gaussian amplitudes at each
C    channel.
C
     real ener(100),R1(100,200),R2(100,200),R3(100,200),dE(100)
     real*8 X(100)
C    The following are the fractions for each piece of the total
C    response function:
     frac3=X(4)                !This is the step fraction
     ratio=X(5)                !This is the ratio frac2/frac1
     frac1=(1-frac3)/(1+ratio)     !This is the gaussian fraction
     frac2=frac1*ratio         !This is the skew gaussian fraction
C
     tresp=0.0
     rgauss=0.0
     rskew=0.0
     rsum=0.0
     rstep=0.0
C
     do 115 icent=1,IWID
C
C    Thus,ICENT=1 is the first channel where a response function
C    is centered.  ICENT=IWID is the last channel where a
C    response function is centered.
C
     Elab=ener(icent)
     if (Elab.lt..01)then
     Elab=.01
     endif
     Ecm=(2.0/3.0)*Elab
```

```
C
      ex1=exp(-25.639/sqrt(Ecm))

C     The following term is the assumed form for the yield:
      amp=(dE(icent)/stp(Elab))*(X(1)*(1.0+X(2)*Ecm)/Ecm)*ex1
C
C     The following are the three component terms for the
C     response function:
C
      rgauss=frac1*R1(icent,ichan)
      rskew=frac2*R2(icent,ichan)
      rstep=frac3*R3(icent,ichan)
C     Amp represents the predicted yield at pt. ichan due to
C     the response function with centroid labeled by icent.
C     (recall that the actual centroid is not necessarily an
C     integer).  Tresp is the sum of amp over all possible
C     centroids:
C
      rsum=amp*(rgauss+rskew+rstep)
      tresp=tresp+rsum
C
  115 continue
      return
      end
C
      function stp(E)
C
C     This function calculates the stopping cross section at
C     the given lab energy (E).  The target thickness for a certain
C     incident beam energy (given the fact that we are stopping an
C     80 keV beam in the target) is equal to dE/stp(E).  The
C     parameters are from a fit to the data of Phillips and
C     Reynolds (just like Griffiths did).
C
      if(E .le. 10.0) then
        xnum1=1/((10**.45)*4.7334)
        xnum2=1/((3404.97/10.0)*log(1+593.98/10.0+.0841))
        stp=sqrt(E)/((xnum1+xnum2)*sqrt(10.0))
      else
        slow=4.7334*(E**.45)
        shigh=(3404.97/E)*log(1.0+(593.98/E)+(.00841*E))
        astop=(1/slow)+(1/shigh)
        stp=1/astop
      endif
      return
      end
C
      subroutine eptog(Ep,theta,Egam)
C
C     This subroutine calculates the gamma ray energy for a given
```

```
C     beam energy and a given HPGe detector lab angle.
C
C     The following masses are in keV (i.e. E=M*c*c)
      Md=1875628.0
      Mp=938280.0
      Q=5494.0
      Mr=Md+Mp-Q
C
      t1=(Ep+Q)**2
      t2=2*Mr*(Ep+Q)
      t3=Ep*(Ep+2*Mp)
      t4=2*(Ep+Q+Mr)
      t5=2*cosd(theta)*SQRT(Ep*Ep+2*Ep*Mp)
      Egam=(t1+t2-t3)/(t4-t5)
      return
      end
C
      subroutine gtoep(egam,theta2,Ep)
C
C     This subroutine calculates the incident beam energy for a
C     given gamma ray energy and a given HPGe lab angle.
C
      real*16 den,ta,tb,tsq,ep1,ep2,term1,term2
C     The following are in keV
      Md=1875628.0
      Mp=938280.0
      Q=5494.0
      Mr=Mp+Md-Q
      if ((theta2.gt.89.99).and.(theta2.le.90.0))then
      theta2=89.99
      endif
      if ((theta2.lt.90.01).and.(theta2.gt.90.0))then
      theta2=90.01
      endif
      den=cosd(theta2)*egam
      ta=(egam-Md)/den
      tb=(2*egam*(Q+Mr)-Q*Q-2*Mr*Q)/(2*den)
      tsq=sqrt((ta*tb-Mp)**2-(ta*ta-1)*tb*tb)
      term1=Mp-ta*tb
      term2=ta*ta-1
      Ep1=(term1+tsq)/term2
      Ep2=(term1-tsq)/term2
      if (theta2.le.90.0)then
      Ep=Ep2
      endif
      if (theta2.gt.90.0)then
      Ep=Ep1
      endif
      return
      end
```

```
C
C
      Subroutine calcresp(ener,theta,X,IWID,rmonte,iang,cal,FWHM,
     &            str3,NDATA,R1,R2,R3)
C
      real R1(100,200),R2(100,200),R3(100,200)
      real*8 X(100)
      real str3(100,21)
      BETA=X(6)/cal
      CTOP=X(3)
      do 501 icent=1,IWID
C
C     The following will convolute the kinematic response function,which
C     has been stored in str3 as a function of Ep (i.e. str3(Ep,channel)),
C     with all of the intrinsic response functions.  The
C     normalized results are returned in R1,R2,R3.
C
      DCENT=CTOP-IWID+icent
C     Where DCENT is the data channel corresponding to the
C     centroid number icent.  In other words, it is the location
C     of the response function centroid.
C
      call gauss(icent,dcent,NDATA,IWID,FWHM,str3,R1)
      call skewgauss(icent,dcent,NDATA,BETA,IWID,FWHM,str3,R2)
      call step(icent,dcent,NDATA,IWID,FWHM,str3,R3)
C     The following line continues the Ep loop over all possible
C     centroid values:
  501 continue
C
      return
      end
C
C
      subroutine gauss(icent,dcent,NDATA,IWID,FWHM,str3,R1)
C
C     Calculates the gaussian piece of the response function
C     for a beam energy Ep (i.e. for a centroid channel dcent).  The
C     response function is calculated for all channels, 1 to NDATA.
C
      real R1(100,200),str3(100,21)
      sigma=FWHM/2.354
      pi=3.1415927
      fac=1/(2*pi)
      sfac=sqrt(fac)
      zres=0.0
C     The first step is to normalize the response function:
C     (the gaussian response function should already be normalized,
C     but I do it again just to be sure).
      tgauss=0.0
      do 600 ipos=1,NDATA
```

```
      YY=ipos-dcent
      pgauss=(sfac/sigma)*exp(-(1/(2*sigma*sigma))*
     &       YY*YY)
      tgauss=tgauss+pgauss
  600 continue
C
C     Now I do the convolution!
C
C     This sum is over the channel of the final response
C     function:
C
      do 602 ipos=1,NDATA
C
C     The next sum is over the str3 centroid (i.e. the channels where
C     a kinematic response strength exists...this strength will
C     be the amplitude of the str3 function):
      rtot=0.0
      index=0
      do 610 zcentr=dcent-10.0,dcent+10.0,1.0
      index=index+1
      YY=ipos-zcentr
      pgauss=(sfac/(sigma*tgauss))*exp(-(1/(2*sigma*sigma))*
     &      YY*YY)
      pgauss=pgauss*str3(icent,index)
      rtot=rtot+pgauss
  610 continue
C
C     We have now summed up the 21 gaussians at pt. ipos.  This
C     is the unnormalized total response function at pt. ipos.
C
      R1(icent,ipos)=rtot
      zres=zres+rtot
  602 continue
C
C     Now the response function will be normalized.
C
      do 620 ml=1,NDATA
      R1(icent,ml)=R1(icent,ml)/zres
  620 continue
C
      return
      end
C
C
      Subroutine skewgauss(icent,dcent,NDATA,BETA,IWID,FWHM,str3,
     &                     R2)
C
C     This subroutine makes a skewed gaussian function "centered" at
C     dcent (the centroid of this skewed function is actually off center,
C     but that is due to the functional form used).  The form of this
```

```
C     function is obtained by convoluting a gaussian response function
C     with a low energy exponential tail.
C
      real R2(100,200),str3(100,21)
      sigma=FWHM/2.354
      pi=3.1415927
      fac=1/(2*pi)
      sfac=sqrt(fac)
      zres=0.0
C     The first step is to normalize the response function:
      tskew=0.0
      do 700 ipos=1,NDATA
       YY=ipos-dcent
       t2=exp(YY/beta)*erfc((YY/(1.41421*sigma))+
     &    (sigma/(1.41421*beta)))
       tskew=tskew+t2
  700 continue
C
C     Now I do the convolution!
C
C     This sum is over the channel of the final response
C     function:

      do 702 ipos=1,NDATA
C
C     The next sum is over the centroid (i.e. the channels where
C     a kinematic response strength exists...this strength will
C     be the amplitude of the response function):
      rtot=0.0
      index=0
      do 710 zcentr=dcent-10.0,dcent+10.0,1.0
      index=index+1
      YY=ipos-zcentr
      t2=(1/tskew)*exp(YY/beta)*erfc((YY/(1.41421*sigma))+
     &   (sigma/(1.41421*beta)))
      t2=t2*str3(icent,index)
      rtot=rtot+t2
  710 continue
C
C     We have now summed up the 21 response functions at
C     the pt. ipos.  This is the unnormalized total response function:
C
      R2(icent,ipos)=rtot
      zres=zres+rtot
  702 continue
C
C     Now normalize the response function:
C
      do 720 ml=1,NDATA
      R2(icent,ml)=R2(icent,ml)/zres
```

```
 720 continue
C
      return
      end
C
C
      Subroutine Grkin2(Ep,theta,iang2,rkin)
C     This program calculates gamma ray energy for a particular
C     beam energy in the d(p,g) reaction. It should give the same
C     results as the program rkin, but I derived it independently
C     just so I would understand what's going on. All quantities are in
C     the lab frame.
C     -Greg Schmid, 9/94
C
      real iang2(21),rkin(21)
C     The following masses are in keV (i.e. E=M*c*c)
      Md=1875628.0
      Mp=938280.0
C     The following is the Q-value for the d(p,g) reaction in keV.
      Q=5494.0
C
      Mr=Mp+Md-Q
      it=int(theta+.5)
      jj=0
      do 810 l=it-10,it+10,1
      jj=jj+1
      thet=float(l)
      t1=(Ep+Q)**2
      t2=2*Mr*(Ep+Q)
      t3=Ep*(Ep+2*Mp)
      t4=2*(Ep+Q+Mr)
      t5=2*cosd(thet)*SQRT(Ep*Ep+2*Ep*Mp)
      Egam=(t1+t2-t3)/(t4-t5)
      iang2(jj)=l
      rkin(jj)=Egam
 810 continue
      return
      end
C
      Subroutine Step(icent,dcent,NDATA,IWID,FWHM,str3,R3)
C
C     This subroutine calculates a smoothed step function.
C
      real R3(100,200),str3(100,21)
      sigma=FWHM/2.354
      pi=3.1415927
      fac=1/(2*pi)
      sfac=sqrt(fac)
      zres=0.0
C     The first step is to normalize the response function:
```

```
      tstep=0.0
      ctop=dcent+IWID-icent
      do 900 ipos=1,NDATA
       YY=ipos-ctop
       t3=erfc(YY/(1.41421*sigma))
       tstep=tstep+t3
  900 continue
C
C     Now I do the convolution!
C
C     This sum is over the channel of the final response
C     function:

      do 902 ipos=1,NDATA
C
C     The next sum is over the centroid (i.e. the channels where
C     a kinematic response strength exists...this strength will
C     be the amplitude of the response function):
      rtot=0.0
      index=0
      do 910 zcentr=dcent-10.0,dcent+10.0,1.0
      index=index+1
      YY=ipos-zcentr
      t3=(1/tstep)*erfc(YY/(1.41421*sigma))
      t3=t3*str3(icent,index)
      rtot=rtot+t3
  910 continue
C
C     We have now summed up the 21 response functions at
C     the pt. ipos.  This is the unnormalized total response function:
C
      R3(icent,ipos)=rtot
      zres=zres+rtot
  902 continue
C
C
C     Now normalize the response function:
C
      do 920 ml=1,NDATA
      R3(icent,ml)=R3(icent,ml)/zres
  920 continue
C
      return
      end
```

References

[A&Z77] H.H.Anderson, J.F. Ziegler, *Hydrogen Stopping Powers...*, Pergammon Press, 1977

[Ald93] C. Alderliesten et al., NIM **A335**, 219 (1993)

[Am94] The QCD-1 from Amersham Corp., Arlington Heights, IL (1994)

[And77] D.A.Andrews, G. Newton, J. Phys. D **10**, 845 (1977)

[Bai70] G.M. Bailey, G. M. Griffiths, M.A. Olivio, R.L. Helmer, Can. Journ. Phys. **48**, 3059 (1970)

[Bai67] G.M. Bailey, G.M. Griffiths, T.W. Donnelly, Nucl. Phys. **A94**, 502 (1967).

[Bar71] H.H. Barschall, W. Haeberli ed. *Polarization Phenomena in Nuclear Reactions,* University of Wisconsin Press, Madision, Wisconsin xxv (1971)

[Bas72] R. Bass, S. Brinkmann, C. von Charzewski, H. Hanle, NIM **104**, 33 (1972)

[Bet50] H.A. Bethe, C. Longmire, Phys. Rev. **77**, 647 (1950)

[Bet37] H.A. Bethe, Rev. Mod. Phys. **9**, 69 (1937)

[Bev69] P.R. Bevington, *Data Reduction and Error Analysis...*, MacGraw-Hill, New York, 1969

[Bod66] P. Bodenheimer, The Astrophysical Journal **144**, 103 (1966)

[Bra89] B.H. Bransden, C.J. Joachain, *Introduction to Quantum Mechanics*, Longman Scientific & Technical, England, 1989

[Bru94] C.R. Brune, Ph.D. Thesis, California Institute of Technology, 1994

[Che91] C.R. Chen, C.L. Payne, J.L. Friar, B.F. Gibson, Phys. Rev. **C44**, 50 (1991)

[Chr61] R.F. Christy, I. Duck, Nucl. Phys. **24**, 89 (1961)

[Cle90] T.B. Clegg, Rev. Sci. Instr. **61**, 385 (1990)

[Cml94] C.M. Laymon, Circulated notes, TUNL, 1994

[Coe83] H.T. Coelho, T.K. Das, M.R. Robilotta, Phys. Rev. **C 28**, 1812 (1983)

[Coo79] S.A. Coon, M.D. Scadron, P.C. McNamee, et. al, Nucl. Phys. **A317**, 242 (1979)

[Del72] L.M. Delves, *Advances in Nuclear Physics,* Vol. 5, p.1-224, M. Baranger , ed., Plenum Press, New York, 1972

[Dev72] R.M. DeVries, J.L Perrenoud, Ivo Slaus, Nucl. Phys. **A188**, 449 (1972)

[Don67] T.W. Donnelly, Ph.D. Thesis, University of British Columbia, 1964

[Eml86] Emling, The GELIFT and GAGA peak fitting programs, Argonne National Laboratory (1986)

[Eis85] R. Eisberg, R. Resnick, *Quantum Physics of Atoms...*, John Wiley & Sons, New York, 1985

[Eva55] R.D. Evans, *The Atomic Nucleus,* McGraw-Hill, New York, 1955

[Fad60] L.D. Faddeev, Zh. Eksp. Teor. Flz. **39**, 1459 (1960)

[Fer65] A.J. Ferguson, *Angular Correlation methods...*, John Wiley & Sons, New York, 1965

[Fol57] L.L. Foldy, W. Tobocman, Phys. Rev. **105**, 1099 (1957)

[Fri92] J.L. Friar, Lectures presented at "Fifth Indian-Summer School on Intermediate Energy Physics," Sazava, Czechoslovakia, Sept. 6-11, 1992

[Fri91] J.L. Friar, B.F. Gibson, H.C. Jean, G.L. Payne, Phys. Rev. Lett., **66**, 1827 (1991)

[Fri90] J.L. Friar, B.F. Gibson, G.L. Payne, Phys. Lett. **B 251**, 11 (1990)

[Fri83] J.L Friar, B.F. Gibson, G.L. Payne, Z Phys.**A312**, 169 (1983)

[Gal95] D. Galli, F. Palla, F. Ferrini, U. Penco, The Astrophysical Journal, **443**, 536 (1995)

[Gam28] G.Z. Gamow, Z. Phys. **51**, 204 (1928)

[Gre66] R.M. Green, R.J. Finn, NIM **34**, 72 (1965)

[Gri63] G.M. Griffiths, M. Lal, C.D. Scarfe, Can. Journ. Phys. **41**, 724 (1963)

[Gri62] G.M. Griffiths, E.A. Larson, L.P. Robertson, Can. Journ. Phys. **40**, 402 (1962)

[Hae67] W. Haeberli, Ann. Rev. Nucl. Sci. **17**, 373 (1967)

[Hay62] C. Hayashi, R. Hoshi, D. Sugimoto, Suppl. of the Prog. Theor. Phys. **22**, 1(1962)

[Jac75] J.D. Jackson, *Classical Electrodynamics,* John Wiley & Sons, New York, 1975

[Jam77] F. James, M. Roos, *MINUIT*, CERN Computer Centre Program Library, 1977

[Jor77] H.H. Jorsch, J.L. Campbell, NIM **143**, 551 (1977)

[Jur82] E.T. Jurney, P.J. Bendt, J.C. Browne, Phys. Rev. **C 25**, 2810 (1982)

[Kie94] A. Kievsky, M. Viviani, S. Rosati, Nucl. Phys. **A 557**, 511 (1994)

[Kie93] A. Kievsky, M. Viviani, S. Rosati, Nucl. Phys. **A551**, 241 (1993)

[Kin84] S.E.King, N.R. Roberson, H.R. Weller, et. al., Phys. Rev. **C30**, 1335 (1984)

[Kin83] S.E.King, Ph.D. Thesis, Duke University, 1983

[Kle29] O. Klein, Y. Nishina, Z. Phys. **52**, 853 (1929)

[Kno89] G.F. Knoll, *Radiation Detection and Measurement,* John Wiley & Sons, New York, 1989

[Kra92] L.H.Kramer, Ph.D. Thesis, Duke University, 1992

[Kra88] K.S. Krane, *Introductory Nuclear Physics,* John Wiley & Sons, New York, 1988

[Laf82] J.M. Lafferty, S.R. Cotanch, Nucl. Phys. **A373**, 363 (1982)

[Lit70] A.E. Litherland, G.T. Ewan, S.T. Lam, Can. Journ. Phys. **48**, 2320 (1970)

[LWF59] L.W. Fagg, S.S. Hanna, Rev. Mod. Phys. **31**, 711 (1959)

[Ma95] L. Ma, TUNL, Private Communication

[Maz80] I. Mazzitelli, M. Moretti, The Astrophysical Journal, **235**, 955 (1980)

[Mit90] C. Mitterschiffthaler, P. Bauer, NIM **B48**, 58 (1990)

[Mon95] G.J. Schmid, The MONTE computer simulation, TUNL, 1995

[Mos65] S.J. Moss, W. Haeberli, Nucl. Phys. **72**, 417 (1965)

[Nel85] W.R. Nelson, H. Hirayama, D.W.O. Rogers, The EGS4 code system (SLAC-Report-265, SLAC, 1985)

[Pet91] C. Petitjean, et. al., *Proceedings of an International Symposium on Muon Catalyzed Fusion*, ed. J.D. Davies, Rutherford Appleton, 1990

[Pic92] A. Picklesimer, Lectures presented at "Hampton University Graduate Studies at CEBAF (HUGS)", CEBAF, Newport News, Va., 1992

[Rei68] R.V. Reid, Ann. Phys. **50**, 411 (1968)

[Ric95] B.J. Rice, G.C. Kiang, L. L. Kiang, TUNL, Private Communication.

[Rol88] C.E. Rolfs, W.S. Rodney, *Cauldrons in the Cosmos*, Univ. of Chicago Press, 1988

[Rol73] C. Rolfs, Nucl. Phys. **A217**, 29 (1973)

[Ros53] M.E. Rose, Phys. Rev. **91**, 610 (1953)

[Sat58] G.R. Satchler, Nucl. Phys. **8**, 65 (1958)

[Sey79] R.G. Seyler, H.R. Weller, Phys. Rev. **C20**, 453 (1979)

[Sta88] S.W. Stahler, The Astrophysical Journal **322**, 804 (1988)

[Sch95] Rocco Schiavilla, CEBAF, Private Communication

[Sch92] R. Schiavilla, R.B. Wiringa, V.R. Pandharipande, J. Carlson, Phys. Rev. **C45**, 2628 (1992)

[Sch37] L.I. Schiff, Phys. Rev. **52**, 242 (1937)

[Ter68] G.E. Terrell, M.F. Jahns, M.R. Kostoff, E.M. Bernstein, Phys. Rev. **173**, 931 (1968)

[Thw92] D.I. Thwaites, NIM **B69**, 53 (1992)

[Thw85] D. I. Thwaites, NIM **B12**, 84 (1985)

[Tor91] W. Tornow, G. Mertens, I. Slaus, H. Witala, et al., Phys. Lett. **B 257**, 273 (1991)

[Tor83] J. Torre, B. Goulard, Phys. Rev. **C 28**, 529 (1983)

[Vet85] M.C. Vetterli, Ph.D. Thesis, McMaster University, 1985

[Ver50] M. Verde, Helv. Acta **23**, 453 (1950)

[Viv95] M. Viviani, Pisa, Italy, Private Communication, 1995

[Wel95] H.R. Weller, Duke University, Private Communication

[Wel92] H.R. Weller, J. Langenbrunner, R.M. Chasteler, et. al., Atomic Data and Nucl. Tables, **50**, 29 (1992)

[Wel88] H.R. Weller, D.R. Lehman, Ann. Rev. Nucl. Part. Sci. **38**, 563 (1988)

[Wen52] W.A. Wenzel, W. Whaling, Phys. Rev. **87**, 499 (1952)

[Wha52] W.Whaling, W.A. Wenzel, Phys. Rev. **85**, 761A (1952)

[Wil93] W.S. Wilburn, Ph.D. Thesis, Duke University, 1993

[Wil52] D.H. Wilkinson, Phil. Mag. **43**, 659

[Wil74] J.R. Williams, Ph.D. Thesis, North Carolina State Univ., 1974

[Wir91] R.B. Wiringa, Phys. Rev. **C43**, 1585 (1991)

[Wir84] R.B. Wiringa, R.A. Smith, T.L. Ainsworth, Phys. Rev. **C29**, 1207 (1984)

[Wol49] L. Wolfenstein, Phys. Rev. **75**, 1664 (1949)

[Xu] Y.J. Xu, G.S. Khandelwal, J.W. Wilson, Phys. Rev. **A32**, 629 (1985)

Biography

Gregory Joseph Schmid

Personal: Born in San Francisco, CA, August 28, 1967

Education: High School Diploma, Henry M. Gunn Senior High School
Palo Alto, CA, June 1985

B.S. Physics, Rensselaer Polytechnic Institute (RPI)
Troy, NY, May 1989

M.A. Physics, Duke University
Durham, NC, December 1991

Ph.D. Nuclear Physics (expected), Duke University
Durham, NC, September 1995

Positions: Research Assistant in Nuclear Physics
Triangle Universities Nuclear Laboratory, 1991-1995

Teaching Assistant
Department of Physics, Duke University, 1989-1991

Research Assistant in Low Temperature Physics
Department of Physics, Stanford University, Summer 1989

Research Assistant in Solid State Physics
Department of Physics, RPI, 1988-1989

Research Assistant in Plasma Physics
Department of Electrical Engineering, RPI, 1987-1988

Publications: *Radiative Capture of Polarized Deuterons on ^7Li*
G.J. Schmid, R.M. Chasteler, C.M. Laymon, D.R. Tilley, H.R. Weller
Physical Review C **48**, 441 (1993)